Soft tissue structural assessment using mechanical measurements

<Matthias Richard Hien>

Submitted for the degree of Doctor of Philosophy

Heriot-Watt University

<Mechanical Engineering/EPS>

<July> <2010>

ABSTRACT

The overall aim of the work presented in this thesis is the development of quantitative relationships between the structure (histological make-up and/or tissue architecture) and the mechanical properties of soft biological tissue. The purpose of the research is to contribute towards the assessment of "tissue quality" using mechanical probing (instrumented palpation). The work focuses particularly on two case studies; the eyeball, where tissue quality relates to the corneal stiffness and the intra-ocular pressure (IOP); and the periodontal ligament (PDL), where tissue quality relates to the load displacement-time behaviour of teeth to which external forces are applied (such as in orthodontic treatment).

The experimental work involves static and dynamic testing of two porcine tissues (eyeballs and periodontal ligament) and also a mechanical system (mechanical eyeball) devised to investigate separately the components expected to influence mechanical behaviour; cornea stiffness, IOP, fluid inertia and leakage rate. Special test rigs were designed, calibrated and assessed for their measurement and process capabilities and the results were compared with quasi linear visco elastic (QLV) models to identify an appropriate mechanical way of characterising the tissue for comparison with its quality.

The larger part of the work concentrated on the eye with the ultimate aim of identifying symptoms of glaucoma more accurately. Dynamic testing identified a suitable indentation frequency range of 20Hz to 24Hz, the amplitude ratio in this range being capable of measuring IOP within an error of ±7mmHg which is only slightly above the ±5mmHg target for the latest tonometers. The cornea tissue was found to have 20% viscous behaviour and 80% elastic behaviour. The data were analysed using dynamic visco elastic models with an additional term for the inertia of the fluid in the eyeball. The work on the mechanical eyeball showed that it is possible to separate the effects of IOP and the stiffness of the cornea, which is of great significance in determining the true IOP, as opposed to one derived from a tonometer reading which makes assumptions about cornea stiffness.

The other main contribution is on the assessment of the periodontal ligament, which plays an important shock-absorbing role during mastication and is the initiator for orthodontic tooth movement (OTM), when loads are applied to teeth using orthodontic appliances. The force-relaxation behaviour of one lower premolar in pig mandibles was

measured and the resulting force relaxation curves analysed using three different visco elastic spring damper models. The analysis showed that, when longer relaxation times are allowed three or even four parameter models are not adequate to describe the behaviour. It is suggested that a more appropriate model is a multi component Maxwell model which uses more or less Maxwell components depending on the allowed relaxation time.

Overall, the work shows that instrumented palpation, supported by the development of suitable models can play a significant role in measuring tissue quality. Also, using simplified models of the stress-strain behaviour, it was possible to demonstrate that the measurements made here were in general accord with those reported in the literature for eyes, corneas and periodontal ligament.

ACKNOWLEDGEMENTS

I really have to thank Professor Reuben, for giving me the life time opportunity to do a PhD in Mechanical Engineering. Not just offering me a place, also the funding to do this research was offered by him through EPSRC. During the three years Professor Reuben always had time and advice for all my scientific problems, and with his calm and patient manner, working with him was always an exciting and instructional business.

I also want to thank the superintendent George Smith and the technicians Richard Kinsella and Cameron Smith who were very helpful during my time as PhD. Their experience made it possible to find fast, cheap and available solutions for daily problems and they have made big contribution to finishing all experiments within time. I am also very thankful to all secretaries at HWU who always had time to help through the administrative processes.

I am very much thankful to my wife Conny Hien for being always there for me and supporting me in daily life decisions. She gave up her job in Germany and had to find new opportunities in Edinburgh to support me in doing a PhD at Heriot Watt University.

Last but not least I want to thank my mother Marianne Hien, my father Josef Hien and my brother Stephan Hien for supporting my decision to go abroad.

Declaration

ACADEMIC REGISTRY
Research Thesis Submission

Name:	Matthias Richard Hien		
School/PGI:	School of Engineering and Physical Sciences		
Version: *(i.e. First, Resubmission, Final)*	Final	Degree Sought (Award **and** Subject area)	Doctor of Philosophy/Mech Eng

Declaration

In accordance with the appropriate regulations I hereby submit my thesis and I declare that:

1) the thesis embodies the results of my own work and has been composed by myself
2) where appropriate, I have made acknowledgement of the work of others and have made reference to work carried out in collaboration with other persons
3) the thesis is the correct version of the thesis for submission and is the same version as any electronic versions submitted*.
4) my thesis for the award referred to, deposited in the Heriot-Watt University Library, should be made available for loan or photocopying and be available via the Institutional Repository, subject to such conditions as the Librarian may require
5) I understand that as a student of the University I am required to abide by the Regulations of the University and to conform to its discipline.

* *Please note that it is the responsibility of the candidate to ensure that the correct version of the thesis is submitted.*

Signature of Candidate:		Date:	

Submission

Submitted By (name in capitals):	MATTHIAS RICHARD HIEN
Signature of Individual Submitting:	
Date Submitted:	

For Completion in Academic Registry

Received in the Academic Registry by *(name in capitals)*:			
Method of Submission *(Handed in to Academic Registry; posted through internal/external mail)*:			
E-thesis Submitted ***(mandatory for final theses from January 2009)***			
Signature:		Date:	

LIST OF PUBLICATIONS

1 Hien, M., Yang, T. H., Reuben, R. L., *et al.* (2008). "Dynamic measurement of intraocular pressure using a mechanical model of the human eye." *Stud Health Technol Inform*, 133, 112-22. (Chapter 4.2.2.2)

2 Hien, M., Reuben, R. L., Hammer, J., *et al.* (2008). "Physical and dynamic models of the eye for tonometry applications." *4th European Conference of the IFMBE*, 22, 2223–2227. (Chapter 4.2.2.2)

3 Tohill, R., Hien, M., McGuinness, N., *et al.* (2008). "Measurement of the short-term viscoelastic properties of the periodontal ligament using stress relaxation." *4th European Conference of the IFMBE*, 22, 1467-1470. (Chapter 4.3)

4 Tohill, R., Hien, M. R., McGuinness, N., *et al.* (2009). "Short-term stress relaxation of porcine periodontal ligament – finding an appropriate visco elastic model." *IFMBE proceedings series*, 25/11, 335-338. (Chapter 4.3)

5 Hien, M. R., and Reuben, R. L. (2009). "Dynamic palpation device to evaluate IOP; simulation on a mechanical eyeball system." *IFMBE proceedings series*, 25/11, 339-342. (Chapter 4.2.2.2)

LIST OF FIGURES AND TABLES

NOMENCLATURE

QLV	quasi linear visco elasticity
ECM	extracellular matrix
PDL	periodontal ligament
LEHI	linear, elastic, homogenous and isotropic material
POAG	primary open angle glaucoma
ACG	angle closure glaucoma
IOP	intra ocular pressure
AH	aqueous humour
SC	Schlemm's canal
EW	Schlemm's canal external wall
AC	anterior chamber
TM	trabecular meshwork
CCT	central cornea thickness
OTM	orthodontic tooth movement
GAT	Goldmann applanation tonometry
F_{CCT}	force to deform the centre of the cornea
F_{ST}	surface tension force
Cg	potential index for measurement system (gage potential index)
Cgk	capability index for measurement system (gage capability index)
xm	true value of master or standard
xg	average of measurement system
T	tolerance
LSL	lower specific limit
USL	upper specific limit
Cp	process performance
Cpk	process capability
E*	complex modulus
E_L	loss modulus
E_S	storage modulus
MRI	magnetic resonance imaging
MRE	magnetic resonance elastography

RF	radio frequency
B_0	permanent magnetic field of an MRI (normally 1.5T)
BPH	benign prostate hyperplasia
TURP	transurethral resection of the prostate
DRE	digital rectal examination
SLS	standard linear solid (three parameter model)
DRIE	deep reactive ion etching

TABLE OF CONTENTS

Chapter 1: Introduction

The aim of this research was to investigate how the structure of soft biological tissue can influence its mechanical properties, with a view to using mechanical measurements to help make clinical diagnosis.

A mechanical method called “instrumented palpation” through which the mechanical properties of the tissue are measured in much the same way as they might be by a physician pressing on the surface. The effectiveness of indentation testing is based on the fact that many diseased or abnormal tissues change their mechanical behaviour, and instrumenting the palpation process allows a record of the force-deflection history to be kept in order to create a data-base of tissue quality within and between patients. Cancer, for example, produces very different cell types to the surrounding tissue, and leads to a local stiffening, which can often be detected as a lump, measured stiffening of the tissue [1]. However, the current work recognises that most biological tissues are visco elastic and that changes in mechanical properties may be more subtle than simply a change of elastic modulus. Accordingly, part of the work is devoted to finding visco elastic models which can appropriately describe the tissue behaviour under static and dynamic testing.

Two quite different systems were used where the mechanical properties of tissue may be of use and the specific objectives are associated with these. In the first of system, the objective was to identify and understand how, within the complex structure of the eyeball including the cornea, sclera and aqueous humour, a mechanical device might be able to measure the intraocular pressure (IOP) in a way that is independent of other effects, such as that of the cornea thickness or its creep behaviour. In the second, the objective involved the mechanical behaviour of orthodontic tooth movement (OTM) in the short-term, where the periodontal ligament (PDL) plays a major role. Here the focus was which visco elastic model can best describe the force relaxation curve and what frequencies and displacements can be used to design an *in vivo* device to measure PDL properties on the patient.

This chapter introduces the two different systems studied with a brief description of the purpose of measuring structural behaviour. This is followed by a chapter-by-chapter summary of the thesis.

1.1 Measuring IOP as an indicator of glaucoma

Over the past century, many scientists have developed devices to measure the pressure in the eyeball more and more accurately and efficiently. The pressure in the eyeball is of interest because it is not constant in each human being and a heightened IOP can cause visual distortion and, ultimately, blindness. It is not the pressure itself which causes the visual distortion, but rather that it squeezes the optic nerve and, in extreme cases, may sever it entirely. Thus, the higher the pressure in the eyeball is, the more likely it is that the optic nerve will be damaged.

There are several causes of increased IOP, all of them known under the generic term "Glaucoma". The risk of glaucoma increases with age with a 2% recorded incidence at age 40 rising to 10% at age 75 [2]. With early diagnosis, there is a good chance of treating glaucoma using drugs which reduce the pressure by making the cornea more permeable or by reducing the production of aqueous humour [3]. Also laser treatment has been mentioned as a good method to reduce the IOP by cutting several small scars in the trabecular meshwork which help to increase the flow of fluid out of the eye [4].

However, there still remains the problem of detection of glaucoma. The most accurate device on the market is the so-called Goldmann applanation tonometer (GAT). This device deforms the cornea until a certain area of the indenter is parallel with the cornea. The force required to deform the cornea to this shape is related to the IOP. In the original design, Goldman acknowledged [5, 6] that the relationship is only valid for an average cornea thickness, an average cornea stiffness and an average cornea creep behaviour.

This leads to the point, weather the dynamic palpation method can be used to filter variations in CCT, IOP and creep behaviour. The visco elastic models help to define parameters which can be used to separate for example CCT and IOP. In order to seek an improvement, a dynamic palpation method has been devised in this work, whereby the cornea is deformed at certain frequencies and predefined displacements. A piezo driven actuator provides an oscillating displacement of an indenter at frequencies up to 60 Hz, while a load cell carried on the actuator records the force required to deform the cornea. This set-up was used to study the time dependent force-displacement behaviour

under a range of IOP. Static force relaxation tests were also performed on pig eyeballs to compare the possible visco elastic models.

1.2 Identifying PDL properties to optimise OTM

Orthodontic tooth movement is the clinical process of realigning teeth using sustained forces and moments, applied using a system of wires and brackets, known as braces. Any given treatment is a compromise between the speed, measured in terms of rate of tooth movement, and possible side-effects, such as pain and root resorption.
A force applied for the purpose of OTM is conditioned by the deformation of the periodontal ligament (PDL) which separates the tooth and the mandible. PDL is therefore very important as it acts like a shock absorber to protect bone and tooth from damage due to impact and controls the way in which force is supported at the tooth-mandible interface. Understanding the short-term visco elastic behaviour of PDL will help to optimise the OTM within the first few days [7, 8], but it is also possible that individual long-term responses may be predictable from short-term visco elastic behaviour. More generally, the PDL is the most accessible tissue of this type in the human body, being easily loaded *in vivo* through the relatively undeformable tooth, and its study can contribute generally to understanding of the *in vivo* behaviour of tissue.

Pig mandibles were used to study the visco elastic behaviour of PDL, in this work in order to assess the likely range of properties which might be encountered in human subjects. A test rig was devised to displace the tooth by a fixed amount and the relaxation of the force with time was recorded. A range of visco elastic models of various orders were fitted to the relaxation curves in order to obtain the visco elastic parameters of the PDL over different time periods to give a sense of the importance of the length of the *in vivo* measurement in describing the deformation behaviour. It furthermore gives important knowledge about designing of a new *in vivo* device which can be used on Patients.

1.3 Mechanical systems and models

Two types of test were used in the work in order to determine mechanical properties, stress relaxation and dynamic testing. In both cases, displacement control was used and the resulting forces recorded and the output of experiments was the force-time response from a given pattern of displacement. Stress relaxation testing has the advantage that a wider range of orders of models can be investigated because the relevant differential equations can be solved analytically. Dynamic testing has the advantage of a high degree of averaging and the opportunity to use patterns of response with frequency to give additional identification of behaviour compared with models. The majority of the eyeball experiments were carried out dynamically, whereas the majority of the PDL experiments were carried out statically. The reason for this was that the diagnostic target of the eye palpation is not so much cornea properties (although these are measured), but IOP, whereas it is of much more interest in the PDL to know what type of model is appropriate to describe the deformation behaviour.

The mechanical system of an eyeball can be considered as a thin visco elastic shell (the cornea), fixed around the edges by a relatively stiff visco elastic material (the sclera) and backed by a damping material (the vitreous humour under the IOP). The dynamic behaviour can therefore be described by using a visco elastic model consisting of springs and dampers, although, in some instances, it was necessary to use an inertial term. The role of springs and dampers in an oscillating system is shown schematically in Figure 1-1. After the pre-installed (mean) displacement has been reached, the indenter will oscillate around this value at the predetermined frequency Figure 1-1 a). The force response combines in-phase, spring like features (Figure 1-1 b) corresponding, say, to elastic stretching of fibres in a tissue, and dashpot-like features (Figure 1-1 c) which are 90° out of phase in the way that liquid would behave in a tissue. In a given tissue both components are present and therefore the phase will be between 0 and 90° (Figure 1-1 d) and will vary with frequency in a way that is characteristic of the system.

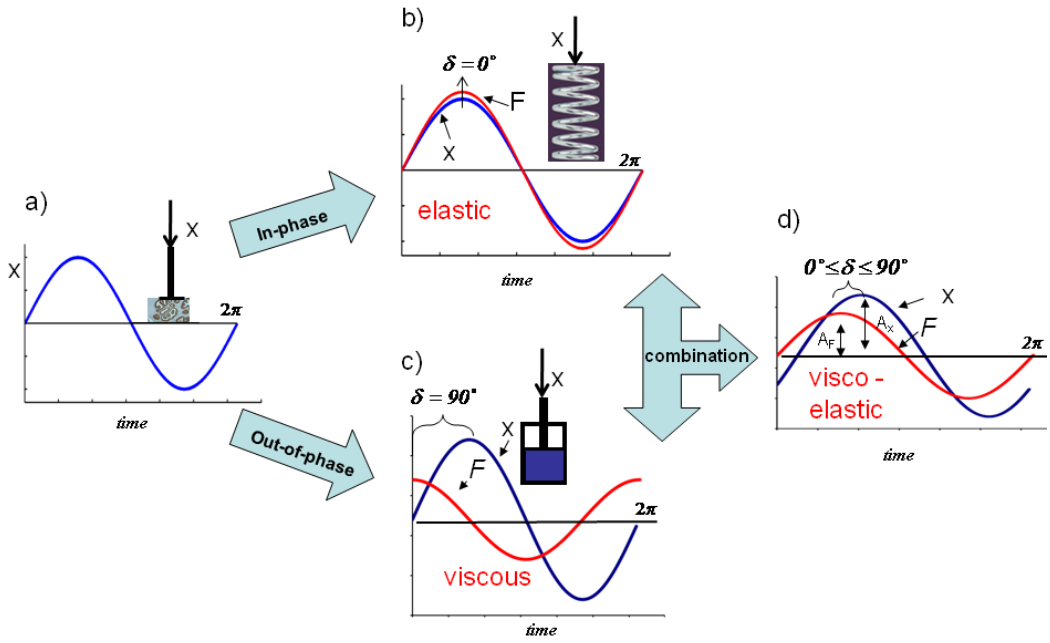

Figure 1-1: Schematic diagram of a visco elastic material compared with spring and damper

The mechanical system of the PDL can be considered as a visco elastic bearing, interpolated between two relatively undeformable components (tooth and mandible). Applying a force to the tooth results in compression of one half of the PDL and tension in the other. A static test method was applied which measured the force relaxation of the PDL during time by simply displacing the tooth in the socket.

1.4 Thesis structure

The thesis consists of 8 main chapters which will be described briefly in the following:

Chapter 1 gives the essential clinical background motivating the work. It furthermore defines the essential mechanical engineering science used and describes how this is brought to bear to address the clinical aims and introduces the instrumented palpation method to identify the quality of soft tissue.

The literature review in Chapter 2 first discusses some general issues about tissue quality, particularly the role of structure-property relationships in diagnosis. Next the anatomy of the eyeball, the importance of aqueous humour for IOP and the most important kinds of glaucoma are described, followed by a critical review of current devices and measurement systems for IOP. Next, the context of orthodontic treatment

mechanics is described and such research as has been done on the properties of the periodontal ligament discussed. The final section examines methods that have been used to characterise the mechanics of soft tissue with a critical review of their ability to identify mechanical properties.

Chapter 3 first describes the quasi linear viscous (QLV) models that have been used to analyse both static and dynamic measurements and introduces a new type of model including an inertial term for systems where this is relevant. Some of the models have already been solved for static and dynamic palpation, and new solutions are presented for others.

Chapter 4 first describes the sensors and the measurement process capability followed by the process capability of all actuators. Next, the three experimental arrangements are described; the "mechanical eyeball" simulation of the cornea and vitreous humour for IOP assessment, the corresponding set-up for porcine eyeball measurements and the set-up for measurement on the periodontal ligament in porcine jaws. Finally, the methods of data processing are described in preparation for the analysis of the results using the various visco elastic models developed in Chapter 3.

Chapter 5 presents the results of the experiments for the three experimental arrangements studied; the mechanical eyeball, the porcine eyeballs and, finally, the porcine jaws. The treatment of the results for the mechanical eyeball is focused on the capability of the experimental configuration and also the balance between the behaviour of the mechanical cornea and the mechanical aqueous humour. The results for the biological materials yield specific mechanical models and their associated properties.

Chapter 6 discusses the significance of the experimental measurements made in four areas. Firstly, the mechanical eyeball is discussed in terms of its usefulness to separate the IOP, cornea and drainage effects in a real eyeball *in vivo* and more generally on how dynamic palpation can be used to separate the contributions from components which are more fluid-dominated from those which are more solid-dominated in multi-component biological architectures. This prepares the way for a discussion on how the results from the mechanical eyeball and those from the porcine eyeball can be combined using the damper parameter to address the potential for enhanced IOP measurement. Next, the

clinical application of *in situ* measurements on human teeth is assessed and, finally, the general contribution in the area of soft tissue mechanical properties is discussed, focussing on the mechanical properties measured and how these compare with the work of other authors.

Chapter 7 forms the overall conclusion of the work that was done and the relevant contribution to science.

Chapter 8 describes on-going and future work arising from the contribution made in this thesis, including a description of improvements or modifications for the test rigs for further *in vivo* and *in vitro* studies.

Chapter 2: Literature Review

The subject of this research is to investigate the use of mechanical measurements to assess soft biological tissue with specific reference to two cases; the eye and the periodontal ligament, the focus of interest being on human tissue.

This literature review will first discuss some general issues about tissue quality, particularly the role of structure-property relationships in diagnosis. Next, the condition of glaucoma is described, followed by a discussion of the state-of-the-art in ocular tonometry and the role of cornea properties. The second case is introduced in the context of orthodontic treatment mechanics, and such research as has been done on the properties of the periodontal ligament and other relevant soft tissues is reviewed. The final section examines methods that have been used to characterise the mechanics of soft tissue with a critical review of their ability to identify mechanical properties.

2.1 Biomechanics and soft tissue

"Biomechanics" has been described by Fung as "mechanics applied to biology" [9], although others (e.g. Humphrey [10]) are more inclusive: "Proteins, cells, tissues, organs and organisms reveal an incredible spectrum of material structures and properties, which in turn govern their wonderfully diverse functions".

Biomechanics can be more precisely defined as "the development, extension, and application of mechanics to answer questions of importance in biology and medicine" [11]. This definition encompasses the fact that biomechanics can help to understand the cause of diseases and injuries and also assist diagnosis and treatment. New technologies and inventions offer the possibility to make more and more sophisticated measurements on tissue, histological components and even cells, many of these mechanical in nature. The motivation of the current research is specifically to contribute to the understanding of the relationship between mechanical measurements and the structure of the tissue being probed, "structure" being interpreted in its broadest sense.

Compared with engineered materials, biological tissues have very complex structures which have evolved to fulfil biological functions as well as mechanical ones. One example of such adaptation is the anisotropy of many biological structures which are stiffer or stronger in a direction of most significant loading, a property which can even be enhanced, or deteriorate, during life. For example, tendons can withstand high pulling forces and bone and cartilage are able to withstand high compression forces [12], and their properties can change with time during healing and/or training processes. For soft tissue, which is not "structural", this adaptive aspect usually means that the tissue is only as robust as necessary to fulfil its function, but it is recognisable that certain conditions of soft tissues (e.g. disease and/or injury and/or inflammation) can disproportionately affect their mechanical properties, somewhat in contrast to hard tissue.

Biological tissues generally consist of cells and extracellular matrix (ECM), which fills the spaces between the cells. The ECM is primarily made of protein fibres (such as collagen, elastin and reticulin), the ground substance (non fibrous protein and other molecules) and a viscous substance that consists mainly of water [11, 13]. There are two different kinds of tissues; hard tissues (e.g. bone and tooth), and soft tissue. All viscera, muscle, skin and vessels are composed of soft tissue, and this work is focused entirely on non-skeletal supporting or connective tissue.

To describe such tissue structurally it is convenient to identify a structural matrix, and the nature and proportion of this matrix, relative to the watery ground substance, which acts rather like a gel [14], and other watery components. Together with the internal pressure (which may locally be elevated in some components), these components will dominate the mechanical characteristics of the tissue and, since a liquid or gel component is involved, it might be expected that the mechanical characteristics will be viscous. The structure of soft tissue can therefore be regarded as a composite and, like engineering composites, the scale of mixture (i.e. sizes of the structural elements) can have as much influence on properties and their measurement as the proportions of the components and their individual properties. For example, prostate tissue consists of an intimate mixture of collagen/muscle matrix with watery glandular components, whereas the eye can be regarded as a much coarser-scale composite with the collagenous cornea and sclera, surrounding a macroscopic watery component.

The two most common protein fibres of the ECM are elastin and collagen. Both are discussed briefly below, including their mechanical behaviour and properties.

2.1.1 Elastin

As its name suggests, elastin exhibits mostly elastic behaviour with an almost linear tensile stress – strain characteristic up to a certain extension. Elastin is a protein and found in all vertebrates. It is present in skin, the walls of arteries and veins, and lung tissue. Fung [9] has carried out uniaxial tensile tests at a constant (although unspecified) strain rate on elastin. He used bovine *ligamentum nuchae*, which consists mainly of elastin and has measured a Young's modulus of about 0.6MPa up to extensions of around 15%. Elastin is nonlinear and exhibits hysteresis under loading and unloading, although the differences between the loading and unloading curves remain very small up to an extension of 60% [15]. Non-linearity and creep in elastin had been observed somewhat earlier by Carlton [16], who also tested elastin from bovine *ligamentum nuchae*. He noted that single elastin fibres micro dissected from a short fragment (5mm × 1mm ×1mm) had less deformability and dissimilarity in stress-strain behaviour than strips (70mm × 3mm × 3mm) which contained bundles of elastin fibres. He explained this in terms of the configuration of the elastic network in the strip, which improves the ability to stretch as fibres can slide or shift along the network, in a similar way to networks in chain-forming engineered polymers [17]. Humphrey [11] showed a linear force – deformation curve for equine *ligamentum nuchae* (from earlier work by Hoeve and Flory [18]) with a strain of up to 50%, which suggested a Young's modulus of about 0.3MPa at 0.5 °C, increasing to 0.4MPa at 50.5°C. Here, again, no strain rate was mentioned. The tensile secant modulus E_{sec} of purified elastin (8 h autoclaving at 103kPa) from porcine aorta was measured in the circumferential direction by Lillie and Gosline [19, 20] by carrying out linear regression fitting to stress-strain data. They found E_{sec} to change with the position of samples obtained from the descending thoracic aorta. The ring section samples (Figure 2-1) were tested to two different strains, 20% and 70%, although the change in Young's modulus by varying the final strain was within 1%. The values of secant modulus were 0.88MPa in the proximal tissue close to the aortic arch and 1.2MPa in the distal tissue near the diaphragm. The axes of the elastin fibres in the aortic walls are predominantly in

circumferential or longitudinal direction, although the proportion of elastin fibres between these two might change with position. A higher circumferential Young's modulus therefore means that more fibres are aligned in the circumferential direction and so Lillie and Gosline concluded that the anisotropy ratio of circumferential to longitudinal fibre direction increases from the proximal descending thoracic aorta to the distal tissue near the diaphragm.

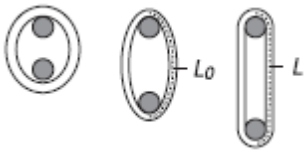

Figure 2-1: Tensile test on a descending thoracic aorta ring section from [19]

2.1.2 Collagen

Collagen is also a type of protein and is the main component of soft and hard connective tissue [9, 21], making up one quarter to one third of the total body protein [12]. Collagen owes its good mechanical properties to a hierarchical nano- to micro-structure whose basic element, the collagen molecule, can be regarded as a microscopic rope consisting of three polypeptide chains coiled together (Figure 2-2). Each chain consists of a combination of amino acids and is differentiated by the number and order of amino acids present. The length of each rope of polypeptide chains is around 300nm with a pitch of 8 – 9 nm between the chains, which are themselves about 1.5nm in diameter (Figure 2-2). Groups of collagen molecules form themselves into fibrils (10-500nm in diameter) and the fibrils in turn assemble into collagen fibres (1-500μm in diameter) (Figure 2-3). The organisation and orientation of collagen fibres, cells and ground substance (mostly water) form the tissue and determine its mechanical properties, much in the same way as do fibre reinforced engineered composites. Collagen exists in fibril and non-fibril forming structures, where the fibril forming structures provide mechanical strength [22, 23]. Aqueous humour, for example, includes non-fibril forming Type II collagen and will not therefore strengthen the eyeball structure. Up to now, 29 distinct collagen types have been identified [24] with Type I collagen being the most abundant, found throughout the human body [22]. Besides Type I collagen three other collagen types are relevant to this research, Type III, found in PDL [25], Type II in vitreous humour and Type V in cornea. Sun *et al.* [26] have observed that Type I

collagen has a Young's modulus of 350MPa, slightly higher than Type II collagen (here as fibril forming structure), with a modulus of 270MPa. Here the Young's modulus was derived from the persistence length, which is an indicator of Young's modulus of a polymer chain and was given by Sun *et al.* [27] as 11.2 nm for the Type II collagen and 14.5nm for Type I. The persistence length was measured using an optical tweezers/interferometer system, which stretches molecular chains and measures the molecular strain. The procollagen molecule was adhered between two beads each of diameter 2.2 μm and one of the beads was moved away from the laser beam centre at a strain rate of $24s^{-1}$.

The main differentiating features between the different types of collagen are their molecule chain length, their three dimensional structure, their chain composition and the degree of glycolisation (process to link carbohydrates to proteins) [9]. Table 2-1 summarises the key structural features of types of collagen relevant to this research.

Type	Structural features	Representative Tissue
I	300-nm-long fibrils with two out of three different α- chains*	Skin, tendon, bone, ligaments, dentin, interstitial tissue
II	300-nm-long fibrils with three equivalent α- chains*	Cartilage, vitreous humour
III	300-nm-long fibrils with three equivalent α- chains*; often with type I	Skin, muscle, blood vessels, 20% in PDL[25]
V	390-nm-long fibrils two out of three different α- chains*	Cornea, teeth, bone, placenta, skin, smooth muscle

*each of the collagen types has a distinct number and order of amino acids

Table 2-1: Selected collagen types and their presence in tissues and structural features, compiled from [9, 28]

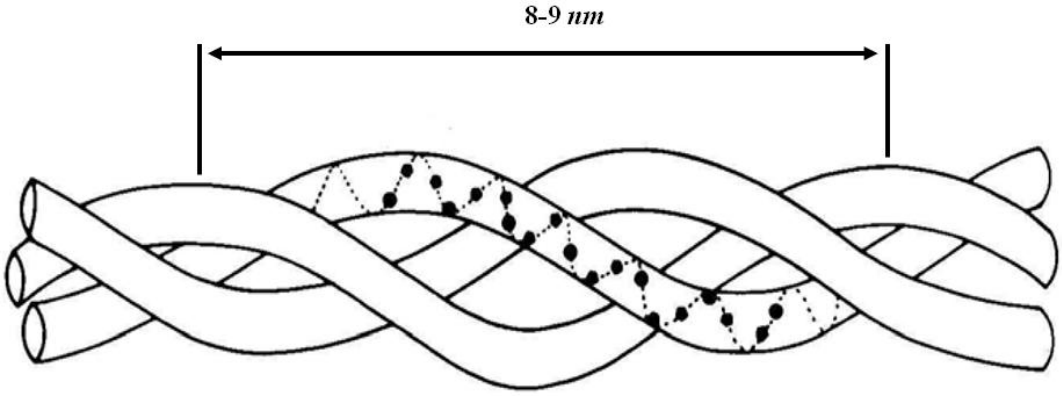

Figure 2-2: Collagen triple helix, from [9]

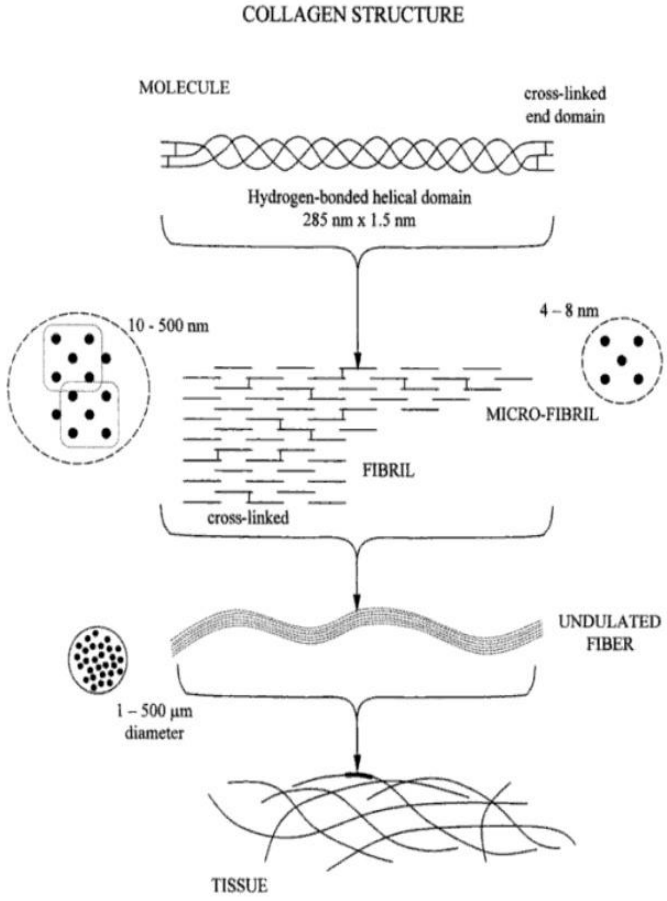

Figure 2-3: Collagen structure from molecule to tissue, from Humphrey [11]

More relevant to this research, the mechanical properties of various collagen types have also been widely investigated using tensile tests carried out on tendons at constant strain rate [23, 29-31]. The animal source of the tendon (e.g. from pigs, rats, sheep, cattle or chickens) does not appear to have a major influence on the mechanical properties

compared with the sample conditions. Hydrated collagen Type I samples from bovine Achilles tendons (tested in phosphate buffered saline) exhibited a Young's modulus of 0.6±0.2GPa, which was lower than, dried samples (dried for 24 hours in ambient air) with a range of 2.5±0.9GPa [22, 32]. More detailed tests of tendon behaviour were carried out by Wu *et al.* [33] and Lynch *et al.* [34], who both varied the strain rate. Wu *et al.* worked with chicken tendons (tested in Bioplus bath containing physiological saline solution) and measured the Young's modulus at 427±10MPa, 653±21MPa and 837±11MPa for strain rates of $0.006s^{-1}$, $0.012s^{-1}$ and $0.05s^{-1}$, respectively. Lynch *et al.* divided the stress strain curves for sheep tendons (not dried but measured in ambient air) into two sections (initial "toe" and linear section) the gradient of the toe section always being smaller than that of the later linear section. The gradient of the toe section was 13.9±7.7MPa and 11.6±8.7MPa for a strain rate of $0.01\%s^{-1}$ and $1\%s^{-1}$ respectively and the material was therefore not considered to be strain rate sensitive. The modulus of the linear section was 58.5±22.62MPa for a strain rate of $0.01\%s^{-1}$ compared with 66.4±36.8MPa at a strain rate of $1\%s^{-1}$.

Puxkandl *et al.* [29] used an X-ray diffraction technique to monitor fibril elongation while stretching the whole tendon. The strain of a fibril (ε_D) was always strain rate related and smaller than the strain of the whole tendon (ε_T). The explanation is illustrated in Figure 2-4 where the whole tendon is stretched with a strain ε_T and the collagen fibrils (*cf*) slide or shear along the fibre direction. The proteoglycan-rich matrix (*pg*) between the fibrils makes the sliding possible and the friction between the two adjacent fibrils is strain rate related.

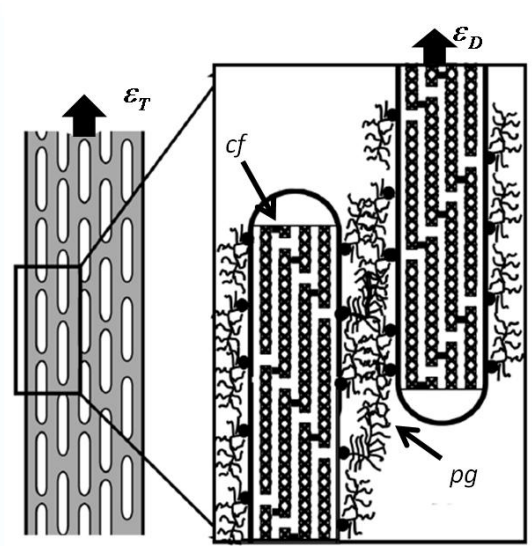

Figure 2-4: Elongation of a tendon, where the fibrils and the pg share the whole deformation, from [29]

Other workers [22, 35] have carried out tests on the fibrils themselves. Using the AFM as an indenter, Wenger *et al.* [35] measured a Young's modulus of 5-11.5GPa on rat tail tendon. Yang [22] did a tensile test on collagen Type I fibrils with an AFM at different strain rates ($2.5\times10^{-3}s^{-1}$ and $0.25s^{-1}$) and found that the hundredfold increase in strain rate resulted in a 60% increase in Young's modulus from 1.6 to 2.6GPa for tests in ambient air. The same test for fibrils in saline solution resulted in a smaller Young's modulus of 0.70GPa at a strain rate of $2.5\times10^{-3}s^{-1}$ increasing to 0.94GPa at a strain rate of $0.25s^{-1}$.

The variation of Young's modulus with strain rate suggests visco elastic behaviour, although relatively few researchers have determined visco elastic properties for collagen. Stromberg and Wiederhielm [21, 36] investigated the creep behaviour of mouse tendon by holding the load constant and measuring the strain with time. By assuming a three parameter standard linear solid (SLS) model (see Chapter 3) and fitting its associated exponential creep function to the data, these authors obtained values of 8×10^3MPa, 2×10^3MPa and $1.7 \times 10^5 Ns/m^2$ for the parameters E_{Kelvin}, E_{spring} and η_{Kelvin}, respectively.

Hubbard and Chun also considered visco elastic behaviour in analysing the results of their tests on canine tendons. The tendons were tested cyclically in tension up to 4 different strain levels (2%, 3%, 4%, 6%) at a constant strain rate of $5s^{-1}$. A power law function was used to describe the non linear stress-strain behaviour [37]:

$$\sigma = \alpha(\varepsilon - \varepsilon_s)^{\beta} \tag{2-1}$$

where σ and ε are stress and strain, ε_s is the "slack strain" which is the difference between initial strain (first cycle) and the smallest strain to initiate load bearing in the specimen, α is the scale factor and β is the power coefficient which describes the nonlinearity of the stress strain curve. With increasing strain level, the slack strain between cycles 2 and 4 increased significantly; for example at a 2% strain level a slack strain of 0.6% occurred at the second cycle, whereas the equivalent slack strain at a 6% strain was 1.0%. After the fourth cycle the slack strain was 0.7% for the 2% strain level and 2.7% for the 6% strain level. The power coefficient β showed similar behaviour with values of 1.7 for 2% strain level in the first cycle increasing to 2.1 for the fourth

cycle. The strain level of 6% had values of 1.9 and 2.1 for the first and fourth cycle respectively. The scale factor α remained constant between the different strain levels at 20GPa.

2.2 Glaucoma and the role of ocular tonometry

The World Health Organisation has estimated that, around the world, about 12.5 million people go blind from glaucoma and as many as 66 million are affected by this disease. In the United Kingdom, 2% of people older than 40 have primary open angle glaucoma (POAG) and this increases to almost 10% for people older than 75 years [2]. The UK has 150 000 patients diagnosed with glaucoma and The National Collaborating Centre for Acute Care in UK, have estimated that about the same number of people remain undiagnosed [2].

There are several different kinds of glaucoma, but all have a common disease pattern which starts with optic visual field loss with the final stage being blind. The two most common glaucoma diseases are primary open angle glaucoma (POAG), having a slow and not-so-noticeable onset, and angle closure glaucoma (ACG), which tends to be more recognisable. Measuring intra ocular pressure (IOP) is a reliable method of identifying the disease and its progress [2]. In order to offer an approach to measuring IOP, it is important to understand elements of the anatomy of the eye, the functions of the various components and how these functions are affected by glaucoma. Sections 2.2.1 to 2.2.5, therefore, offer a brief overview of important parts of the eyeball and their function, where especially the cornea and its mechanical properties will be discussed, followed by the conditions that intensify the development of glaucoma. Section 2.2.6 reviews the most important tonometers and compares their advantages and disadvantages.

2.2.1 The eye

The human eye is situated in a cavity in the skull (the orbit) which protects it from injury. An eyeball typically has a diameter of 24mm and weighs about 7.5 grams. The eyeball comprises two outer segments, the anterior and posterior. The posterior

segment is the larger part of the sphere and accounts for about 5/6 of the volume. It includes the back portion of the eye with the vitreous body. The anterior segment, which includes the front part of the eye (iris, lens, cornea and aqueous humour), again is divided into anterior and posterior chamber [13, 38]. The separation between anterior chamber and posterior chamber is made by the iris and the lens, where a small pathway (posterior pathway) between iris and lens connects the two chambers. This pathway allows the flow of aqueous humour from the posterior chamber to the anterior chamber. The outer envelope of the eye consists of three layers or tunics, the outer, fibrous tunic (cornea and sclera), the intermediate vascular tunic (iris, ciliary body and choroid) and an inner neural tunic (retina) (Figure 2-5).

Aqueous humour, which is produced in the posterior chamber, helps to maintain the pressure in the eye and gives both segments (anterior and posterior) their spherical shape. Without this fluid, the three tunics would not be stiff enough to hold their shape [39]. The shape of the eye is important to obtain the best visual field and a constant pressure of about 2.1kPa (about 16mmHg) is required in order to maintain shape.

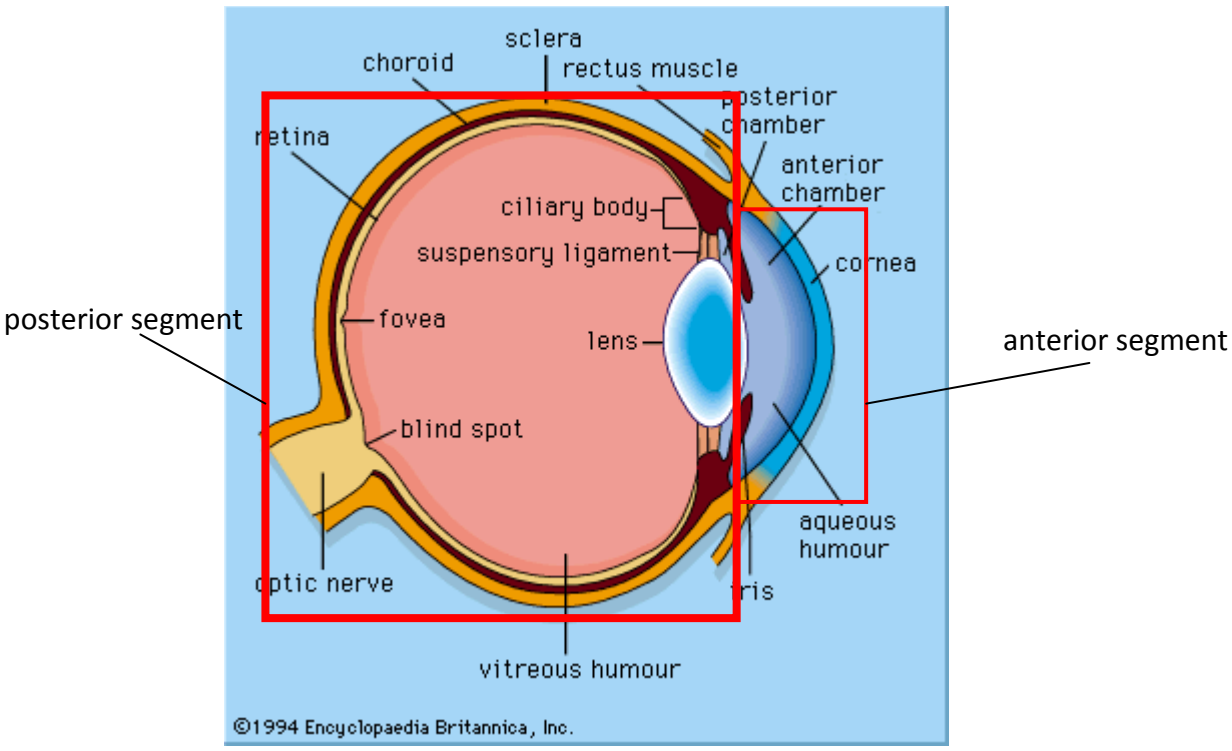

Figure 2-5: Sagittal section of a human eyeball [40]

2.2.2 Aqueous humour and its flow in the anterior segment

The ciliary artery supplies the eyeball with the blood from which the aqueous humour is filtered out [41]. The aqueous humour is secreted from epithelial cells in the ciliary body's ciliary processes [42]. The epithelial cells regulate the secretion rate which is typically 1.5-3.0µl/min and the humour also supplies the anterior chamber (AC) with nutrients and oxygen [43-46]. The filtration and transport of aqueous humour is an energy consuming process and reduces the pressure from ciliary artery pressure, about 60mmHg (8.0kPa), to an average pressure of about 16 mmHg (2.1kPa) which is acting in the healthy human eyeball [47]. Although the pressure drop can be seen as a function produced by a pressure control valve, the main task of the ciliary body is to produce a sufficient amount of liquid [41, 48] (Figure 2-6).

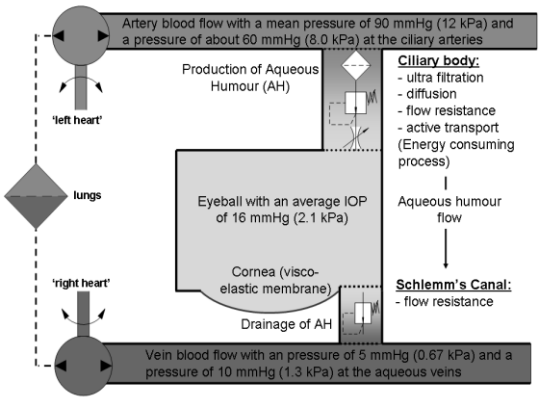

Figure 2-6: The flow and pressure drops of aqueous humour within the blood circulation

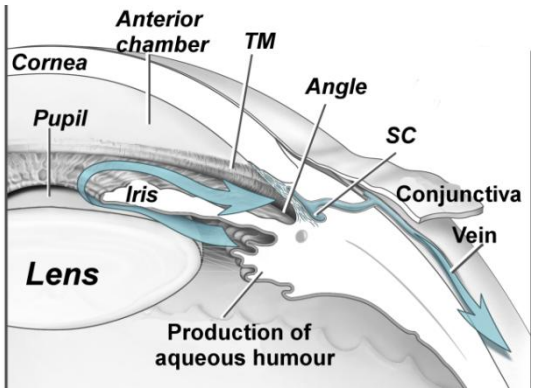

Figure 2-7: Aqueous humour flow in the anterior segment [49]

From the posterior chamber, the fluid proceeds through the posterior pathway, which is defined by lens and iris, to the anterior chamber (Figure 2-7).

A regular flow of aqueous humour passes through a spongy tissue, known as trabecular meshwork (TM), and Schlemm's canal (SC). Flexing of the TM pumps aqueous humour from the anterior chamber to SC through a series of valves spanning SC. The valves deliver the aqueous humour further on to veins in the sclera [38, 50, 51]. The aqueous flow is controlled and powered by the pressure difference during systole and diastole of the cardiac cycle, the respiration, blinking and eye movement [51]. The residence time of approximately 100 minutes of the fluid allows the exchange of nutrients and waste to and from the lens and cornea [43, 52]. A pressure drop of about 0.8kPa (6 mmHg) occurs as the aqueous humour progresses into the aqueous veins but

this pressure drop can increase drastically in eyes affected by glaucoma [52]. Figure 2-8 illustrates how a pressure increase causes the aqueous valves within the TM to compress, decreasing the lumen drastically and reducing outflow and therefore causing an accumulation of AH leading to still higher IOP [51, 53]. The maximum pressure that can occur in an eyeball is set by the highest pressure level in the ciliary artery, which is, on average, about 60mmHg (8.0kPa) (Figure 2-6). Beswick *et al.* [54] and Heys *et al.* [55] define the trabecular meshwork permeability (k_{TM}) which they estimate to be $2.1 \times 10^{-9} ms^{-1}Pa^{-1}$ for normal IOP.

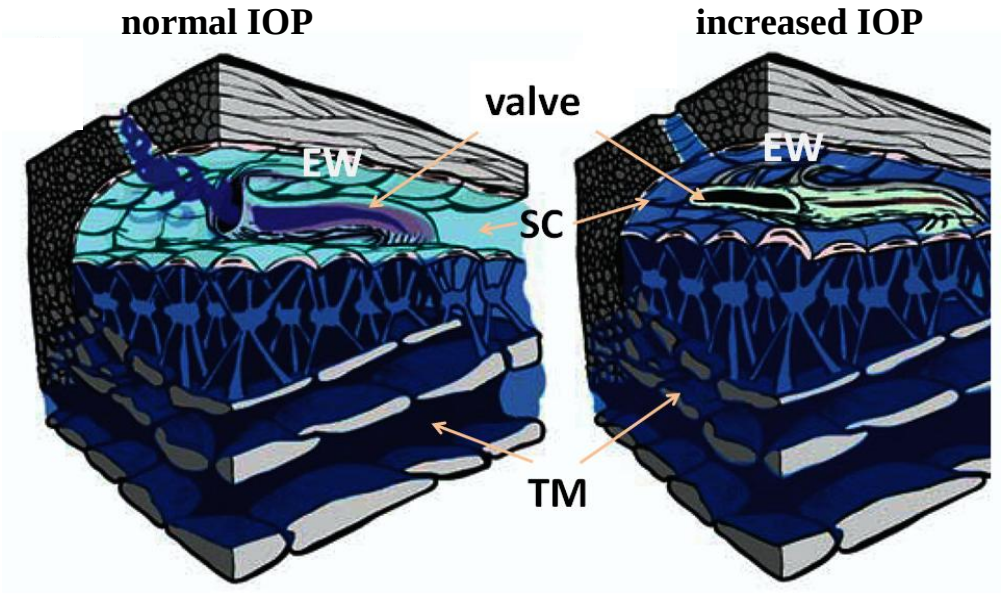

Figure 2-8: Outflow of aqueous humour through the trabecular meshwork (TM) for normal IOP and increased IOP. The valves for increased IOP between the external walls (EW) of Schlemm's canal (SC) are compressed so decreasing the lumen size. From [51]

2.2.3 The cornea

The cornea is a transparent membrane and belongs to the external part of the outer fibrous tunic. The main function of the cornea is to refract light into the eye. The curvature of the cornea is greater than the rest of the eye and the junction with the sclera is known as *sulcus sclerae*. The thickness of the cornea varies between 1.2mm and 0.5mm from the outer ring of the cornea, the *sulcus sclera*, to the centre. The central corneal thickness (CCT) varies by +/-20% between individuals [13, 56].

Feltgen *et al.* [57] reported that they had measured CCT in 72 patients and found a range of 0.448 to 0.713mm. Elsheikh *et al.*[58] have used CCT values of 0.32mm to 0.72mm in their numerical model to simulate deformation differences of the cornea when applying an applanation device (Goldman applanation tonometer). Doughty and Zaman [56] calculated the CCT from 300 data sets from literature (from 1968-1990) and calculated the CCT for corneas which were designated as normal and found the average to be 0.534mm. The radius of curvature of human corneas has been found to be 7.9mm [56, 57, 59].

The cornea consists of 5 layers: the corneal epithelium, the anterior limiting membrane (Bowman's membrane), the main body of the cornea, *substantia propria*, the posterior limiting lamina and the endothelium of the anterior chamber (Figure 2-9).

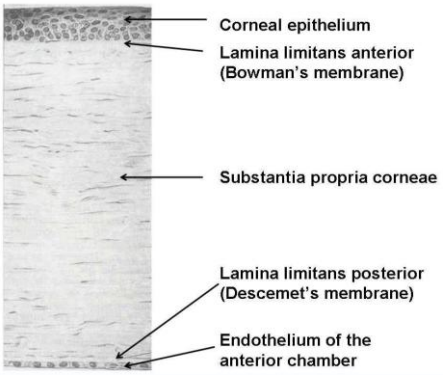

Figure 2-9: Section through the layers of the human cornea [13]

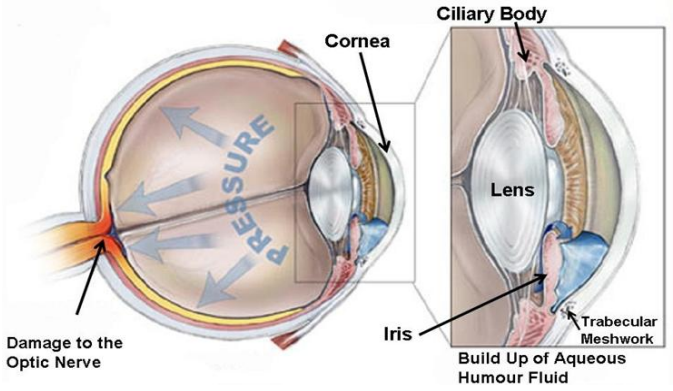

Figure 2-10: Development of glaucoma [60]

The Young's Modulus of cornea has been measured using a variety of test methods. Smolek *et al.* [61], for example, have applied an internal pressure to human eyeballs *in vitro* and have measured the resulting radius of curvature. They then calculated the Young's Modulus using LaPlace's Law, i.e. assuming that the eyeball behaves as a thin-walled sphere with constant radius of curvature and wall thickness:

$$\sigma = P \cdot r/2t \tag{2-2}$$

where P is the known pressure in the eyeball, r is the known measured curvature radius which can be rearranged to strain in the cornea and t is the known measured central cornea thickness. In the pressure range of 2.1kPa (16mmHg) to 2.8kPa (21 mmHg)

they found Young's Modulus to be constant at 1.03GPa. Hoeltzel *et al.* [37] carried out uniaxial cyclic tensile tests on four cornea strips cut from human eyes of average CCT 0.82mm, length 10mm-30mm and width about 2mm. The samples were tested up to strains of 0.08% at a strain rate of $2.7\times10^{-4}s^{-1}$ to $8.3\times10^{-4}s^{-1}$ depending on sample length (constant deformation rate 0.05mm/min). To characterize the data, the same power law was used as Hubbard and Chun [37] (Equation (2-1)). The value of β was almost constant at close to 2.0 for all 4 cyclic loadings, coinciding with the power coefficient for collagen obtained by Hubbard and Chun. The α-value increased from 54.32MPa for the first cycle to 98.97MPa for the fourth cycle. The tangent moduli to the stress levels of 6.4kPa and 260kPa were 0.34MPa and 0.56MPa respectively, roughly equivalent to internal pressures of 1.3kPa and 53kPa (10mmHg and 400mmHg) respectively.

Elsheikh *et al.* [62] presented values of Young's modulus in relation to intraocular pressure and age. They used a cornea-sclera section and applied pressures up to 3.1kPa (35mmHg). Three different age groups (50-64, 65-79, 80-95) were tested and two different rates of increase of pressure were used (37.5mmHg/min and 3.75mmHg/min) [63]. The results can be seen in Figure 2-11 and show a clear reduction in Young's modulus for lower rates of increase of pressure and a clear increase in Young's modulus with age. All the measured Young's moduli were in the range of 0.16MPa and 0.96MPa.

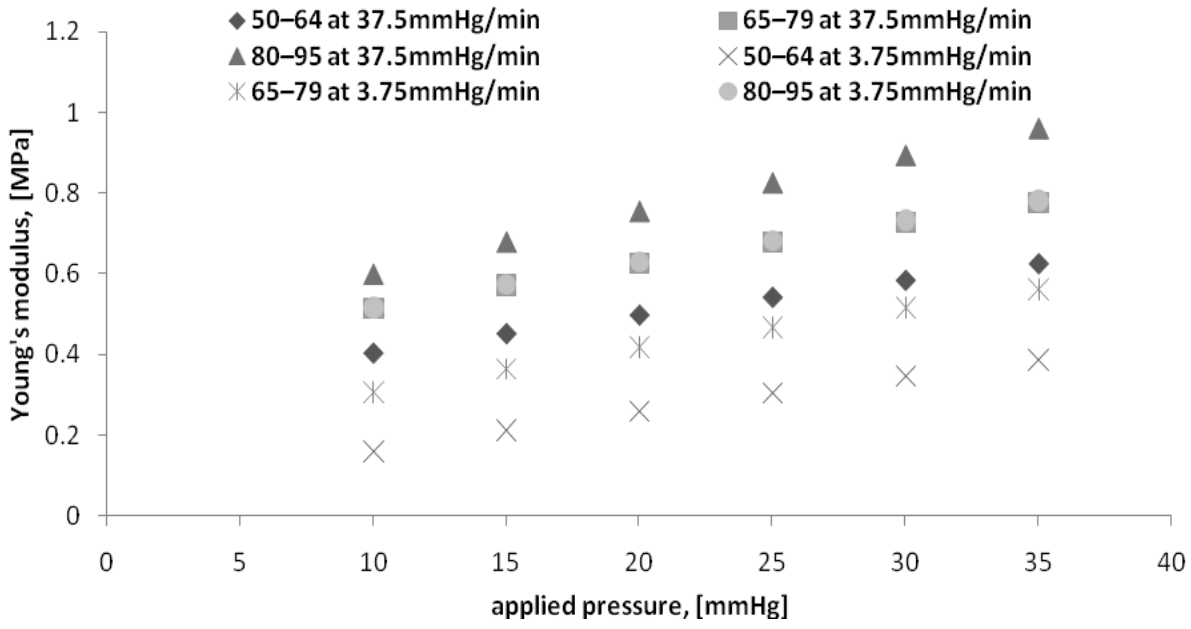

Figure 2-11: Effect of age and loading rate on Young's modulus of cornea-sclera discs [62]

FEM simulations of the cornea have shown that values below 0.01MPa are not realistic due to the fact that the curvature radius would increase to twice that of the unpressured condition when pressurised with 2.1kPa (16mmHg) and that would entail a 400% volume expansion [59]. The large variation in the measured properties reviewed above can be explained with the different tests used to measure the properties (inflation and tensile testing) and the highly visco elastic behaviour of the cornea which leads to a nonlinearity of the stress-strain curve and sensitivity to variations with strain rate. Therefore the "known" Young's modulus varies from 0.01 to 1000MPa [54, 58, 59, 61, 64-67].

2.2.4 Development of glaucoma

In simple terms, aqueous humour flows from the posterior chamber through the posterior pathway (gap between lens and iris) to the anterior chamber and drains there through the trabecular meshwork (Figure 2-10). Glaucoma is defined as the condition whereby aqueous humour is not able to drain at the normal rate through the trabecular meshwork. Even though the outflow is limited, the production of aqueous humour in the ciliary body continues and this leads to a pressure increase in the eyeball. The pressure increase distorts soft tissue within the eye because the eye cannot freely expand due to the fibrous coating around the sclera. If the pressure in the eye reaches double its normal pressure of about 2kPa (16 mmHg), distortion of the nerve fibres begins and the visual field reduces or becomes out of focus. Because the optic nerve has to pass through all three tunics (fibrous tunic, vascular tunic and neural tunic), it is not enclosed in connective tissue and this makes it vulnerable to damage in glaucoma [38]. If glaucoma can be recognized at its early stages, it might be treatable using drugs which reduce the production of aqueous humour and/or constrict the pupil and put the edge of the iris into tension which makes its surface more permeable to aqueous humour [68].

2.2.5 Types of glaucoma

There are more than 10 different types of glaucoma which can be categorized into two main groups. Primary glaucomas have no connection to other diseases of the eyeball,

whereas secondary glaucomas are those where the increase in IOP is due to injury, inflammation or tumour of the eyeball. The two most common types are primary open angle glaucoma and primary angle closure glaucoma.

Primary open-angle glaucoma (POAG) is the leading cause of blindness [69, 70]. It can be characterised by an intraocular pressure above 21mmHg, an open, normal appearing anterior chamber angle, no ocular or systematic abnormality that might account for the raised IOP and typical glaucomatous visual field and optic nerve damage [71]. Figure 2-12 shows the increase of IOP caused by POAG. The black arrow shows the flow of aqueous humour from the posterior chamber to the anterior chamber. When the fluid reaches the trabecular meshwork it cannot drain through the TM due to blockage and the pressure increases in the eyeball.

Patients with primary angle-closure glaucoma (PACG) also exhibit an increase in IOP (higher than 21mmHg), the eye is red and the pupil is mid-dilated. To test whether the trabecular meshwork is blocked by the iris it is necessary to assess the anterior chamber angle. Figure 2-13 illustrates how the iris can narrow the angle between itself and the cornea thereby blocking the outflow of aqueous humour through the TM [71, 72].

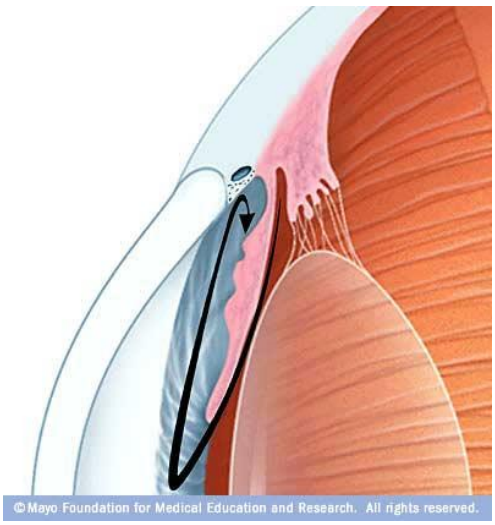

Figure 2-12: Increase of IOP caused by primary open angle glaucoma (POAG) [72]

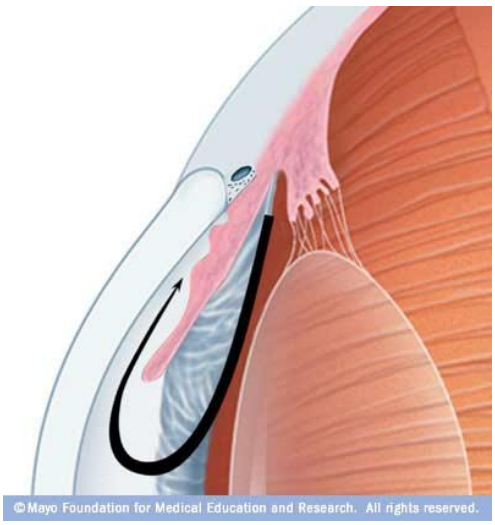

Figure 2-13: Increase of IOP caused by primary angle-closure glaucoma (PACG) [72]

2.2.6 Tonometers

The basic principle used to measure IOP has not changed in the last century and is still based on the deformation of the cornea. The methods of measuring IOP can be separated into two main techniques, indentation tonometry and applanation tonometry. In both cases, the cornea can be deflected either by using a pre-defined force and the deformation of the cornea measured or by using a pre-defined deformation and measuring the associated force [39, 73].

In addition to these two tonometer techniques a relatively new development uses air pressure to deform the cornea. Here the tonometer applies an external air pressure of about 6.6kPa- 9.3kPa (50 -70mmHg) and measures the deformation with light sensors [74].

All the methods assume that the cornea has no rigidity and the measured force is the reaction of the IOP. Furthermore they do not take account of the pressure increase caused by the compression associated with deforming the cornea [39]. Although a lot has been done in recent years to compensate for the influence of the cornea, or to keep the influence small, there is currently no device that can measure IOP independently of the rigidity of the cornea [75].

In the following sections indentation tonometry, applanation tonometry, dynamic contour tonometry and air puff tonometry are each explained in terms of their basic measurement method.

2.2.6.1 Indentation tonometer

Indentation tonometers use a plunger to deform the cornea and this is one of the earliest types used (Schoitz tonometer, 1905). The indentation depth is measured when a known force is applied to the plunger (dependent on IOP but arround 0.5mm) [80-82]. The force is controlled by applying a certain small weight to the plunger, while an integrated scale converts the indentation depth to an IOP reading. To work this device, the pressure P_T, resulting from the plunger weight acting over its area has to be bigger

than the intraocular pressure P_{IOP}. The plunger deforms the cornea and produces a back-pressure P_B in the eyeball which adds to the real IOP so that [39]: $P_T = P_{IOP} + P_B$

The back pressure P_B results from the rigidity of the cornea P_c, the depth of indentation P_i and a small component due to the adhesive force P_a, which acts against the other two components.

$$P_B = P_c + P_i - P_a \tag{2-3}$$

Friedenwald [76, 77] calibrated the device and implemented a rigidity constant *r* which is inversely proportional to the volume change ΔV of the eyeball resulting from the deformation of the cornea.

$$r = \frac{\lg(P_T) - \lg(P_{IOP})}{\Delta V} \tag{2-4}$$

The problem here is that *r* is constant although the rigidity of the cornea increases with increasing IOP [78]. This leads to an underestimate of the true IOP [39].

Razeghinejad *et al.* [79] measured IOP with a Schoitz tonometer in 168 eyes (85male, 83 female) with an average corneal thickness of 547±53µm (measured with a pachymeter). This study showed that an IOP error of 1kPa (7.7mmHg) could be expected per 100µm thickness change in CCT. Moses [80] applied 4 different dead weights (5g, 7.5g, 10g and 15g) to a plunger of diameter 3.5mm to 20 enucleated human eyes using a Schoitz tonometer and determined the associated indentation depth. The undeformed radii of curvature of the 20 eyes were measured and found to be in the range of 7.17mm to 8.10mm. During the test, the IOP was increased from 2.0kPa (15mmHg) to 6.1kPa (46mmHg) in increments not defined by the authors. They then used equation (2-5) to correlate the plunger indentation depth x_p to the ratio of applied force $F_{Plunger}$ to intraocular pressure P_{IOP} using two constants *A* and *B*. A strong correlation was found for the cornea curvature ($p < 0.001$) but there was no correlation for thickness variation [80, 81].

$$A + B\frac{F_{Plunger}}{P_{IOP}} = x_P \tag{2-5}$$

Friction and adhesion forces of the tear film between cornea and plunger were mentioned by Moses *et al.* [82] as influencing the reading and they suggested making the plunger out of Teflon to reduce the friction forces. The time of application of the plunger to the eye also causes errors and this has been attributed to the expulsion of liquid from the anterior chamber [39] and/or creep of the cornea [83]. In either case the IOP will be underestimated. Pallikaris *et al.* [84] and Elsheikh *et al.* [63] also found that the age-related stiffening of the cornea affects the indentation method. A final disadvantage is that this method only can be used when the patient is lying down.

The indentation method has been gradually supplanted by applanation tonometers and non contact tonometers. As early as 1965 Sticksel [85] reported that the Schoitz tonometer cannot compete against the more accurate measurement method from Goldmann tonometers.

2.2.6.2 Applanation tonometer

Applanation tonometers all derive from the Goldmann Applanation Tonometer (GAT), first introduced in 1957 [5]. The GAT is still regarded as the most accurate way of measuring IOP and is used to calibrate other tonometers. The applanation method is based on the Imbert-Fick Law, equation (2-6) [86] and deforms the cornea until a certain area of the plunger (probe) is in contact with the cornea.

$$IOP = \frac{F_{GAT}}{A} \tag{2-6}$$

which states that the contact area A multiplied with the intraocular pressure IOP results in a force F_{GAT} . The equilibrium suggested by this equation does not account for (visco) elastic forces from the cornea nor surface adhesion forces, and so is only valid for an infinitely thin perfectly elastic dry cornea. These shortcomings were recognised by Goldmann and Schmidt [5] and they expanded the Imbert Fick Law using a parameter P_B which is the pressure increase for applanating the cornea and also accounted for the surface tension of the tear film P_a which acts against the IOP:

$$IOP + P_B = \frac{F_{GAT}}{A} + P_a \tag{2-7}$$

To find both P_B and P_a in relation to the applanation area they tested human corneas *in vitro* using applanation diameters from 3mm to 7mm at pressures from 10mmHg to 50mmHg. When $P_B - P_a = 0$ the associated forces on the applanation area are equal and cancel out in Equation (2-7). By comparing the tonometer reading with the applied pressure, it has been found that the best results were obtained for an applanation area *A* of 7.35mm^2 (3.06mm diameter, i.e. the smallest) [5, 6] whereas the IOP was always overestimated for the other diameters used. Goldmann and Schmidt [5] did no tests on smaller diameters to see if here the tonometer would underestimate the IOP, which should happen when the tear film adhesion force is higher than that due to the back-pressure P_B.

To control the exact contact area in clinical practice, the device is combined with a microscope and a slit lamp. An optical prism is brought into contact with the cornea and a fluorescing dye drop on the cornea highlights the contact area. The ophthalmologist will observe two semicircles in the microscope. When the two semicircles are in contact with each other the device is perfectly deforming the cornea and a precise IOP reading can be taken [39, 87].

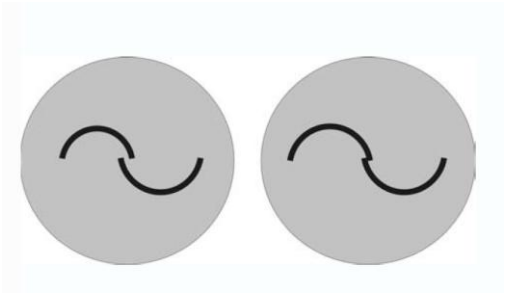

Figure 2-14: View of alignment in applanation tonometer: (left) the two semi circles are not in contact (inaccurate reading), (right) alignment of the two semi circles for optimised IOP reading

Applanating the cornea has a similar effect to the indentation method, but the applanating area of the GAT does not indent the cornea to such an extent as the Schoitz tonometer, thus reducing the backpressure which, in turn, reduces the influence of the rigidity and the CCT. Nevertheless, the error in IOP associated with CCT is estimated to be linear and increases by 0.2kPa to 0.6kPa (1.5 - 4.5mmHg) per 100µm increase in thickness [88-90] over the average CCT of 0.522-0.530.

A slightly different applanation tonometer, the Tono-pen, uses a principle, introduced by Mackay and Marg [91], whereby a ring-shaped ground plate applanates the cornea, carrying the forces associated with the rigidity of the cornea and the surface tension, and a smaller, central plunger can then record the true IOP (Figure 2-15). Due to the fact that the whole applanation area is not considered for the measurement, the complex alignment method of the GAT is no longer required making this technique applicable for a handheld device.

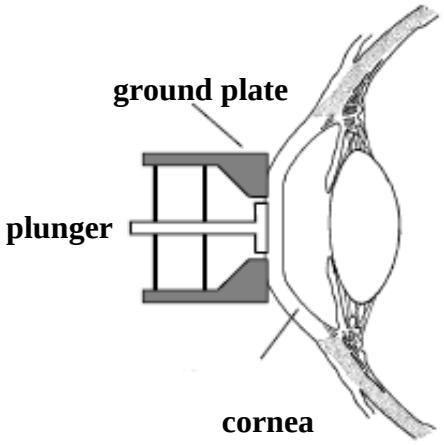

Figure 2-15: Principle of the Mackay-Marg Tono-pen [39]

The Tono-pen is a handheld device with a plunger diameter of 1.5mm. A force sensor connected to the plunger measures the IOP and a built-in microprocessor processes the data and displays it on digital display. The Tono-pen can be used to measure IOP with the patient in any position. However this fast and easy method of measuring IOP is not as accurate as the GAT [39]. Dohadwala *et al.* found that the IOP indicated by the Tono-pen is dependent on the CCT [39], the error increasing at 2.9mmHg/0.1mm CCT change for males (based on 165 male patients with an average age of 45.4) and at 1.3mmHg/0.1mm CCT change for females (based 161 female patients with an average age of 44.9). Here, again, all measurements are referred to the average CCT of 0.522mm and the IOP decreases for thinner corneas.

2.2.6.3 Dynamic contour tonometry

The Pascal Dynamic Contour Tonometer DCT uses a new technique to record IOP, which, according to Kanngieser [92, 93], is independent of corneal properties. The DCT is based on Pascal's principle, which states that a pressure applied to an enclosed

fluid is transmitted equally within the fluid, including to the walls. Applying a tonometer with a contour radius of 10.5mm (Figure 2-16) and a force of 9.81mN (1g) on the cornea will keep the cornea in an unstressed condition and the cornea will adopt the curvature of the tonometer plunger. The pressures on the interior and anterior surfaces of the cornea will be equal and the pressure in the eye can then be measured outside the eyeball, which, in the DCT design, is measured by a pressure sensor located in the centre of the plunger. The DCT measures continuously over 5 seconds at a sample rate of 100 S/sec [94] monitoring systolic and diastolic pressure in the eyeball [95] and delivers the mean reading as the true IOP. Francis *et al.* [96] have shown in the largest such study so far (more than 2000 patients), that the DCT is less affected by CCT than is the GAT. However, the DCT results were more affected by the radius of curvature of the cornea than the GAT and, furthermore, the calculated mean IOP for all patients measured using the GAT was significantly lower (14.4 ±3.2 mmHg) than using the DCT (16.0 ±3.6; $P \leq 0.0001$).

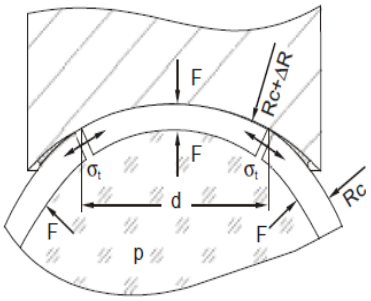

Figure 2-16: Dynamic countour tonometer from Kanngiesser [92]

2.2.6.4 Air puff tonometer

Air puff tonometers, also known as non contact tonometers (NCT), use air to deform the cornea. Several devices are currently in routine clinical use and, depending on the device, the air impulse is produced with a pump and a piston (e.g. NCT-II) or else a compressor generates the relevant pressure which released through a nozzle (Pulsair) [39]. The impulse pressure step can be chosen to be either from 0-4kPa (0 to 30 mmHg) or from 0-8kPa (0 to 60mmHg). This depends on the IOP level of the patient and usually the ophthalmologist starts with 0 to 4kPa [39]. The applied pressure deforms the cornea and collimated light shone onto to the cornea centre is reflected onto a detector (Figure 2-17) to give the curvature [97]. There are two ways such devices

measure IOP. Some devices record the time taken for the cornea to change shape under a certain pressure, and the speed of cornea deformation is related to the IOP. Other devices measure the pressure required to achieve a certain cornea deformation. Here the pressure is increased at a known rate and, once the light sensor recognises a certain topography pattern of the cornea, the necessary pressure is recorded and converted to the IOP value.

The obvious advantage of non-contact tonometers is that the danger of infection is minimized as no tonometer part touches the eye. Furthermore, air puff devices need no anaesthetic or eye drops, are more comfortable for patients and non-ophthalmologists can be trained to use them.

Doughty *et al.* [98] have shown that changes in CCT increase the IOP error reading of a Pulsair tonometer (Model 2000, Keeler Instruments, Windsor, UK). Measurements on 104 children (boys and girls) with an average age of 10.3 years indicated an error of 0.17kPa (1.3mmHg) per 10% thickness change from the average 0.53mm CCT. The effect of CCT for adults (75 male adults with an average age of 46.1 years) was somewhat less than for children at 0.1kPa (0.8mmHg) per 10% thickness change. The largest effect of CCT was in elderly adults (91 men and women with an average age of 72.6 years) at 0.35kPa (2.6mmHg) per 10% thickness change. This last finding corroborates the observation of Elsheikh *et al.* [63] that there is a significant increase in Young's modulus of cornea with age.

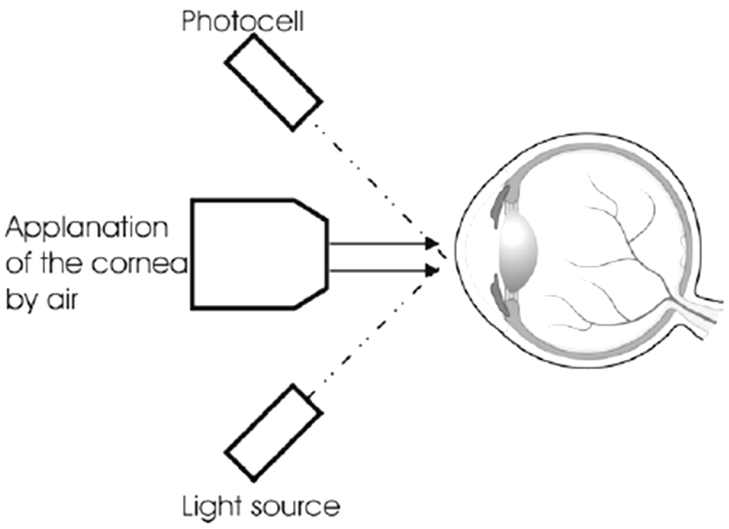

Figure 2-17: Air puff tonometer [97]

2.2.6.5 Summary of Tonometer errors

As has been seen, no tonometer is without error in estimating the IOP, and all use a static or quasi-static measurement. Table 2-2 summarised the relative advantages and disadvantages of the devices discussed.

Author(s)	Tonometer	error reading	caused by
Razeghinejad *et al.* [79]	Schoitz Tonometer	1.0kPa/100µm CCT	change in CCT per 100µm from average (547µm)
Razeghinejad *et al.* [79]	GAT	1.2kPa/100µm CCT	change in CCT per 100µm from average (547µm)
Moses *et al.* [82]	Schoitz Tonometer	no error stated only correlation was given	curvature radius; affects measurement
Kohlhaas *et al.*[99]	GAT	0.54kPa/100µm CCT	change in CCT per 100µm from average (550µm)
Boehm *et al.*[88]	DCT	0.14kPa/100µm CCT	change in CCT per 100µm from average (550µm)
Shimmyo *et al.* [89]	GAT	0.24kPa/100µm CCT	change in CCT per 100µm from average (552µm)
Dohadwala *et al.* [39]	Tono-Pen	0.39kPa/100µmCCT	change in CCT per 100µm from average (552µm)
Doughty *et al.* [98]	Air Puff (model 2000 Keeler)	0.7kPa/100µm CCT	change in CCT per 100µm from average (553µm)
Martinez-de-la-Casa *et al.*[100]	Air puff (ORA Reichert Inc., Depew, NY),	significant error increase with CCT change	change in CCT; just stated with a $p<0.0001$

Table 2-2: Tonometers with their error readings

2.3 Orthodontic tooth movement (OTM)

Orthodontic tooth movement OTM, is the movement of teeth by the application of a sustained force, most commonly applied using orthodontic braces. The teeth change their position permanently as a result of bone remodelling but the forces are applied through the periodontal ligament. The orthodontist is interested in achieving the movement as quickly as possible, but excessive forces can lead to root resorption and hyalinisation of the PDL, in which the fibres are compressed and become acellular and homogenous [101]. The interest here is therefore in describing the mechanical response of the PDL in a way that it could be assessed for a given patient *in vivo* prior to planning an optimal treatment for OTM [102].

2.3.1 Periodontal ligament (PDL)

PDL is the connective tissue between the root of the tooth and the bony socket [103]. PDL plays a very important role especially during mastication, where it acts as a shock-absorber, reducing the damage to the tooth when it comes in contact with another tooth or other hard material [104]. As the process of mastication can give rise to short-term maximum forces of up to 500N, it is very important that the displacement of the tooth gets damped by blood vessels in the PDL which drain into the blood circulation system [104, 105]. Orthodontic tooth movement and mobility of the tooth are dependent on the functionality of the periodontal ligament [106, 107]. Alveolar bone remodelling during OTM strongly depends on the stresses and strains that are initiated in the PDL [108, 109].

2.3.2 Different theories and phases for OTM

OTM is the result of a mechanical stimulus, created by forces acting on the crown of a tooth. These forces turn into biological reactions in the socket with bone modelling and remodelling [110] and consequent permanent changes in the position of the tooth. However, first reactions occur within the PDL which reacts to tension on one side of the tooth while the other side is compressed. On the compression side, the blood circulation is reduced, while the collagen fibres within the PDL uncoil initially under

tensile forces and thereafter stretch, becoming more resistant to displacement. Applying excessive force to the tooth leads to intra alveolar displacement of the tooth with a deformation of the alveolar bone.

Two major mechanisms of OTM are generally accepted. The pressure – tension theory explains the initial movement of the tooth in the socket in terms of bending and deforming the socket wall which includes the compression and tension of the PDL [111-113]. PDL covers the root and by applying a lingual force to the tooth, the PDL will be compressed on the lingual side but will be in tension on the labial side [114]. The bioelectric theory considers the bioelectric potential within the bone built up by metabolic activity during remodelling. This produces electronegative charges which can change the interaction between cell membranes and mechanical forces [103, 115], for example by stimulating cell metabolism and collagen synthesis [116, 117]. This theory is supported by the observation that applying a low voltage or electromagnetic field to the alveolar bone helps to increase OTM [116, 117].

Commonly, four different phases are identified during displacement of a tooth [7]. Figure 2-18 shows a displacement-time curve under constant force (creep curve) of the premolar measured on live young adult male beagles over a time period of 120 days. Phase 1 represents the initial tooth movement in the socket which increases in an approximately linear fashion with time under constant applied force acting on the PDL [8] and is furthermore related to the constant applied force [7]. Phase 2, known as arrested tooth movement, where the displacement is static irrespective of the force [118]. Phase 3, accelerating tooth movement, reflects the start of the remodelling of PDL and alveolar bone until it reaches a maximum rate [7]. Once the maximum rate is reached, Phase 4, with a constant speed of movement, commences. The experiments in this work are aimed at determining the visco elastic behaviour of the PDL, and are of most relevance to Phase 1.

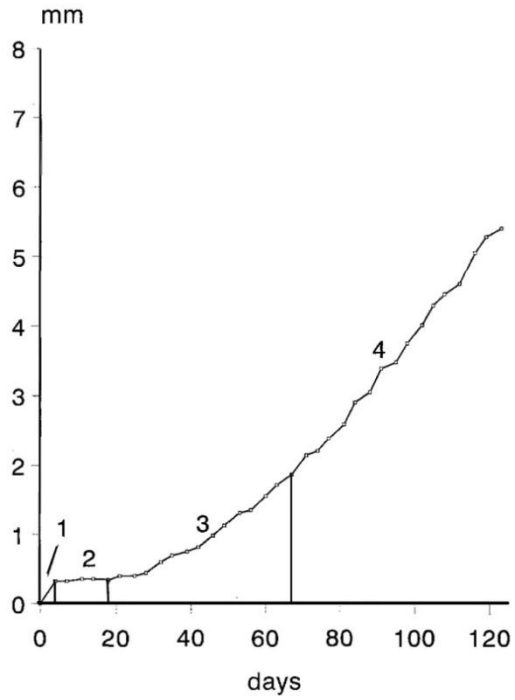

Figure 2-18: Four phases of tooth movement over 120 days with constant applied force [7]

2.3.3 Forces used for OTM

An optimised OTM (achieving the required movement in the minimum time without damage or pain) is only likely to be possible with independent control of six degrees of freedom in forces and moments as a function of time. Existing wire-bracket systems put some constraints on this control, but, even so, the stress will vary for a given force depending on the individual tooth and patient and will also vary with time. Therefore, it is of interest to know the theoretical centre of resistance C_{ro} (centre of rotation). For single-rooted teeth, C_{ro} is generally defined as one third of the root length measured apically from the alveolar crest, but this varies, and is dependent on the geometry of the root, the magnitude, direction and point of action of the load, and the time of application of the load [102, 113, 119, 120]. Choy *et al.* [121] has modelled the geometry of a simplified 2D canine tooth in Visual Basic 4.0 and calculated the centre of resistance for varying root shapes (from rectangle to triangle (Figure 2-19)). For all shapes, a length of 16.0mm was used and the distance between the centre of resistance and the alveolar crest decreased from 8.0mm (50% of total length) to 5.4mm (33% of total root length) for rectangular to triangular roots. With a distance of 6.7mm (42% of total root length) the canine shaped root was between the two shapes as expected. Using the axis of rotation at the apex of the root, Choy *et al.* [121] suggested that a force applied to the

canine 5.4mm coronal of the alveolar crest (a=12.1mm and b=9.3mm Figure 2-20) should not exceed 0.5N (47g) to prevent the capillaries in the PDL, which keep their shape due to blood pressure (16kPa at systolic pressure) from being damaged (Figure 2-20). The area of the PDL was defined as 94.1mm^2.

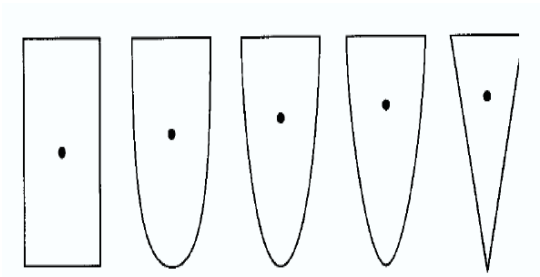

Figure 2-19: Various root shapes with their centre of resistance from [121]

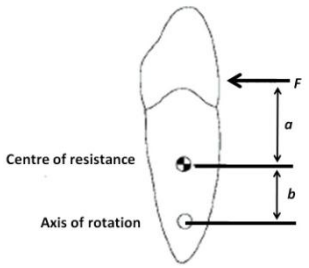

Figure 2-20: Canine tooth applied with a force *F* at a distance (*a*+*b*) from the axis of rotation and the PDL keeps equilibrium at the centre of resistance with a distance *b* [121]

Provatidis [114] calculated the distance h_{Cro} between the centre of rotation C_{ro} and the alveolar crest and the distance h_{Cr} between the alveolar crest and centre of resistance C_{re} (Figure 2-21) using an FEM simulation. He modelled a human central incisor with a root height h of 13.0mm (distance from alveolar crest to the end of the root) for a paraboloidal shaped tooth with a diameter of 7.8mm. The PDL, which covered the root, was assumed to have a uniform thickness of 0.229mm. The mechanical properties of the PDL were simulated first as linear elastic material with a Young's modulus of 0.68MPa (Model 1) and then as anisotropic nonlinear tissue with different fibre directions which were represented as springs aligned at different angles to the root (Model 2: parallel fibres normal to the root axis, Model 3: parallel fibres normal to the root surface and Model 4: fibres gradually inclined to root axis (Figure 2-22)). The constitutive model was expressed as creep behaviour:

$$\varepsilon = 0.494 - 0.461e^{-0.074t} \tag{2-8}$$

which can be identified as the creep behaviour of the SLS model, a spring (with index s) in parallel with a Maxwell model (of index 1) (see 3.1.1.3 Static response of the Standard Linear Solid (SLS)):

$$\varepsilon(t) = \frac{\sigma}{E_s} - \frac{\sigma E_1}{(E_1 + E_s)E_s} e^{-\frac{E_1 E_s}{\mu(E_1+E_s)}t} \tag{2-9}$$

Using the moment about the centre of rotation and assuming that the modulus in compression is equal to the modulus in tension, it is possible to determine the stress in the centre of resistance (simplified single reaction force at the centre of resistance) using a PDL area of 101.4mm^2 (4/6×7.8mm×13mm×2 two times the area of a parabolic segment) for an applied force F (1N) at a distance H=5.8mm from the alveolar crest and therefore it is possible to determine E_1, E_s and μ for Model 3 (see 3.1.1.3) yielding: 0.47MPa, 0.034MPa and 0.43MPas for E_1, E_s and μ respectively.

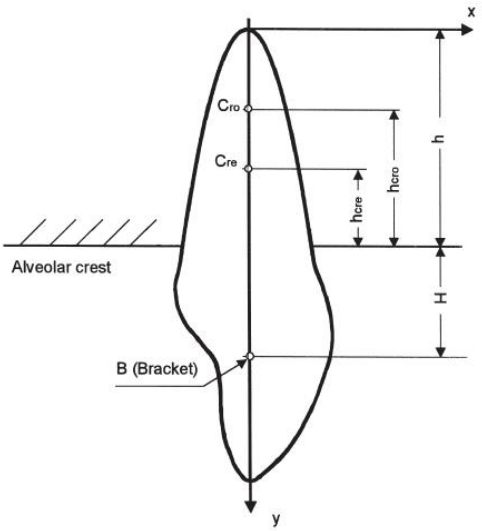

Figure 2-21: Geometry of a central incisor with the positions of centre of resistance C_{re} , centre of rotation C_{ro} and the bracket (B) for applying horizontal force from [114]

Provatidis also considered possible differences between the compression modulus E_{comp} and the tension modulus E_{tension} for the PDL using the ratio:

$$R_E = \frac{E_{comp}}{E_{tension}} \tag{2-10}$$

where R_E is the compression-tension ratio so that, for R_E =0, the PDL would behave like a rope with no compression resistance, and, for R_E =∞, the material will have no tension resistance, like a stack of bricks. The centres of rotation C_{ro} used for all calculations were between 38,9% - 68,6% (h_{Cro} /h) and the centres of resistance C_{re} were between 25% - 64% (h_{Cre} /h) but always smaller than the centre of rotation. A detailed listing for the different models (Model 1-4) can be seen in Table 2-3.

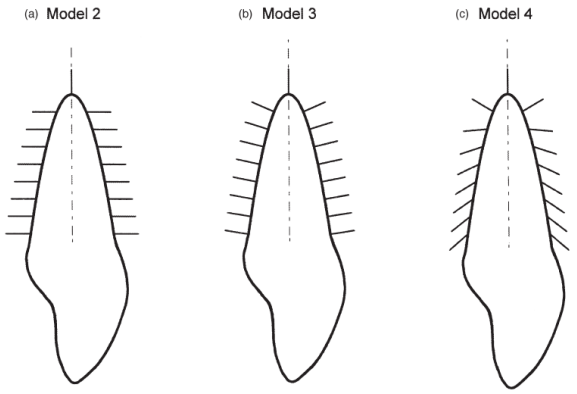

Figure 2-22: Models with different collagen fibre arrangement within the PDL to determine centre of rotation C_{ro} and the centre of resistance C_{re} : with a) Model 2: parallel fibres normal to the root axis, b) Model 3: parallel fibres normal to the root surface and c) Model 4: fibres gradually inclined to root axis from [114]

The centre of rotation and the centre of resistance will therefore be influenced by the applied force which again influences the stress strain behaviour of the PDL. Also, the fastest movement of a tooth is not the best solution for the patient, since large forces cause pain, necrosis (death of all or some of the cells), hyalinisation and "undermining resorption", which is loss of bone or tooth substance in a hyalinised area, with an growing risk of root resorption [111, 122]. Applying the right level of force to the tooth will result in tooth movement by frontal resorption [102, 123] but, if insufficient force is applied, there will be no permanent movement. The correct force strongly depends on the area of the root, which differs from tooth to tooth and also differs from patient to patient. The best solution for a group of teeth could, in principle, be arrived at if the force displacement response of each tooth could be tested with an easy-to-deploy dynamic indentation device, and this is the essential motivation for the research.

Model	R_E	h_{Cre}/h in %	h_{Cro}/h in %
Model 1	1	36.5	44.5
Model 2	independent of R_E	40	$\frac{\left[h_{Cre}+0.0068\mathrm{h}^2\frac{\mathrm{M}}{\mathrm{F}}\right]}{h}$ (2)
Model 3	1	25	42,5
	100	34	-
	3	-	40.7
	5	-	38.9
Model 4	1		57
	5	54-64(3)	59.8
	0		68.6

(2) with *h* as the root length, *M* is the resultant moment on the bracket and *F* as the applied force
(3) could not been accurately determined

Table 2-3: Centre of rotation C_{ro} and centre of resistance C_{re} for a human central incisor calculated using different PDL properties

2.3.4 Mechanical properties of OTM and PDL

Tanne [124] has observed that OTM during loading has been studied extensively but most of the results are reported as linear elastic parameters, Young's modulus, *E*, and Poisson's ratio *v*. Because strain rates are rarely reported, the results from different researchers are difficult to compare, and values of linear elastic parameters can differ by as much as a factor of 10^5 [106, 125] (Table 2-4). Furthermore, the characteristics of the PDL are determined in a number of different ways, for example by drawing inferences from observed tooth movement *in vivo* and *in vitro* [7, 109, 125], or by using samples of a section through bone, PDL and tooth [104, 126-128]. Figure 2-23 a) illustrates the jaw of a 4-month-old rabbit and the cut position (X) where a strip section was taken by Komatsu *et al.* [127, 128]. Figure 2-23 b) shows how the sample was cut into a size 1.64mm wide × 10mm long × 0.24 mm thick where the PDL length was recorded as 0.46±0.07mm as seen in Figure 2-23 c). The specimen was then elongated to 7.6% (35µm) at a strain rate of $2.28s^{-1}$(63mm/min). This deformation was kept constant for 300s to obtain a stress–relaxation curve. The specimen was then returned to its original width at the same speed and, after a 300s recovery period, the stress–relaxation tests were repeated to strains of 12% (55µm), 16% (75µm), and 21% (95µm).

The stress-relaxation curve was then plotted as a normalised relaxation modulus (Equation (2-11)) and fitted with a triple exponential function (Equation (2-12)):

$$Gr(t) = \frac{\sigma(t)/\varepsilon(t)}{\sigma(0)/\varepsilon(0)} \tag{2-11}$$

$$Gr(t) = A_1 \cdot e^{\frac{-t}{\tau_1}} + A_2 \cdot e^{\frac{-t}{\tau_2}} + A_3 \cdot e^{\frac{-t}{\tau_3}} + C \tag{2-12}$$

Komatsu *et al.* [127] showed that the ratios of parameters A_1 to A_3 are smaller at higher deformations. The A_1 parameter was 20% at 35µm deformation and decreased to 10% for 95µm. The A_3 parameter was 50% at 35µm and decreases to 25% at 95µm. The A_3 parameter did not show a significant change with deformation, but the C parameter was 3.7 times higher over the range with 55% at 95µm compared to only 15% at 35µm deformation. The retardation times were 0.2s-0.4s, 2s-4s and 100s-400s for τ_1, τ_2 and τ_3 respectively. The Young's modulus for 7.6% strain and 21% strain was 6.9MPa and 8.8MPa respectively for a strain rate of $0.036s^{-1}$.

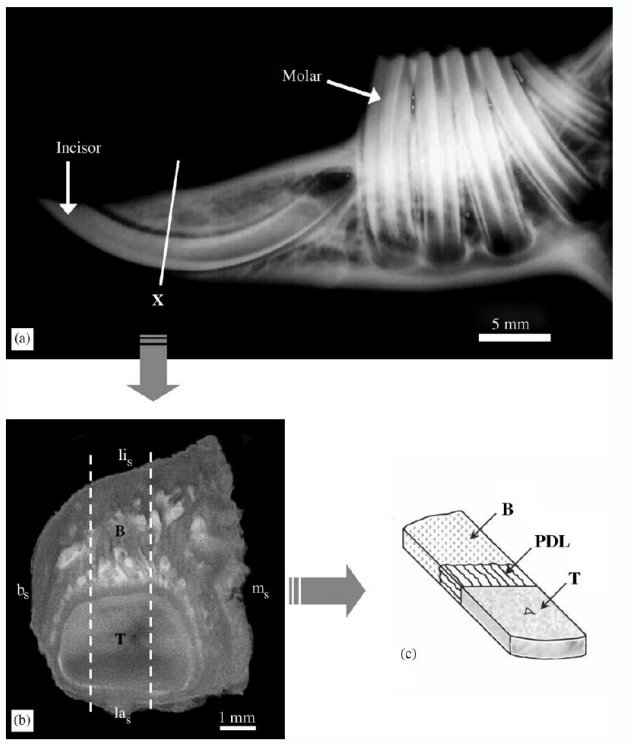

Figure 2-23: Example of sample preparation for PDL property assessment a) Radiograph of dissected rabbit mandible b) plane section of the cut section through (X) c) Remaining specimen of bone (B), PDL and tooth (T) [128]

Pini *et al.* [106] measured the mechanical behaviour of bovine PDL using sections of dimensions 10mm×5mm×2mm which included dentin, PDL of a thickness of between 0.3 and 0.5mm and alveolar bone. The 32 samples were taken at 5 different root depths and came from 4 molars. A further 16 samples came from three different root depths from 6 incisors. The samples were tested cyclically in compression at a strain rate of $7.5\%s^{-1}$ and in tension at a strain rate of $75\%s^{-1}$. The lower compression strain rate was chosen to reduce the influence of the interstitial fluid flow which was observed beforehand. The compression loading (CL) was up to 20% followed by a unloading (CU) and was only used for preconditioning. The sample was then elongated up to rupture (TL) which was around 40%-70% strain (Figure 2-24). The Young's modulus E was taken from the tangent of the TL curve and determined for all section depths. Increasing the root depth on molars did not significantly affect the Young's modulus which was in the range of 2MPa-10MPa. The Young's modulus of the incisor increased with decreasing depth from around 1±0.2MPa for section depth one, 2±1MPa for section depth two and 5±3.7MPa for section depth three but this was not deemed to be significant.

Jónsdóttir *et al.*[129] measured the creep behaviour of PDL *in vivo* on 7 Beagle dogs aged between 1 and 1.5 years. To test the PDL of a certain tooth *in vivo* adjacent teeth were extracted and replaced with implants to obtain an anchor for a measurement reference. The implant carried the LVDT which was connected with a crown to the tooth under test. Rubber bands with a predefined pulling force (0.5N, 1N and 3N) were used to deform the tooth in the socket, and the LVDT recorded the tooth movement over 5 hours. The test was repeated with a different force after 2 weeks recovery time. All tested teeth exhibited an instantaneous deformation within the first few seconds followed by a slow creep movement. The displacement rate recorded in the first minute varied significantly between the different dogs from 90µm/h to 5400µm/h at a constant force of 1N. In the following hour the deformation rate decreased drastically and became more reproducible with a range of 0.5-20µm/h. The effect of changing the force was greater than the difference between dogs with an applied force of 0.5N giving significantly less tooth movement for all time periods than an applied force of 3N. The total displacement d after 5 hours followed a power law equation *with* applied force f with an R^2 of 0.94:

$$d = f^{0.59} \tag{2-13}$$

A very common method is the inverse FE (Finite element) modelling, which uses the experimental results to change the mechanical parameters in the simulation until simulation and experiment match together. Van Driel *et al.* [109] used the same principle and experiment as Jónsdóttir *et al.* [129] on 5 Beagle dogs. A section of one dog's jaw was later removed to observe the shape and dimensions of the tested tooth *in situ* with PDL and bone. An FEM mesh was created and the PDL parameter was determined by correlating the experimental results with the FEM simulation. A Young's modulus of 0.015MPa gave the best fit for the experimental and simulated creep behaviour.

Andersen *et al.* [130] tested the mechanical properties of PDL in human cadaver mandibles. The three cadavers tested were of persons aged 15, 20 and 80 and sections including the mandible, the first molar and the first and second premolars were tested. The mandibles were fixed on a test rig and a dead weight of 1N used to displace the tooth. The load was applied at different occlusoapical levels in the buccal-labial direction to determine the centre of resistance, which was found to be located 3.7mm, 6.5mm and 7.9mm apically from the alveolar crest for the 15, 20 and 80 year old specimens, respectively. Dead weights between 0.05N and 2.5N were applied 3.8mm apical from the crown centre to obtain the force-displacement curve. The displacement at the crown was recorded after 120 seconds and the force – displacement curve was linear with apical position, being 0.107N per mm away from alveolar crest at the point where the force was applied. Andersen *et al.* sectioned the samples to obtain the dimensions of the bone, PDL and tooth and simulated the structure using FEM to reconstruct the tooth movement. They found a Young's modulus of 0.07MPa for the PDL to give the best correlation with the experimental data.

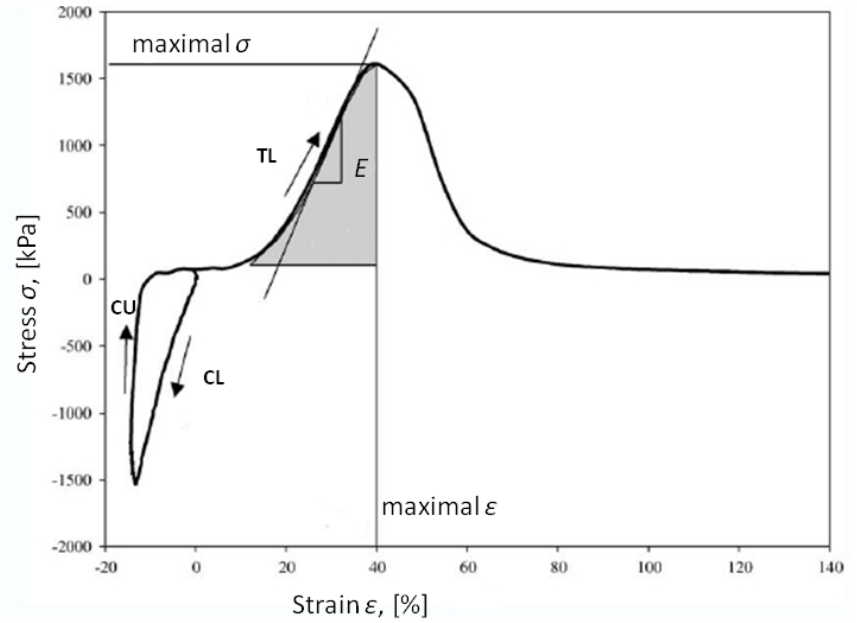

Figure 2-24: Typical stress σ [kPa] versus strain ε [%] curve from a molar showing loading (CL)- and unloading (CU)- for compression test and loading (TL) for tensile test [106].

Author(s)	**Elastic modulus *E* (MPa)**	**Poisson ratio ν**
Anderson *et al.* [131]	0.07	0.49
Tanne and Sakuda [132, 133]	0.70	0.49
Williams and Edmundson [134]	1.50, 100.0	0-0.45
Korioth and Hannam [135]	2.5-3.2	0.45
Takahashi et al. [136]	9.8	0.45
Atmaran and Mohammed [137]	171.6	0.45
Thresher and Saito [138]	1379.0	0.45
Jones *et al.* [139]	50	0.45
Poppe [140]	Bilinear E_1=0.05 E_2=0.28	0.3
Ziegler [141]	Bilinear E_1=0.05 E_2=0.18	0.3
van Driel [109]	0.015	0.25

Table 2-4 Elastic properties of PDL obtained by fitting FEM simulations to experimental data

2.4 Measuring mechanical properties of soft biological tissue

Even leaving aside the fact that they adapt, biological tissues, particularly soft tissues, show little long-range order (creep relaxation over several years) and their mechanics cannot be expected to be as simple as, say, a crystalline material or even a polymer. It is also necessary to have an idea of the microscopic and macroscopic structure of the tissue in order that appropriate mechanical tests can be devised. This section of the review covers the main types of testing that have been applied to soft biological tissues in an attempt to find the most appropriate approach for the systems in question, PDL and the eye and its components. Although Humphrey [11] has said that each biological tissue has a different behaviour, there are common characteristics to most of the soft tissues [148]. Soft tissues such as skin, prostate, PDL and cornea are known to exhibit complex constitutive behaviour, being visco elastic, inhomogeneous, anisotropic and nonlinear. Bischoff [149] also noted that soft tissue exhibits a susceptibility to irreversible damage during the initial cycles of loading, known as "preconditioning" or "strain softening" in biomechanics.

Soft tissue can be classified according to whether it is solid-like, fluid-like or solid-fluid-like. In this work, all of the structures tested are solid-fluid-like as any fluid-like components are contained (at least partially) within a solid structure or matrix. It is therefore possible to describe the tissues using constitutive material equations. The one exception to this is the mechanical eyeball where the behaviour of the partially-contained fluid has an effect on measured properties and this is a matter for discussion in Chapter 6.

The following sections review test methods that have been applied to soft tissues. These can be divided into contact and non-contact methods. Contact methods, where the test probe touches the specimen, can be static, quasi-static or dynamic, and are normally applied in tension or compression. Non contact methods use transmitting and receiving probes and include elastography and magnetic resonance elastography (MRE).

.

2.4.1 Static testing

Uniaxial static testing (ramp and hold method) can be carried out in tension or compression and at constant stress (or force) or at constant strain (or displacement). If a constant stress (or force) is used to compress or elongate the specimen the strain (or displacement) is recorded over a certain time period. For linear elastic materials, an immediate strain will be recorded and no further change will occur with time, but visco elastic materials will continue to deform and this behaviour is called visco elastic creep. For example, Boyce *et al.* have tested cornea strips in a solution bath and applied constant stresses of 500, 300 and 100kPa to obtain three creep curves (Figure 2-25) [150]. They found also that preconditioning was required at the beginning of the test in order to obtain reproducible test results. Figure 2-25 also shows some recovery curves when the applied stress is removed and the tissue begins to return to its original shape.

If the specimen is compressed or stretched to a certain strain (or displacement) and the stress (or force) measured with time, the phenomenon for visco elastic materials is known as visco elastic stress relaxation. As an example, Figure 2-26 shows the force response when a probe has been moved into a sample of lung tissue at a strain rate of $100\%s^{-1}$ (about 54cm/min) [151] following 10 cycles of preconditioning. The 9mm depth was reached after 1 second and this was held for a further 8 seconds in order to obtain the relaxation behaviour. The application was to identify tumours which were simulated using artificial tumour stones implanted into the lung tissue, giving a significantly different relaxation curve.

Creep, stress relaxation and recovery curves are all reliable measurement methods for determining the visco elastic behaviour of a material. To quantify the viscous and elastic components, it is necessary to apply a visco elastic model to the data and some examples are discussed in Chapter 3.

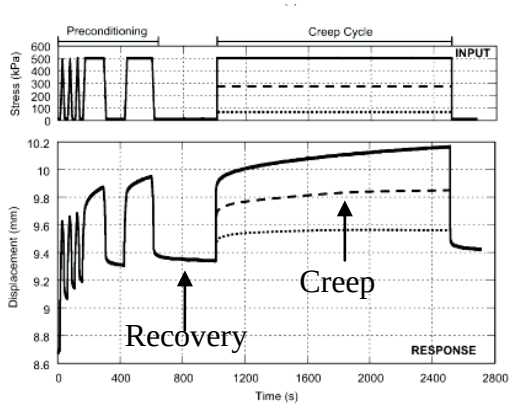

Figure 2-25: Stress-time and displacement-time records showing creep response of cornea strips over 1500 seconds [150]

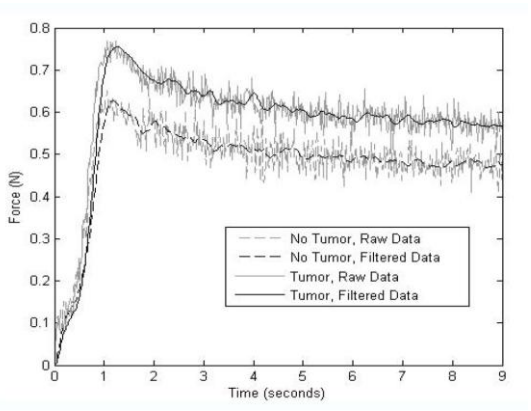

Figure 2-26: Stress relaxation for probe indenting 9mm into lung tissue for tumour detection [151]

2.4.2 Quasi static testing

The quasi static test is a fast and easy way to determine mechanical properties of elastic materials but its use can lead to confusion when applied to visco elastic and non-linear materials such as soft tissue. The method uses a certain strain rate, either tensile or compressive, to deform the specimen and the measured stress is used to produce the familiar stress-strain (or load-extension) curve. The main difficulties with soft tissue are that the shape of the stress-strain curve is different at different strain rates, generally becoming steeper at higher strain rates, and that the effective modulus (if a single modulus is used) depends on the strain at which the test is terminated. Many authors fail to record either the terminal strain or the strain rate, making comparison of results very difficult, if not impossible.

Fung [1] has identified three stages in a typical tensile stress-strain curve for samples of tendon, reproduced in Figure 2-27. In the first stage (OA), the force increases exponentially with strain, and this was identified by Fung as the normal working range in a body. The second part (AB) is more-or-less linear with a gradient α, where tan (α) is an elastic stiffness (N/m) and is used by most researchers to define Young's modulus of the tissue (when multiplied by the specimen length and divided by its cross-sectional area). The third part (BC) is again nonlinear up to tissue rupture at point C. For tendons, the point C is usually reached at an elongation of about 10 to 15% [9, 152]. For cyclic tests, it is necessary to stay in the range OB, otherwise the material will be

progressively damaged between cycles and the preconditioning effect would not be detectable.

Figure 2-28 shows results of a quasi static tensile test in which cornea specimens were tested for three cycles with a strain rate of $2.7\times10^{-4}s^{-1}$ to $8.3\times10^{-4}s^{-1}$ depending on the sample length (constant deformation rate 0.05mm/min) [65]. The difference in starting point and slope between the first and second cycles was attributed to preconditioning, although it is uncommon for there to be no further change after only two cycles. Ahearne *et al.* [153] tested whole circular cornea discs, clamped between two O-rings, and brought a micro indenter down into the centre of the cornea to 0.7 mm deflection with a deformation speed of 0.15 cm/min. Here, the preconditioning is not yet over after the fifth cycle (Figure 2-29).

Preconditioning is strongly dependent on the extent of deformation and on the strain rate, as visco elastic materials exhibit hysteresis in their loading and unloading curves, Figure 2-30 [154, 155]. The reason for this behaviour is because creep and relaxation happen during deformation which makes the loading and unloading different.

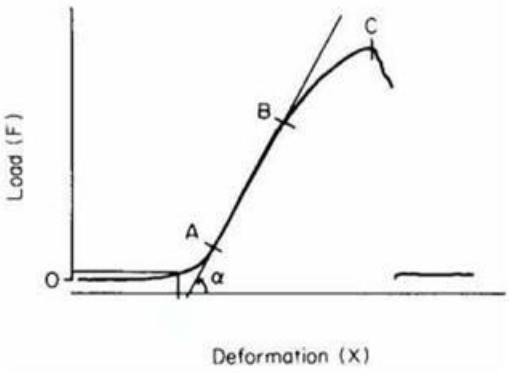

Figure 2-27 Load-extension curve for a rabbit limb tendon until failure, from Fung [9]

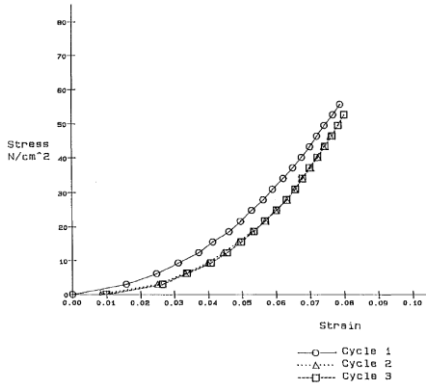

Figure 2-28 Repeated uniaxial tensile stress-strain test for human cornea, from Hoeltzl [65]

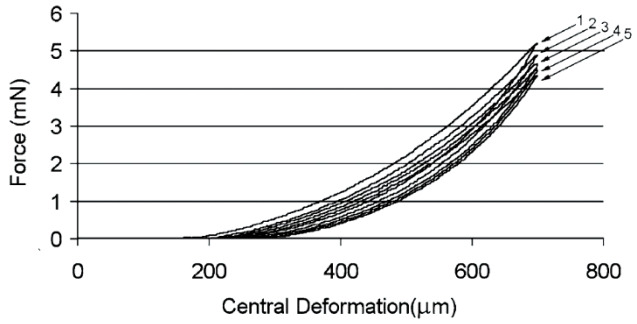

Figure 2-29: Loading -unloading of a suspended human cornea deflected to a depth of 0.7mm for 5 cycles [153]

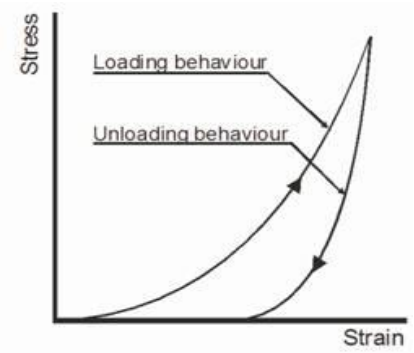

Figure 2-30: Hysteresis in loading and unloading, from Elsheikh [154]

2.4.3 Dynamic testing

The dynamic test method (also referred to as dynamic measurement analysis, DMA) involves probing the material over a certain frequency bandwidth using predefined stress (or force) amplitudes or strain (or displacement) amplitudes [156]. In most cases, in order to apply an oscillating condition, the material has to be pre-deformed (or pre-stressed) either in compression or tension, so that the mean stress (or mean strain) is always of the same sense as the amplitude. Once a quasi-stationary state has been reached, a sinusoidal applied stress (force) will produce a sinusoidal strain (displacement) and the properties of the material can be determined from the phase difference, the amplitude ratio, and also the mean ratio. A similar analysis can be applied to a displacement–control experiment, where a sinusoidal strain is applied.

As an example, Kiss *et al.* [157] determined the magnitude of the complex modulus (i.e. the amplitude ratio) $|E^*|$ and the phase difference, expressed as tan δ for samples of uterus and cervix with and without leiomyoma from 24 women, Figure 2-31. The

samples were cut into 10mm to 20mm rectangular pieces with a thickness of 5mm. Only the uterus samples were tested in compression either in the fibre direction || or orthogonal to the fibre direction $\perp$. All samples were tested using two values of pre-compression (1% and 2%) and at a range of compression amplitudes (1%, 2%, 3% and 4%) over the frequency range from 0.1Hz up to 100Hz. All samples showed an increase in the magnitude of the complex modulus $|E^*|$ with increasing frequency. Higher values of pre-compression and also higher compression amplitudes caused a higher modulus. The phase of all experiments had a minimum at about 0.5-1Hz. Compression tests along the fibre direction had a slightly higher modulus than compressing in the orthogonal direction Most importantly from a diagnostic perspective, the samples affected by leiomyoma exhibited a modulus more than two times higher than those not affected. No statistically significant difference was found in the phase difference for the different tissues.

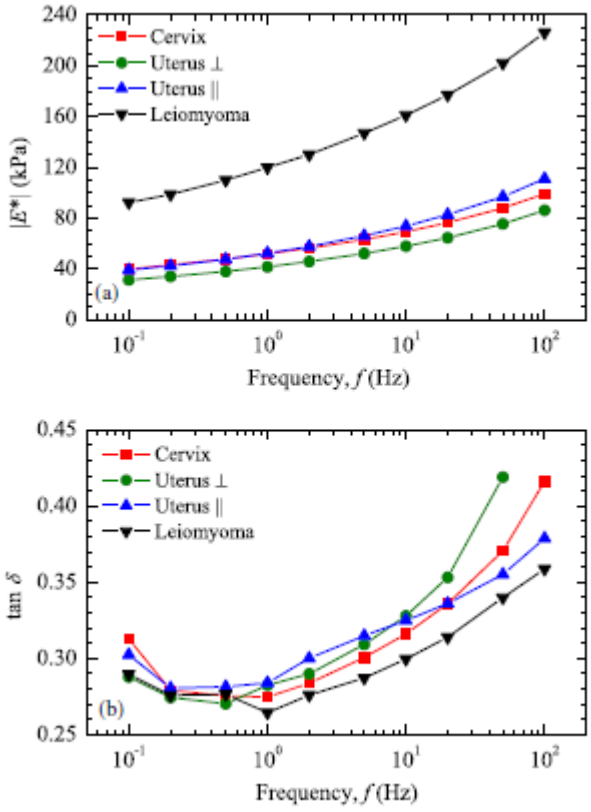

Figure 2-31: Phase and amplitude ratio vs frequency for samples of cervix, uterus|| , uterus$\perp$, leiomyoma[157]

2.4.4 Elastography

Elastography is a method, derived from medical ultrasound imaging, which uses sound or ultrasound to measure mechanical properties of a body or tissue indirectly. The sound or ultrasound is injected into the body or tissue and is reflected by an amount which depends on the tissue density, speed of sound and temperature [158, 159]. Elastic properties can be determined if consecutive ultrasound images are taken before and after the application of a displacement to the tissue, and tracking algorithms can then be used to express a contrast in the amount of displacement of components of the tissue. Elastography is therefore a combined contact and non-contact technique.

Whereas the technique is, in principle, very powerful, the ultrasound response from biological tissue can be quite variable and dependent on the location of the exposed tissue. Any abnormality must have a certain volume to be detected [160]. Elastography is popular for breast cancer and prostate cancer detection, and can be used in an A-scan (simple point reflection) or B-scan (2-D map) mode. Both A- and B-scan elastography are used in ophthalmology to detect abnormalities in the eye, to produce cross sectional areas of the eye and also to measure the cornea thickness (Pachymeter).

Zheng and Mak [161] have demonstrated a hand-held elastography system designed to measure soft tissue quality *in vivo*. The *in vitro* calibration involved an ultrasound transducer and receiver used to measure the deformation and the thickness change, while a tensile testing machine applied compression to porcine tissue samples (100mm×100mm×25mm) at speeds of 0.5mm/s and 1.0mm/s up to a strain of 20%. The tensile test machine was used to calibrate the ultrasound reading (deformation and thickness) and later tests were carried out only with the hand-held device on three human subjects [162]. The *in vivo* tests were performed on the skin of the underarm about 10cm distal from the elbow with and without contracted underarm muscle. The effective Young's modulus was calculated from equation (2-14):

$$E = \frac{(1-\upsilon^2)}{2\alpha\kappa(\upsilon,\frac{a}{h})}\frac{F}{d} \qquad (2\text{-}14)$$

where E is the effective Young's modulus, F and d are the recorded force and the applied deformation respectively, a and h are the indenter radius and tissue sample thickness, υ is Poisson's ratio and κ is a scaling factor according to Hayes *et al.*[163].

The values of *E* with non contracted muscle (14.0±5.0kPa) were significantly lower than with contracted muscle (58.8±1.7kPa). No difference was detected for varying the indentation speed (six different velocities starting from 0.75mm/s to 7.5mm/s). Zheng and Mak also noticed that the sample thickness increased by 26% when contracting the muscle.

Krouskop *et al.* carried out a similar experiment, testing soft tissue on the surface of an amputee's residual limb [164]. Their ultrasound device had three transducers which measured displacement and skin and muscle thickness. The strain rate of $0.4s^{-1}$ was applied to the limb at 10Hz with a DC motor which transferred rotational movement into linear movement. A pyramidal ultrasound transducer was used with three transducers emitting ultrasound in three directions. Krouskop *et al.* measured the tissue behaviour with contracted and non-contracted muscle and found a much smaller Young's modulus (6.2±0.48kPa) for the non contracted than for the contracted muscle (109±2.1kPa).

2.4.5 Magnetic resonance elastography (MRE)

MRE is a new technique for measuring the mechanical properties of tissues within the body combining low frequency sound waves with magnetic resonance imaging (MRI) [165]. The MRE produces tissue contrast images while the components are differentially mechanically excited by the sound waves (10-1000Hz) [166]. Stiffer components can be detected because the waves will travel faster through them and have therefore longer wavelength [165, 167] (Figure 2-32), and it is already known that abnormal, diseased tissues can display a shear modulus up to 100 times that of normal tissue [166]. The MRI is used to store time dependent images which are phase-related to the applied acoustic waves, and so, by adding an algorithm, an elastic modulus map can be generated which can be plotted as a 2D or even 3D image with the shear stiffness in [kPa] of the tissue. Figure 2-33 shows a picture of part of a female breast, where a significant (4cm) area was detected with a 5-20 times higher stiffness (about 20kPa to 30kPA) than the surrounding fibro glandular and adipose tissues with about 1.5kPa to 6kPa. The area was later proven to be cancerous by biopsy.

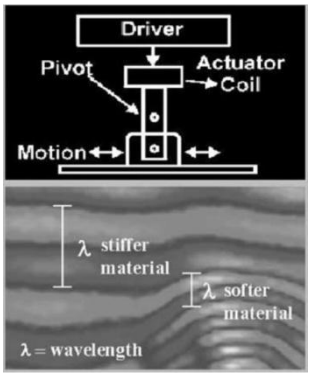

Figure 2-32: Schematic drawing of a MRE – system showing waves travelling through an object, from [165]

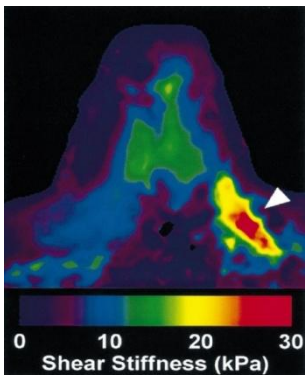

Figure 2-33: MRE of a breast with a 4cm abnormality. from [166]

Huwart *et al.* have tested MRE on 96 patients with chronic liver disease due to various causes (viral, alcohol abuse, non-alcoholic steatohepatitis or autoimmune disease) [168, 169]. The disease was classified in each of the patients using biopsy into 5 fibrosis scores from no disease to acute and, before scanning, a transducer was placed close to the bottom ribs with the patient in the supine position and the skin palpated with a frequency of 65Hz. The shear modulus of the liver determined from the MRE was able to separate the different classes with a success rate of 97% and the groups F0-F1 (mild), F2-F3 (moderate) and F4 (severe) were statistically significantly different ($p \leq 0.05$) [170]. The shear modulus increased with the fibrosis score as illustrated in Figure 2-34.

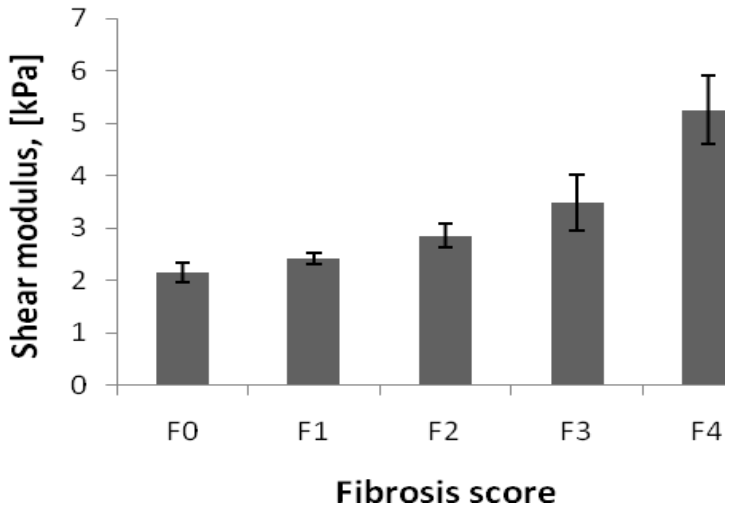

Figure 2-34: MRE shear modulus results for different liver disease stages [169]

Chapter 3: Mechanical Analysis

As mentioned in Chapter 2, a number of different test methods have been used in this work to investigate the mechanical behaviour of soft tissue. These direct actuation methods can be classed as quasi – static or dynamic, in both cases with displacement control, measuring the load response.

This chapter first describes the visco elastic models that have been used to analyse both static and dynamic measurements and introduces a new type of model, including an inertial term, for systems where this is relevant.

Finally, the methods of data processing are described in preparation for the analysis of the results (in Chapter 5) using the various visco elastic models developed in this chapter.

3.1 Visco elastic models

Material properties can often be described using combinations of viscous components (dampers or dashpots) and elastic components (springs). Spring components show an instantaneous deformation x_s directly proportional to the applied force F_s (Equation (3-1)), whereas, the force F_d applied to displace a damper is proportional to the velocity of deformation $\dot{x}_d$ (Equation (3-2)).

$$F_s = x_s \cdot c \tag{3-1}$$

$$F_d = \dot{x}_d \cdot d \tag{3-2}$$

Using these two components, an endless variety of visco elastic models can be created using combinations of springs and dampers in series and/or in parallel. Two basic rules help to identify the constitutive behaviour of a given combination (model). First of all, parallel components must always deform the same distance x and the force F required to deform parallel components by an amount x is the sum of forces in each parallel component. Secondly, the force F, required to deform series components by a total amount x is the same in each component, but, here, all of the individual deformations x_i

have to be added together to give the total deformation x. The simplest series model is the Maxwell model (one spring and one damper in series) and the simplest parallel model is the Kelvin model (one spring and one damper in parallel). However, neither of these two models can alone explain overall visco elastic behaviour with creep, relaxation and recovery. The Maxwell model can be used to describe stress relaxation but cannot describe creep whereas the Kelvin model is not able to describe stress relaxation but can describe creep and recovery. The simplest models which are able to describe both creep and relaxation use three parameters. Maxwell, Kelvin and three-parameter models are widely used for describing visco elastic materials in the literature and so their differential constitutive equations (DEs) are described below and solved using boundary conditions for creep, relaxation and recovery. Also, the principle for solving the DEs for dynamic tests for amplitude ratio and phase lag will be explained. Further models which are useful in describing PDL and cornea with IOP will be derived along with their respective solutions for stress relaxation, amplitude ratio and phase lag.

3.1.1 Static response

In a static response test, either the force is held constant and the strain varies with time (creep) or the displacement is held constant and the force varies with time (stress relaxation). To describe experimental results for either case, it is necessary first to write down the constitutive differential equation and then solve this using appropriate boundary conditions.

3.1.1.1 Static response of Maxwell model

The Maxwell model consists of a spring and a dashpot in series (Figure 3-1). Parameters in series each have to carry the applied force and the total deformation x is the sum of the deformations of the spring and the dashpot [21, 171] so:

$$F = F_s = F_d \tag{3-3}$$

$$x = x_s + x_d \tag{3-4}$$

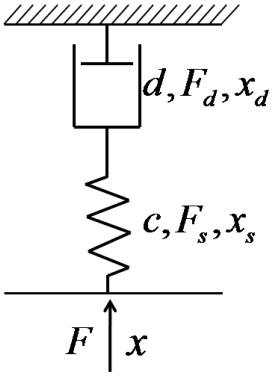

Figure 3-1: Maxwell Model

Differentiating equation (3-4) and replacing $\dot{x}_d$ and $\dot{x}_s$ with equations (3-1) and (3-2) gives:

$$\dot{x} = \frac{\dot{F}}{c} + \frac{F}{d} \tag{3-5}$$

hence:

$$\dot{F} + \frac{c}{d} \cdot F = c \cdot \dot{x} \tag{3-6}$$

If the deformation is kept constant, the deformation rate $\dot{x} = 0$, and so:

$$0 = \frac{\dot{F}}{c} + \frac{F}{d} \tag{3-7}$$

Solving this differential equation with the boundary condition $F = c \cdot x$ at $t = 0$ gives the relaxation response:

$$F(t) = c \cdot x \cdot e^{-\frac{c}{d}t} \tag{3-8}$$

If, on the other hand, an instantaneous force *F* is applied at $t = 0$ and kept constant until $t = t_1$ (creep), $\dot{F} = 0$ and therefore equation (3-6) becomes:

$$\dot{x} = \frac{1}{d} \cdot F \tag{3-9}$$

Solving this differential equation using the initial condition $x = x_s = \frac{F}{c}$ at $t = 0$ gives the creep response:

$$x(t) = \frac{F}{c} + \frac{F}{d}t \tag{3-10}$$

If the force F is removed after a time $t = t_1$ the spring will recover an instantaneous amount $x_s = \frac{F}{c}$ but the dashpot will stay deformed and therefore a residual deformation of $x_{re} = \frac{F}{d} t_1$ will remain, so the exhibit visco elastic recovery.

Figure 3-2 summarises schematically the creep/recovery and relation behaviour of a Maxwell model. As can be seen, the stress relaxation behaviour shows an exponential decay to zero, but the creep behaviour is linear with time and there is no viscous recovery.

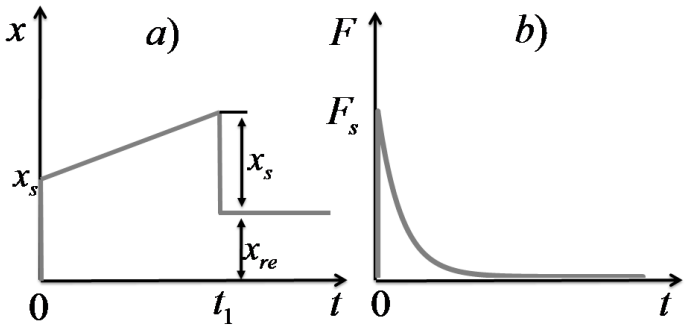

Figure 3-2: Mechanical behaviour of Maxwell model a) creep and recovery; b) relaxation

3.1.1.2 Static response of Kelvin model

The Kelvin model has a spring in parallel with a dashpot (Figure 3-3). For parallel components, the force in each component has to be summed up to obtain the overall force (Equation (3-11)), and the deformation is equal for dashpot and spring (Equation (3-12)) [21, 172]:

$$F = F_s + F_d \tag{3-11}$$

$$x = x_s = x_d \tag{3-12}$$

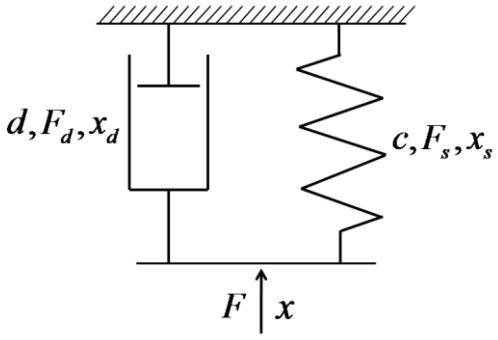

Figure 3-3: Kelvin model

Using the force-displacement equations for the spring (Equation (3-1)) and the dashpot (Equation (3-2)) in equation (3-11) and combining with equation (3-12) gives the constitutive differential equation for the Kelvin model:

$$\dot{x} + \frac{c}{d}x = \frac{F}{d} \tag{3-13}$$

When the deformation rate $\dot{x} = 0$, the force simply remains constant:

$$F = c \cdot x \tag{3-14}$$

For the creep equation, solving equation (3-13) with the initial force $F = F_0$ at $t = 0$ gives:

$$x(t) = \frac{F_0}{c}\left[1 - e^{-\frac{c}{d}t}\right] \tag{3-15}$$

When $t \to \infty$ the maximum displacement is controlled by the spring with $x_{(\infty)} = \frac{F_0}{c} = \frac{F_s}{c}$

If the force is removed at a time $t = t_1$ the recovery is described by:

$$\frac{c}{d}x + \dot{x} = 0 \tag{3-16}$$

Solving with the initial condition $x = x_1$ at $t_{re} = 0$ where the new time variable $t_{re} = t - t_1$ leads to the recovery equation for the Kelvin model:

$$x(t_{re}) = x_1 e^{-\frac{c}{d}t_{re}} \tag{3-17}$$

The initial displacement x_1 for the recovery depends on the time duration of the preceding creep as described in equation (3-15). Thus, the displacement x_1 at t_1 is:

$$x_1 = \frac{F_0}{c}\left[1 - e^{-\frac{c}{d}t_1}\right] \tag{3-18}$$

Figure 3-4 summarises the visco elastic behaviour of the Kelvin model. As can be seen, creep and recovery are reversible, following exponential growth to a limit and exponential decay to zero, respectively. The Kelvin model does not exhibit force relaxation, however.

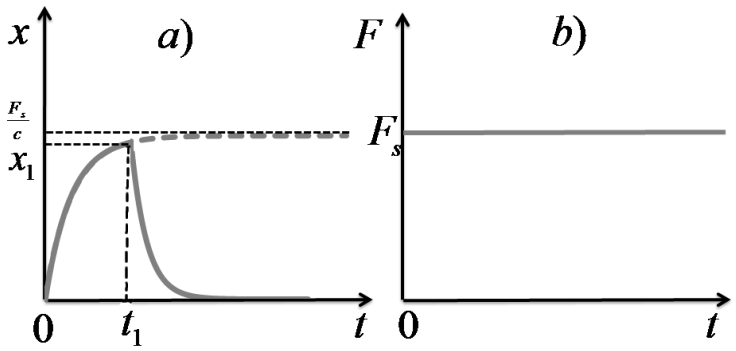

Figure 3-4: Mechanical behaviour of a) creep and recovery b) relaxation

3.1.1.3 Static response of the Standard Linear Solid (SLS)

As seen above, the Maxwell model is able to describe force relaxation for a visco elastic material and the Kelvin model is able to describe reversible creep, but neither can describe both relaxation and creep. The description of a visco elastic solid generally requires both behaviours and the standard linear solid (Figure 3-5) has been widely advocated for its simplicity and ability to describe both creep and relaxation [21, 171, 173]. It is easy to see that, when the spring constant c_2 is very small relative to c_1, the SLS behaves like a Maxwell model, whereas, if c_1 is very big compared to d, it reduces to a Kelvin model.

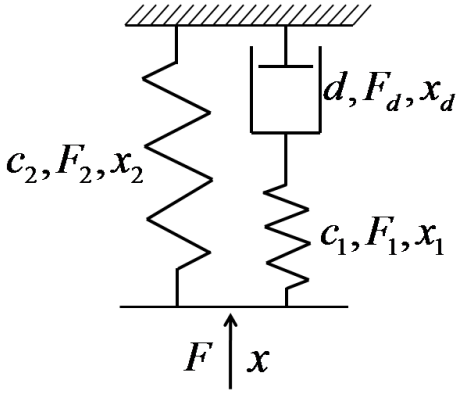

Figure 3-5: Standard linear solid (SLS) model

Force and displacement of the SLS model can be described by:

$$F = F_2 + F_1 = F_2 + F_d \tag{3-19}$$

$$x = x_2 = x_1 + x_d \tag{3-20}$$

The SLS also can be seen as a Maxwell model in parallel with a spring. Using the differential equation of the Maxwell model, equation (3-5) $\dot{x}_m = \frac{\dot{F}_m}{c_m} + \frac{F_m}{d}$ with $F_{SLS} = F_m + F_s$ and $x_{SLS} = x_s = x_m$ gives:

$$\dot{x}_{SLS} = \frac{\dot{F}_{SLS} - \dot{F}_s}{c_m} + \frac{F_{SLS} - F_s}{d} \tag{3-21}$$

Using $F_s = c_2 \cdot x$ and $\dot{F}_s = c_2 \cdot \dot{x}$, the constitutive DE is found:

$$\dot{x} = \frac{\dot{F} - c_2\dot{x}}{c_1} + \frac{F - c_2 x}{d} \tag{3-22}$$

To describe creep behaviour the force is kept constant at F_0 and therefore $\dot{F} = 0$. Using the known conditions at x_0 and x_∞ equation (3-22) can be solved to give:

$$x(t) = \frac{F_0}{c_2} - \frac{F_0 c_1}{(c_1 + c_2)c_2} e^{-\frac{c_1 c_2}{d(c_1+c_2)}t} \tag{3-23}$$

If the force is removed at some time $t = t_1$, when the displacement is x_1, both F and $\dot{F}$ are equal to zero and equation (3-22) becomes :

$$(dc_1 + dc_2)\dot{x} + c_1 c_2 x = 0 \tag{3-24}$$

When the load is removed, there is an instantaneous elastic recovery $x_0 = \frac{F_o}{c_1+c_2}$ so that $x' = x_1 - \frac{F_o}{c_1+c_2}$ at $t' = 0$, where the modified time variable if $t' = t - t_1$. This initial condition allows the DE to be solved for recovery:

$$x(t') = (x_1 - \frac{F_0}{c_1 + c_2})e^{-\frac{c_1 c_2}{d(c_1+c_2)}t'} \tag{3-25}$$

For stress relaxation the displacement rate $\dot{x} = 0$ and thus equation (3-22) becomes:

$$0 = \frac{\dot{F} - c_2\dot{x}}{c_1} + \frac{F - c_2 x}{d} \tag{3-26}$$

Solving this with the initial condition $F = (c_1 + c_2)x$ at $t = 0$ gives:

$$F(t) = c_2 x + c_1 x e^{-\frac{c_1}{d}t} \tag{3-27}$$

Figure 3-6 summarises the mechanical behaviour of the SLS. The creep curve Figure 3-6 a) starts with an instantaneous displacement $x_0 = \frac{F_0}{c_1+c_2}$ at $t = 0$ and, if the force remains in place, the displacement will tend to $x_\infty = \frac{F_0}{c_2}$ for $t \to \infty$. The recovery curve starts with an instantaneous elastic recovery to $x' = x_1 - \frac{F_0}{c_1+c_2}$ followed by an exponential decay towards zero. The relaxation curve, Figure 3-6 (b), is a simple exponential decay from $F_0 = (c_1 + c_2)x$ towards $F_\infty = c_2 x$.

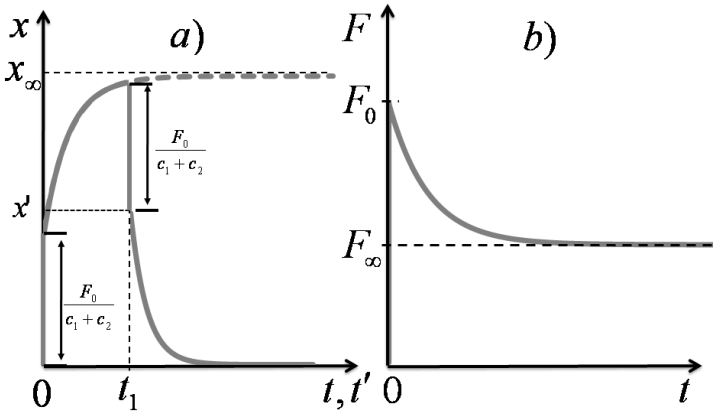

Figure 3-6: Mechanical behaviour of the SLS a) Creep and recovery and b) relaxation

3.1.1.4 Static response of Kelvin + Spring model

An alternative three parameter model can be devised with a spring in series with a Kelvin element, Figure 3-7, hereinafter referred to as the "Kelvin + Spring" model.

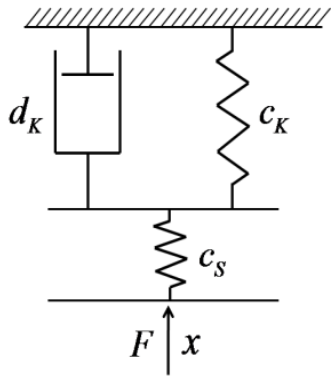

Figure 3-7: Kelvin + Spring model

The constitutive differential equation can be identified by noting that the force going acting on the series spring F_S is equal to the force in the Kelvin element F_K and the total deformation x is the sum of the deformations in the spring and the Kelvin element, x_S and x_K, respectively:

$$F = F_K = F_S \tag{3-28}$$

$$x = x_K + x_S \quad \rightarrow \dot{x} = \dot{x}_K + \dot{x}_S \tag{3-29}$$

Equation (3-13) can be used for the force on the Kelvin element and equation (3-1) for the force on the spring, so:

$$F = F_K = c_K \cdot x_K + d_K \cdot \dot{x}_K \tag{3-30}$$

$$F = F_S = c_S \cdot x_S \rightarrow x_S = \frac{F}{c_S} \rightarrow \dot{x}_S = \frac{\dot{F}}{c_S} \tag{3-31}$$

Substituting the two solutions from equation (3-31) into equation (3-29) and substituting the result into equation (3-30) the differntial equation can be written:

$$\dot{F} + F\left(\frac{c_S}{d_K} + \frac{c_K}{d_K}\right) = c_K \cdot x + d_K \cdot \dot{x} \tag{3-32}$$

As before the creep behaviour is determined by keeping the force constant at F_0 and so $\dot{F} = 0$. Again, using the known conditions at x_0 and x_∞ equation (3-32) can be solved:

$$x(t) = \frac{F_o(c_s + c_K)}{c_S c_K} - \frac{F_0}{c_K} e^{-\frac{c_1 c_2}{d(c_1+c_2)}t} \tag{3-33}$$

For the force relaxation, $\dot{x} = 0$ and, using the boundary conditions $F_{(t=0)} = x \cdot c_s$ and $F_{(t\to\infty)} = x \cdot \frac{c_K c_s}{c_K + c_s}$ the differential equation (3-32) can be solved:

$$F(t) = x \cdot \frac{c_K c_s}{c_K + c_s} - x \frac{{c_s}^2}{c_K + c_s} e^{-\frac{c_K + c_s}{d_K}t} \tag{3-34}$$

The force relaxation retardation time for the spring in series with Kelvin model model is therefore $\frac{d_K}{c_K + c_s}$.

Figure 3-8 summarises the mechanical behaviour of the Kelvin + Spring model. The creep curve, Figure 3-8 a), starts with instantaneous displacement $x_0 = \frac{F_o}{c_s}$ at $t = 0$ and, if the force remains in place, the displacement will tend to $x_\infty = \frac{F_o(c_s + c_K)}{c_S c_K}$ for $t \to \infty$. Similar behaviour to the SLS model is exhibited in recovery and stress relaxation.

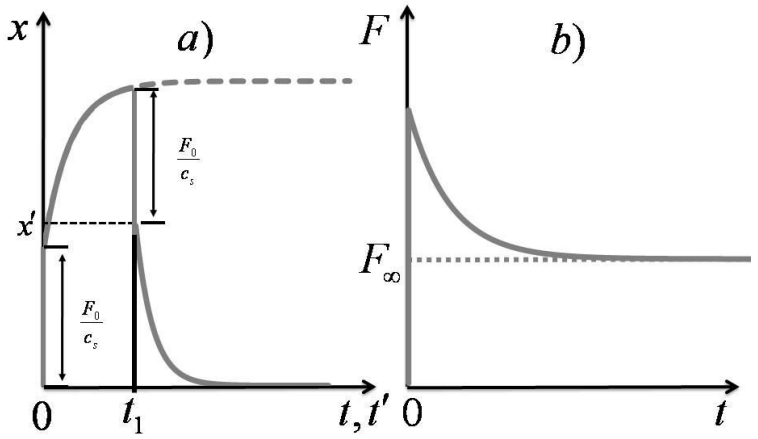

Figure 3-8: Mechanical behaviour of the Kelvin + Spring model a) Creep and recovery and b) relaxation

3.1.1.5 Static response of Multi element models

Simple exponential (single retardation time) responses in creep or force relaxation are sometimes not sufficient to explain or describe real materials. It is possible to give a more flexible representation of force relaxation using a generalized Maxwell model in parallel with a spring (Figure 3-9) [173] and to describe creep behaviour using a generalized Kelvin model (Figure 3-10). The differential equations of these models cannot always be solved as, often, there are insufficient boundary conditions to arrive at a particular solution. However multi – element models can still be solved under certain conditions.

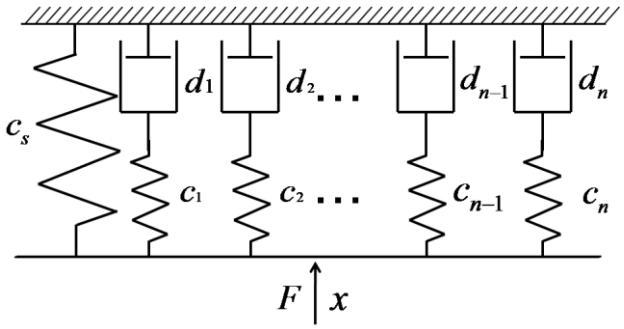

Figure 3-9: Generalized Maxwell model for force relaxation

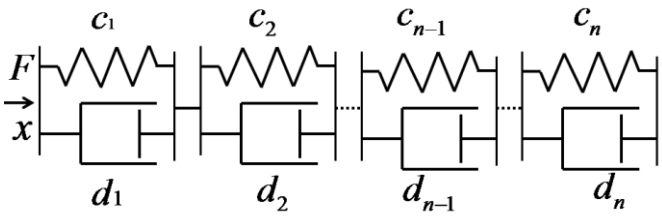

Figure 3-10: Generalized Kelvin model for creep

For example, the force relaxation of the generalized multi component Maxwell model can be described by extension of the simple Maxwell model and the SLS. Given equation (3-8) for a Maxwell model and equation (3-27) for a Maxwell model in parallel with a spring, it can be seen that the force relaxation for a series of Maxwell units in parallel with a spring is:

$$F(t) = x\left[c_s + \sum^{n} c_n e^{-\frac{c_n}{d_n}t}\right] \tag{3-35}$$

where $\frac{d_n}{c_n} = \tau_n$ is the time constant for each individual Maxwell unit.

Similarly, for creep simulation, series Kelvin units (Equation (3-15)) can individually be summed giving:

$$x(t) = \frac{F_0}{c_1}\left[1 - e^{-\frac{c_1}{d_1}t}\right] + \frac{F_0}{c_2}\left[1 - e^{-\frac{c_2}{d_2}t}\right] + \cdots \frac{F_0}{c_{n-1}}\left[1 - e^{-\frac{c_{n-1}}{d_{n-1}}t}\right] + \frac{F_0}{c_n}\left[1 - e^{-\frac{c_n}{d_n}t}\right]$$

$$\Rightarrow x(t) = F_0\left[\sum^{n} \frac{1}{c_n}(1 - e^{-\frac{c_n}{d_n}t})\right] \tag{3-36}$$

3.1.2 Dynamic response of visco elastic models

A number of measurements in this work involve dynamic mechanical testing, or dynamic measurement analysis (DMA). The advantage of DMA compared to a static testing (fixed force or displacement) or quasi static testing (linearly increasing force or displacement) is that the effects of strain, strain rate (velocity of displacement) and acceleration of displacement can be examined simply by increasing or decreasing the frequency during testing. Also, by using a number of cycles, effects such as slackness and irregular noisy sinusoidal waveforms can be dealt with by signal averaging to give robust data.

All of the tests in the current work are carried out under displacement control and, for the dynamic tests, the complex modulus $E^* = E_s + iE_L$, where the modulus of this complex number $|E^*|$and the phase difference tan δ are used to describe the sample material. The complex modulus (here Amplitude ratio (complex Stiffness) $|S^*|$ [N/m]) is a frequency related modulus and shows the elastic component at a certain frequency. The phase lag states the relation of purely viscous components (90° out of phase) to purely elastic components (0° out of phase). In order to make the results useful beyond the particular domain of measurement, it is of interest to relate the dynamic modulus to a visco elastic model, which can be done by examining the effect of frequency on $|E^*|$and $\tan\delta$.

In this section, a sinusoidal strain boundary condition is applied to each model and a sinusoidal stress response is expected with a given phase difference and complex modulus, is used. Due to the fact that the sample will exhibit neither homogeneous stress nor strain, force is used instead of stress and displacement instead of strain. Because the solutions represent a quasi-steady state with no transients and constant mean values, the sinusoidal deformation will lag behind the sinusoidal force, even when

the strain is controlled. The schematic Boltzmann superposition (Figure 3-11 a) illustrates this somewhat counter-intuitive effect. In each increment of deformation the force starts to relax but, because the increments of displacement are not uniform, the peaks of the true relaxation curves are lower toward the maximum deformation. This causes the mean force sinusoid to reach its maximum before the controlled displacement reaches its maximum. The Boltzmann superposition principle can be described mathematically by considering a force relaxation series in which incremental displacements, $\Delta x_1,\ \Delta x_2,\ \Delta x_3, \ldots$ are added at times $\Delta t_1,\ \Delta t_2,\ \Delta t_3, \ldots$ respectively. The total force at time *t* is then given by [173]:

$$F(t) = \Delta x_1 G(t - t_1) + \Delta x_2 G(t - t_2) + \Delta x_3 G(t - t_3) \ldots$$

with G as stiffness (Figure 3-11 b)

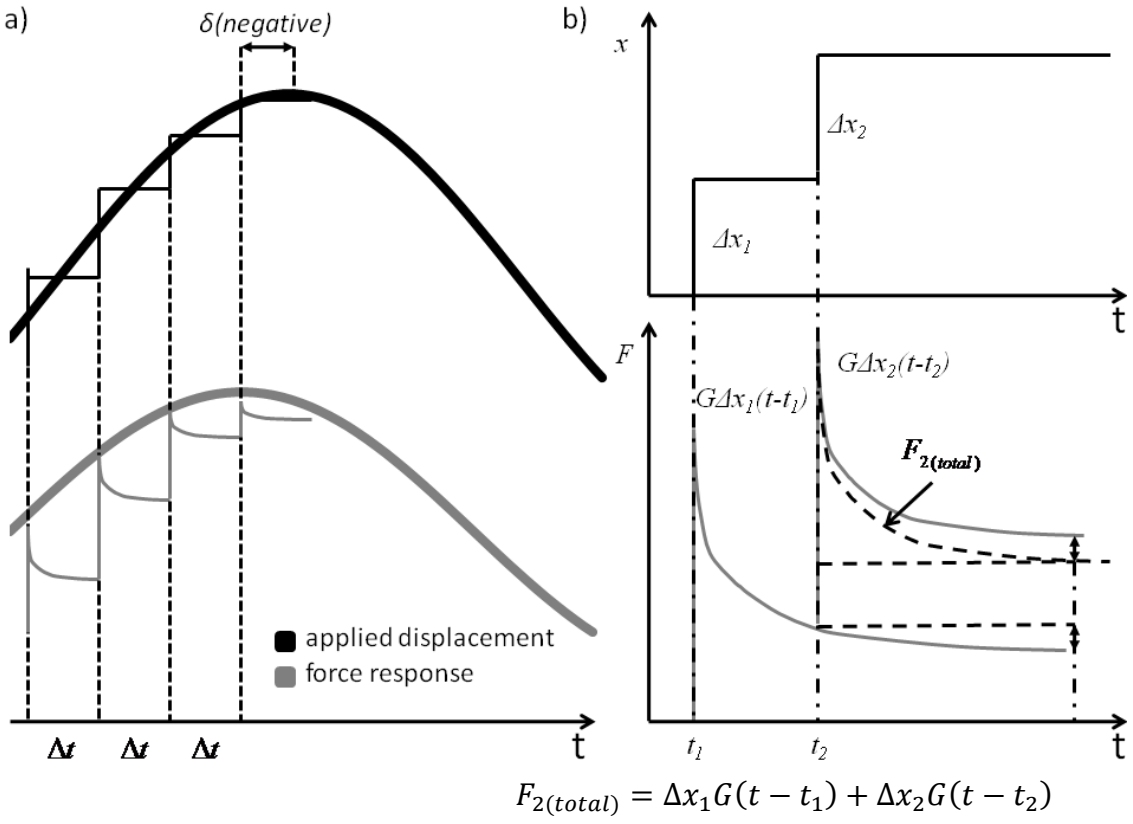

Figure 3-11: Schematic of the Boltzmann principle to illustrate the algebraic sign of the phase

When a visco elastic material is deformed in a sinusoidal fashion (Equation (3-37)) the force will respond in a sinusoidal fashion, but will lead the displacement, equation (3-38).

$$x(t) = x_0 \sin(\omega t) \tag{3-37}$$

$$F(t) = F_0 \sin(\omega t + \delta) \tag{3-38}$$

where ω is the angular frequency, δ is the phase lag and x_0 and F_0 are the amplitudes of the deformation and force respectively. Rewriting equation (3-38):

$$F = F_0 \sin(\omega t)\cos\delta + F_0 \cos(\omega t)\sin\delta \tag{3-39}$$

shows the force response to have two components, one in phase with the displacement and one 90° out of phase with the displacement. The relationship between force and displacement can further be described by an in phase stiffness, S_s, the so-called storage stiffness and an out of phase stiffness, S_L, the so-called loss stiffness.

$$F = x_0 S_S \sin(\omega t) + x_0 S_L \cos(\omega t) \tag{3-40}$$

where

$$S_S = \frac{F_0}{x_0}\cos\delta \quad and \quad S_L = \frac{F_0}{x_0}\sin\delta \tag{3-41}$$

The amplitude ratio S^* can be defined using a phasor diagram (Figure 3-12) and is the vector sum of S_S (elastic component) and S_L (viscous component). If

$$x = x_0 e^{i\omega t} \quad \text{and} \quad F = F_0 e^{i(\omega t+\delta)} \tag{3-42}$$

Then

$$S^* = S_S + i \cdot S_L \tag{3-43}$$

and the phase lag $\tan\delta$ can be written as:

$$\tan\delta = \frac{S_L}{S_S} \tag{3-44}$$

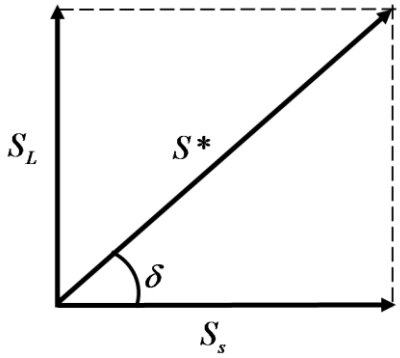

Figure 3-12: Phasor diagram for amplitude ratio and phase lag [173, 174]

The complex modulus $|E^*|$ and the phase lag $\tan\delta$ for several visco elastic models have already been described by Yang [21]. The modifications below simply transform these results to describe force and displacement and the corresponding complex stiffness.

Dynamic response of Maxwell model

The complex force-displacement relationship for the Maxwell model can be described simply by substituting equation (3-42) into the differential equation (3-5):

$$x_0 i\omega e^{i\omega t} = \frac{1}{c} F_0 i\omega e^{i(\omega t+\delta)} + \frac{1}{d} F_0 \omega e^{i(\omega t+\delta)} \tag{3-45}$$

$$\Rightarrow i\omega = \frac{i\omega}{c} \frac{F_0 i\omega e^{i(\omega t+\delta)}}{x_0 e^{i\omega t}} + \frac{1}{d} \frac{F_0 \omega e^{i(\omega t+\delta)}}{x_0 e^{i\omega t}} \tag{3-46}$$

$$\Rightarrow i\omega = \frac{i\omega}{c} S^* + \frac{1}{d} S^* \tag{3-47}$$

hence

$$S^* = \frac{i\omega d c^2}{c + i\omega d} \tag{3-48}$$

Multiplying the numerator and the denominator by the complex conjugate of the denominator, equation (3-48) becomes:

$$S^* = \frac{i\omega d c^3 + \omega^2 d^2 c^2}{c^2 + \omega^2 d^2} \tag{3-49}$$

The vector amplitude ratio $|S^*| = \sqrt{{S_s}^2 + {S_L}^2} = \frac{F_0}{x_0}$ helps to rewrite equation (3-49) in a dimensionless form:

$$\frac{|S^*|}{c} = \frac{\frac{\omega d}{c}}{\sqrt{\left[\left(\frac{\omega d}{c}\right)^2 + 1\right]}} \tag{3-50}$$

and the phase lag can be calculated using equation (3-49), identifying $\tan\delta = \frac{S_L}{S_S}$.

$$\tan\delta = \frac{c}{\omega d} \tag{3-51}$$

The behaviour of the dimensionless amplitude ratio versus ω and phase difference versus ω for the Maxwell model can be seen in Figure 3-13. It is clear that increasing the frequency causes the amplitude ratio of the Maxwell model to increase, initially in a linear fashion, but eventually settling to a value of unity where it behaves like a simple spring. As $\omega \to 0$ the amplitude ratio tends towards zero which is not an appropriate model to describe low frequency dynamic behaviour [21]. As the phase difference continuously decreases for increasing frequency and, for $\omega \to 0$, the phase difference becomes $\tan\delta \to \infty$ which would be 90° out of phase, which is also not appropriate. The effect of varying the ratio of $\frac{d}{c}$ at a given frequency is the same as the effect of varying frequency at a given ratio of $\frac{d}{c}$.

Dynamic response of Kelvin model

Modifying the differential equation (3-13) and substituting equation (3-42) results in:

$$cx_0\omega e^{i\omega t} + dx_0 i\omega e^{i\omega t} = F_0\omega e^{i(\omega t+\delta)} \tag{3-52}$$

$$\Rightarrow \frac{F_0 e^{i(\omega t+\delta)}}{x_0 i\omega e^{i\omega t}} = S^* = c + di\omega \tag{3-53}$$

and so the dimensionless amplitude ratio for the Kelvin model becomes:

$$\frac{|S^*|}{c} = \sqrt{1 + \left(\frac{\omega d}{c}\right)^2} \tag{3-54}$$

with a phase difference of:

$$\tan\delta = \frac{d\omega}{c} \tag{3-55}$$

The amplitude ratio and phase difference for the Kelvin model show a reasonable behaviour for low frequencies where the model will tend towards a spring like behaviour with $S^* = 1$and $\tan\delta \to 0$ (Figure 3-13). With increasing frequency both the phase difference and the amplitude ratio will increase.

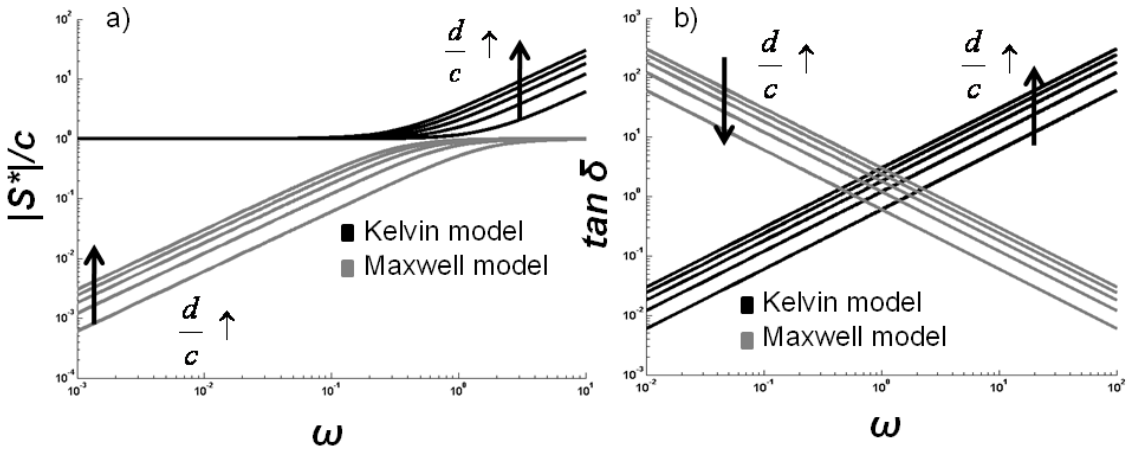

Figure 3-13: a) amplitude ratio versus ω b) phase difference versus ω for Maxwell and Kelvin model with changing d/c.

3.1.3 Further models and their amplitude ratio and phase angle

The amplitude ratio and phase difference of three parameter models can be derived in the same way as the Maxwell and the Kelvin models. Table 3-1 lists the three possible configurations of three parameter model with their corresponding amplitude ratio and phase difference.

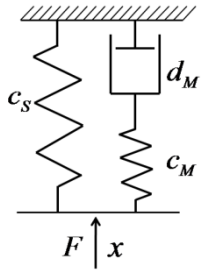	**Standard linear solid SLS model** Amplitude ratio: $$\frac{\lvert S^* \rvert}{c_s} = \sqrt{\frac{\left[\frac{c_S}{c_M} + \left(\frac{\omega d_M}{c_M}\right)^2 \left(1 + \frac{c_S}{c_M}\right)\right]^2 + \left(\frac{\omega d_M}{c_M}\right)^2}{\left(\frac{c_S}{c_M}\right)^2 \left[1 + \left(\frac{\omega d_M}{c_M}\right)^2\right]^2}}$$	Phase difference: $$\tan\delta = \frac{\frac{\omega d_M}{c_M}}{\frac{c_S}{c_M} + \left(\frac{\omega d_M}{c_M}\right)^2 \left(1 + \frac{c_S}{c_M}\right)}$$
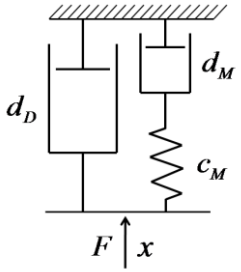	**Damper in parallel with Maxwell model** Amplitude ratio: $$\frac{\lvert S^* \rvert}{c_M} = \sqrt{\frac{(c_M d_M \omega)^4 + \left(\omega d_D {c_M}^2 + \omega d_M {c_M}^2 + \omega^3 {d_M}^2 d_D\right)^2}{{c_M}^2\left(\omega^2 {d_M}^2 + {c_M}^2\right)}}$$	Phase difference: $$\tan\delta = \frac{d_D {c_M}^2 + d_M {c_M}^2 + \omega^2 {d_M}^2 d_D}{\omega c_M {d_M}^2}$$
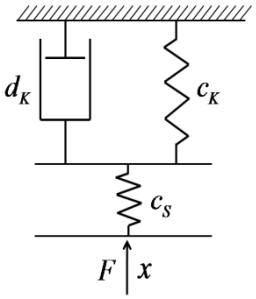	**Spring in series with Kelvin model** Amplitude ratio: $$\frac{\lvert S^* \rvert}{c_s} = \sqrt{\frac{\left({c_k}^2 + \omega^2 {d_k}^2\right)}{\omega^2 {d_K}^2 + {c_S}^2 + 2c_K c_S + {c_K}^2}}$$	Phase difference: $$\tan\delta = \frac{\omega d_K c_s}{\omega^2 {d_K}^2 + c_K c_S + {c_K}^2}$$

Table 3-1: The three possible three parameter models with their Amplitude ratio and Phase difference

The amplitude ratio and phase angle of the SLS model can be seen in Figure 9-1, with a) showing dimensionless amplitude ratios and Figure 9-1 b showing the tangent of the phase lag for various parameter combinations. All the amplitude ratio curves exibit essentially the same behaviour, changing between unity and an upper shelf value at low and high frequencies, respectively. Similarly the phase curves all increase from zero at zero frequency, passing through a maximum and return again to zero at high frequency. Changing the spring ratio $\frac{c_M}{c_S}$, changes the height of the shelf in amplitude ratio and the maximum value $\tan\delta$, with a minor change in its frequency. Increasing the damping ratio $\frac{d_M}{c_M}$ has the effect of bringing the shelf value to a lower angular frequency and shifting the peak value of $\tan\delta$ towards lower frequencies. The SLS model can also be made to reduce to a Maxwell or Kelvin model simply by taking $c_S = 0$ or $c_M \to \infty$, respectively.

Putting the damper in parallel with the Maxwell model gives a completely different behaviour to the SLS model (Figure 9-2). For both the amplitude ratio and the phase lag, the behaviour of the Maxwell model is dominant at lower frequencies whereas, at higher frequencies, the model follows a purely Kelvin-like behaviour. Modifying the two damper parameters merely helps to extend the range of the Maxwell behaviour or starts the Kelvin behaviour earlier. The undesirable properties of the Maxwell model that, when $\omega \to 0$ $\frac{|S^*|}{c_M} \to 0$, cannot be eliminated in this model. If the parallel damper parameter d_D becomes zero this model reduces to the Maxwell model, whereas increasing the damper parameter $d_M \to \infty$ the simple Kelvin model is reproduced.

Figure 9-3 shows the amplitude ratios and phase differences of a spring in series with a Kelvin model. This model exhibits the same range of shapes as the SLS model in that the amplitude ratio goes from a lower shelf to an upper shelf and the phase increases from zero to a peak and then returns to zero. The only difference in the amplitude curve is that the upper shelf is unity and the lower shelf is not unity, being controlled by the c_K parameter. At higher frequencies, the Kelvin element cannot respond and the model is dominated by the spring c_s. In the SLS model, the Maxwell element carries zero force at very low frequencies and the parallel spring dominates. The phase difference shows exactly the same behaviour as the SLS model it being possible to shift the maximum peak along the x-axis and increase or decrease the maximum value. If the

limiting cases of $t = 0$ and $t \to \infty$ for the SLS model and for the Kelvin + spring model are the same, it can be said that:

$$c_{s(Kelvin+spring)} = c_{s(SLS)} + c_M \quad \text{for} \quad t = 0 \tag{3-56}$$

and

$$\frac{c_K c_{s(Kelvin+spring)}}{c_K + c_{s(Kelvin+spring)}} = c_{s(SLS)} \quad \text{for} \quad t \to \infty \tag{3-57}$$

Also the retardation time follows the same behaviour and therefore:

$$\frac{d_K}{c_K + c_{s(Kelvin+spring)}} = \frac{d_M}{c_M} \tag{3-58}$$

Putting the identities (3-56),(3-57)and (3-58) into the two phase lag equations for Table 3-1 it is possible to identify the SLS model parameters with the Kelvin + spring model parameters, so:

$$\tan\delta = \frac{\frac{\omega d_M}{c_M}}{\frac{c_{S(SLS)}}{c_M} + \left(\frac{\omega d_M}{c_M}\right)^2 \left(1 + \frac{c_{S(SLS)}}{c_M}\right)} = \frac{\omega d_K c_{S(Kelcin+spring)}}{\omega^2 {d_K}^2 + c_K c_{S(Kelvin+spring)} + {c_K}^2} \tag{3-59}$$

when:

$$c_{s(SLS)} = \frac{c_K c_{s(Kelvin+spring)}}{c_K + c_{s(Kelvin+spring)}} \tag{3-60}$$

and

$$c_M = c_{s(Kelvin+spring)} - \frac{c_K c_{s(Kelvin+spring)}}{c_K + c_{s(Kelvin+spring)}} \tag{3-61}$$

and

$$d_M = \frac{\left(c_{s(Kelvin+spring)} - \frac{c_K c_{s(Kelvin+spring)}}{c_K + c_{s(Kelvin+spring)}}\right) d_K}{c_K + c_{s(Kelvin+spring)}} \tag{3-62}$$

Therefore both models express the same dynamic behaviour, emphasising the fact that they are merely models and the configuration has no direct physical meaning.

3.2 Visco elastic models with an inertial component

Some of the structures investigated in this work have significant mass associated with them and appropriate models are akin to visco elastic systems but also need to consider the inertial effect of spring- and damper-mounted masses. Vibrating systems always have at least two storage modes, potential energy and kinetic energy. For such systems the potential energy is related to the displacement and a spring is used to model it, whereas the kinetic energy is related to the displacement rate (velocity). The inertia is represented by masses and their associated accelerations. All systems lose energy and this dissipation can be modelled using dashpots or dampers. A so-called Mass – Spring – Damper system (MSD system) can represent any behaviour of a vibrating system. The degrees of freedom (DOF) are determined by the number of dimensions in which masses can freely move. This means that a system has more than one DOF if it has more than one mass, or one mass which can move in several independent directions [175]. In this work, a single DOF MSD system was sufficient to explain all observed behaviour. The classical way to write the single degree-of-freedom, one-dimensional equation of motion of an MSD system is to use the differential equation of motion of second order [175].

$$m\ddot{x} + F_d(\dot{x}, x, t) + F_c(x, t) = F(t) \tag{3-63}$$

where m is the mass for the inertia properties. The damping force F_d depends primarily on the displacement rate $\dot{x}$ but also may depend on the displacement x and, independently, the time t .The elastic force F_c depends primarily on the displacement x but may also depend on the time t. If the system is excited from outside, excitation forces $F(t)$ have to be introduced.

Equation (3-63) is a non linear second order differential equation which is not easy to solve and is unnecessarily complicated for the problem in hand. For the simplest case, the elastic and the damping values are constants [176], hence it becomes:

$$m\ddot{x} + d\dot{x} + cx = F(t) \tag{3-64}$$

where m, d and c represent the constant mass, and the damping and elastic coefficients, respectively. Once the differential equation has been solved, it is possible to calculate amplitude ratio S^* (stiffness equivalent to the magnitude of the complex modulus, E^*)

and the phase difference ($\tan\delta$) for the required system. Three MSD models with one degree of freedom are developed in the following sections, which investigate both the configuration and the position of the excitation system with the amplitude and phase lag, as was done for the visco elastic models. In dynamics analysis it is usually the difference between the excitation displacement and that of the freely moving mass that is of interest. Hence most sources simply state the resonance function *V* and the phase difference $\tan\delta$ of the two out of phase displacements. However, in this work, a modification is introduced to show the force amplitude, the displacement amplitude and the phase lag between the two in order that the models can be used to explain the experimental results.

3.2.1 Series model – displacement excitation of spring

The free body diagram (Figure 3-14) allows us to write:

$$F = d\dot{x}_2 + m\ddot{x}_2 \tag{3-65}$$

$$F = c(x_1 - x_2) \tag{3-66}$$

Substituting equation (3-42) into (3-65) and (3-66) gives:

$$F_0 e^{i(\omega t+\delta)} = d\hat{x}_2 i\omega e^{i\omega t} - m\hat{x}_2\omega^2 e^{i\omega t} \tag{3-67}$$

$$F_0 e^{i(\omega t+\delta)} = c(\hat{x}_1 - \hat{x}_2)e^{i\omega t} \tag{3-68}$$

with $\hat{x}_i$ giving the amplitude for each displacement.
Solving equation (3-67) for $\hat{x}_2$:

$$\hat{x}_2 = \frac{F_0 e^{i(\omega t+\delta)}}{di\omega e^{i\omega t} - m\omega^2 e^{i\omega t}} \tag{3-69}$$

substituting into equation (3-68):

$$F_0 e^{i(\omega t+\delta)} = c(\hat{x}_1 - \frac{F_0 e^{i(\omega t+\delta)}}{di\omega e^{i\omega t} - m\omega^2 e^{i\omega t}})e^{i\omega t} \tag{3-70}$$

and solving for *S**:

$$S^* = \frac{F_0 e^{i(\omega t+\delta)}}{\hat{x}_1 e^{i\omega t}} = \frac{c\omega(id - m\omega)}{c + id\omega - m\omega^2} \tag{3-71}$$

Since $S^* = S_S + iS_L$, equation (3-71) can be re-expressed by multiplying the numerator and the denominator by the complex conjugate of the denominator giving the dynamic modulus:

$$\frac{|S^*|}{c} = \sqrt{\frac{(d^2 + m^2\omega^2)\omega^2}{m^2\omega^4 - 2cm\omega^2 + d^2\omega^2 + c^2}} \tag{3-72}$$

and the phase:

$$\tan\delta = \frac{cd}{\omega(m^2\omega^2 - cm + d^2)} \tag{3-73}$$

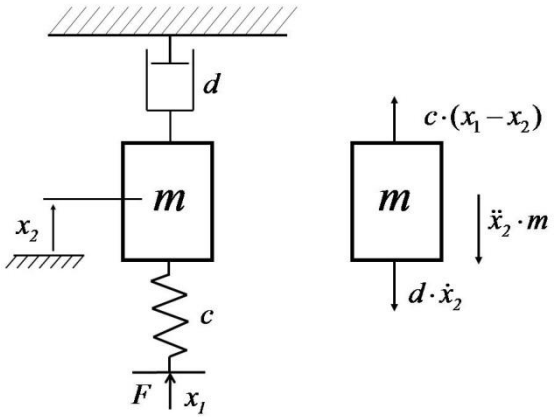

Figure 3-14: Series model with displacement excitation of spring. Force balance on mass system shown on right.

3.2.2 Series model – displacement excitation of damper

For the dashpot in series to a mass and in series to a spring, the forces must be the same on all three elements (Figure 3-15):

$$F = d(\dot{x}_1 - \dot{x}_2) \tag{3-74}$$

$$F = cx_2 + m\ddot{x}_2 \tag{3-75}$$

Substituting equation (3-42) into equation (3-74) and (3-75) gives:

$$F_0 e^{i(\omega t+\delta)} = di(\hat{x}_1 - \hat{x}_2)\omega e^{i\omega t} \tag{3-76}$$

$$F_0 e^{i(\omega t+\delta)} = (c\hat{x}_2 - m\hat{x}_2\omega^2)e^{i\omega t} \tag{3-77}$$

Solving (3-77) for $\hat{x}_2$ and substituting it into equation (3-76):

$$S^* = \frac{F_0 e^{i(\omega t+\delta)}}{\hat{x}_1 e^{i\omega t}} = \frac{i\omega d(c - m\omega^2)}{c + id\omega - m\omega^2} \tag{3-78}$$

Equation (3-78) can be re-expressed by multiplying the numerator and the denominator by the conjugate of the denominator giving the magnitude of the dynamic stiffness:

$$S^* = \frac{F_0 e^{i(\omega t+\delta)}}{\hat{x}_1 e^{i\omega t}} = \frac{(\omega^2 d^2 c - \omega^4 \omega d^2 m) + i(\omega d c^2 - 2m\omega^3 dc + \omega^5 dm^2)}{(c + id\omega - m\omega^2)(c - id\omega - m\omega^2)} \tag{3-79}$$

The dimensionless amplitude ratio $\left[|S^*| = \sqrt{{S_s}^2 + {S_L}^2}\right]$ is:

$$\frac{|S^*|}{c} = \sqrt{\frac{\omega^2 d^2 (c - m\omega^2)^2}{(m^2\omega^4 - 2cm\omega^2 + d^2\omega^2 + c^2)c^2}} \tag{3-80}$$

and the corresponding phase difference is:

$$\tan\delta = \frac{c - m\omega^2}{\omega d} \tag{3-81}$$

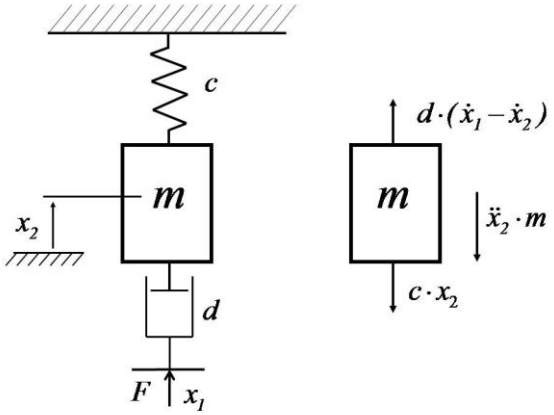

Figure 3-15: Series model with displacement excitation of damper. Force balance on mass system shown on right.

3.2.3 Parallel-series model – displacement excitation of parallel element

For a combination of components in series and in parallel,the parallel forces are added togetether and series forces are equal (Figure 3-16).

$$F = d_2\dot{x}_2 + c_2x_2 + m\ddot{x}_2 \tag{3-82}$$

$$F = d_1(\dot{x}_1 - \dot{x}_2) + c_1(x_1 - x_2) \tag{3-83}$$

Substituting equation (3-42) into (3-82) and (3-83):

$$F_0e^{i(\omega t+\delta)} = d_2\hat{x}_2i\omega e^{i\omega t} + c_2\hat{x}_2e^{i\omega t} - m\hat{x}_2\omega^2e^{i\omega t} \tag{3-84}$$

$$F_0e^{i(\omega t+\delta)} = d_1(\hat{x}_1 - \hat{x}_2)i\omega e^{i\omega t} + c_1(\hat{x}_1 - \hat{x}_2)e^{i\omega t} \tag{3-85}$$

Solving equation (3-84) for $\hat{x}_2$:

$$\hat{x}_2 = \frac{F_0e^{i(\omega t+\delta)}}{d_2i\omega e^{i\omega t} + c_2e^{i\omega t} - m\omega^2e^{i\omega t}} \tag{3-86}$$

and substituting into equation (3-85) gives:

$$F_0 e^{i(\omega t+\delta)} = d_1\left(\hat{x}_1 - \frac{F_0 e^{i(\omega t+\delta)}}{d_2 i\omega e^{i\omega t} + c_2 e^{i\omega t} - m\omega^2 e^{i\omega t}}\right) i\omega e^{i\omega t} + c_1\left(\hat{x}_1 - \frac{F_0 e^{i(\omega t+\delta)}}{d_2 i\omega e^{i\omega t} + c_2 e^{i\omega t} - m\omega^2 e^{i\omega t}}\right) e^{i\omega t} \tag{3-87}$$

The amplitude ratio is:

$$S^* = \frac{F_0 e^{i(\omega t+\delta)}}{\hat{x}_1 e^{i\omega t}} = \frac{i\omega d_1 c_2 - \omega^2 d_1 d_2 - i\omega^3 d_1 m + c_1 c_2 + i c_2 \omega d_2 - c_1 \omega^2 m)}{(c_1 + c_2 - m\omega^2) + (i d_2 \omega + i d_1 \omega)} \tag{3-88}$$

Again, to separate into real and imaginary parts, the imaginary part of the denominator is eliminated by multiplying the numerator and the denominator by the complex conjugate of the denominator, giving the amplitude:

$$|S^*| = \sqrt{\frac{\left({c_1}^2 + {d_1}^2\omega^2\right)\left(m^2\omega^4 + (-2c_2 m + {d_2}^2)\omega^2 + {c_2}^2\right)}{m^2\omega^4 + [-2c_1 m - 2c_2 m + (d_1 + d_2)^2]\omega^2 + (c_1 + c_2)^2}} \tag{3-89}$$

and the phase

$$\tan\delta = \frac{\left[d_1\omega^4 m^2 + \left({d_1}^2 d_2 + \left(-2c_2 m + {d_2}^2\right)d_1\right)\omega^2 + {c_1}^2 d_2 + d_1 {c_2}^2\right]\omega}{\left(c_1 m^2 - {d_1}^2 m\right)\omega^4 + \left(-{c_1}^2 m + \left(-2c_2 m + {d_2}^2\right)c_1 + {d_1}^2 c_2\right)\omega^2 + c_1 c_2 (c_1 + c_2)^2} \tag{3-90}$$

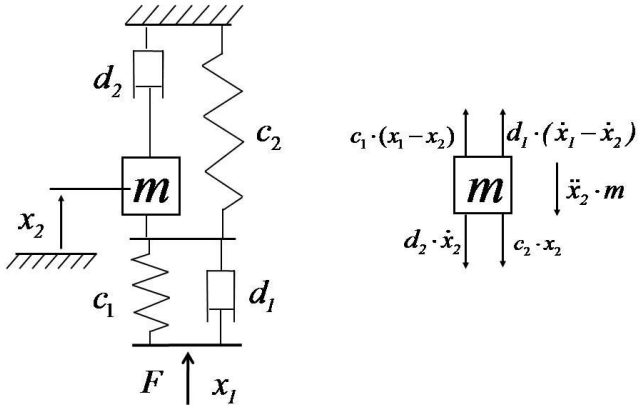

Figure 3-16: Series model with displacement excitation of parallel elements. Force balance on mass system shown on right.

Figures 3.20 to 3.23 show the three MSD model behaviours as their spring, damper and mass values are varied. As can be seen, a very wide range of evolutions of phase and amplitude with frequency are revealed and these are sufficient to describe even the most complex experimental results.

3.3 Preparation of results for analysis

All experimental data were stored as text files and were subsequently prepared by Excel or MatLab 2007a for analysis using the various visco elastic models developed in this Chapter. This section describes the preparation of the text files.

3.3.1 Preparation of dynamic results

As described later in Chapter 4, the data were acquired at a sampling rate dependent on the frequency, varying from 1 kS/sec for 2Hz up to 30 kS/sec for 60Hz, and 10 full cycles were recorded at each frequency. Each text file included force, displacement and pressure readings. First, the 10 displacement waves were averaged to a single period and then the force readings were treated similarly, preserving the time correlation (phase). This can be done because the intended frequency is known and averaging can therefore be achieved by adding values exactly one period apart in the record, and then dividing by the total number of periods in the record.
Next the data needed to be corrected for inertial effects. The piezo actuator produces a displacement:

$$s(t) = A\sin(\omega t) \tag{3-91}$$

and, because the load cell is carried on the actuator, there is an inertial force:

$$F(acc) = m \cdot a(t) \tag{3-92}$$

where

$$a(t) = -A\omega^2\cos(\omega t) \tag{3-93}$$

Because the acceleration force *F(acc)* is parallel to the indentation force *F(real)*, the measured signal needs to be conditioned by subtracting the inertial force:

$$F(real) = F(measured) - F(acc) \tag{3-94}$$

Figure 3-17 shows a typical measured force output $F(measured)$ (blue curve) at 30 Hz when the probe is in contact with the sample and the corresponding inertial force $F(acc)$, measured separately by oscillating the load cell was oscillated at the same frequency without touching the sample (green curve). Subtracting the blue curve from the green curve gives the true force $F(real)$ (red curve) caused by deforming the sample.

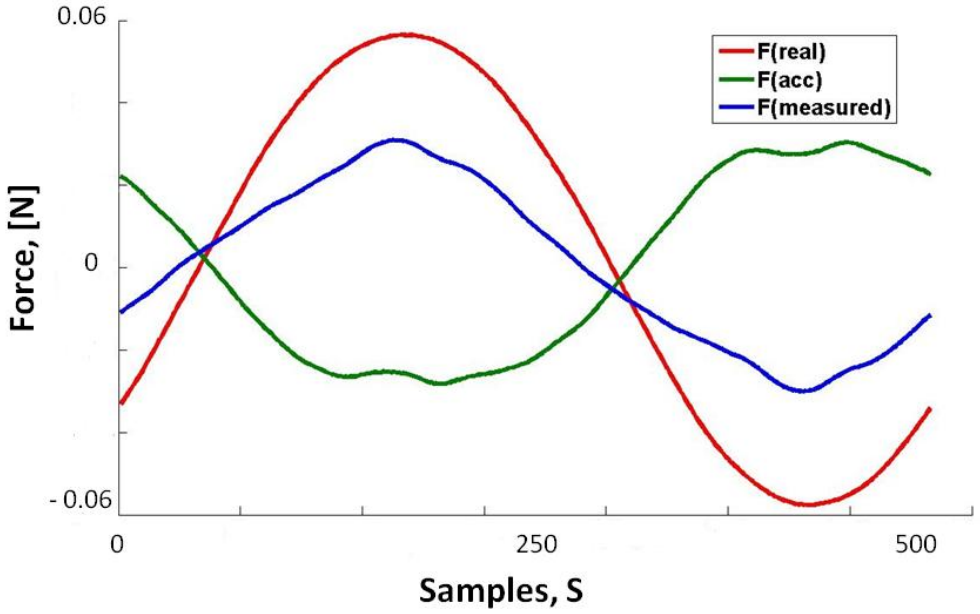

Figure 3-17: Force signals at 30 Hz when the probe is not in contact with the sample (inertia force) (green line), when the probe is in contact with the sample (blue line) and the true force sinus wave (red curve) when the inertia force (green curve) is substracted from the actual measured force (blue curve).

This signals can be further investigated by applying Fourier analysis to the force wave and the displacement wave. A sinusoidal wave can be written [21, 177]:

$$f(t) = a_0 + \sum_{1}^{\infty} a_n \cos(n\omega t) + \sum_{1}^{\infty} b_n \sin(n\omega t) \tag{3-95}$$

where the coefficients a_n and b_n are:

$$a_n = \frac{2}{T} \int_{-T/2}^{T/2} f(t) \cos(n\omega t)\, dt \tag{3-96}$$

$$b_n = \frac{2}{T} \int_{-T/2}^{T/2} f(t) \sin(n\omega t)\, dt, \quad with\ \omega = \frac{2\pi}{T} \tag{3-97}$$

and the mean is:

$$a_{mean} = \frac{1}{T} \int_{-T/2}^{T/2} f(t)\, dt \tag{3-98}$$

Again exploiting the fact that the frequency is known and controlled, the amplitude of the signal at the controlled frequency can be obtained from the first Fourier Coefficients, a_0 and $\underline{b}_0$:

$$A = \sqrt{{a_0}^2 + {b_0}^2} \tag{3-99}$$

Similarly, the phase (relative to a pure sine wave) can again be obtained from the first Fourier Coefficients:

$$\delta = tan^{-1}\left(\frac{a_0}{b_0}\right) \tag{3-100}$$

The amplitude ratios and phase differences could then be obtained as a function of frequency for further analysis.

3.3.2 Preparation of static and quasi static results of pig eyeballs and porcine PDL

The macro tool in Microsoft Excel 2007 was used to extract the force relaxation curves from the raw text files (Figure 3-18). The preparation of the data was necessary to implement the values into the curve fitting tool of Matlab 2007a. The curve fitting tool determined stiffness parameters *c* and viscosity parameters *d*. The SLS model (three parameter model) and a five parameter model (Figure 3-20 constant parameter with two exponential functions) were used to analyse the results (Figure 3-19) of the static pig eyeball experiment. The SLS model was also implemented to analyse the data at two different relaxation times, one after 3 seconds and one after its full allowed relaxation

time of 10 seconds. Differences in stiffness, viscosity and R^2 were plotted and statistically analysed.

The PDL relaxation curves were analysed in Matlab 2007a with a three parameter model (constant parameter and one exponential function), a four parameter model (two exponential functions) and a five parameter model (constant parameter and two exponential functions). The three models can be represented by the following equations (Figure 3-20). All parameters were plotted and statistically compared with a one-way analysis of variance (ANOVA) test.

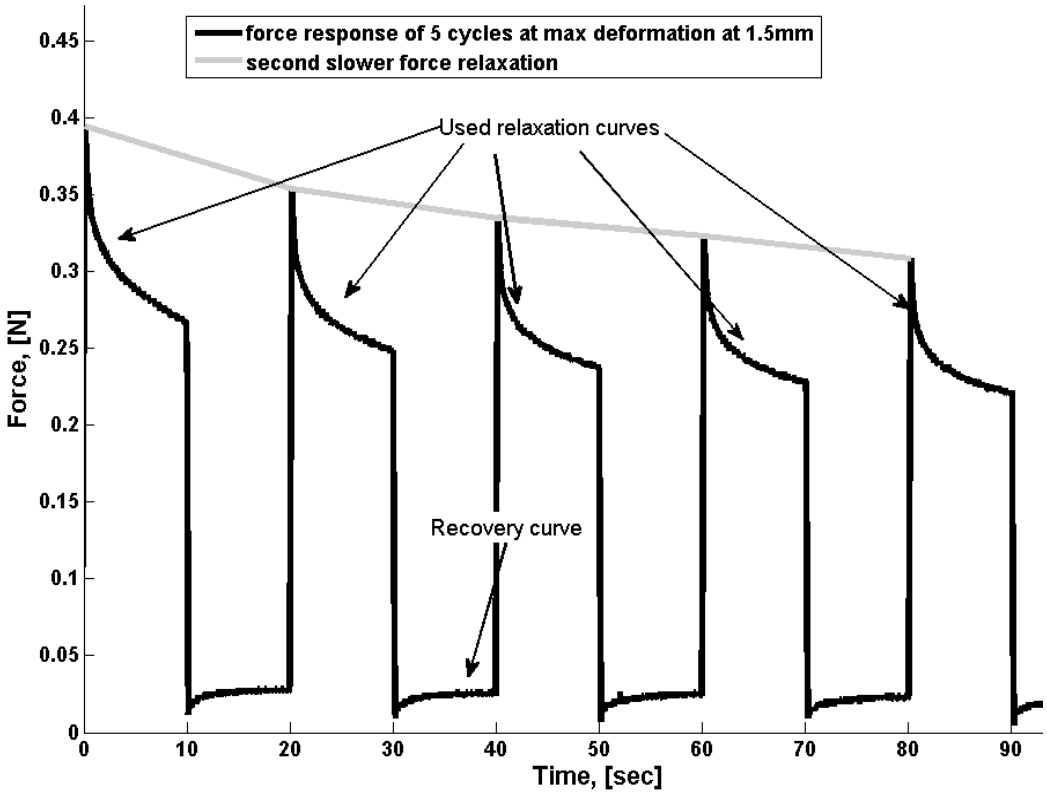

Figure 3-18: Quasi-static test performed on the pig eyeball with an IOP of 6.2kPa

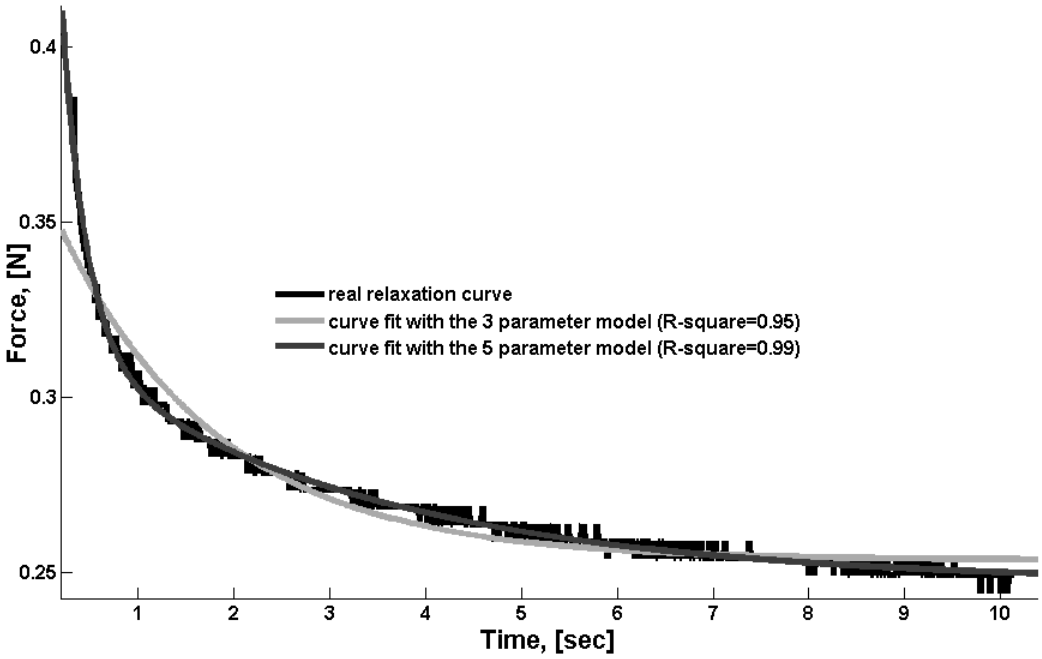

Figure 3-19: Curve fitting in MatLab using the SLS model and a 5 parameter model

constant parameter with one exponential function	two exponential functions	constant parameter with two exponential functions
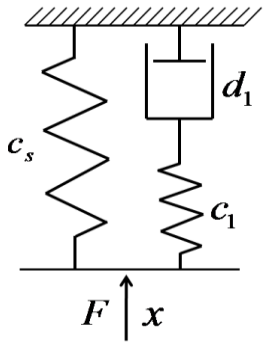	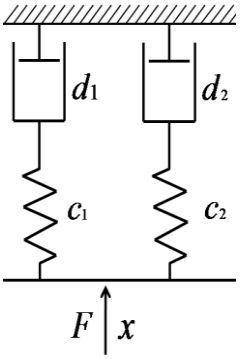	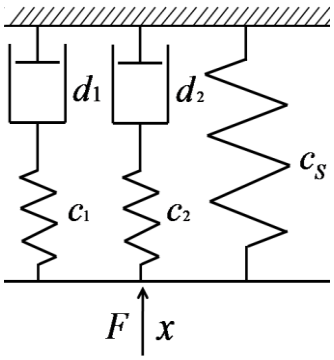
$F(t) = x\left[c_S + c_1 \cdot e^{-\frac{c_1}{d_1}t}\right]$	$F(t) = x\left[c_1 \cdot e^{-\frac{c_1}{d_1}t} + c_2 \cdot e^{-\frac{c_2}{d_2}t}\right]$	$F(t) = x\left[c_S + c_1 \cdot e^{-\frac{c_1}{d_1}t} + c_2 \cdot e^{-\frac{c_2}{d_2}t}\right]$

Figure 3-20: Three models applied for force relaxation curves with their equations

Chapter 4: Materials, Methods and Experimental Procedures

The experimental work associated with this thesis requires the measurement of force and displacement where the relationship between the two is a function of time. A series of configurations have been chosen in which a dynamic force-displacement relationship was expected and where the relationship would offer a diagnostically significant assessment.

Although a range of different configurations were used, a common set of sensors were employed. Therefore, this chapter first describes the sensors and the measurement process capability followed by the process capability of all actuators.

Next, the three configurations are described along with the associated experimental procedures; the "mechanical eyeball" simulation of the cornea and vitreous humour for IOP assessment, the corresponding set-up for porcine eyeball measurements and the set-up for measurement on the periodontal ligament in porcine jaws.

4.1 Calibration, measurement capability and process capability of the test rig

Any test rig consisting of sensors and actuators has to be calibrated. To qualify a test rig for its accuracy and repeatability the sensors have to work in a specific range and should be 10 times more accurate than the required tolerance for the clinical devices. While the sensors have to exhibit the necessary measurement capabilities, the actuators need to be tested for their stability in a working process. The approach taken here is to develop capability indices for the measurement system and for the process as suggested by Dietrich and Schultze [178]. The measurement system considers the whole environment which can influence the output reading. This includes the sensor or actuator itself, the amplifiers used connected in their test environment (e.g. temperature, humidity and electrical noise from other devices), the analogue-digital converter (DAQ card BNC-2110 with PCI6024E from National Instruments), the wiring and the PC with Software (National Instruments LabView 7.1).

The sensors used for this work (LVDT, load cell, pressure sensor) all proved to be linear within their working range and their respective calibrations are represented by best-fit linear regression of the output of the sensor (Voltage) onto the relevant unit (e.g. Force [N] for the load cell) along with the associated correlation coefficient.

The concept of measurement capability is used to investigate the repeatability, accuracy and short time capability, and was assessed for each of the sensors. The concept assumes that the required tolerance is defined and aims for a measurement system that has a ten times better performance (Figure 4-1). The probability distribution of the measurement system needs first to be determined and this was obtained by making 50 measurements on a standard piece with known dimension x_m (e.g. for the load cell, a specific weight). The standard deviation s_g and the average x_g of the 50 values were determined and the capability index, C_g, and C_{gk} were calculated from Equations 4-1 and 4-2. If the value of C_g is greater than 1.33, then at least 99.7% of all the measured data points were ten times better than the claimed tolerance, T. The index C_{gk} indicates any drift of the mean value x_g relative to the standard piece value x_m taking account of the distribution of values. If C_{gk} is greater than 1.33 then the capability is given, but if it is less than 1.33 and C_g is greater than 1.33, then the mean value is shifted to the left or right whereas the distribution is still within tolerance. This behaviour could occur if there is a drift in the zero offset, in which case a new calibration will help to improve the measurement system. A programme was designed in Excel according to the layout of Dietrich and Schulze in [178] to calculate and display the indices (Figure 4-2).

$$C_g = \frac{0.1 \cdot T}{6 \cdot s_g} \geq 1.33 \tag{4-1}$$

$$C_{gk} = \frac{0.05 \cdot T - |x_m - x_g|}{3 \cdot s_g} \geq 1.33 \tag{4-2}$$

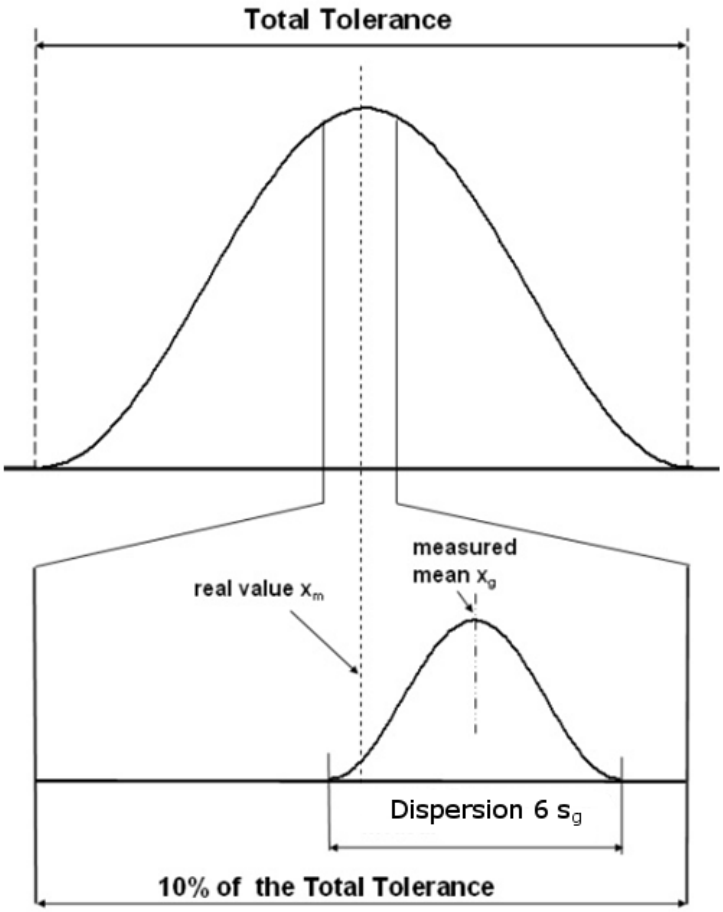

Figure 4-1: Probability distribution of the tolerance and the probability distribution of the measurement system with 10 times better range with a slight drift to the right (higher measured values) [178]

Date:	04.12.2006	Name :	Hien Matthias	Location :	HW/NS G.09		
Measuring device		Measurement standart		Attribute			
Name of device	Pressure Sensor	Normal bez.	Watercolumn	Attribute m: DAQ (output		OSG	0.5
Number of device	-	Normal Nr.	-	Spec. size	11.379	USG	0.5
Resolution	0.001	Normal value	80 cm (Watercolumn)	Unit	mV		
Reason for test	Measurement of IOP	Unit	PSI				

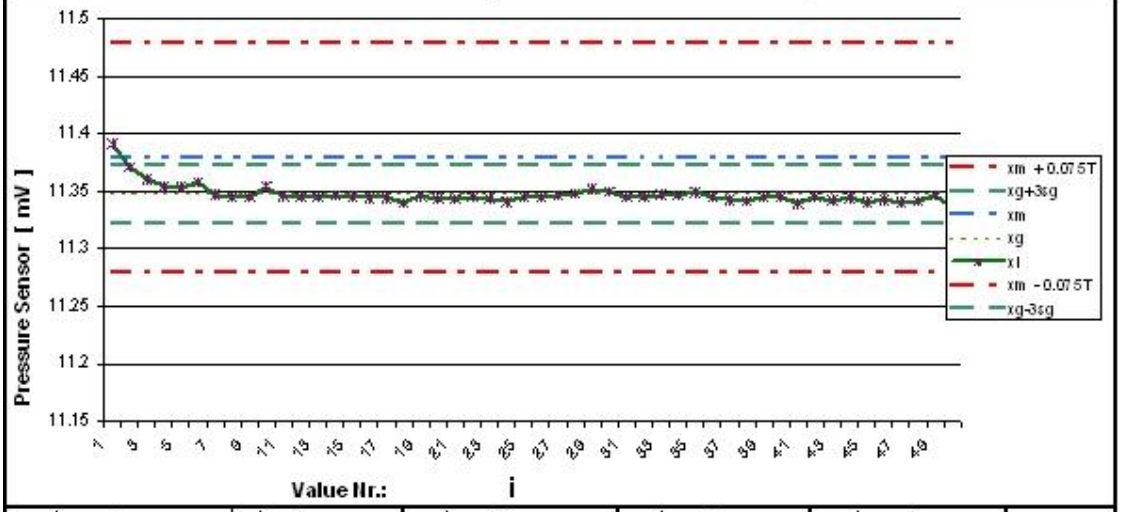

i	x_i	i	x_i	i	x_i	i	x_i	i	x_i
1	11.391	11	11.346	21	11.343	31	11.345	41	11.339
2	11.371	12	11.345	22	11.345	32	11.345	42	11.345
3	11.361	13	11.345	23	11.344	33	11.347	43	11.342
4	11.354	14	11.347	24	11.341	34	11.347	44	11.344
5	11.353	15	11.345	25	11.345	35	11.349	45	11.341
6	11.358	16	11.344	26	11.344	36	11.345	46	11.343
7	11.347	17	11.344	27	11.347	37	11.343	47	11.340
8	11.344	18	11.340	28	11.348	38	11.341	48	11.342
9	11.345	19	11.346	29	11.352	39	11.344	49	11.347
10	11.354	20	11.344	30	11.350	40	11.345	50	11.337

Values of the Normal		Measured Values		Statistic Values	
x_m	11.379	x_{min}	11.391	x_g	11.347
USG	10.879	x_{max}	11.337	s_g	0.00859
OSG	11.879	R_g	0.055		
T	1			$\lvert x_g - x_m \rvert$	0.03191323
x_m + 0.1T	11.479	n_{ges}	50		
x_m - 0.1T	11.279				

C_g= 2.91084016

C_{gk}= 2.642529531

$$C_g = \frac{0.1 \cdot T}{6 \cdot s_g} \geq 1.33$$

$$C_{gk} = \frac{0.05 \cdot T - |x_m - x_g|}{3 \cdot s_g} \geq 1.33$$

Figure 4-2: Scheme for calculating measurement capability indices C_g and C_{gk}

Once all sensors had been calibrated and the measurement capabilities had been established, the actuators were tested for their process stability. The process capability index C_p is used to show if the process can achieve the required tolerance or, where the tolerance is not specified, the index will give accurate information as to what tolerance the test rig can achieve. The capability here would be given when the tolerance, *T*, over

the spread of measured process values (6 times the standard deviation, s_g, for a normal distribution) is greater than 1.33.

$$C_p = \frac{tolerance\ T}{processspread} \geq 1.33 \tag{4-3}$$

Requirements for the sensors used for intraocular pressure measurement

ISO standard, ISO 8612:2001, together with ISO 15004:1997, specifies the minimum requirements for tonometers intended for routine clinical use in the estimation of IOP. The standard for new tonometry methods is for a tolerance *T* within ±0.66kPa (±5.0mmHg) [125, 126]. To qualify the test rig, it should always be compared with the "gold standard" which is the Goldmann tonometer. Such calibration is necessary for measurements on human patients, where it is not possible to install a pressure sensor to obtain the true pressure in the eyeball and it is necessary to rely on indirect methods. For measurements on the mechanical eyeball and on pig eyeballs a pressure sensor could be used to replace the Goldmann tonometer as a standard.

Requirements for the sensors used for periodontal ligament measurement

For the measurement on PDL there are no specific measurement tolerances, as orthodontic force is not currently a diagnostic measurement. Nevertheless, there are guidelines for acceptable forces and displacements which can be applied to human teeth, and these can be used to determine the coarsest acceptable control. Ren *et al.* [102] suggests forces between 0.18N and 15N applied on the centre of the tooth and Kamatsu *et al.* [127] found deformations from 35 to 90 μm appropriate for testing the PDL in the socket.

4.1.1 Sensor specifications

The following sub-sections list all of the sensors used for the experiments along with their associated specifications, calibration procedures and the resulting capabilities.

4.1.1.1 Gauge pressure sensor (from Honeywell) for experiments on the mechanical eyeball and on pig eyes

A gauge (differential) pressure sensor (from Honeywell; PartNo:24PCBFA6G) with a measurement range of 0-34.5kPa was used. To calibrate the pressure transducer, a Plexiglas tube of length 80cm and diameter 20mm was prepared with a sealed bottom. Near the bottom, a press fit hole was drilled and the pressure sensor glued into it. A graduated scale (16 marks, 50mm apart) was used and the column was filled up to each of the scale marks with distilled water and the corresponding output of the pressure sensor recorded. The pressure of the water column at height, h_i, was calculated from (Equation (4-4)).

$$P_{watercolumn} = \rho_{water} \cdot g \cdot h_i \tag{4-4}$$

According to the supplier's technical specification, the sensor had a full scale output (FSO) of 50mV with a sensitivity of 1.5mV/kPa. The output of the sensor was amplified (three channel OEM amplifier with standard LM 741 op amps) and calibrated as can be seen in Figure 4-3. The best-fit straight line $y = 0.2482x$ gives the calibration and the R^2 value of unity shows the sensor to be linear. Using the calibration curve, the ISO standard tolerance can be calculated to be ±0.16 V (corresponding to C_g = 2.91 and C_{gk} = 2.64) for the distribution determined at a standard pressure of 2kPa (corresponding to 200 mm water column height).

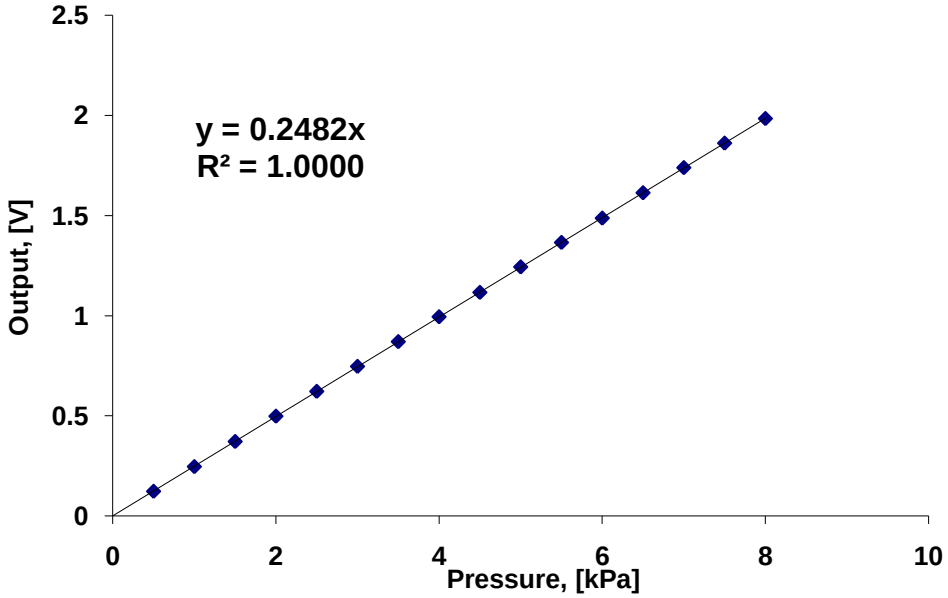

Figure 4-3: Calibration of the differential pressure sensor from Honeywell

4.1.1.2 Load cell for experiment on pig eyes

This load cell (Honeywell Model 31 low range precision miniature load cell) was calibrated using dead weights applied in increments of 5g up to 50g followed by weights of 75g and 100g. Before the calibration, the amplifier (2311 signal conditioning amplifier from Vishay Measurement Group Instrument Division) was re-set to zero. The calibration (Figure 4-4) gave an R^2 of 1 for the linear fit with an offset of less than 0.4% of the maximum value. A dead weight of 10g was then placed 50 times onto the load cell to determine the capability indices C_g and C_{gk}. The tolerances were set to the required pressure of ±0.66kPa times the area of the indenter used in the experiments $(7.068\times10^{-6}m^2)$ which results in a force of 1.7mN. For the given tolerance, C_g = 1.77 and C_{gk} = 1.68 , which again complies with the ISO standard.

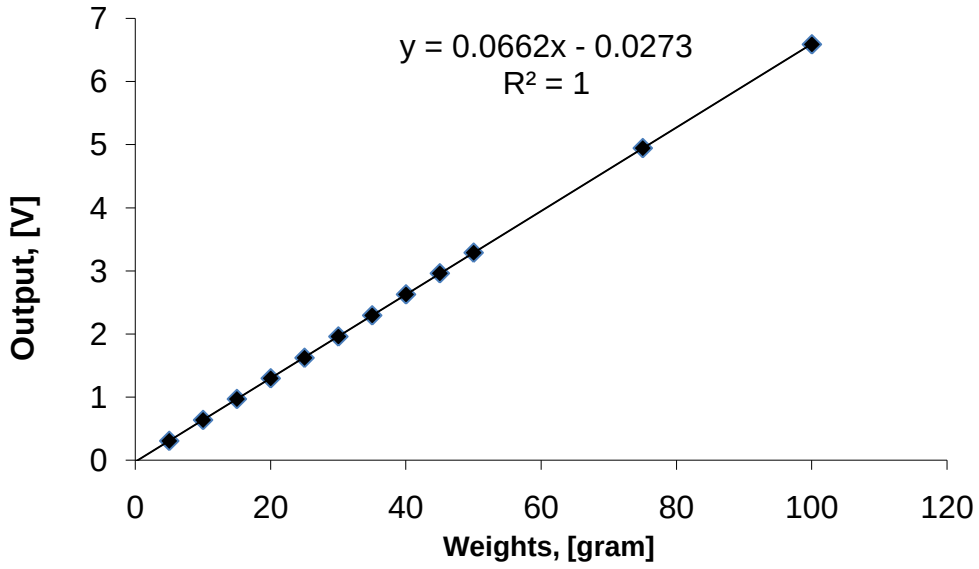

Figure 4-4: Calibration of Honeywell Model 31 load cell

4.1.1.3 Proximity probe for mechanical eyeball and pig eye experiments

This probe was a Bentley Nevada 3300 XL 11mm Proximity Transducer System with an Incremental Scale Factor (ISF) of 4.297V/mm. The sensor was calibrated against a micrometer screw which had a minimum graduation of 1µm with a maximum displacement of 3mm. The sensor was calibrated in incremental steps of 100µm up to 2.0mm (Figure 4-5), and the standard deviation was under 1% of the ISF. The lowest standard deviation of 0.0016-0.0021mm was obtained in the range between 1.0mm and

1.2mm, so, to work at maximum accuracy, the sensor should to be placed within this range. For measurements within 6µm, the capability for this sensor was achieved, with C_g = 1.33 and C_{gk} = 1.33.

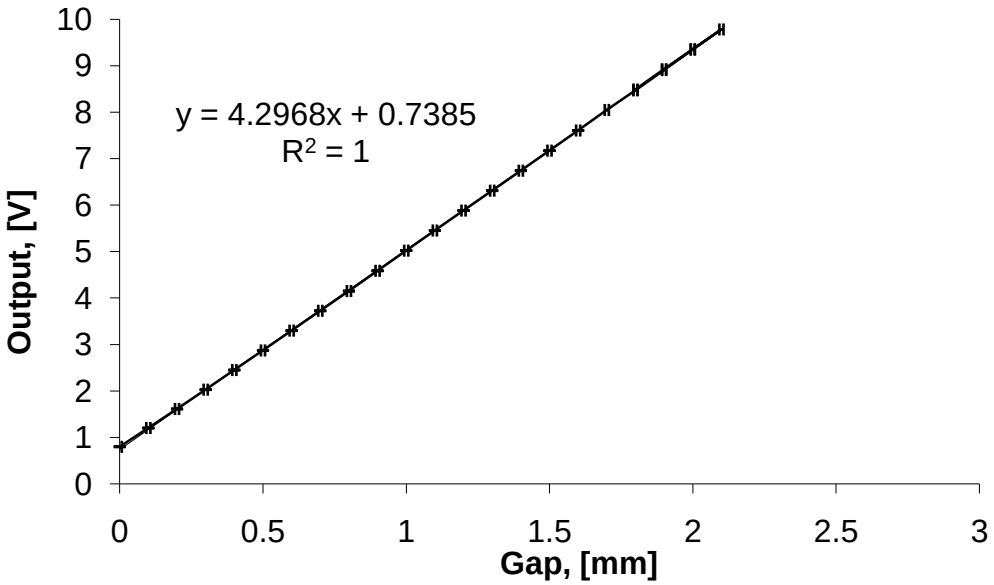

Figure 4-5: Calibration of the proximity probe

4.1.1.4 Load cell for PDL measurement

A Honeywell Model 34 semi precision miniature load cell was sufficient for deforming the tooth up to 0.3mm and still was in the specific working range. As no specific requirements for the test rig were known, the measurement capability was used to specify the accuracy and reproducibilty of the system. For a tolerance T of ±1mV corresponding to 2mN, C_g and C_{gk} values of 2.13 and 1.75, respectively, were achieved. The calibration was carried out over a generous range up to 2kg (Figure 4-6).

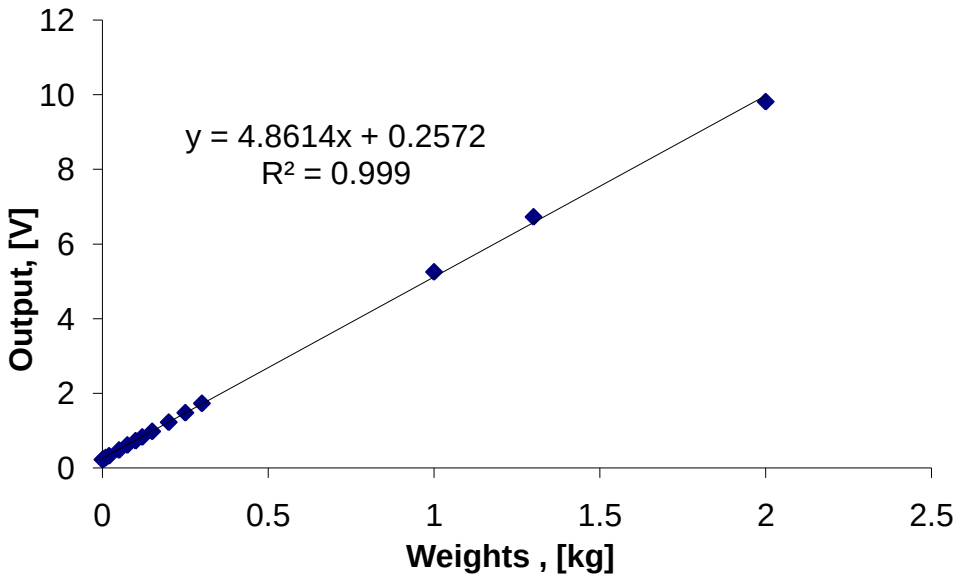

Figure 4-6: Calibration of Honeywell Model 31 load cell

4.1.2 Actuator specifications

The following sub-sections list the actuators used for the experiments along with their associated specifications and process capabilities.

4.1.2.1 Piezo actuator for mechanical eyeball and pig eye experiments

The piezo actuator (Physik Instrumente PI P-601.30) was tested with the already-calibrated LVDT for its linearity, range and reproducibility, in order to identify its process capability. A driving signal corresponding to an amplitude of 0.115mm was applied at frequencies from 2-60Hz and the LVDT was used to measure the actual amplitude delivered. A signal generator (DSG2 from Farnell) was used to produce sinusoidal waves with an amplitude of 1V and an amplifier (E-610 LVPZT from PI) amplified the signal up to 87V. This voltage deforms the piezo and delivers an amplitude of 0.115mm through a cantilever. The amplitude was measured 10 times at each frequency and the average of each point was used to plot figure Figure 4-7 . The repeatability of the amplitude at a given applied frequency was less than ±5µm. Over the whole bandwidth tested, the amplitude of the piezo showed a C_p of 1.33 for a tolerance of ±9.8µm and an accuracy better than 10% of the amplitude level (0.115mm) for the maximum oscillation was achieved. A slight increase in amplitude

with increasing frequency was observed (Figure 4-7), but this did not compromise the process capability.

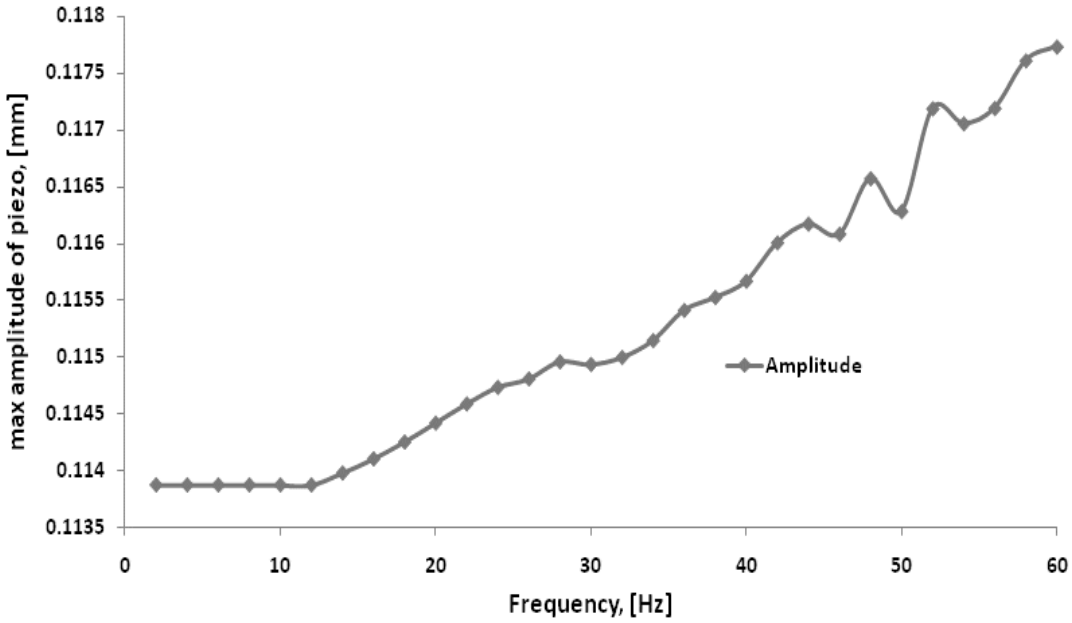

Figure 4-7: Maximum amplitude of the Physik Instrumente PI P-601.30 actuator over the frequency range from 2-60Hz

4.1.2.2 Stepper motor for mechanical eyeball and pig eyeball experiments

The linear stepper motor (Standa 8 MT173-20) was calibrated to give a coarse movement, driving by a distance of either 0.5mm or 1.5mm, which corresponded to 200 steps or 600 steps, respectively. A LabView program was devised to deliver the required control signals via an OEM controller to make the stepper motor drive precisely the preinstalled steps without losing or adding a step. According to the data sheet, the accuracy of one step is 1.25μm±5% so, as this device was more precise than the measurement system (LVDT), no C_p index could be calculated**.**

4.1.2.3 Translation stage for pig eyeball experiments

A simple translation stage (VT-80 from Micos) was used for the static tests, where the requirement was to drive 1.5mm into the sample, rest for 10 seconds, drive back to the initial position and wait again for 10 seconds. The device was calibrated for its resolution and repeatability by repeating the advance-retract cycle 5 times and using the calibrated proximity probe to measure the position of the actuator. The resolution was

better than ±7microns and the bi-directional repeatability within a tolerance T of ±10microns gave a C_p of 1.33.

4.1.2.4 Stepper motor for PDL measurement

Another stepper motor (Johnston Electronic, UBL) was used to move the teeth in their sockets in increments of 0.035mm up to 0.275mm (ten steps). The large range travel of more than 56mm made adjusting the actuator position relatively easy. A micro controller and a self-designed program in LabView were used to control the steps. For a given tolerance of ±8µm, this motor exhibited a C_p of 1.33.

4.1.3 Dynamic calibration for phase and amplitude

It was necessary to amplify the load cell without any time delay (comparing the input of the amplifier with the output of the amplifier) to measure phase difference and amplitude ratio of displacement and force, which can be varying at frequencies of up to 100Hz. The displacement sensor did not need to be amplified and its signal was accurate without amplitude drop or phase shift up to 100Hz. The load cell was connected to a signal conditioning amplifier (2311 from Vishay Measurement Group Instrument Division) and the amplifier was tested by applying a sine wave from a signal generator directly to it, calculating the amplitude ratio of the input sinusoidal waveform with respect to the amplified output sinusoidal waveform. Both signals were fed to the DAQ card (PCI6024E from National Instruments) and LabView 7.1 controlled the sample rate. The amplifier was tested at a constant sample rate and at constant samples per cycle (500 samples per cycle). The constant sample rate of 1kS/sec was installed from 2Hz to 14Hz and 10kS/sec from 16Hz to 60Hz for the constant sample rate experiment (grey rectangles Figure 4-8 and Figure 4-9). A drop in phase appears between 14 and 16 Hz, due to the change in sampling rate from 1kS/sec to 10kS/sec. The gradient and the drop in phase can be reduced by always using the same number of samples per cycle (black triangles Figure 4-8). A phase difference still occurs when it should be zero, but the gradient can be used in a correction function to obtain the true phase (Figure 4-8). A line almost perfectly parallel to the abscissa was achieved for frequencies up to 60 Hz for amplitude ratio in both experiments (Figure 4-9).

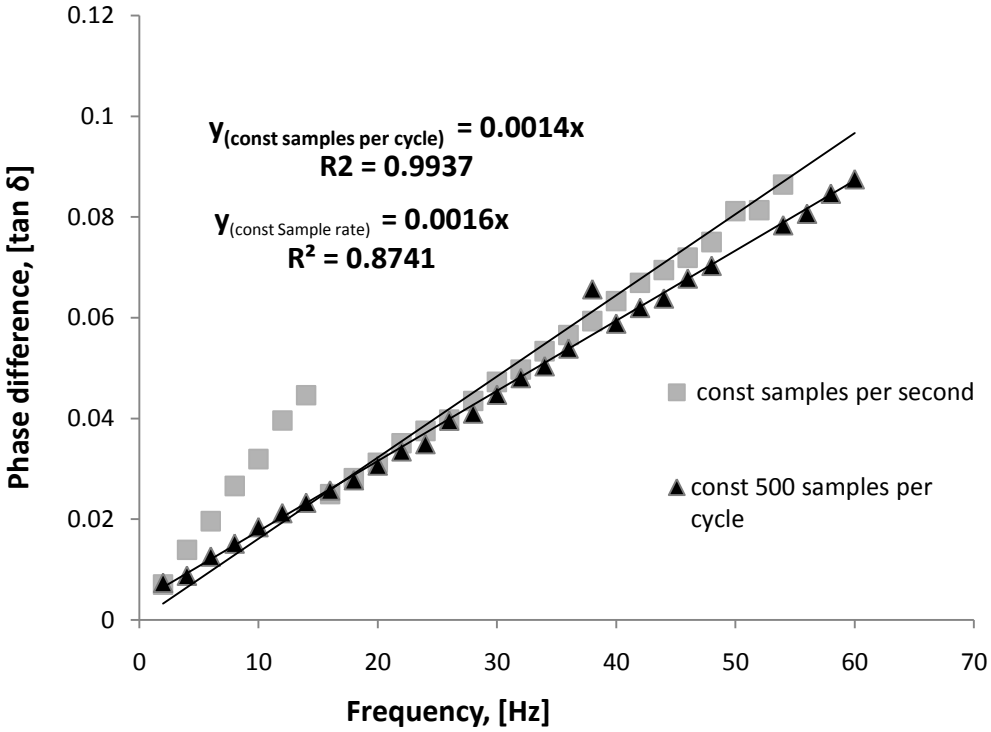

Figure 4-8: Dynamic phase difference for displacement and load amplifiers

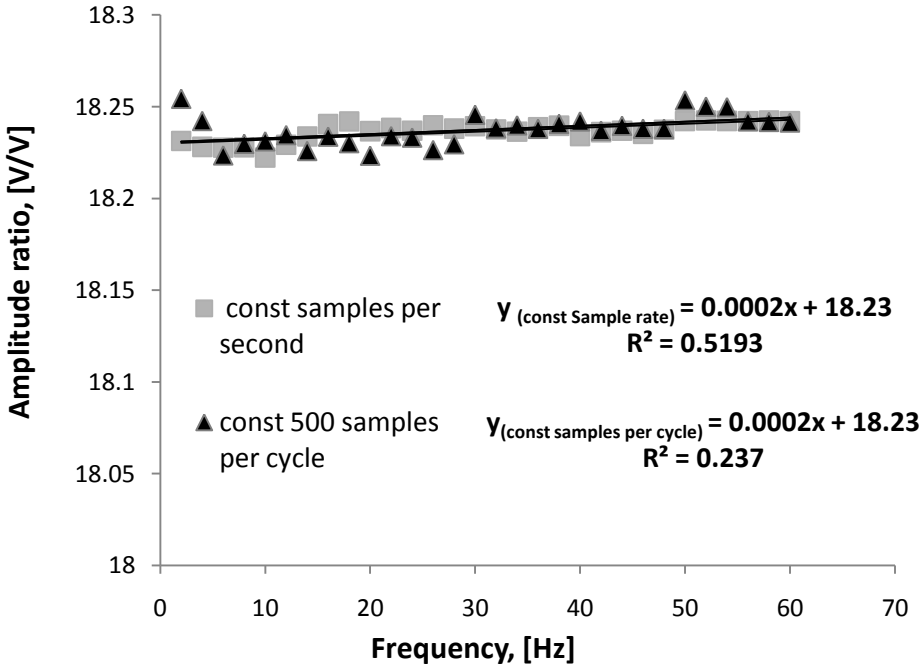

Figure 4-9: Dynamic amplitude ratio for displacement and load amplifiers

4.2 Experimental set-up and procedures

This work includes three major experiments on; a mechanical eyeball, pig eyeballs and porcine periodontal ligament. The experiments on pig eyeballs were done dynamically and statically, the mechanical eyeball configurations were only tested dynamically and the porcine PDL was tested statically for its force relaxation.
All the work where biological tissue was used were carried out under strict cross-infection control procedures (e.g. cleaning with bleach,wearing clinical masks and gloves).

The dynamic test rig was used for both mechanical and pig eyeballs and is described here. All other test rigs were designed individually for each experiment and will be explained in the relevant sections below. The dynamic test rig was designed to deliver an oscillating displacement through a probe to a sample consisting of a pressurised membrane while measuring the probe position relative to the sample, the dynamic pressure and the reaction force on the probe as shown in Figure 4-10. A heavy base plate was used to mount the actuators and sensors making the rig vibration-free for the frequency range used. The piezo driven actuator (Physik Instrumente PI P-601.30) delivered a displacement amplitude of 0.115mm at frequencies of 2Hz to 60 Hz in steps of 2Hz and was powered by an amplifier (PI E-610 LVPZT), itself driven by a 5V amplitude sine wave from a signal generator (Farnell DSG2) (Figure 4-11). The actual movement of the piezo was recorded by a proximity probe (Bentley Nevada 3300 XL 11mm Proximity Transducer System) mounted on the sample holder and addressing a thin steel plate fixed to the probe. The load cell (Honeywell Model 31) was screwed directly onto the piezo and the probe tip, a plain cylindrical rod of diameter 3.0mm, was mounted on top of the plastic carrier and was used to indent the samples. A pressure sensor (Pressure gauge from Honeywell; Part No: 24PCBFA6G), either glued to the mechanical eyeball or attached to a tube with connection to the infusion needle, was used to record the dynamic pressure backing the membrane or the cornea.

The sample was clamped in a sample holder which could be attached to the stepper motor (Standa 8 MT173-20) for coarse movement of the stage. The sample holder was essentially a brass cylinder with a cover plate with a central circular window through which the sample was probed. Four screws around the holder were used to tighten and fine adjust the sample so that the probe tip could indent the sample in the centre.

The stepper motor was used to drive the sample towards the probe, contact being detected when the load cell registered a force above 1mN. After contact, the stepper motor was used to set the pre-displacement using a controller card, which was programmed to drive exactly the required number of steps with a translational speed of 1.25mm/sec.

The load cell and pressure sensor outputs were amplified (2311 from Vishay Measurement Group Instrument Division and LM741 operational amplifier, respectively) and the outputs, along with the displacement sensor output, were connected to an analogue-digital converter (DAQ card BNC-2110 with PCI6024E from National Instruments). The three signals (force, displacement and pressure) were conditioned using a self designed program in LabView7.1, sampling at a rate related to the frequency (500 Samples per cycle) and converting from voltage output to the respective unit (Newton for force, mm for displacement and Pa for pressure). Each record (for force, displacement and pressure) included 10 cycles at each frequency and one experimental folder included all records for all frequencies of one run, defined as an experiment, where all experimental conditions (sample, pressure, membrane thickness, pre-displacement) were kept constant except the frequency

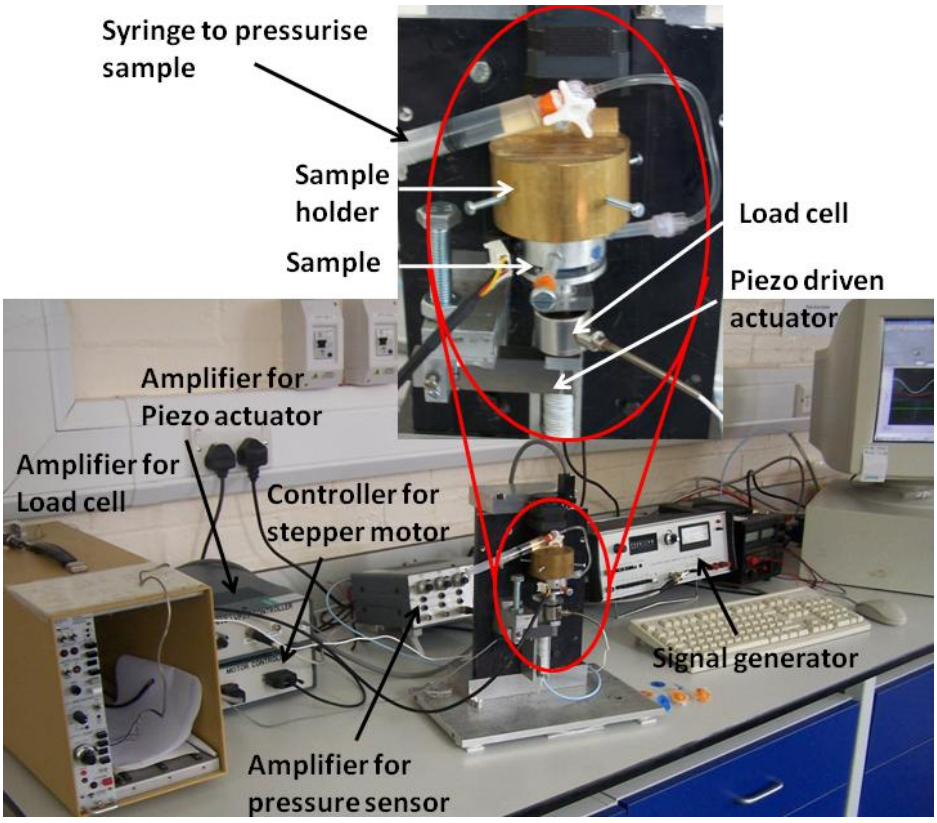

Figure 4-10: Dynamic test rig and peripherals

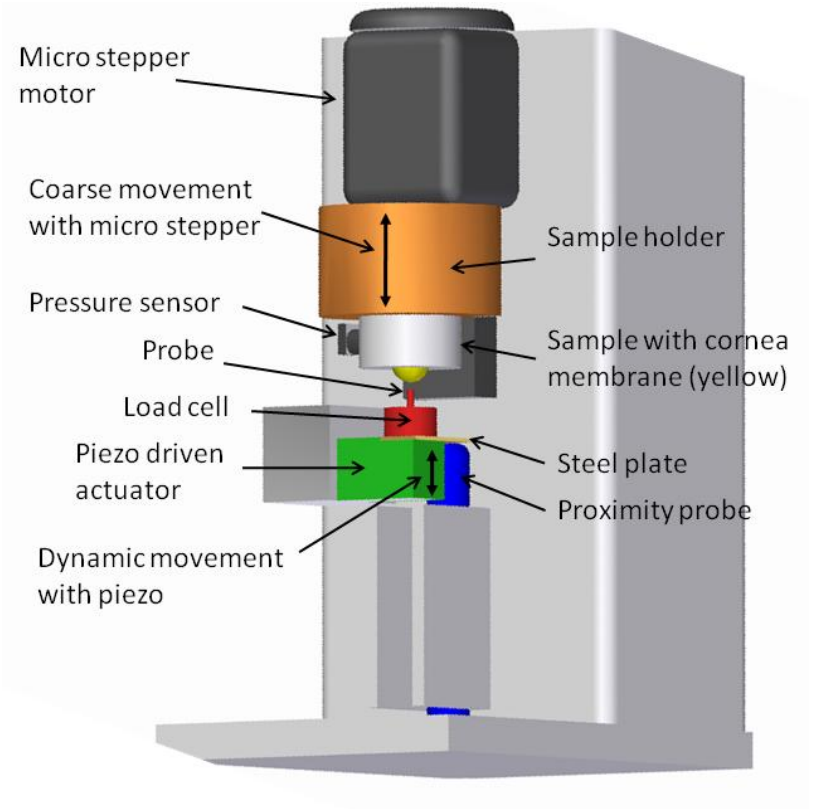

Figure 4-11: Detailed schematic of dynamic test rig

4.2.1 Mechanical Eyeball

The test rig described in the previous section was used to probe mechanical models of the eyeball which were designed to give independent control of the cornea thickness, IOP and fluid drainage. The overall set-up is shown in Figure 4-12 and consisted of a reservoir (simulated vitreous/aqueous humour), covered by a mechanical cornea made from an elastomer and a mechanism (choke and water column) for varying the fluid-mechanical response to palpation of the mechanical cornea. The basic experimental procedure was to apply a pre-displacement and static pressure to the artificial cornea and then oscillate the probe with a variety of frequencies while recording the resulting force and the dynamic pressure.

Three different configurations (Figure 4-12) were used in the experiments, each designed to test a certain aspect of the mechanical behaviour of the composite structure. The first configuration (closed-pressurised, Figure 4-12a) allowed the reservoir to be pressurised through a syringe to values of 1.8kPa and 3.3kPa (lower pressure related to

healthy human eyeball and the higher pressure is already a diseased stage) upon which a valve at the syringe outlet was closed giving a constant volume system where compression of the liquid will cause expansion of the membrane disc. The second configuration (open-ambient, Figure 4-12b) allowed the suspended membrane to be tested alone by removing the water in the reservoir and leaving the cavity open to ambient air. For the third configuration (choked-pressurised, Figure 4-13c), a Perspex tube with an inner diameter of 16mm was attached to the reservoir and filled with water to give a static head at the pressure sensor of 1.8kPa or 3.3kPa. Choke plates with orifice diameters of 1.3, 5.0 or 16.0mm were placed in the tube 15mm away from the cornea membrane to produce a variable flow resistance. The choke flow resistances were small compared with the resistance of Schlemm's canal, but the large diameters were necessary to isolate the effects of flow from cornea distortion [54].

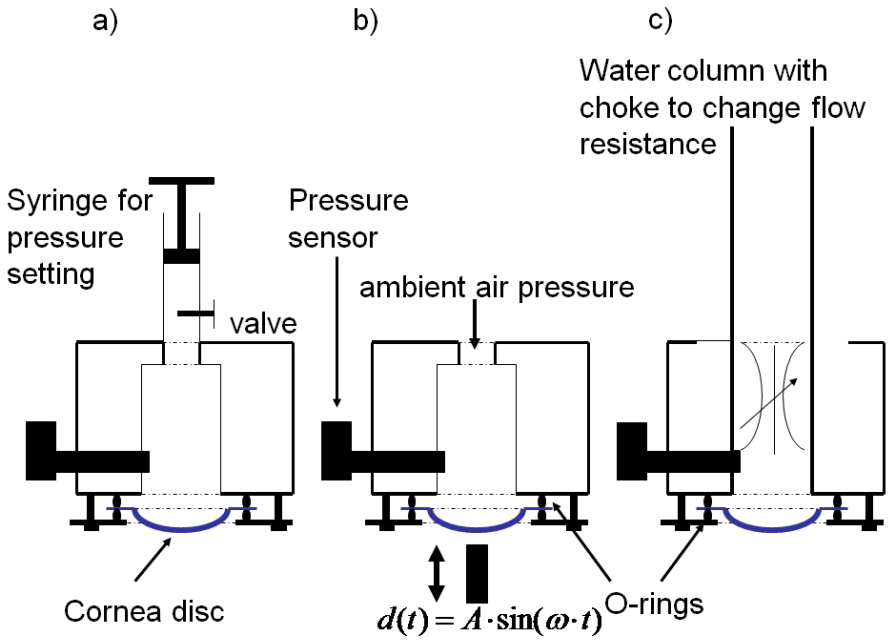

Figure 4-12 The three mechanical eyeball configurations a) closed-pressurised; b) open-ambient, c) choked-pressurised.

The artificial cornea was moulded from a two-part RTV medical grade silicone (Honigum from DMG Chemisch-Pharmazeutische Fabrik GmbH). The mould was made of high density polypropylene to reduce adhesion and a positive and a negative mould were cut to the shape of the average human eye (radius of curvature 7.9mm [56, 57, 59]). Shims of various thicknesses were used to hold the mould faces apart so that cornea discs of thicknesses 0.4mm, 0.6mm and 1.0mm could be produced, reflecting

values used by Elsheikh *et al.* in their numerical model [58], and measurements made on human eyes, Feltgen *et al.* [57] and Doughty and Zaman [56]. The mould disc diameter was 20 mm with the cornea shape occupying the central portion of diameter 16mm, leaving a flange of radial width 2mm. The flange was clamped between two O-rings with an inner diameter of 16mm and suspended over the reservoir which was drilled into an aluminium block.

The micro stepper actuator was used to apply a fixed pre-displacement of 0.5mm to the artificial cornea and the piezo driven actuator applied the dynamic displacement with an amplitude of 0.115mm. The 0.5mm pre-displacement is a comparable value from literature [80-82] for indentation tonometry. With this arrangement, the maximum frequency was restricted to 60Hz so that the resonant frequencies of the piezo and the inertia forces of the load cell could be easily filtered out.

Each configuration (closed-pressurised, open-ambient and choked pressurised) was tested with three different membrane thicknesses (0.4mm, 0.6mm and 1.0mm). One run included 30 different frequencies (2Hz to 60Hz in increments of 2Hz) and each record at a given frequency consisted of 10 cycles. The "closed-pressurised" and "choked-pressurised" configurations were tested under two different pressure settings where the lower one represents a normal healthy eye pressure and the higher one represents glaucoma (1.8kPa and 3.3kPa). Each run was repeated 5 times giving a total of 75 runs, corresponding to 22500 applied cycles.

4.2.2 Measurement of pig eyeballs

In total, 35 eyeballs were tested dynamically and 2 were tested using a quasi static procedure described below. Of the 40 eyeballs acquired, three of them were fresh and 37 had been kept frozen at -12°C and were defrosted over the night before testing (hereinafter referred to as "frozen") and, of these, three became unusable for testing during preparation. The three fresh eyeballs were obtained from a reputable local butcher and the frozen eyeballs came from a local abattoir (Grampian Country Pork Halls in Broxburn).

In order to present the eyeballs to the test probe, a protocol, summarised in Figure 4-13, was developed for mounting them into an aluminium cylinder, which was then placed in the sample holder of the dynamic test rig. The eyeballs were first pressurised using a

0.5mm diameter hypodermic needle (Qosina) inserted through the optic nerve channel and passing through the vitreous body (Figure 4-13a). The needle tip had to be positioned exactly in the anterior chamber where the aqueous humour is located. This was observed simply by looking through the cornea. The main problem encountered was particles from the lens, the iris or the vitreous body blocking the fluid flow in the needle tip. The blocking of the needle was not recognised while liquid drained into the eyeball, but meant that there was no feedback to the pressure sensor when the cornea was deformed and the pressure increased in the eyeball. A simple check, whereby the flexible tube connecting the pressure sensor and the infusion needle was squeezed gently, was developed to ensure the correct positioning and functioning of the needle. While squeezing the tube, the pressure increases and liquid drains into the eyeball. When the flexible tube was released the liquid in the eyeball should flow back into the tube and the pressure read at the sensor should immediately return to the pre-installed pressure. If the needle tip was blocked, the pressure at the sensor becomes a negative pressure reading and the needle could be adjusted accordingly.

Once the needle was positioned correctly, the eye was carefully inserted, cornea first, into a tubular aluminium shell, with one (top) end open and with a bottom cap which contained a 16mm diameter circular cut out. A 16mm internal diameter O-ring was glued to the bottom cap and the pig eyeballs were gently inserted centring the cornea shown in Figure 4-13 b. Wet compresses around the pig eyeball kept it moisturised and a proprietary household polyurethane foam was used to seal the cavity Figure 4-13c. The foam cured within 25 minutes during which the exposed part of the cornea was kept moisturized either with tap water for the frozen eyeballs or saline solution (Optrex®) for the fresh eyeballs. Once cured, the excess foam was trimmed away and the sample assembly was either mounted into the brass sample holder (Figure 4-13d) for dynamic testing (Figure 4-13e) or directly clamped to the translation stage for quasi-static testing.

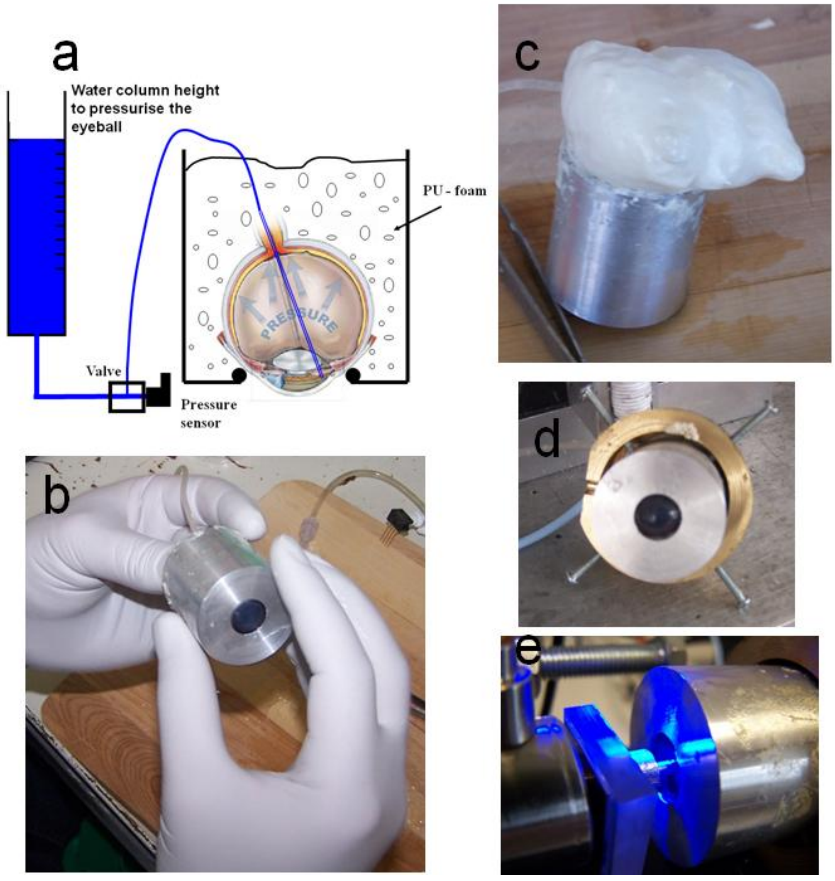

Figure 4-13: Preparation of pig eyeballs a) schematic of the sample assembly b) positioning of the eyeball in the tubular shell c) shell filled with foam d) sample assembly mounted in brass sample holder for dynamic test e) sample assembly mounted in dynamic test rig

4.2.2.1 Quasi static test of pig eyeballs

For this test, the sample assembly was fixed to a 2-axis motorised translation stage (VT-80 from Micos), itself fixed to a right-angled loading frame (Figure 4-14). The load cell (Model 31 from Honeywell) bolted to the base plate of the frame and the probe tip (of diameter 3.0mm, as in the dynamic rig) was fixed to the load cell. After adjusting the sample assembly so that the probe tip was addressing the centre of the cornea, the translation stage with the sample was advanced towards the probe until the force sensor registered 1mN, corresponding to the probe touching of cornea. A PCI controller (SMC Pollux Motor-Controller Module) and a programme in LabView 7.1 was used to indent 1.5mm into the cornea at velocities of 5mm/sec or 15mm/sec. Both velocities were installed at an acceleration of 100mm/sec^2. The displacement of 1.5mm was held for 10 seconds, following which the probe was retracted to the touch-down position and held for another 10 seconds. The advance-retract cycle was repeated 5 times. The load cell

output was recorded using the analogue-digital converter (DAQ card BNC-2110 with PCI6024E from National Instruments) in combination with the LabView program at a sample rate of 1kS/sec.

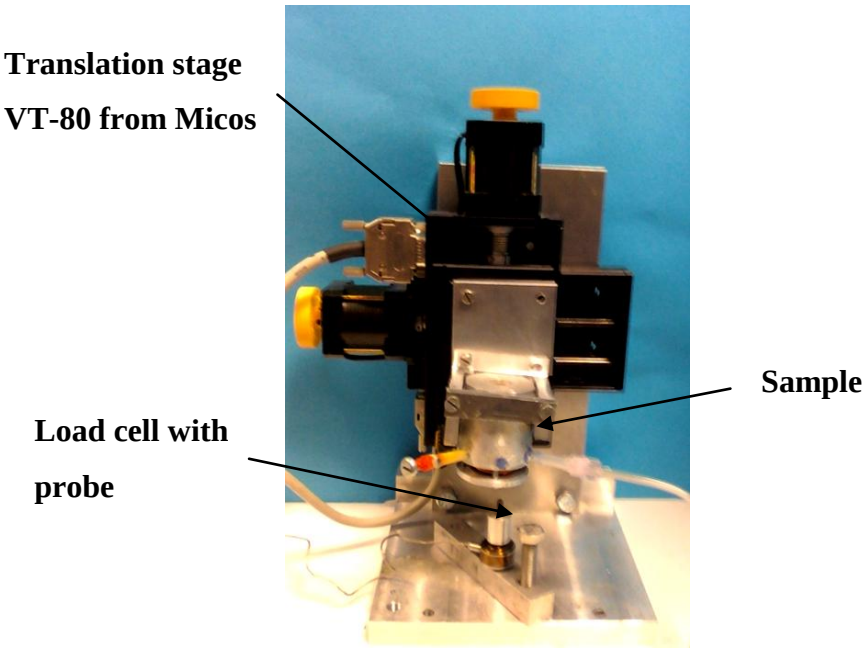

Figure 4-14: Test rig for quasi static tests on pig eyeballs

Two different intraocular pressure (IOP) settings (1.8kPa and 6.2kPa) were used to pressurise the eyeball, and each pressure group was tested once with the connection to the water column open (open-pressurised), and a second time with the valve between the eyeball and the water column closed (closed-pressurised). Each test was done twice so that each eye was deformed under 8 conditions (2 velocities × 2 configurations × 2 pressures), each condition being repeated five times, giving a total of 40 force relaxation curves.

4.2.2.2 Dynamic testing of pig eyeballs

Of the original sample of 35 frozen eyeballs planned for dynamic testing 3 could not be used because it did not prove possible to position the hyperdermic needle into the anterior chamber without leakage. Of the remaining 32, 16 were tested with a pre-displacement of 0.5mm and 16 were tested with a pre-displacement of 1.5mm. The 3 fresh eyeballs were also tested with a pre-displacement of 1.5mm in order to assess the effect of freezing on the properties of the eyes. In addition, two cornea/sclera sections

were tested dynamically by suspending the cornea over the cavity. The fresh eyeball samples were used within 24 hours *post mortem* and saline solution (Optrex®) was used to pressurise them whereas the frozen eyeballs were pressurised with tap water. The saline solution also protects the cornea against the swelling which is caused by non-buffered water [179-181]. Both groups (frozen and fresh) were tested at room temperature, and testing was complete within two hours for each eyeball.

Each eyeball was tested at four different pressures: pressure group 1: 1.8kPa (13 mmHg), pressure group 2: 2.7 kPa (20mmHg), pressure group 3: 4.4kPa (33 mmHg) and pressure group 4: 6.2kPa (47mmHg) starting with the lowest, and increasing to avoid the effects of creep, which could still be recovering if the order were reversed. After setting the pressure, the sample was advanced to the required pre-displacement (0.5mm or 1.5mm) and the oscillation of amplitude of 0.115mm was applied at each of the 20 different frequencies (increments of 2Hz between 2Hz and 40Hz) in random order to avoid any possible effects of time masquerading as frequency. The frequency was limited to 40Hz compared to 60Hz for the mechanical eyeball because the reaction forces on the real cornea were lower than those on the artificial cornea, so that the influence of the inertia forces of the load cell was proportionately higher. Each experiment for a given pre-displacement and pressure was repeated, giving a total of 2 repeats × (16 +16 +3 individual eyeballs) × 4 pressures or 280 runs amounting to 56000 cycles.

For comparison with the mechanical eyeball tests, a second dynamic test was performed with the cornea suspended over the cavity without any backing water pressure. For this test, the cornea plus an additional 4-5mm width of sclera was cut with scissors from two pig eyeballs, which had not been tested before, and these were mounted over the sample cavity (Figure 4-15) and clamped between 16mm diameter O-rings, as for the artificial cornea in the "open-ambient" configuration of the mechanical eyeball. These assemblies were tested with a pre-displacement of 1.5mm, with, as before, a displacement amplitude of 0.115mm and a frequency range from 2 to 40Hz in increments of 2Hz. Each cornea was measured twice.

Figure 4-15: Cornea-sclera section suspended over the aluminium cavity

4.3 Mechanical testing of PDL

In this series of tests, one premolar still attached to the mandibles from four animals was tested using a specially designed rig. The rig was designed to be mounted off the pig mandible to mechanically test the lower premolar (Figure 4-16) in a simulation of the way that a human tooth might be tested *in vivo*. The compliance of the rig was calculated as the moment acting on the screws due to the forces on the tooth (max 20N) and the deformations of the rig were neglectable small compared to the tooth movements. The test rig consisted of a load cell (Honeywell Model 34 semi precision miniature load cell) and amplifier (2311 signal conditioning amplifier from Vishay Measurement Group Instrument Division) a cylindrical probe of diameter 0.2mm and a linear stepper motor (Johnston Electronic, UBL) in series. The pig jaw was fixed with two M6 threaded rods which passed through the bone and were held with nuts on both ends (Figure 4-17) . The stepper motor was used in combination with a controller card with built in Stepper motor controller (NJM3770AD3 DIP16 from RS) and a LabView 7.1 programme controlled the steps. The same LabView programme sampled the output of the load cell amplifier at 1kS/sec through a DAQ card (PCI–6024E).

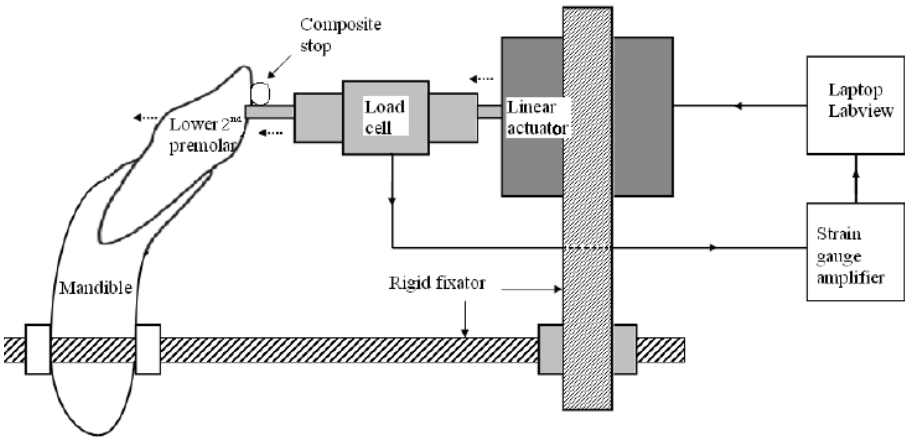

Figure 4-16: Schematic diagram of the force-relaxation rig for PDL [182]

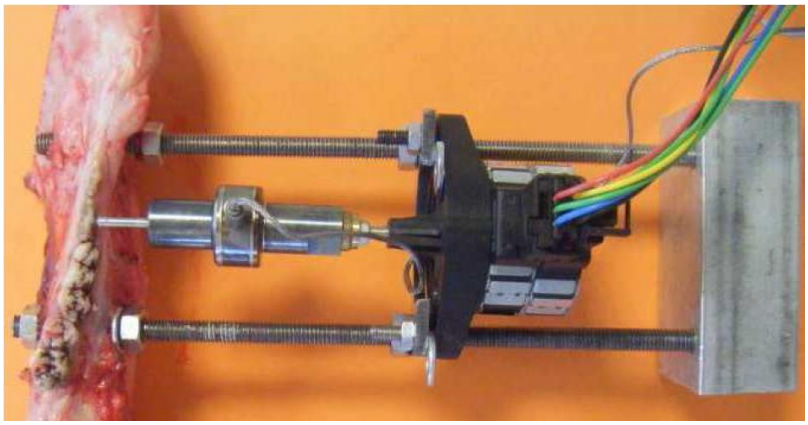

Figure 4-17: Top view of the force relaxation rig with a pig mandible in place [183]

The control programme advanced the probe in steps until the load cell registered a force above 10mN, taken as the point of contact, after which a predetermined initial displacement was applied and held for a predetermined time. Four different initial displacements; 0.070mm, 0.105mm, 0.175 and 0.245 mm and four different hold-times; 5sec, 15sec, 25sec and 35sec were used. The probe advance rate was kept constant at 5 ms/step corresponding to a velocity of 7 mm/sec. The sequence of tests is listed in Table 4-1 and these tests were performed by Tohill [111, 182, 183].

The four pig mandibles were bought from a reputable butcher in Edinburgh at different times. Each of the jaws was sectioned in half and one lower premolar was prepared for testing. First, a steel template was screwed onto the jaw (Figure 4-18a) in order to act as a guide for drilling through the jaw and positioning the probe. The template was 15mm thick in order to guide the drill while two 6mm diameter holes were bored through the jaw (Figure 4-18b). A slightly smaller hole above and midway between the

two 6mm holes was used to mark the position where the probe was later deforming the premolar. After the holes had been bored, the template was removed and the thread rods were put in place. Once the test rig was assembled, the probe / load cell assembly was carefully driven towards the premolar. In order to provide a relatively flat contact with the tapered tooth, a pad of composite resin (Transbond XT Light Cure Adhesive Paste from 3M Unitek) was bonded to the buccal surface of the premolar [111] (Figure 4-18c). The whole assmebly protocol was first tested on a stone model to avoid wasting biological material (Figure 4-19).

	Jaw 1 4 days post mortem	Jaw 2 4 days post mortem	Jaw 3 2 days post mortem	Jaw 3 4 days post mortem	Jaw 4 4 days post mortem
70µm 15s			✓	✓	✓
70µm 15s			✓	✓	✓
70µm 15s			✓	✓	✓
70µm 15s			✓	✓	✓
70µm 15s			✓		✓
105µm 5s	✓	✓	✓	✓	✓
105µm 5s		✓	✓		✓
105µm 5s		✓	✓		✓
105µm 5s		✓	✓		✓
105µm 5s			✓		✓
105µm 5s			✓		✓
105µm 5s					✓
105µm 15s		✓	✓		✓
105µm 25s	✓	✓	✓	✓	✓
105µm 25s		✓	✓	✓	✓
105µm 25s		✓	✓	✓	✓
105µm 25s			✓		✓
105µm 25s					✓
175µm 5s	✓	✓	✓	✓	✓
175µm 5s	✓			✓	
175µm 25s	✓	✓	✓	✓	✓
175µm 25s		✓	✓		✓
175µm 25s		✓	✓		✓
175µm 25s		✓			✓
175µm 25s		✓			✓
175µm 25s		✓			✓
245µm 5s	✓		✓		✓
245µm 35s	✓	✓	✓		✓
245µm 35s		✓	✓		✓
245µm 35s		✓	✓		✓
245µm 35s		✓	✓		✓
245µm 35s		✓			✓
245µm 35s		✓			

Table 4-1: Sequence of pig mandible experiments, prepared by Tohill [111, 182, 183]

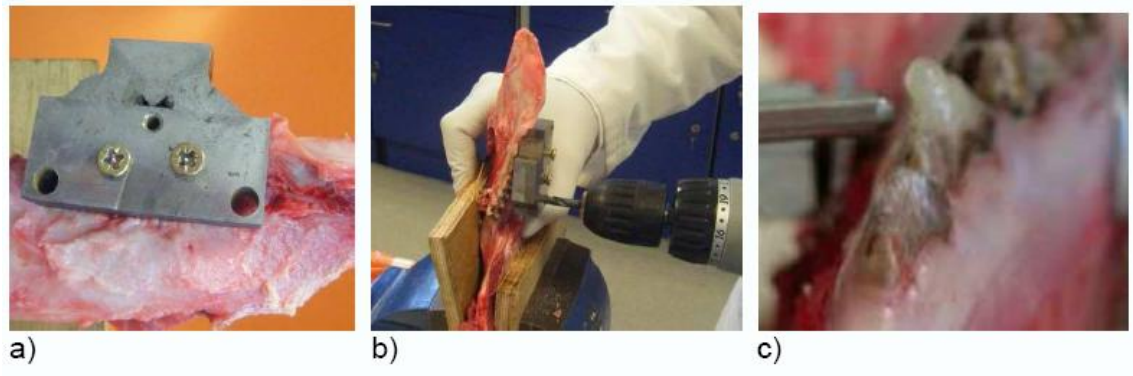

Figure 4-18: Preparation of a pig mandible test rig a) and b) using template for drilling; c) Resin composite pad to prevent slipage of the indenter [111]

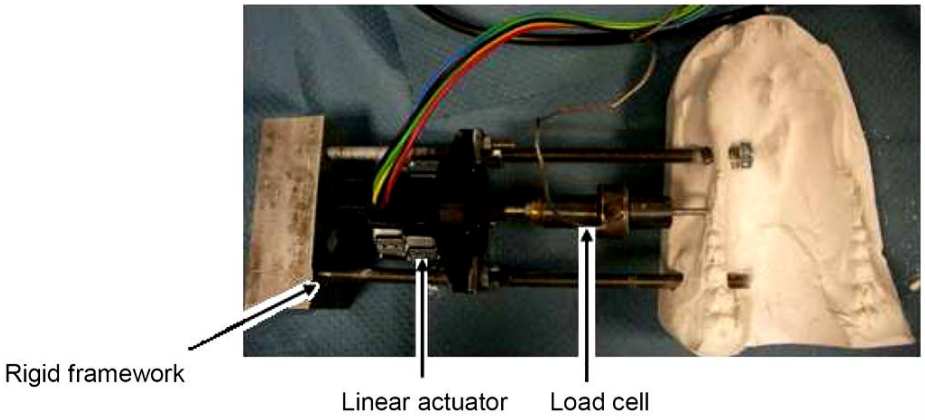

Figure 4-19: Pilot study on a stone model to find the right position for the indenter [111]

4.4 Summary of all experiments

Table 4-2 contains a summary of the data acquired in this work in preparation for the results section.

Experiment class	Test method	Experimental conditions
Mechanical Eyeball measurement	**dynamic**	• three configurations: "closed-pressurised, "open-ambient" and "choked-pressurised" • fixed pre-displacement (0.5mm) • frequency 2–60Hz in increments of 2Hz • fixed displacement amplitude (0.115mm) • two pressures (closed pressurised and choked-pressurised configurations(1.8kPa and 3.3kPa)) • orifice diameter (choked-pressurise (Ø1.3mm, 5.0mm and 16mm)) • membrane thicknesses (0.4mm, 0.6mm and 1.0mm)
Measurement on pig eyeballs	**Static**	• two difrosted eyeballs • two different velocities (5mm/s and 15mm/s) • two different pressure settings (1.8kPa and 6.2kPa) • constant deformation (1.5mm) • fixed relaxation time (10sec)
Measurement on pig eyeballs	**dynamic**	• 35 pig eyeballs (32 defrosted and 3 fresh) • two different pre-displacemeents (0.5mm and 1.5mm) • four diffferent pressure groups (1.8kPa (13 mmHg), 2.7kPa (20mmHg), 4.4kPa (33 mmHg), 6.2kPa (47mmHg)) • fixed displacement amplitude (0.115mm) • frequency 2-40Hz in increments of 2Hz

Experiment class	Test method	Experimental conditions
Measurement on pig eyeballs	**dynamic**	• two defrosted excised cornea sections with an aditional sclera ring (4-5mm); • fixed displacement amplitude (0.115mm) • frequency 2-40Hz in increments of 2Hz • fixed pre-displacement (1.5mm)
Measurement on porcine mandibles	**Static**	• four pig mandibles • four diplacements (70µm, 165µm, 175µm, 245µm) • four Relaxation times (5sec, 15sec, 25sec, 35 sec) • constant deformation rate (7mm/s) • further information about the sequence of testing can be found in Table 4-1

Table 4-2: Summary of all experiments

Chapter 5: Results

This chapter presents the results of the experiments for the three experimental arrangements studied; the mechanical eyeball, the porcine eyeballs and, finally, the porcine jaws.

The treatment of the results for the mechanical eyeball is focused on the capability of the experimental configuration and also the balance between the behaviour of the mechanical cornea and the mechanical aqueous humour. This leads into a discussion (in the following chapter) on multi-component biological architectures and how dynamic palpation can be used to separate the contributions from components which are more fluid-dominated from those which are more solid-dominated.

The results for the biological materials yield specific mechanical models and their associated properties. The focus here is on obtaining property descriptions (i.e. elastic moduli and viscous damping coefficients plus the associated visco elastic moduli) which can be compared with the work of other investigators in the discussion. In addition, the discussion will deal with how the results from the mechanical eyeball and those from the porcine eyeball can be combined to address the potential for enhanced IOP measurement.

5.1 Results for the mechanical eyeball experiment

Three mechanical eyeball configurations were tested in this work; closed-pressurised, open-ambient and choked-pressurised, shown in Figure 4-12(a), (b) and (c), respectively. The configurations were chosen to allow separate investigation of the effects of pressure, cornea stiffness and drainage.

To establish the dynamic range of the test apparatus, a square wave displacement of step height 0.23mm and frequency 2Hz was applied to the artificial eyeball in the closed-pressurised and choked-pressurised configurations for all of the experimental thicknesses, pressures and orifice sizes. Force, displacement and pressure were sampled at 20kS/s to ensure the capture of frequency information up to around 10kHz, well

beyond the range of expected experimental information. The force and pressure readings were transformed into the frequency domain using a Fast Fourier Transform (FFT).

The FFT for the force reading showed a very high peak at a frequency of around 270Hz for all experimental variables tested. Further, smaller peaks appeared below 250Hz and the positions of these changed with the pressure setting, the membrane thickness and the configuration (closed-pressurised or choked-pressurised). The same variable peaks were also present in the pressure spectrum without the dominant peak at 270Hz. Therefore the pressure spectrum was used to show the resonance peaks related to the different mechanical eyeballs. Figure 5-1 shows an example FFT of the pressure for the choked-pressurised configuration with 0.5mm and 16mm orifices at the two different pre-pressure settings. As can be seen, the larger orifice size or the lower pressure setting causes the main resonance to shift to higher frequencies. Table 5-1 lists all the pressure resonance frequencies recorded.

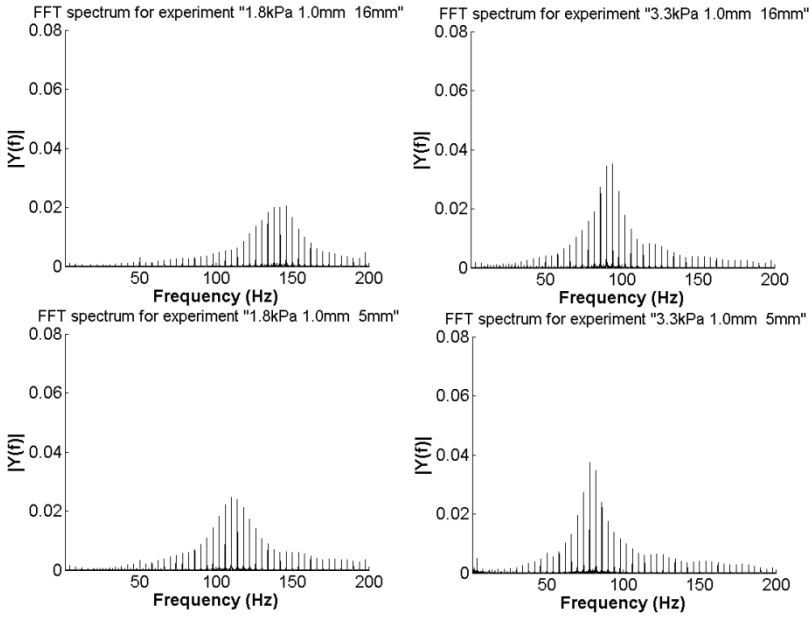

Figure 5-1: Pressure FFT for a 1.0mm thick membrane with different orifice sizes and pressure settings generated with a 2Hz square wave deformation

Configuration closed-pressurised [Hz]

Pre- pressure [kPa]	1.8			3.3		
Disc thickness [mm]						
0.4	240			240		
0.6	248			250		
1.0	In resonance range of piezo					
Configuration open-pressurised [Hz]						
\orifices size	1.3	5.0	16.0	1.3	5.0	16.0
0.4	14	40	44	18	40	44
0.6	20	52	79	20	42	46
1.0	46	112	138	44	78	95

Table 5-1: Resonant frequencies of pressure in response to 2Hz square wave

The FFT spectrum was used to find the working range of the piezo actuator without interference with its Eigen frequency. The resonance frequency was with 250Hz far above the dynamic oscillation which was set from 2Hz to 60Hz. It furthermore proved that the mechanical eyeball resonated between 2Hz and 250Hz dependent on the varying experiments.

The main results for the mechanical eyeball (Figure 5-3 and Figures 5-7to 5-10) are expressed as force relative to displacement and pressure relative to displacement, both shown as a function of frequency in Hz. The force results are given as mean ratio (static stiffness) in Nm^{-1}, amplitude ratio (complex stiffness magnitude) in Nm^{-1} and phase difference between force and displacement (degree) (Figure 5-2). For the pressure results are given as mean pressure in kPa, amplitude ratio in kPa/mm and phase difference between pressure and displacement (degree). Each value was determined over 10 periods of oscillation and each measurement was repeated 4 times with the mean ± the standard deviation being shown in all results. The order of the frequency during a given experiment was chosen randomly in order to eliminate the influence of time while increasing or decreasing the frequency. Frequencies from 2Hz up to 60Hz were used with steps of 2 Hz.

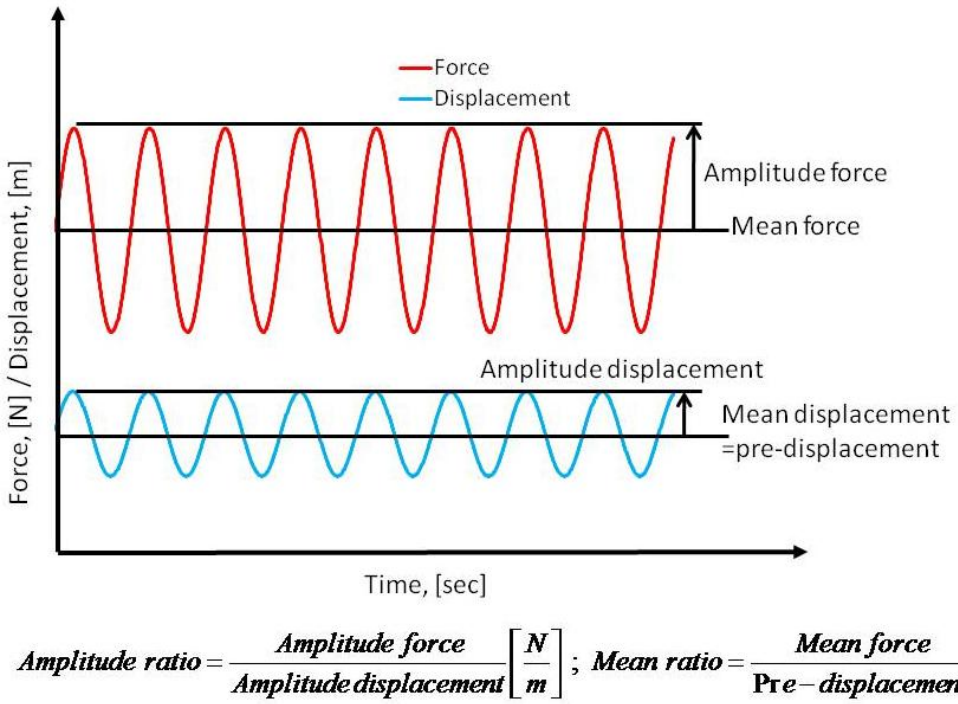

$$Amplitude\ ratio = \frac{Amplitude\ force}{Amplitude\ displacement}\left[\frac{N}{m}\right];\ Mean\ ratio = \frac{Mean\ force}{Pre-displacement}\left[\frac{N}{m}\right]$$

Figure 5-2: Schematic for Mean ratio and Amplitude ratio

Figure 5-3a) shows the force mean ratio versus frequency for all experiments from all three mechanical eyeball configurations. As expected, the force mean ratio is constant with frequency and the highest values are observed for the thicker membranes and the higher pressures. For choked-pressurised configuration, there was no observable difference in force mean ratio between the different orifice sizes and these are therefore plotted as a single series. A much clearer relation for the force mean ratio to membrane thickness and to pre-pressure setting can be seen in Figure 5-4 and Figure 5-5. The two figures clearly show that the chosen membrane thicknesses (0.4mm, 0.5mm and 1.0mm) had a bigger effect to the force mean ratio than the chosen pre-pressure settings (1.8kPA and 3.3kPA) whereby the pressures are in the range of the anatomical case for healthy eyes and diseased eyes, but the membrane Young's modulus was chosen far too high (the cornea had an up to 600 times lower modulus) which was figured out when the first pig eyes were tested. All error bars in the two figures represent the standard deviation of the repeated experiments.

Figure 5-3b) show mean pressure (kPa) versus frequency, again for all experiments. Again as expected, the mean pressure did not vary with frequency and was again highest for the highest pressures and membrane thicknesses. For the choked-pressurised configuration, the mean pressure was again independent of the orifice size

and, unlike the closed-pressurised configuration, was equal to the set pressure and independent of membrane thickness. For the closed-pressurised configuration the membrane thickness and the set pressure setting both affect the recorded mean pressure, indicating that bulging of the membrane plays a part in closed systems. A clearer demonstration supplies Figure 5-6 and shows the pressure increase for thicker membranes and for higher pressure setting, where all error bars show the standard deviation of the repeated experiments.

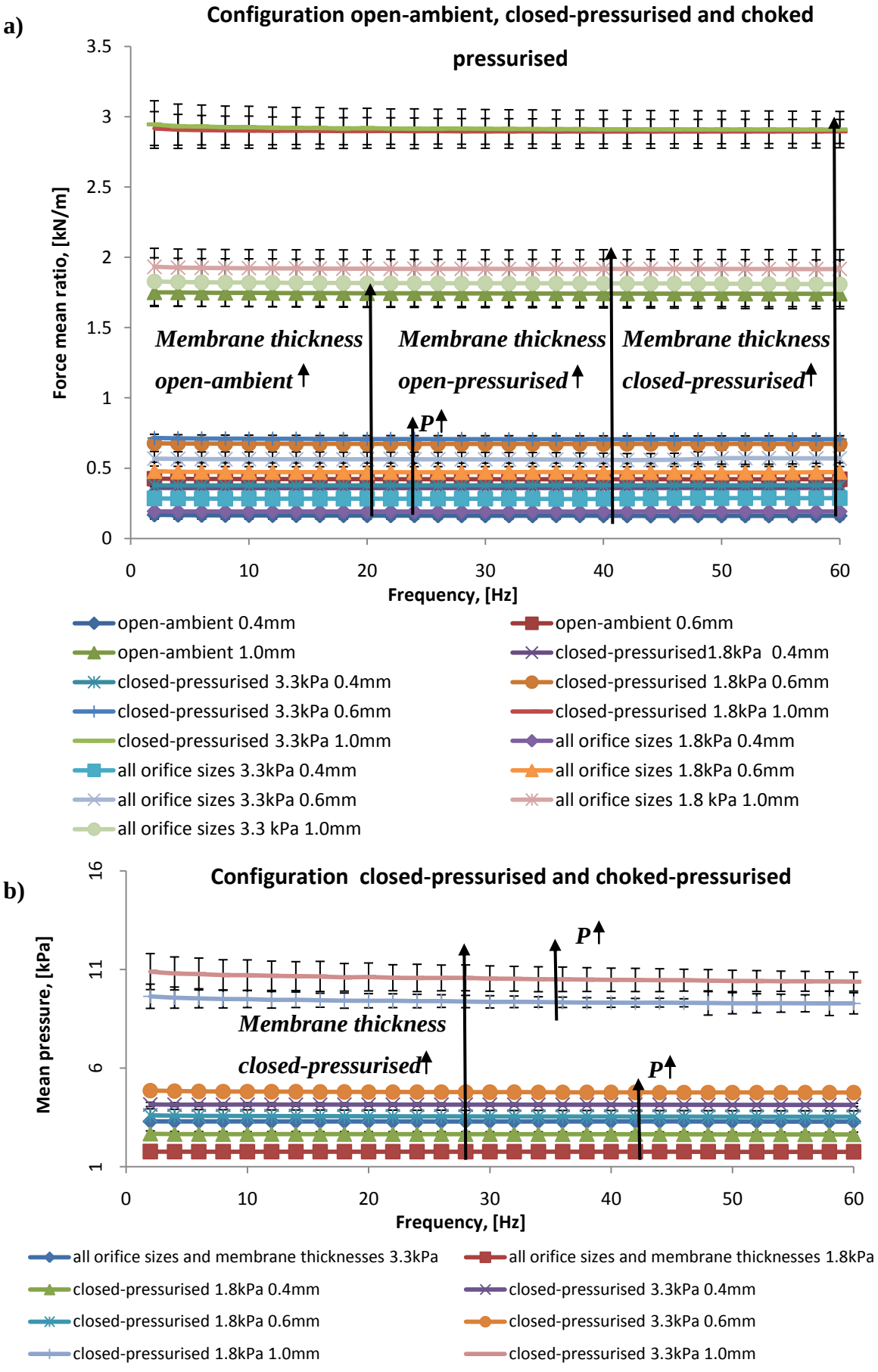

Figure 5-3: Mean ratios vs. frequency for all experiments and configurations of mechanical eyeball a) Mean force ratio [N/m] b) Mean pressure [kPa]

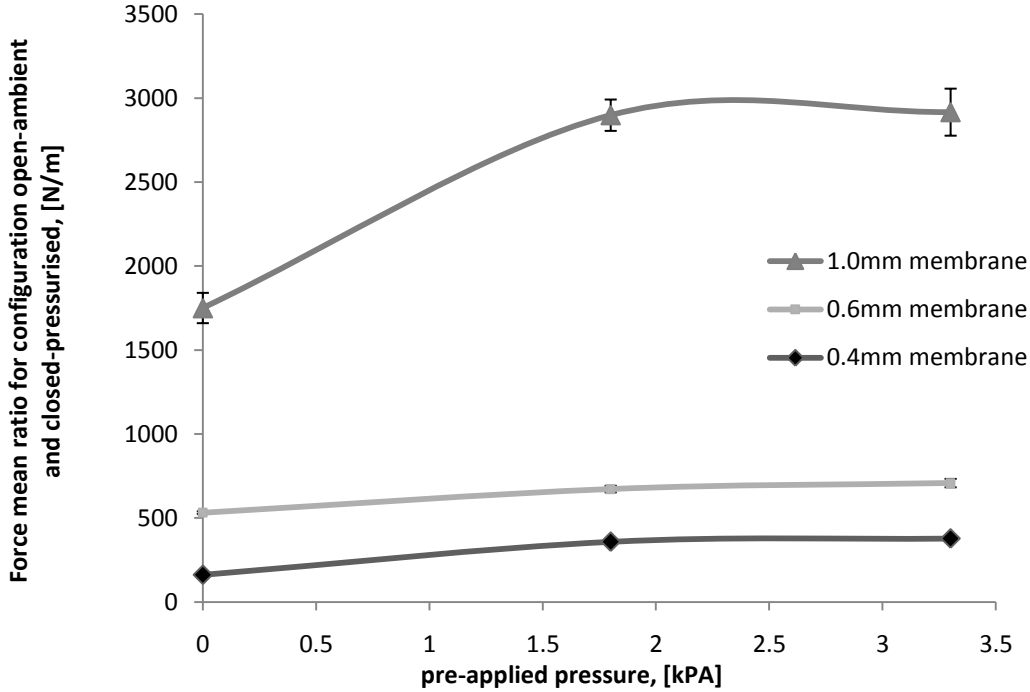

Figure 5-4: Force mean [N/m] ratio for configuration open-ambient and closed-pressurised as a function of pre-applied pressure [kPa]

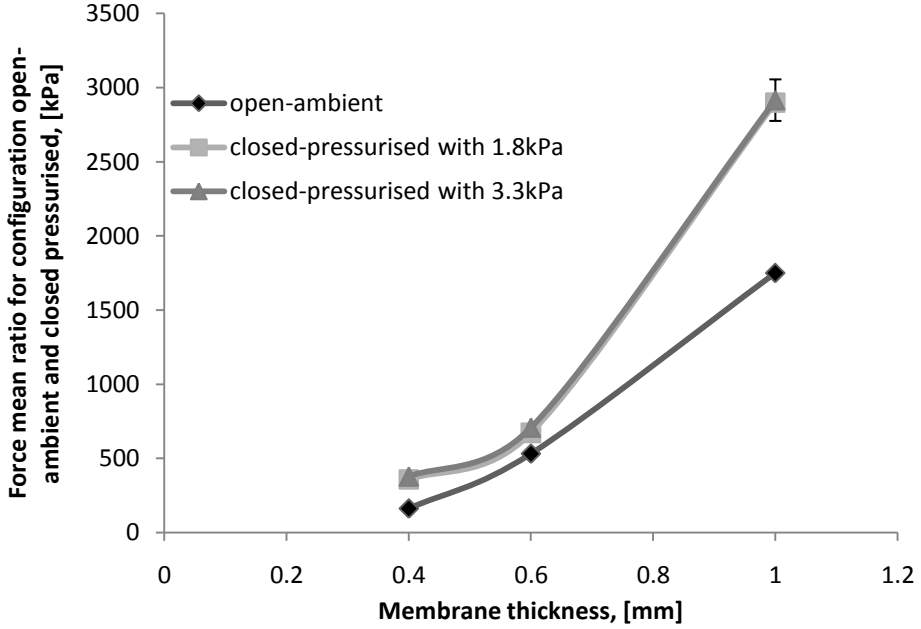

Figure 5-5: Force mean ratio [N/m] for configuration open-ambient and closed-pressurised as a function of pre-applied pressure as a function of membrane thickness [mm]

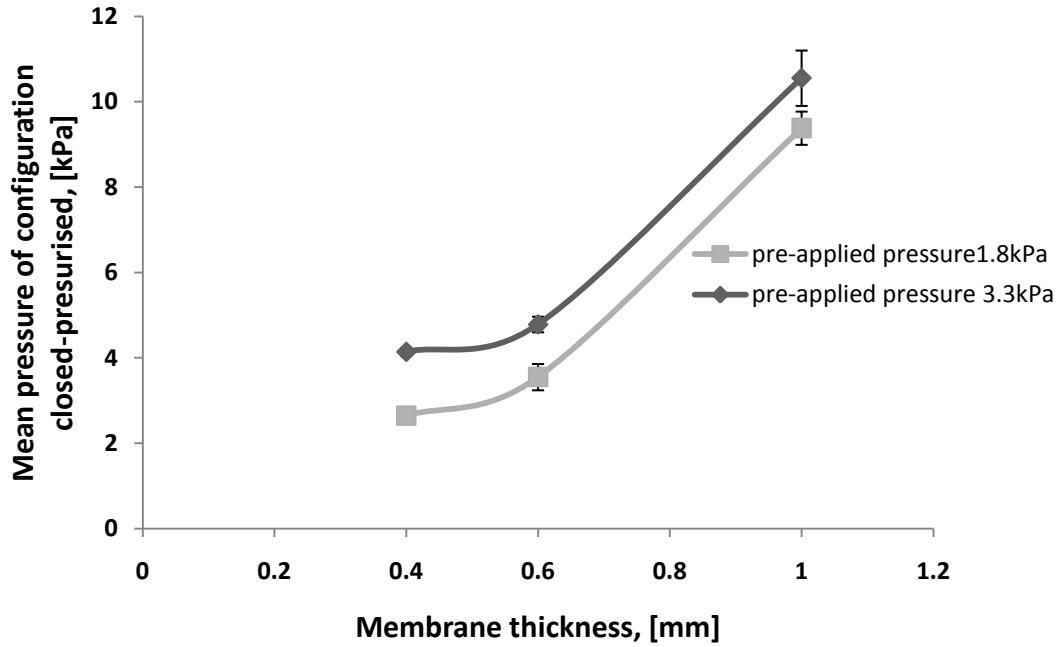

Figure 5-6: Mean pressure [kPa] of configuration closed-pressurised as a function of membrane thickness [mm]

Figure 5-7 a) shows the force amplitude ratio as a function of frequency for all experiments in the closed-pressurised and open-ambient configurations. For all experiments, the magnitude of the complex modulus increases with increasing frequency. As with other monotonic variations, the strength of this change has been estimated using linear regression. Even though the relationship is not expected to be linear, the slope and correlation coefficient are useful in determining if there is a significant effect of frequency. The 1.0mm thick membrane with 3.3kPa set pressure gave the highest gradient of 8.32Nm^{-1}/Hz with R^2 = 0.968, whereas the same thickness with a pressure of 1.8kPa yielded a slightly smaller gradient of 8.21Nm^{-1}/Hz with R^2 =0.967. The smallest gradient is seen with the 0.4mm thick membrane in the open-ambient configuration, where the slope was 1.55Nm^{-1}/Hz with R^2 =0.951.

Figure 5-7 b) shows all the pressure amplitude ratio results versus frequency for the closed-pressurised configuration. Again, the thickest membrane (1.0mm) with the higher pressure (3.3kPa) gave the highest gradient of 0.0541kPam^{-1}/Hz with the highest R^2 = 0.96, and the gradients and R^2 values decreases with decreasing thickness and with decreasing pressure, the membrane thickness again having the greater effect. The lowest gradient was 0.0114kPam^{-1}/Hz with R^2 = 0.63 for the 0.4mm thick membrane with a pressure of 1.8kPa.

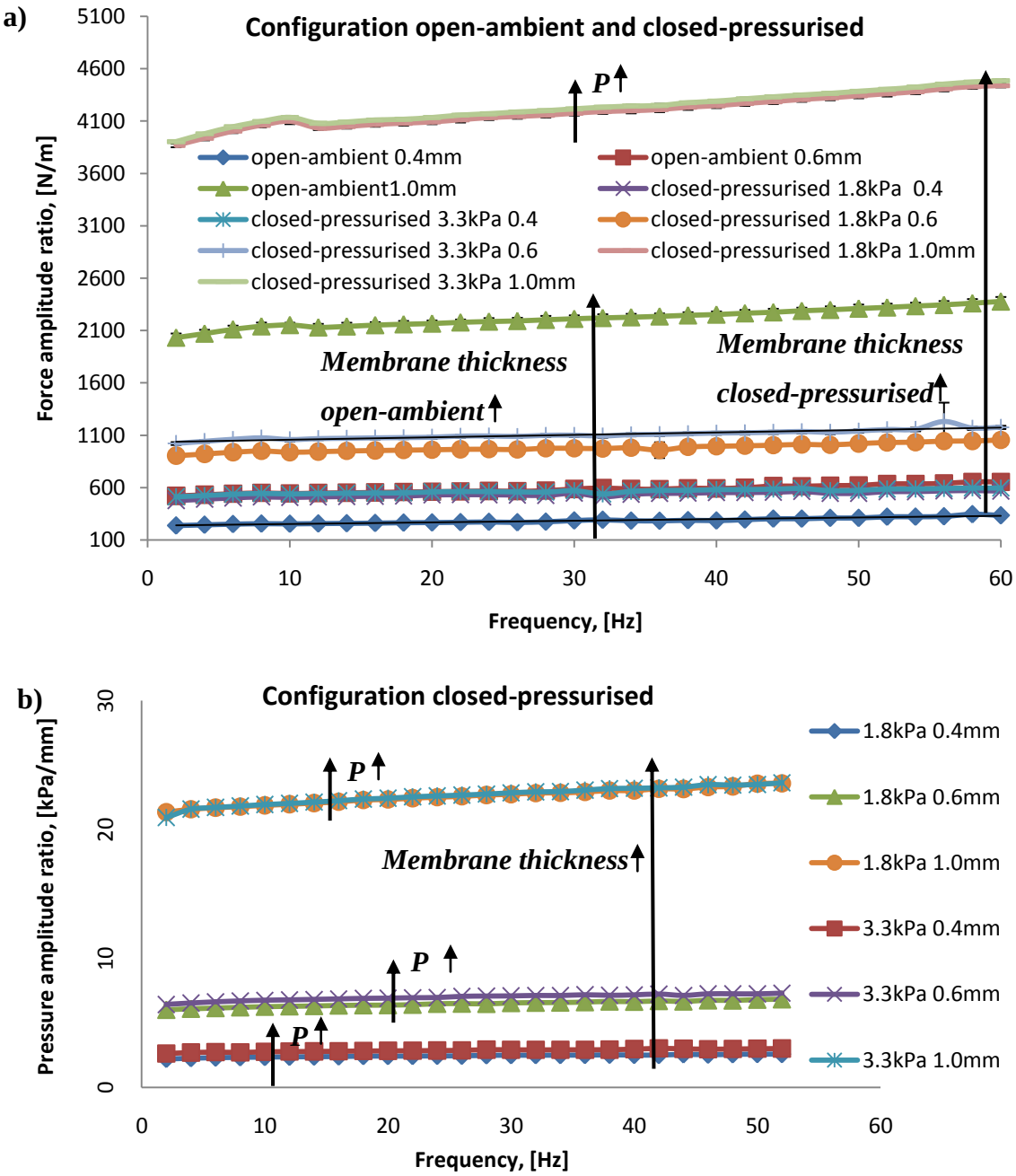

Figure 5-7: Effect of frequency on a) force amplitude ratio [N/m] for closed-pressurised and open-ambient configurations, and b) pressure amplitude ratio [kPa/mm] for closed-pressurised configuration

Figure 5-8 shows the effect of frequency on a) phase difference between force and displacement and b) phase difference between pressure and displacement for the closed-pressurised and open-ambient configurations. All these experiments exhibited very small phase lags with high scatter (relative to the mean) slopes ranging from 0.024°Hz^{-1} for the thinnest membrane with ambient air to -0.048°Hz^{-1} for the thickest membrane at

3.3kPa pressure. The thicker membranes for both configurations also showed the highest R^2 values of between 0.43 and 0.61.

The pressure-displacement phase differences were much clearer, with the different membrane thicknesses exhibiting strong differences at low frequencies, converging at higher frequencies. The 0.4mm thick membrane showed a negative phase over some of its frequency range. The thicker membranes showed higher (positive) phase differences at lower frequencies, although the thinner membranes showed higher gradients. It also seemed that the thinner membranes showed the beginnings of resonant behaviour at the lowest frequencies. The set pressure did not seem to have a significant effect on the pressure phase difference for a given membrane thickness.

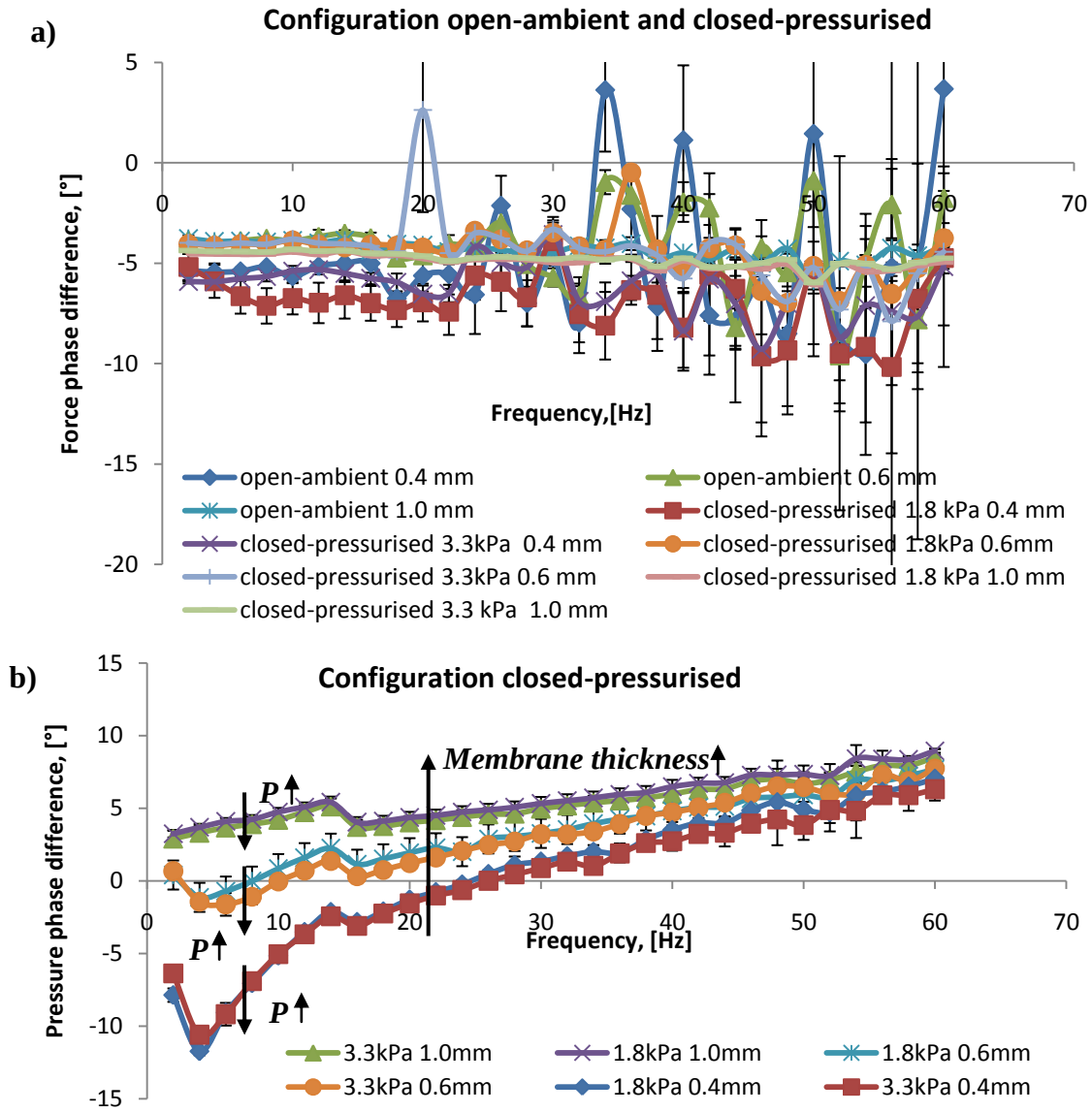

Figure 5-8: Effect of frequency on a) force-displacement phase difference (closed-pressurised and open-ambient configurations) [°]; b) pressure-displacement phase difference for closed-pressurised configuration [°]

Figure 5-9 shows the results for the phase in the choked-pressurised configuration with a 0.6mm thick membrane. For the force-displacement phase (Figure 5-9a), distinct resonances are visible as minima, except in the case of the 1.8kPa pressure and 5mm orifice size where the peak appeared to be just beyond the 60Hz upper frequency working limit of the test rig. Table 5-2 summarises all of the minimum phases and their associated frequencies for 0.4 and 0.6mm thick membranes. For the 1.0mm thick membrane, the peaks could not be identified as they fell outside the working range of the test rig.

The choked-pressurised configuration, pressure phase differences for the 0.6mm membrane, Figure 5-8b), were all higher than 180°, and all showed a transition from 180° to 360° over the frequency range studied. For the smallest orifice (1.3mm), the transition starts at the lowest frequency (around 6Hz) and is very gradual (more gradual for the lower set pressure), not being complete until 44Hz. The transition starts later for the 0.5mm orifice (32Hz), again being more gradual for the lower set pressure. Finally, the transition for the 16mm orifice at 3.3kPa set pressure is just complete within the experimental range, but the transition has only just started for the 1.8kPa set pressure. The starting and finishing frequencies of the transition (transition bandwidths) (0.4/0.6 and 1.0mm thick membrane) are listed in Table 5-3 for the 0.4 and 0.6mm membranes for all orifice sizes. Again, the relevant observations could not be made for the 1mm thick membrane.

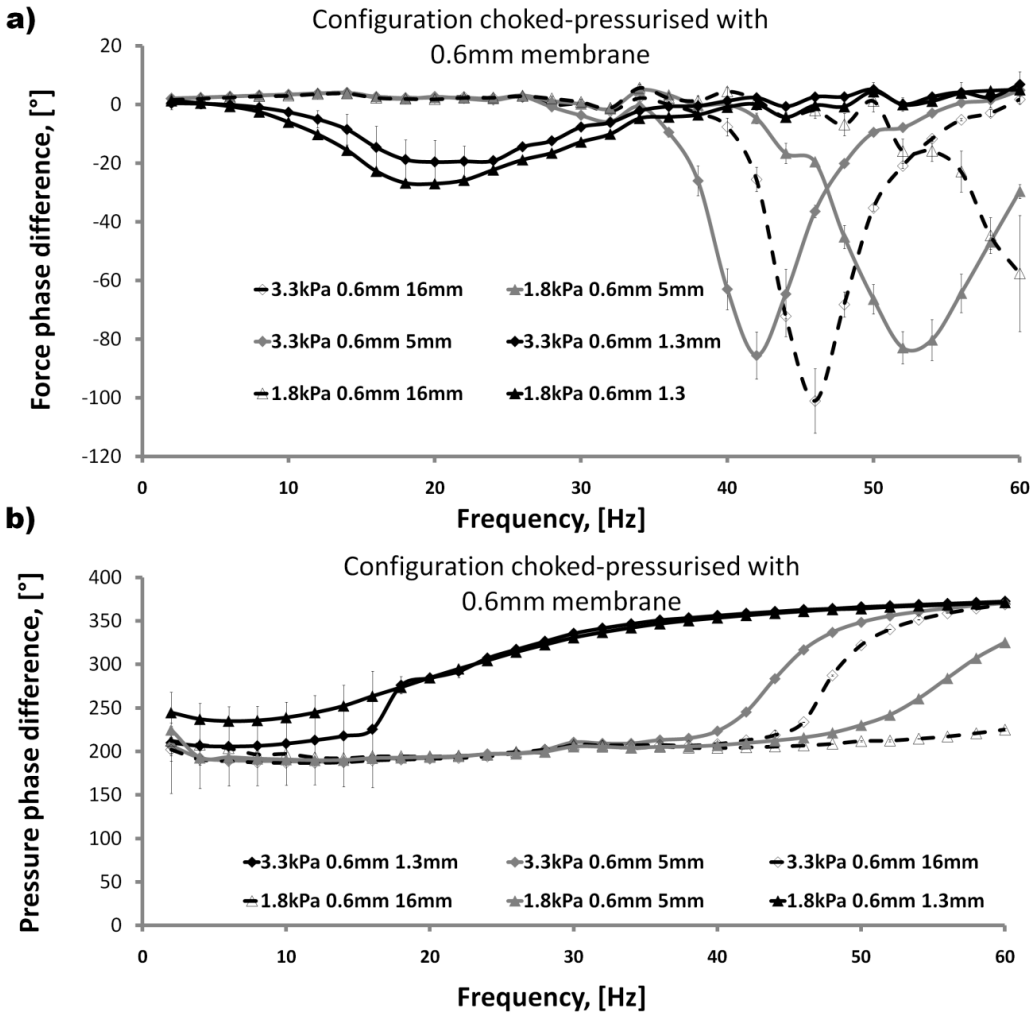

Figure 5-9: Phase difference [°] as a function of frequency for the choked-pressurised configuration with 0.6mm membrane. a) force-displacement and b) pressure-displacement

Figure 5-10 shows the amplitude ratios for the choked-pressurised configuration with the 0.6mm thick membrane. The force amplitude ratio, Figure 5-10a), is typical of all experiments with the choked-pressurised configuration, the value initially dipping slowly to minimum followed by a sharp increase terminating in a maximum. This behaviour was most clearly exhibited with the 5.0mm and 16mm orifices, although it is obviously also present with the 1.3 mm orifice. To describe the curves, the minimum and maximum values of amplitude ratio along with the relevant frequencies were recorded, and these are shown in Table 5-2 along with the corresponding results for the 0.4mm membrane. Again, the relevant observations could not be made with the 1mm membrane within the working range of the test rig.

The pressure amplitude ratio, Figure 5-10b), again has a characteristic shape, starting close to zero at 2Hz and increasing to a maximum before dropping again to a plateau, the full expression of this being seen most clearly for the 1.3mm orifice. The height and frequency of the maximum are listed for the 0.4mm and 0.6mm membranes in Table 5-3, the relevant values for the 1mm membrane again not being observable.

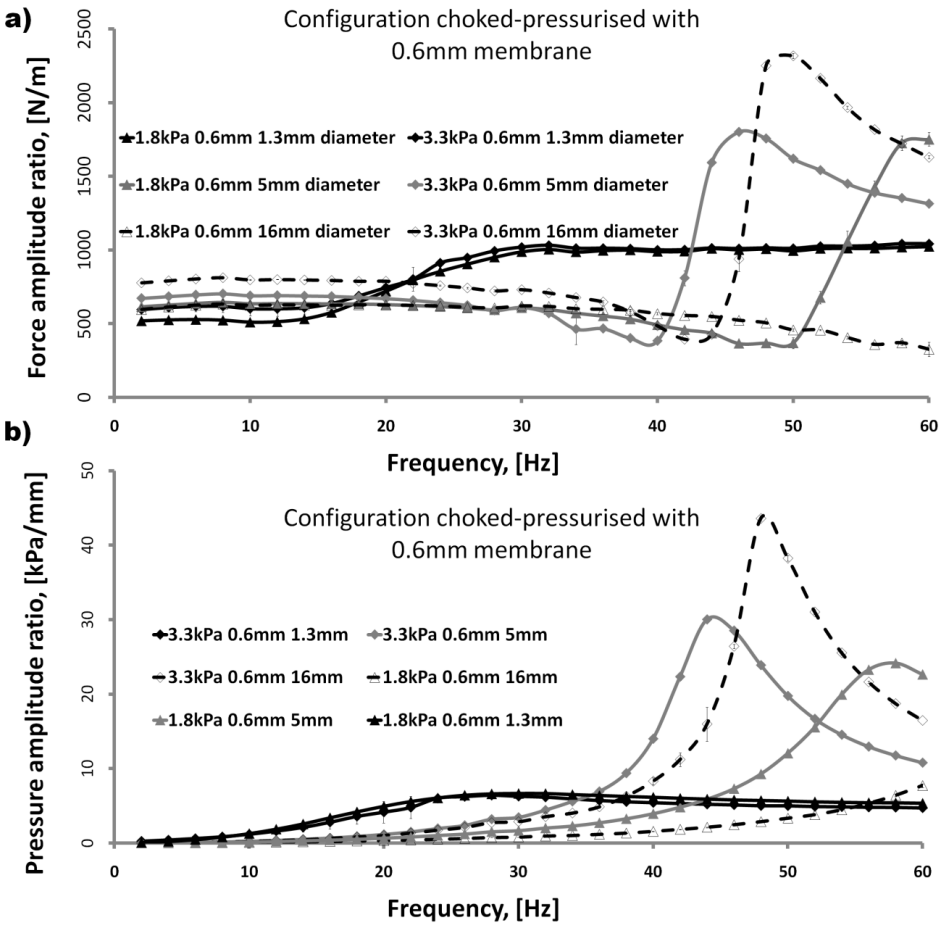

Figure 5-10: Amplitude ratio as a function of frequency for the choked-pressurised configuration with 0.6mm membrane. a) force-displacement [N/m] and b) pressure-displacement [kPa/mm]

Orifice size	Pressure (kPa)	min force amplitude ratio (N/m)	max force amplitude ratio (N/m)	Frequency range (Hz) between max and min amplitude ratio	min force phase lag degree	Frequency (Hz) when minimum phase lag appeared
0.6 mm thick membrane						
1.3	1.8	513	1004	12 – 32	- 27	20
	3.3	628	1032	14 – 32	- 20	20
5.0	1.8	368	1751	50 – 60	- 83	52
	3.3	383	1804	40 – 46	- 86	42
16	1.8	parameter not observable within working range (2Hz-60Hz)				
	3.3	394	2251	42 – 48	- 101	46
0.4 mm thick membrane						
1.3	1.8	275	342	10 – 18	- 7.7	14
	3.3	414	442	10 – 18	- 4.0	18
5.0	1.8	187	637	36 – 44	- 66	40
	3.3	257	710	36 – 44	- 52	40
16	1.8	97	693	40 – 52	- 87	44
	3.3	224	742	42 – 46	- 68	44

Table 5-2: Force-displacement frequency characteristics for choked-pressurised configuration with 0.4 and 0.6mm thick membranes. For 1mm thick membranes, the relevant characteristics could not be observed within the frequency range of the test rig.

Orifice	Pressure (kPa)	max pressure amplitude ratio (kPa/mm)	Frequency (Hz) at max pressure amplitude ratio	Transition Freq. bandwidth (Hz)
0.6 mm thick membrane				
1.3	1.8	6.6	30	* – 44
	3.3	6.4	28	* – 44
5.0	1.8	24	58	36 – *
	3.3	30	44	36 – 54
16.0	1.8	*	*	*
	3.3	44	48	42 – 56
0.4 mm thick membrane				
1.3	1.8	1.6	18	8 – 30
	3.3	1.6	18	* – 30
5.0	1.8	7.4	44	34 – 60
	3.3	12	42	34 – 56
16	1.8	5.2	48	40 – *
	3.3	14	46	40 – 58

*parameter not observable within working range (2Hz-60Hz)

Table 5-3: Pressure-displacement frequency characteristics for choked-pressurised configuration with 0.4 and 0.6mm thick membranes. For 1mm thick membranes, the relevant characteristics could not be observed within the frequency range of the test rig

5.2 Results for pig eyeball experiments

The results summarised in this section are for both the static and dynamic tests on pig eyes. The static results were essentially force relaxation curves and the analysis involved fitting a variety of visco elastic models to these. The dynamic tests used four different pressure settings and two different mean displacements. These were analysed for their dynamic visco elastic behaviour, again to obtain parameters for a best-fit model.

5.2.1 Static tests on pig eyes

Figure 5-11 shows a typical force relaxation curve, of which there were 80 carried out on 2 pig eyes (frozen). The experiments involved two different pressures (1.8kPa and 6.2kPa), two different speeds (5mm/s and 15mm/s) to deform the cornea at 1.5mm displacement for 10 seconds and were tested either closed (pressurised with a syringe) or open (where the pressure was applied with a water column). The fitting was done using a least squares algorithm and the goodness-of-fit was recorded as R^2. The relaxation curves were investigated using an SLS model, applied to the first 3 seconds (short time relaxation) and, separately, to the first 10 seconds (long time relaxation). The 5-parameter multi-component Maxwell model was applied only to the long time relaxation.

Figure 5-12 summarises the average R^2 with the standard deviation of 10 experiments for all tests and shows clearly that the best fit is obtained in all cases using the 5-parameter model, followed by the 3-parameter model for the short relaxation time. The poorest fits were obtained when applying the 3-parameter model to the full relaxation curve of 10 seconds. All fits for the SLS model were better for the higher pressure and the velocity did not appear to affect the fit. Fits were generally better for the open system than the closed system.

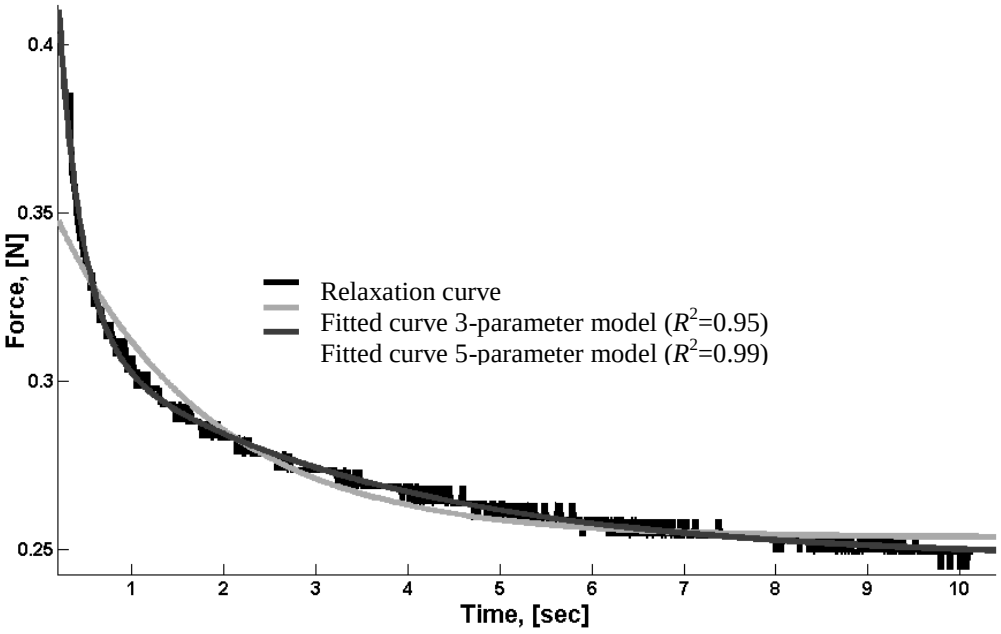

Figure 5-11: Typical force relaxation curve of a pig eyeball for 10 seconds relaxation time with two models (SLS 3-parameter model and 5-parameter model) fitted to the curve

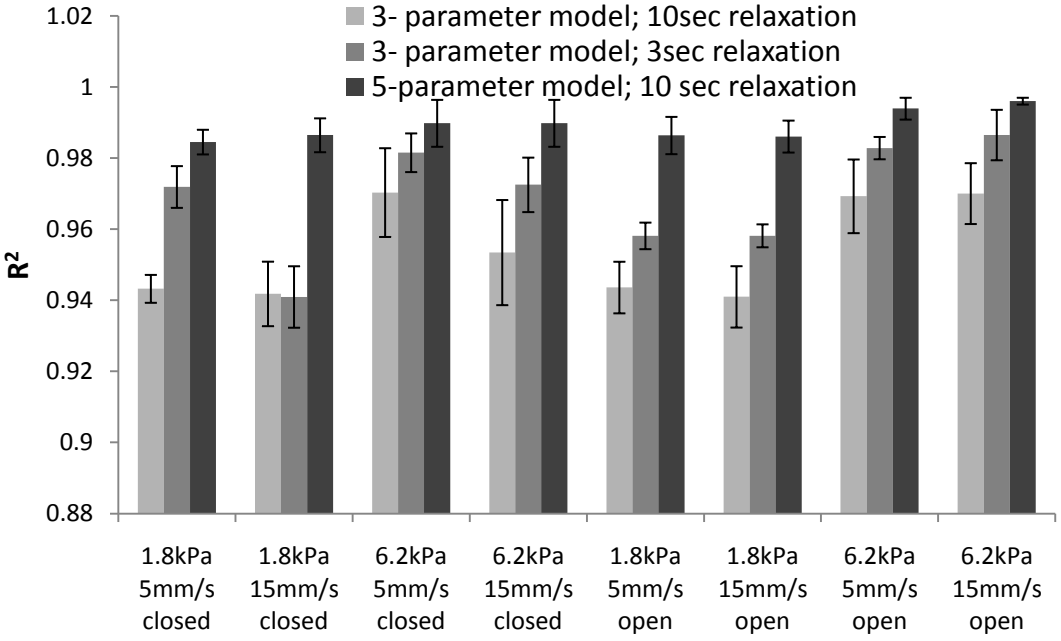

Figure 5-12: Goodness-of-fit (R^2) of 3- and 5-parameter models to static pig eye tests

Figure 5-13 shows the average initial stiffness (see Chapter 3) with the standard deviation from repeated experiments for all of the static data for the three fits described above. As can be seen, the 1.8kPa pressure groups have significantly lower initial stiffness than the 6.2kPa pressure groups. Also, there is no observable difference in the initial stiffness for the two different displacement velocities for a given pressure. The

average initial stiffness for the SLS model applied to the short time relaxation is higher than that for the other two models in 5 cases out of 8. The lowest average initial stiffness is given by the SLS model with the long time relaxation in 7 out of the 8 cases.

The stiffness parameter c_s for the parallel Maxwell spring (see Chapter 3) is shown in Figure 5-14. Here, again, a clear difference between the two pressure groups is visible, with higher pressure being related to higher c_s values and hence higher stiffness. The average value of c_s is consistently highest for the 3-parameter model with the 10 second relaxation time and is consistently lowest for the 5-parameter model. Again no effect was observable of the different indentation speeds.

The series spring stiffnesses are shown in Figure 5-15. As with the other stiffness parameters, the higher pressure tends to give higher values of c_1 and c_2, although the difference between the open system and the closed one seems more marked. In contrast to c_s, the parameter c_1 is consistently higher for the short relaxation time than the long one. Since c_1 and c_2 are parallel springs, it is more appropriate to compare the 3-parameter c_1 values with the sum of c_1 and c_2 from the 5-parameter model. The sum of c_1 and c_2 is to see in Figure 5-16 and shows that the combination of the two parameters is always in the range of the c_1 parameter of the short relaxation time and proves therefore to be able to align very good at the beginning of the force relaxation which could not been said with the SLS model for the 10 sec relaxation time.

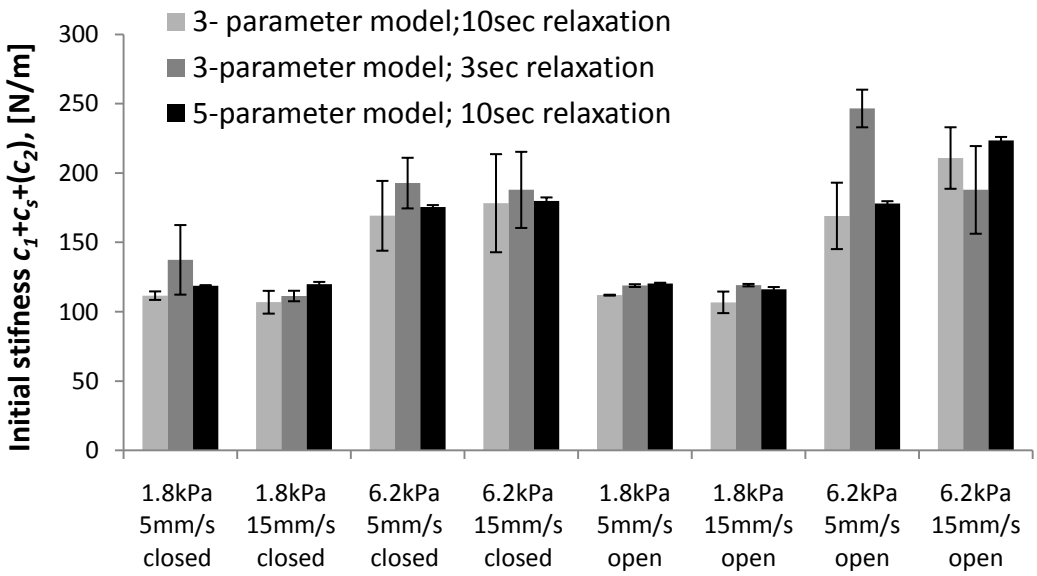

Figure 5-13: Initial stiffness [N/m] of 3- and 5-parameter models from static pig eye test

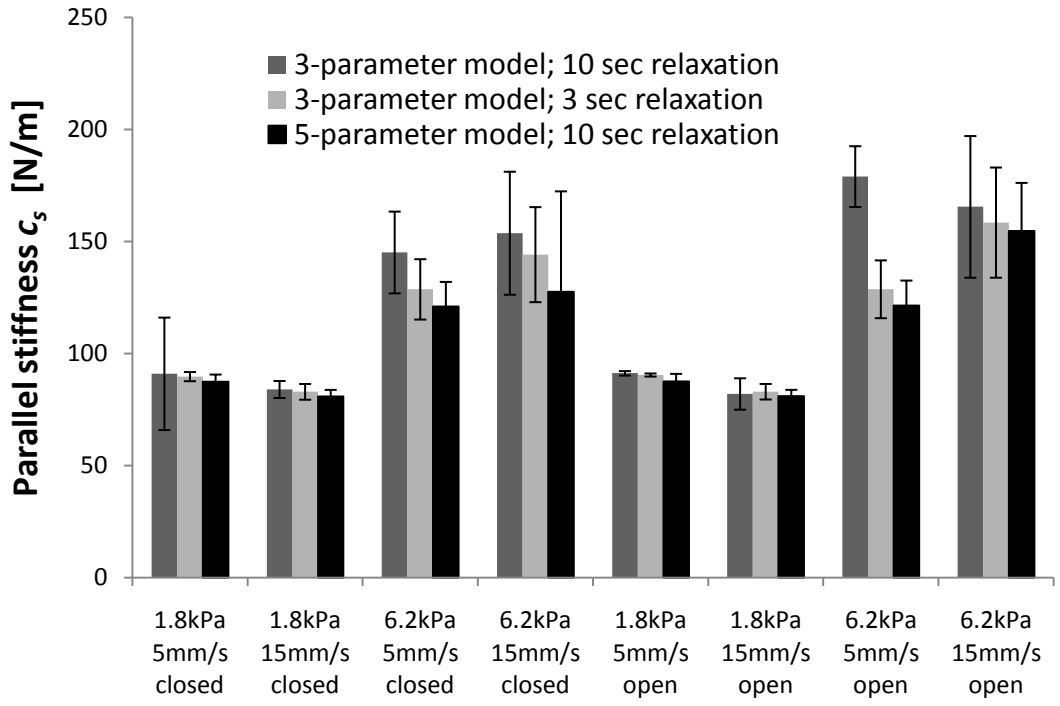

Figure 5-14: Parallel stiffness [N/m] parameter c_S for 3- and 5-parameter models from static pig eye tests

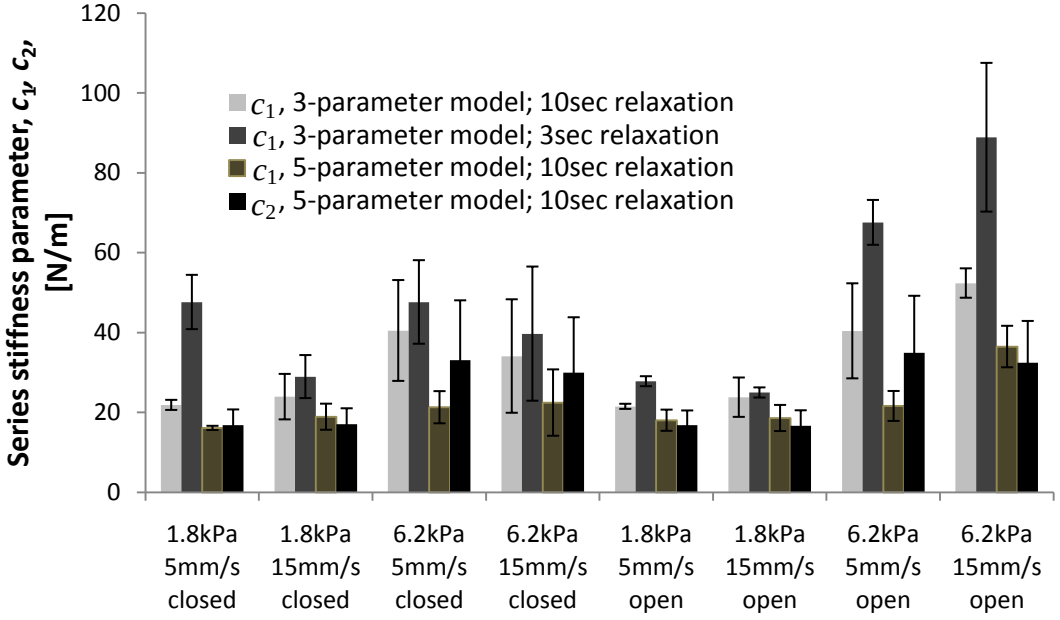

Figure 5-15: Stiffness parameters c_1 (and c_2) [N/m] for 3- and 5-parameter models from static pig eye tests

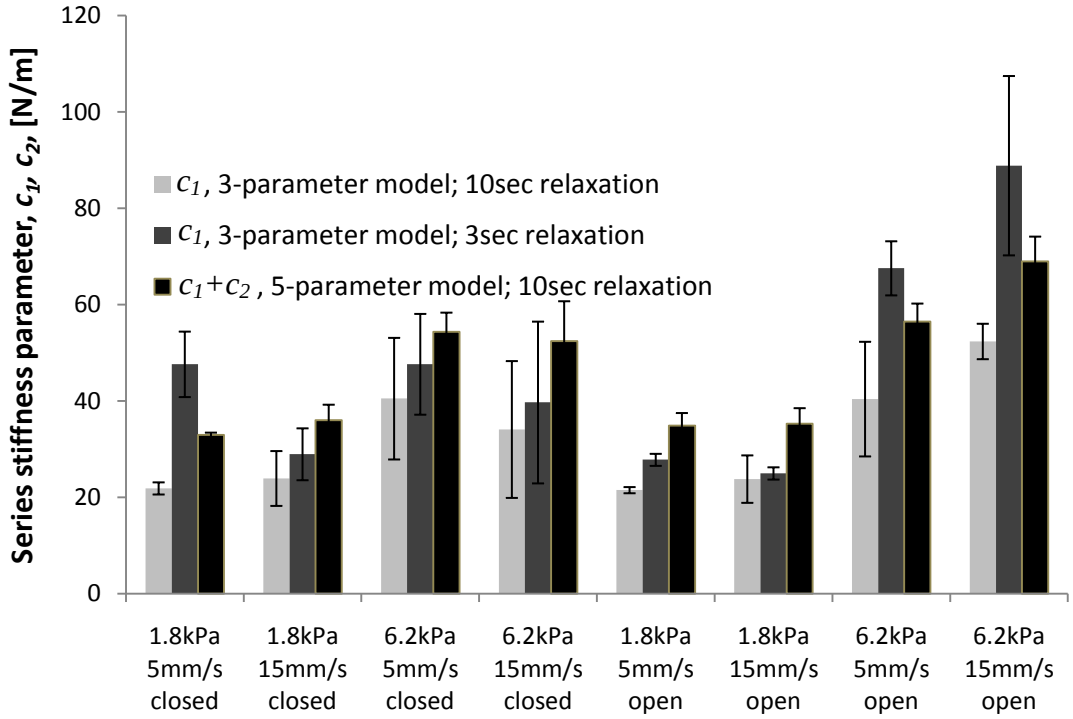

Figure 5-16: Stiffness parameters c_1 for 3- and c_1+c_2 for 5- parameter models from static pig eye

Figure 5-17 shows the viscous parameter d_1 for the three parameter model for both short and long relaxation times. The values obtained for the 3 second relaxation time are generally smaller than those for the 10 second relaxation time and the variance for the long relaxation time curves are much higher than for the short relaxation time.

Figure 5-18 shows the two viscous parameters from the 5-parameter model. Noting that the scale is logarithmeic, it can be seen that a significantly higher value was always obtained for one of the parameters (here given as d_2) than for the other (d_1). No clear variation in d_2 was evident for the different experiments, but a clear trend between the velocities of 5mm/s and 15mm/s and between the low and high pressures (but not between the open and closed configurations) was observed for d_1.

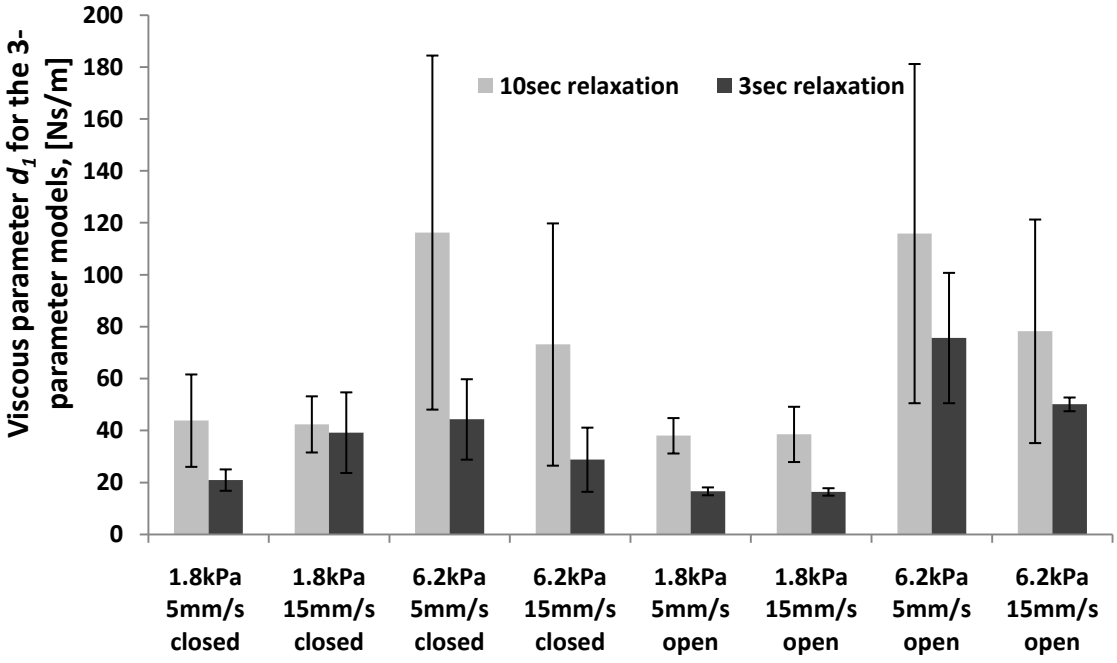

Figure 5-17: Viscous parameter d_1 [Ns/m] for the 3- parameter models from static pig eye tests

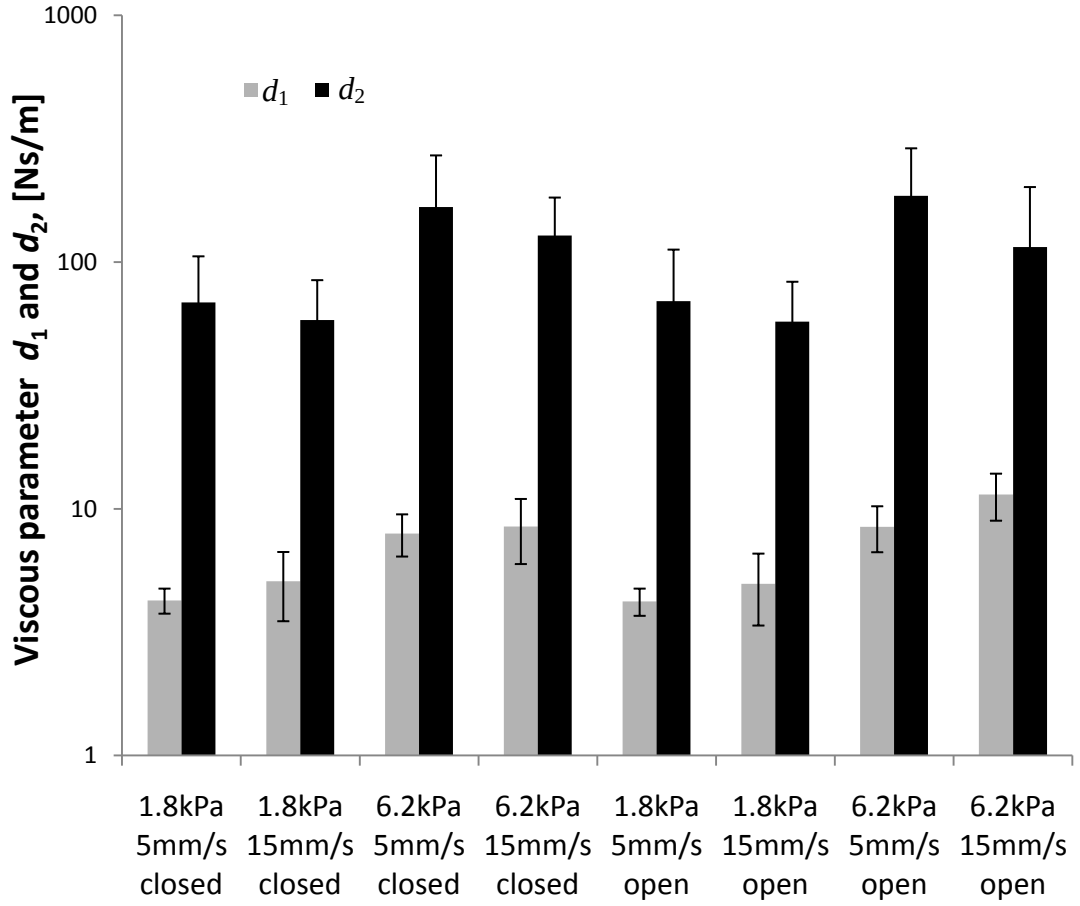

Figure 5-18: Viscous parameters d_1 and d_2 [Ns/m] for the 5-parameter models from static pig eye tests

5.2.2 Dynamic tests on pig eyes

The dynamic test includes experiments done for 35 whole eyeballs which had been frozen on receipt and defrosted prior to testing (hereinafter referred to as “frozen”) and 3 fresh eyeballs. Four pressures were used in the closed configuration and all frozen eyeballs were tested with 0.5mm and 1.5mm pre-displacements whereas the fresh eyeballs were tested only with a 1.5mm pre-displacement as control group. A further dynamic test was done on 2 excised corneas with an attached ring of the sclera, where the ring was clamped and the cornea tested in an open-ambient configuration with a 1.5mm pre-displacement.

No significant difference to the defrosted and the fresh eyeballs could be observed. This was tested for phase difference, amplitude ratio, and mean ratio as to see in Figure 5-19 to Figure 5-21. The pre applied pressure is very hard to control and increases therefore the error bars, which are the standard deviation of the repeated experiments for force amplitude ratio, force phase difference and also for force mean ratio. Applying a linear fit to the force mean ratio vs. applied pressure (Figure 5-20) shows a slight higher gradient for the fresh eyeballs compared to the frozen ones.

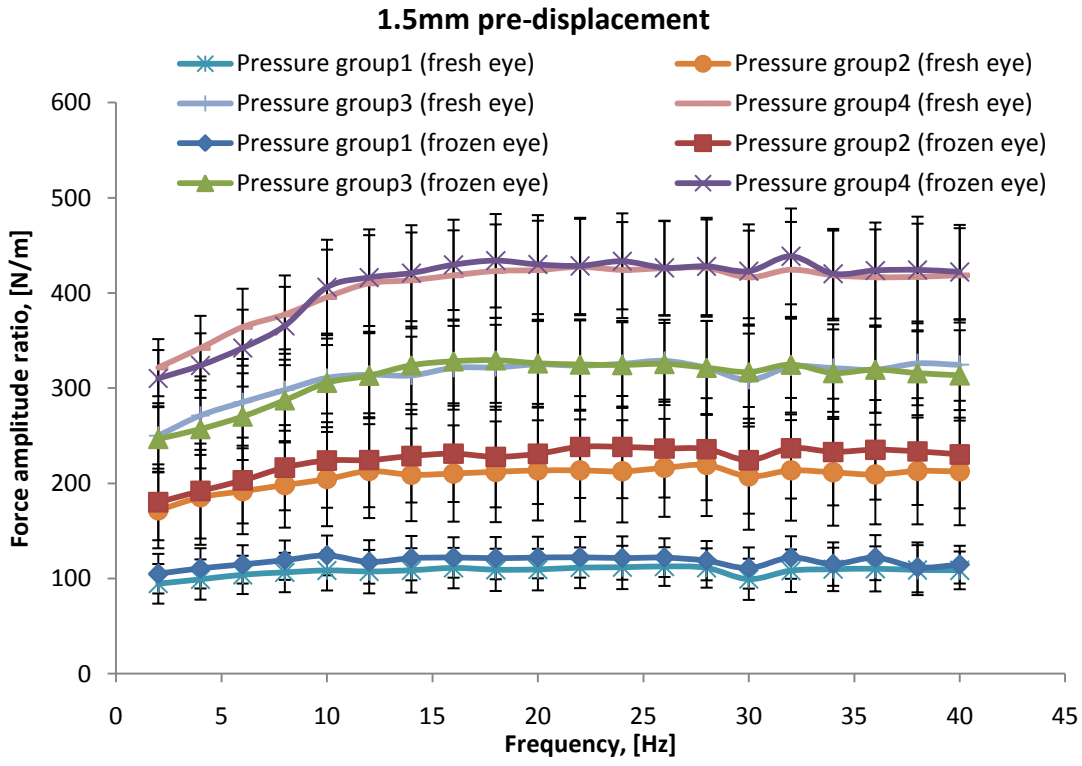

Figure 5-19: Force amplitude ratio [N/m] for fresh and frozen pig eyeballs at a pre-displacement of 1.5mm for all pressure groups

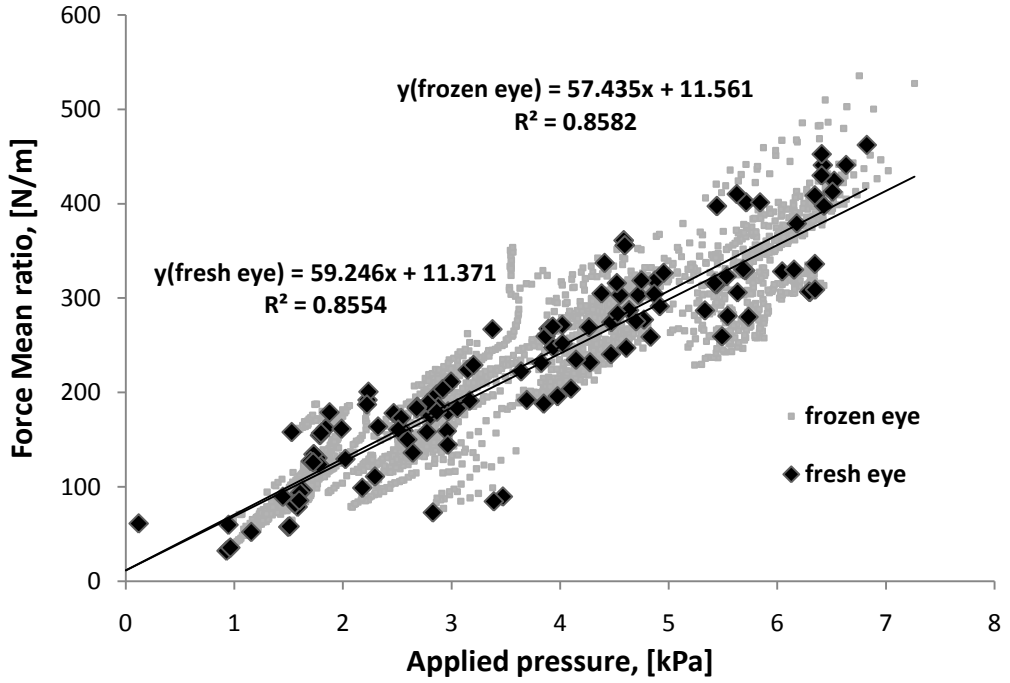

Figure 5-20: Force mean ratio [N/m] for fresh and frozen pig eyeballs at a pre-displacement of 1.5mm

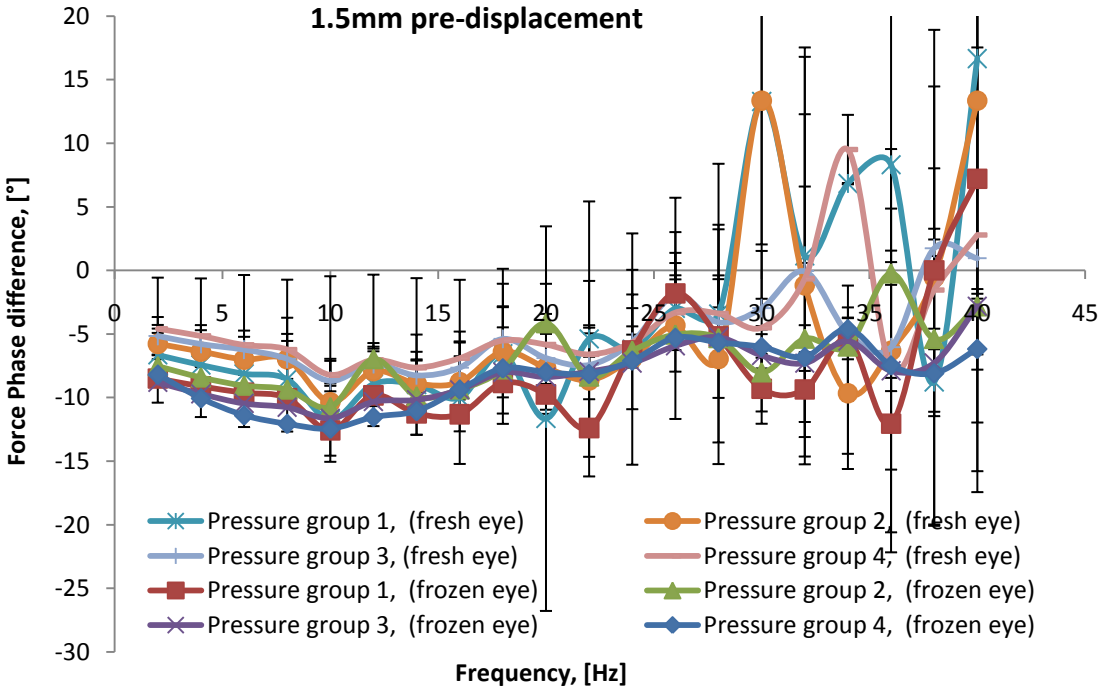

Figure 5-21: Force phase difference [°] for fresh and frozen pig eyeballs at a pre-displacement of 1.5mm for all pressure groups

The results for the corneas tested in the open-ambient configuration are shown in Figure 5-22 to Figure 5-24. The force mean ratio is relatively constant across the frequency range with an average of 6.4±1.2N/m the variance being largely dominated by the differences in values recorded in the 4 tests. The force amplitude ratio is around 5N/m across much of the frequency range but increases relatively sharply to 12N/m after 30Hz which is an indicator for visco elastic behaviour. A change at 30 Hz can also be seen in the phase difference although this is small, with the force being about -4° out of phase with the displacement changing to about -6° for frequencies above 30Hz.

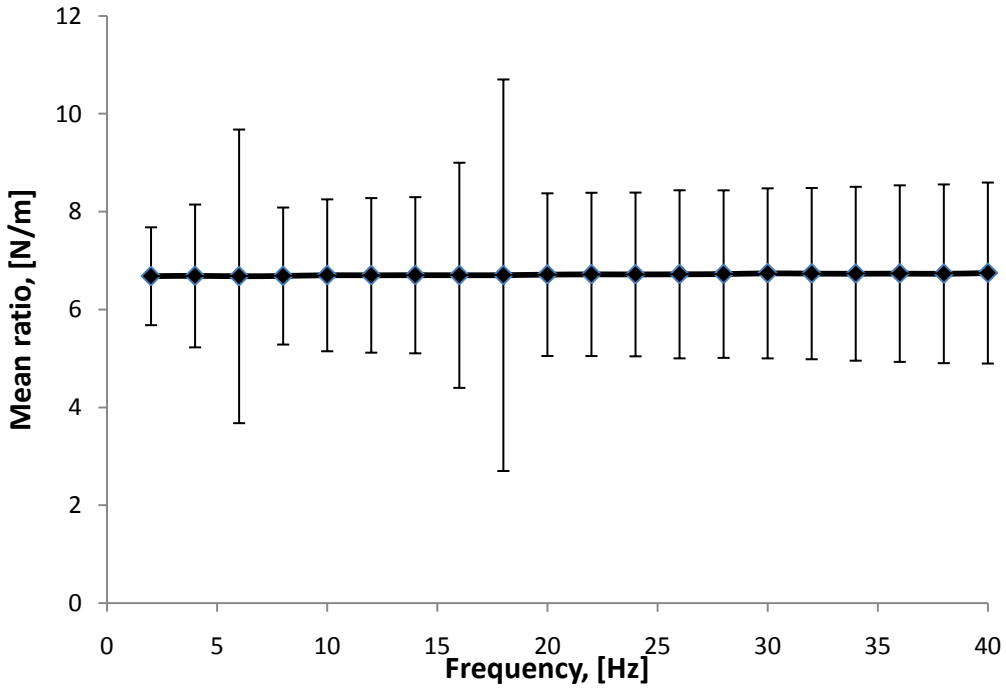

Figure 5-22: Mean ratio [N/m] for cornea and sclera ring in open-ambient configuration

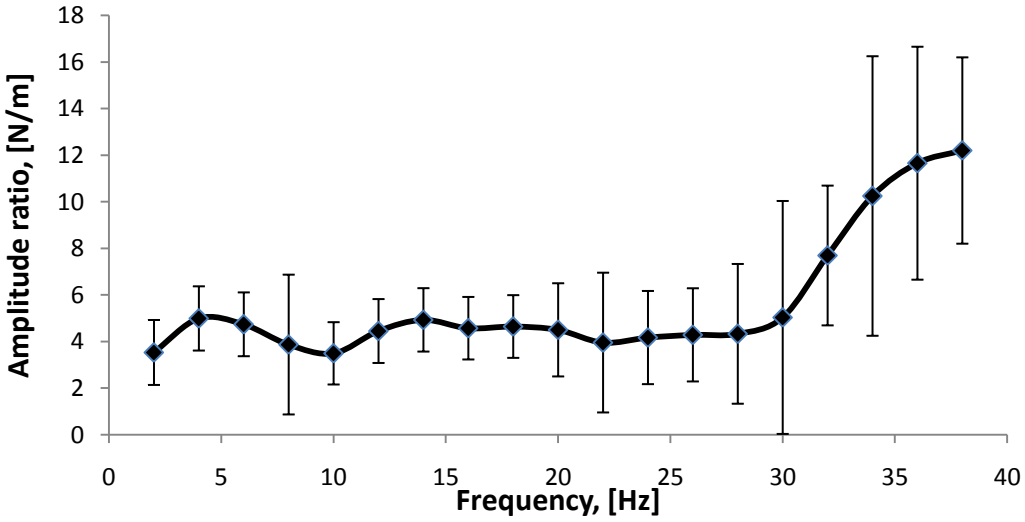

Figure 5-23: Amplitude ratio [N/m] for cornea and sclera ring in open-ambient configuration

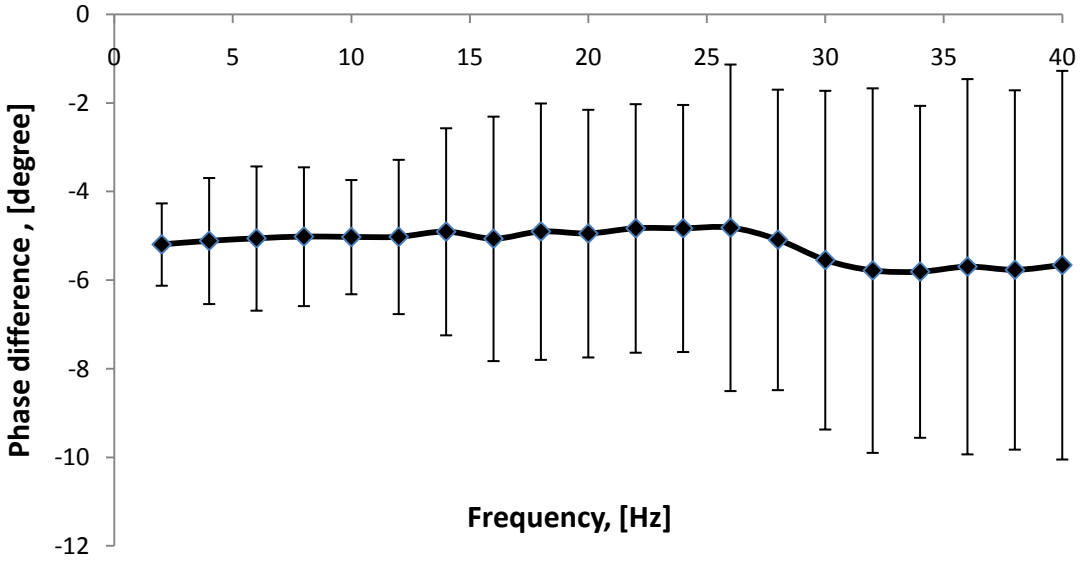

Figure 5-24: Phase difference [°] for cornea and sclera ring in open-ambient configuration

Figure 5-25 a) and b) show the force mean ratio for the 0.5mm pre-displacement and the 1.5mm pre-displacement, respectively, for the whole pig eyes. In both cases, the mean ratio is, as expected, essentially constant across the whole frequency range tested. Again as expected, the mean ratio is consistently higher for the 1.5mm pre-displacement than 0.5mm and for the higher pressure groups over the lower pressure groups. The error bars for the smaller pre-displacement are always higher than the error bars for the 1.5mm pre-displacement.

The average mean ratio for each frequency point is plotted against the applied pressure (IOP) in Figure 5-26) and shows a very good linear relationship. The error bars in the mean ratio were obtained using the standard deviation, where each dot represents an eyeball at a certain pressure for all frequencies, and the error bars in pressure reflect the fact that the pre-set IOP is not precisely the same for each experiment. The best-fit straight lines yield slightly different gradients for the two displacements, the one for the 1.5mm pre-displacement being about 1.2 times higher than that for the 0.5mm displacement. Given that the intercept is quite close to zero in relation to the measured values, the intercept of around 26N/m is reasonably consistent with the value measured in the open-ambient configuration (about 7N/m Figure 5-22).

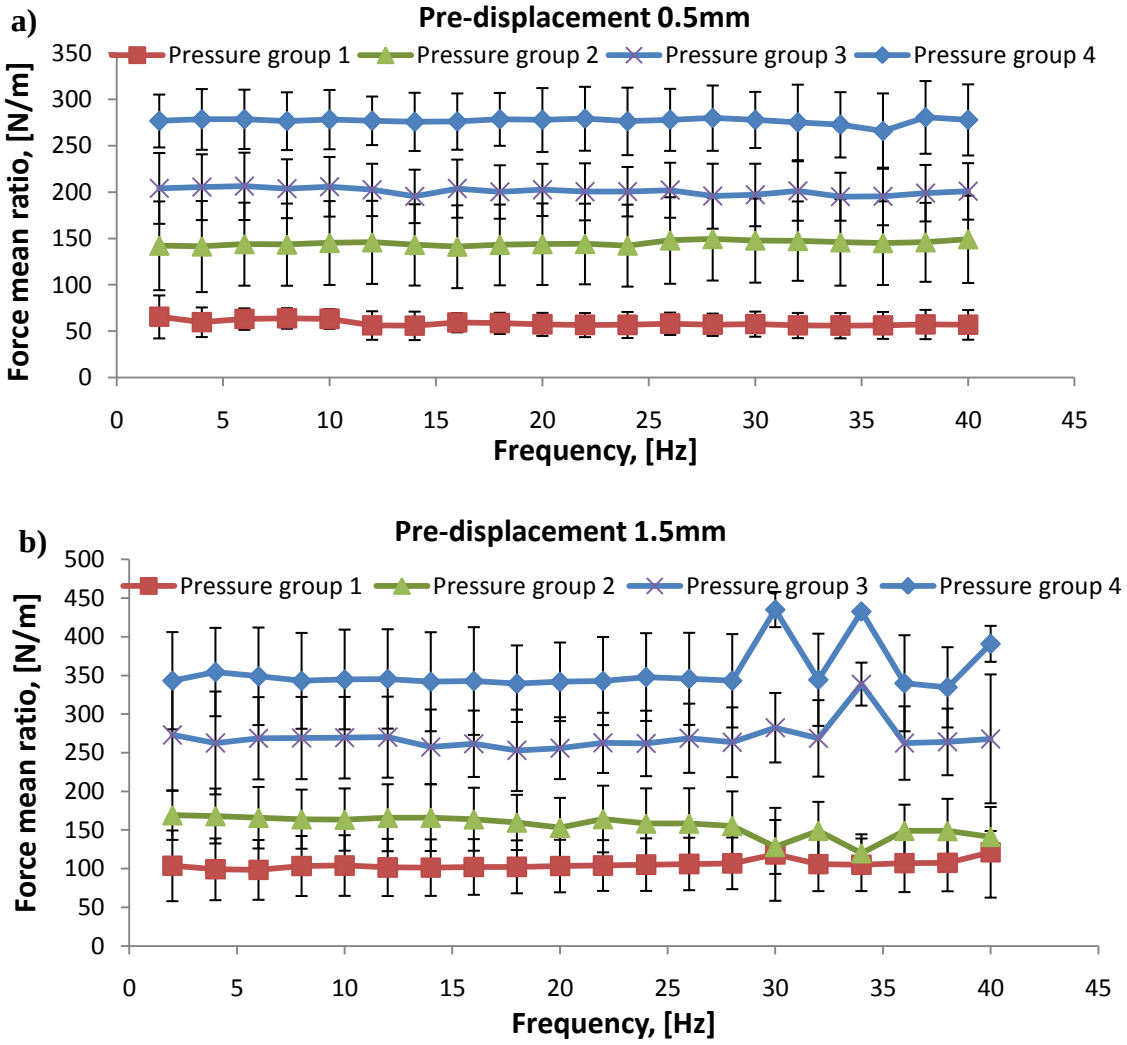

Figure 5-25: Force mean ratio [N/m] versus frequency [Hz], for a) 0.5mm pre-displacement and b) 1.5mm pre-displacement

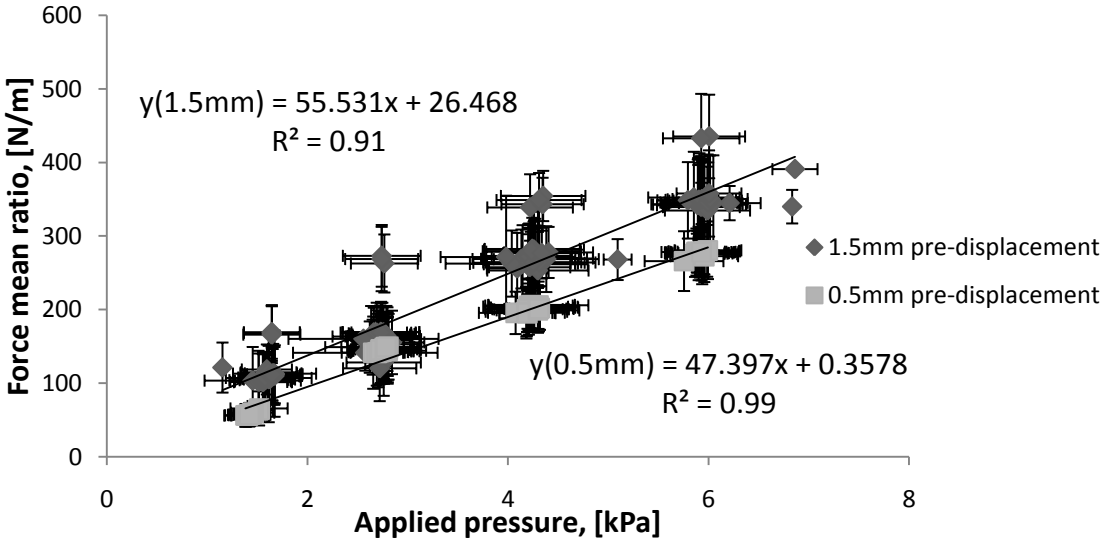

Figure 5-26: Measured force mean ratio [N/m] versus intraocular pressure (IOP) [kPa]

Figure 5-27 shows the phase and amplitude for the 0.5mm pre-displacement. Although the phase, Figure 5-27a), is everywhere quite small there is a clear shift from around -5° through a minimum between 10 and 15Hz to around zero at about 30Hz. After 30Hz the scatter increases drastically and the phase values become indistinguishable from zero. Although it is not all that visible in Figure 5-26b), the amplitude ratio plots all show negative curvature with an initially steeper gradient at 2Hz, becoming almost flat at 40Hz. The different pressure groups show markedly different amplitude ratios at a given frequency, unlike the phase where the pressure groups are barely distinguishable.

The results of the dynamic tests with the pre–displacement of 1.5mm are shown in Figure 5-28. The phase difference shows a similar shape to the 0.5mm pre-displacement, with a minimum at 10Hz but is somewhat lower overall and much less scattered at higher frequencies. Again, no difference was found between the different IOP groups. The amplitude ratio again showed a negative curvature, much clearer than for the 0.5mm pre-displacement. Again, increasing the IOP increases the amplitude ratio significantly and the curvature is more pronounced at higher IOPs.

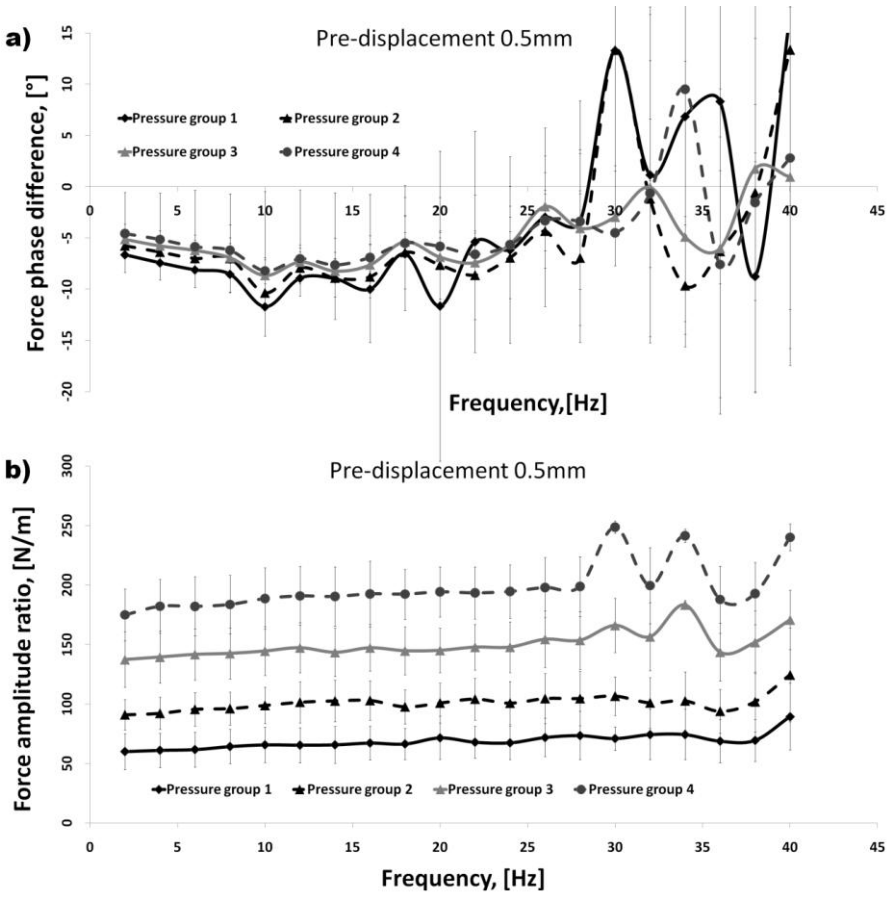

Figure 5-27: Dynamic tests on pig eyes at 0.5mm pre –displacement a) phase difference [°] - b) amplitude ratio [N/m] versus frequency [Hz]

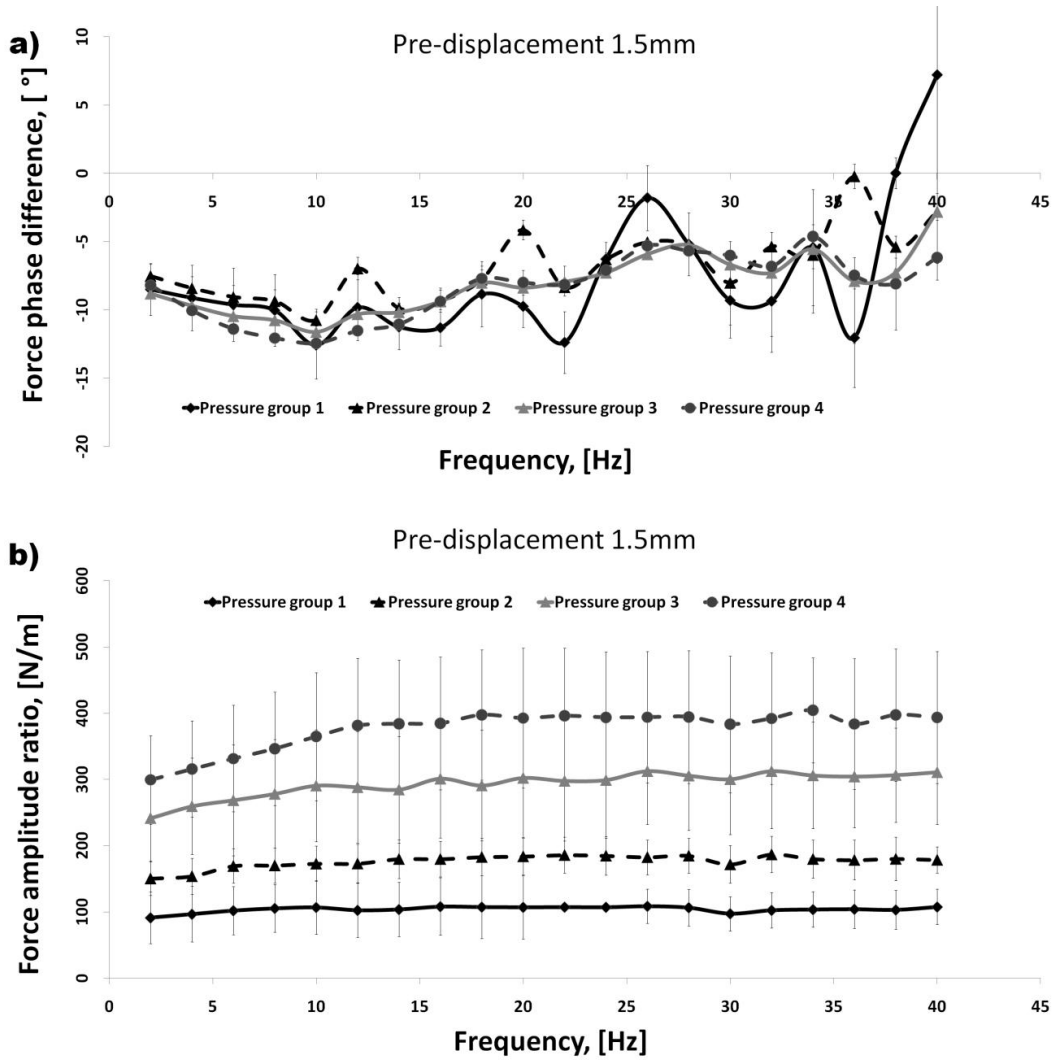

Figure 5-28: Dynamic tests on pig eyes at 1.5mm pre –displacement a) phase difference [°] - b) amplitude ratio [N/m] versus frequency [Hz]

Figure 5-29 shows the phase plots again to facilitate a comparison between the indentation depths at the same IOP. A much clearer difference between the two pre-displacements can be seen for the higher IOP, particularly in the 10Hz range (Figure 5-29b). At the lower IOP the standard deviation of a given point is much larger, especially at frequencies above about 30 Hz.

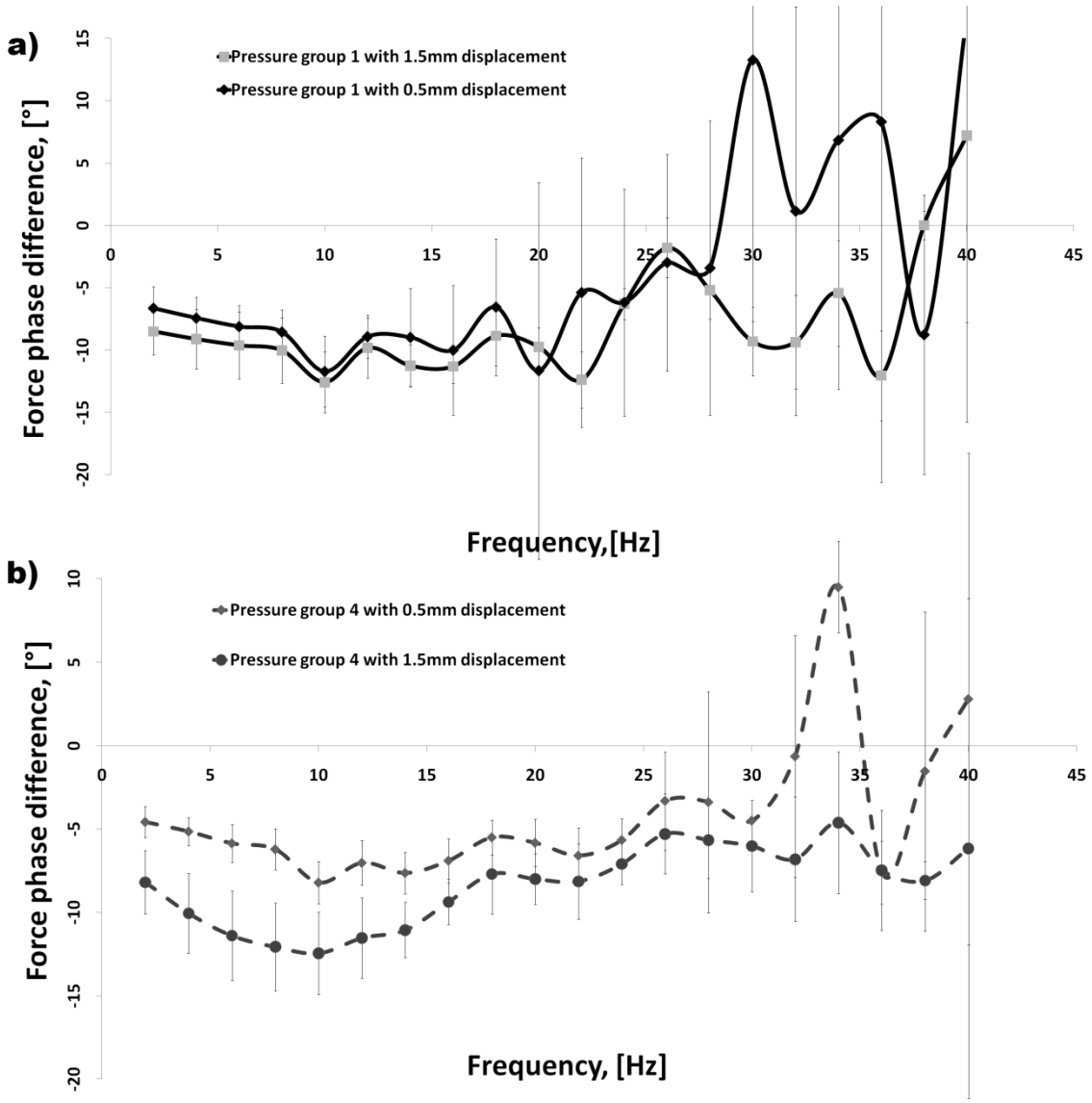

Figure 5-29: Comparison of the phase difference for the two different pre-displacements in dynamic testing of pige eyes

Figure 5-30 shows the amplitude ratio versus IOP (applied pressure) for fresh and frozen pig eyeballs tested at 20Hz with the 1.5mm pre-displacement and for frozen eyeballs tested at 24Hz with a 0.5mm pre-displacement. Both correlations are reasonably good with an R^2 value of about 0.9 and the higher pre-displacement results in a significantly higher slope (a factor of about 2.5 higher).

As before, the intercept of Figure 5-30 is too close to zero compared with the values measured even with the lowest IOP to be able to test whether they extrapolate to the values measured on the freely suspended cornea.

The R^2 of all other linear fits at certain frequencies can be observed in Figure 5-31. This Figure proves that a best linear fit could be achieved in the range between 16Hz and 24Hz for all dynamically tested visco elastic eyeballs. However higher frequencies turned out not to have the best fit, which is again an indicator, that the inertia forces disturbing the force signal.

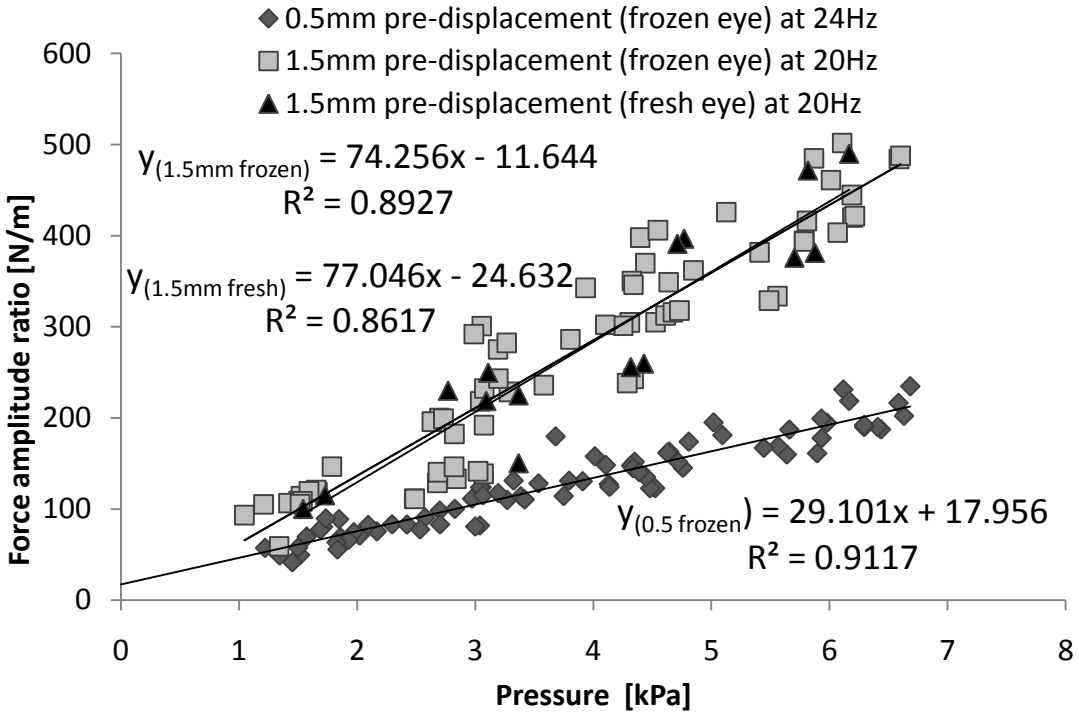

Figure 5-30: Force amplitude ratio [N/m] versus applied pressure (IOP) [kPa] for frozen and fresh eyeballs tested at around 20 Hz with different pre-displacements

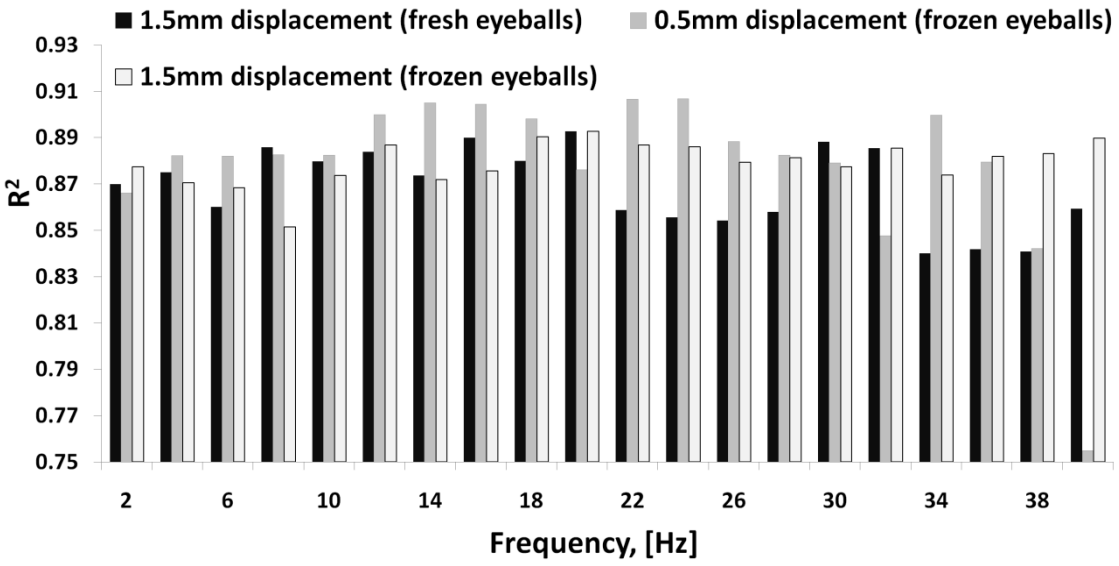

Figure 5-31: Comparison of goodness-of-fit (R^2) of amplitude ratio versus IOP for frozen and fresh eyeballs

Figure 5-32 shows the slope of the pressure phase difference curve as a function of frequency for all applied pressures and for all pre-displacements. The pressure wave starts in phase with the displacement at low frequency but gets out of phase with increasing frequency. Between 30Hz and 40Hz the phase difference starts to settle down which is dependent on the pre-displacement and the different pressure groups. Especially between 30Hz and 40Hz it is to see that higher pressure and higher pre-displacement results in a higher phase difference.

The pressure amplitude (pressure-displacement) as a function of frequency for the different pre-displacements and all pressure groups is to see in Figure 5-33. The slope of all curves behaves similar and starts with a high pressure-amplitude ratio at low frequency. The slope reaches its minimum when the pressure phase difference (Figure 5.32) is between 150° and 240° out of phase and increases thereafter. This behaviour can be related to the friction in the eyeball, which will not allow liquid to be squeezed to the pressure sensor at high frequencies.

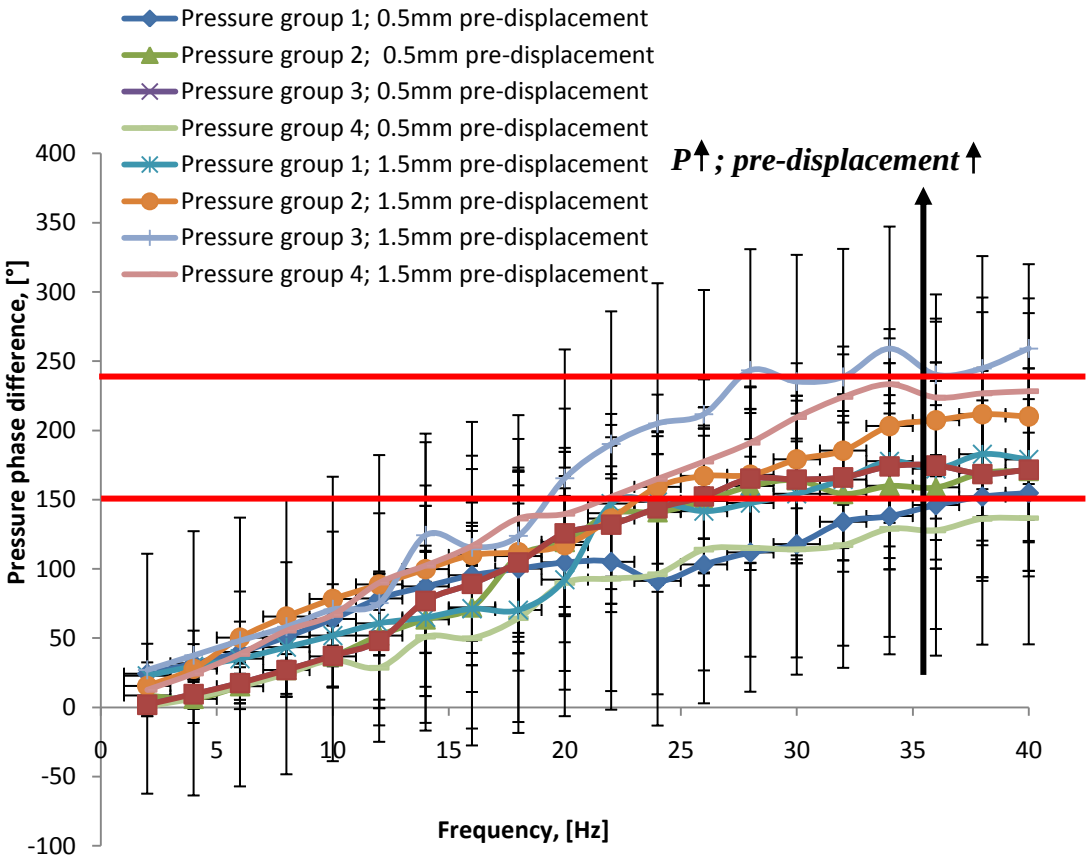

Figure 5-32: Pressure phase difference (pressure-displacement) [°] as a function of frequency [Hz] for all eyeballs tested at different pre-displacement and at different applied pressures

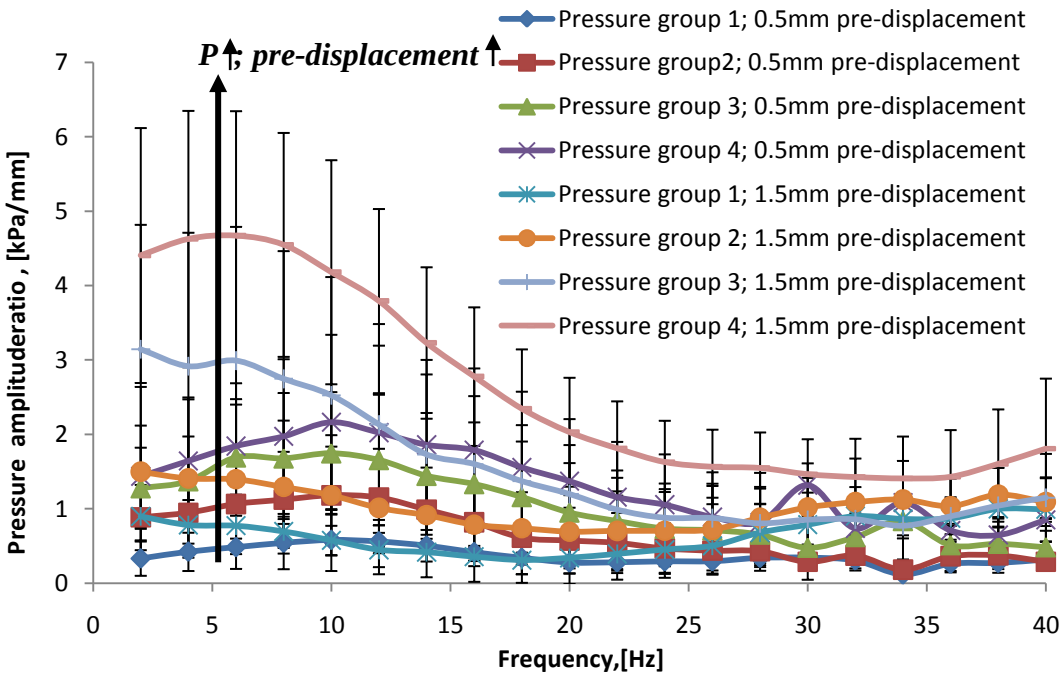

Figure 5-33: Pressure amplitude ratio (pressure-displacement) [kPa/mm] as a function of frequency [Hz] for all eyeballs tested at different pre-displacement and at different applied pressures

5.3 Results for static testing of PDL

Figure 5-34 shows a typical force relaxation curve, of which there were 95 carried out on 4 pig jaws. For this study different indentation depths (initial displacement) with 0.070mm, 0.105mm, 0.175 and 0.245 mm were performed. The time for keeping the initial displacement constant was also varied and was 5sec, 15sec, 25sec and 35sec. The stepping towards the sample was kept constant at 5 ms/step which leads to a velocity of 7 mm/sec. The sequence of testing of all the premolar is listed in Table 4-1. The fitting was done using a least squares algorithm and the goodness-of-fit was recorded as R^2. The relaxation curves were investigated using an 3-parameter model (constant parameter and one exponential function), a 4-parameter model (two exponential functions) and a 5-parameter model (constant parameter and two exponential functions). The equations for these models can be seen in Figure 3.27. The parameter c_s is always used as the parallel spring to the exponential functions and the parameter c_1 and c_2 are always in series with the dashpots d_1 and d_2 respectively.

At the beginning the 3-parameter model was aligned to see the variation between the four pig jaws. The results for each of the three parameters for each of the specimens

were summarized in Figures 5-35 to 5-36. The parameters are reasonably consistent between and within the specimens, and the c_s parameter is clearly lager than c_1 parameter. The viscosity has a much larger scatter than either of the stiffness parameter. However during the observation it was recognised, that the parameters varied more predictably with the initial displacement, and the time for which the initial displacement was applied (allowed relaxation time). It furthermore could been observed that the stiffness parameter were all influenced by the initial displacement and the viscous parameter varied predictably with the allowed relaxation time. Therefore all experiments were separated for allowed relaxation time and for initial displacement. To investigate the damper parameters (d_1 and d_2) of all three applied models (3-,4-and 5-parameter model), all initial displacements were put together and separated for the relaxation time allowed and to investigate the stiffness parameters (c_s, c_1 and c_2) all experiments for varying the allowed relaxation time were put together and the initial displacements were separated.

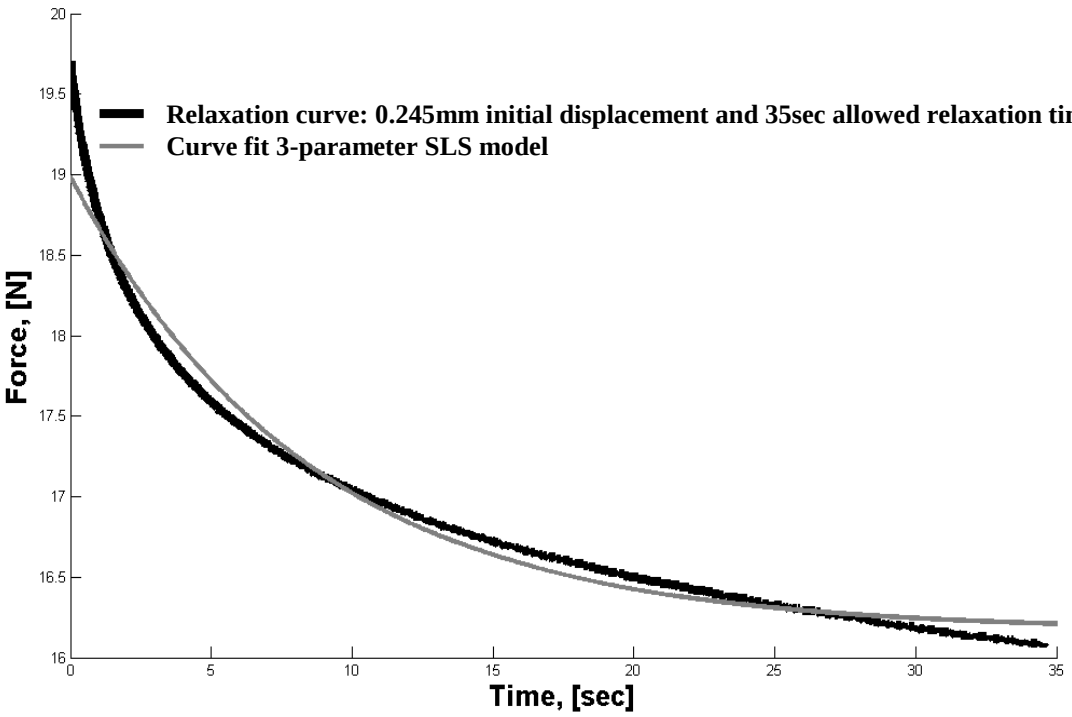

Figure 5-34: Typical force relaxation curve [N] of a deformed pig premolar with initial displacement of 0.245mm and 35 seconds allowed relaxation time [sec] (black curve). The grey curve shows the best fit using a SLS model

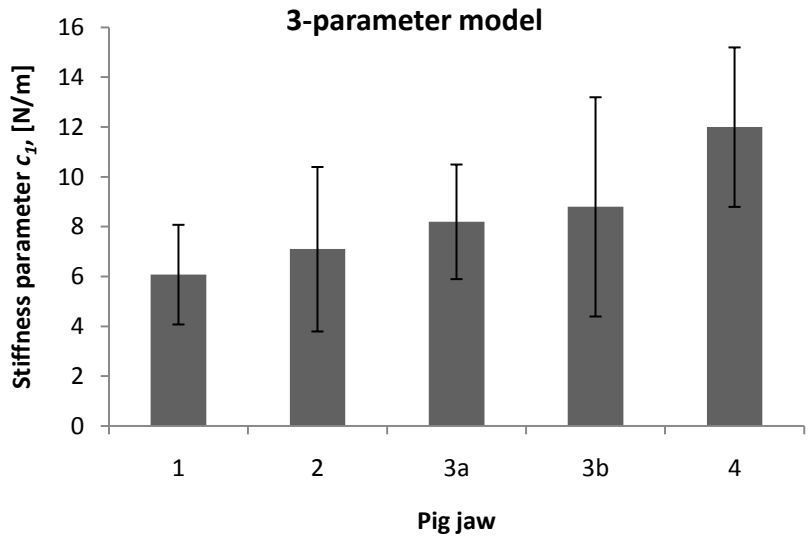

Figure 5-35: Stiffness parameter c_1 [N/m] in the three parameter model applied to different pig mandibles

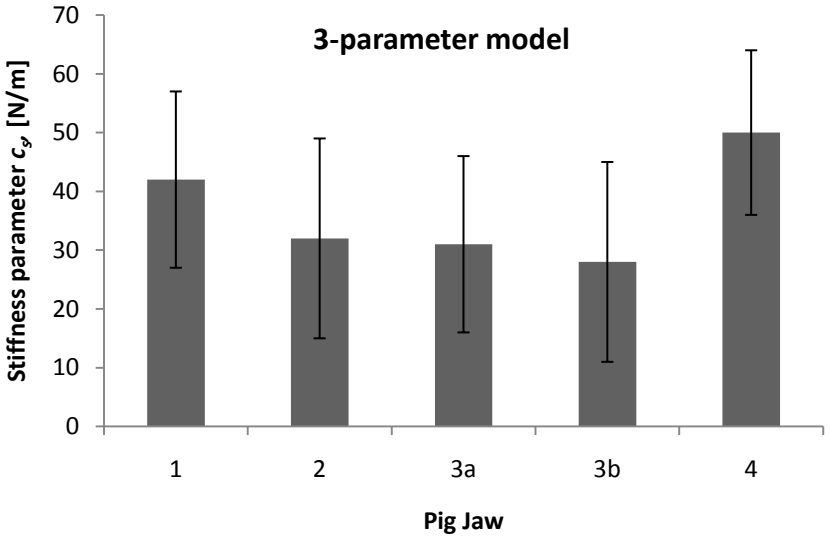

Figure 5-36: Stiffness parameter c_s [N/m] in the three parameter model applied to different pig mandibles

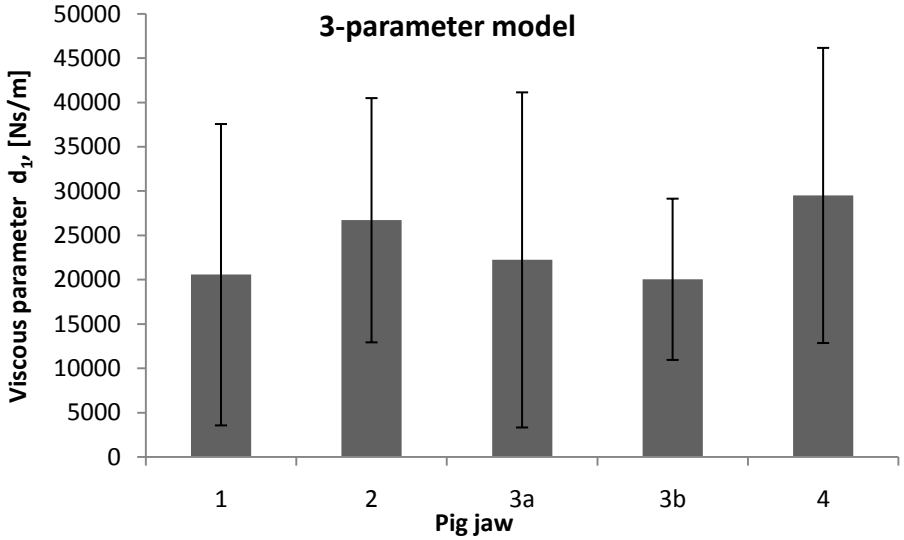

Figure 5-37: Viscous parameter d_1 [Ns/m] in the three parameter model applied to different pig mandibles

The average initial stiffness is seen in Figure 5-38 which is the sum of all in parallel applied springs that will deform at an instantaneous applied displacement. The figure shows the mean of all repeated experiments independent of the allowed relaxation time and its standard deviation. As can be seen, all three models show an increase in initial stiffness with initial displacement until about 0.175mm. The constant parameter with one exponential function has the lowest initial stiffness when fitted to the force relaxation curve, but this is because the model cannot be made to fit both ends of the curve as it is of the wrong shape.

Comparing the goodness-of-fit (R^2) of all models with the data segmented for initial displacement and allowed relaxation time (Figure 5-39 and Figure 5-40). Figure 5-39 shows the mean R2 of all experiments independent of the allowed relaxation time and its standard deviation and Figure 5-40 shows the mean R2 of all experiments independent of the initial displacement. It can be seen that the constant parameter with two exponential functions gives consistently the best fit, followed by the two exponential functions and, finally, the constant parameter with only one exponential function. The variance in the values of the goodness-of-fit independent on the initial stiffness or independent on the allowed relaxation time, reflects the same order. For the constant parameter with one exponential function, R^2 drops with increasing relaxation time, again reflecting its inability to cover the entire curve and highlighting the need for more than one viscous parameter to describe the data.

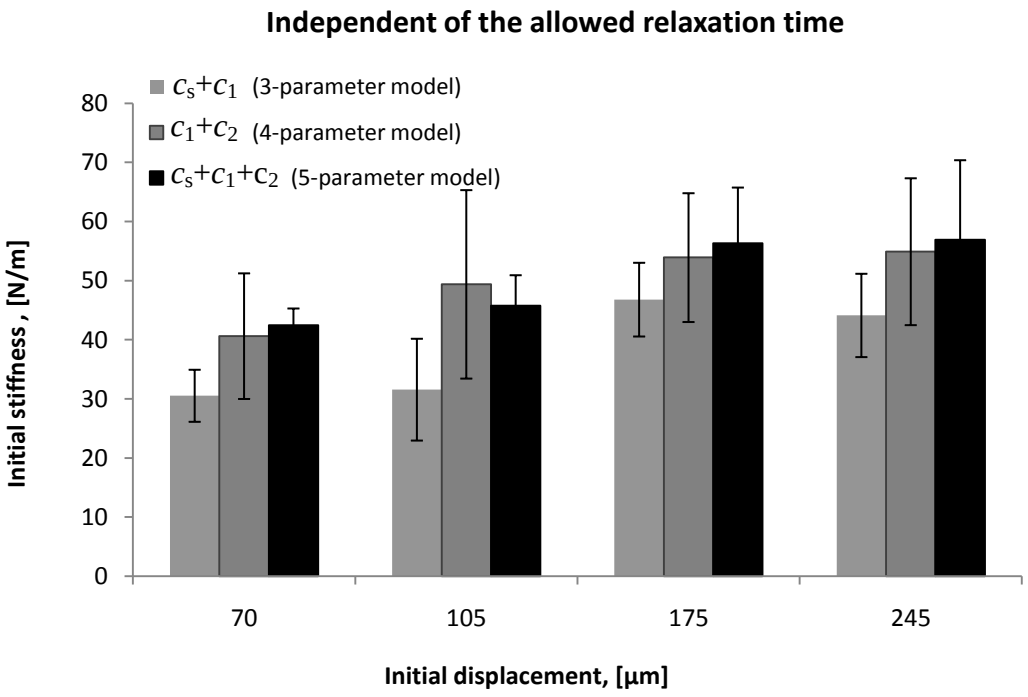

Figure 5-38: Initial stiffness [Ns/m] for the three models independent of the allowed relaxation times as a function of initial displacement [µm]

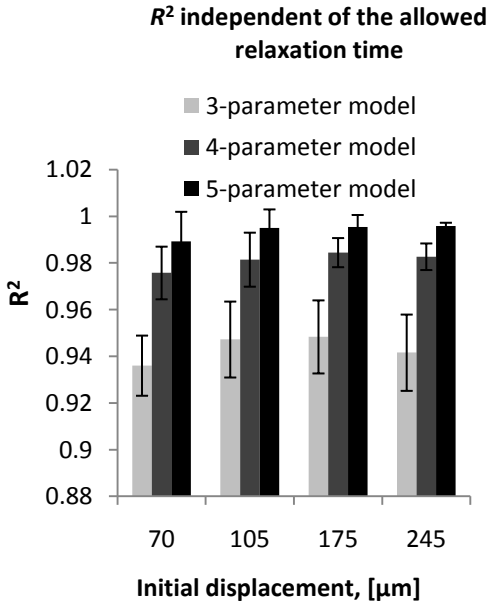

Figure 5-39: R^2 for all three models separated by initial displacement [µm] and independent of the allowed relaxation time

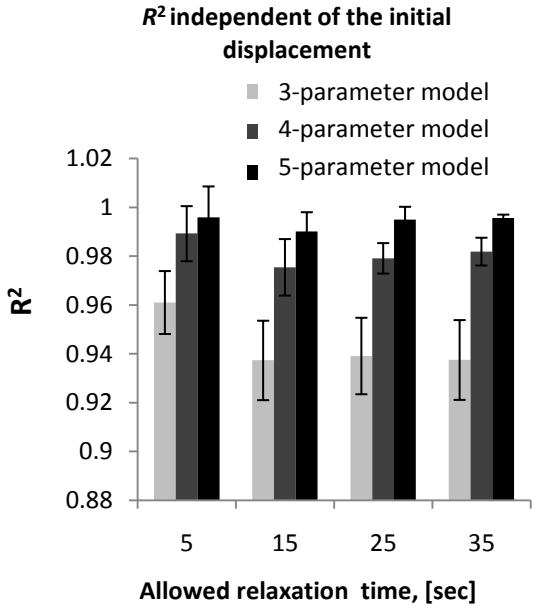

Figure 5-40: R^2 for all three models separated by at different allowed relaxation time [sec] and independent of the initial displacement

The retardation time is the ratio of viscous to spring parameter *d*/*c* of a single Maxwell element, and indicates how quickly the Maxwell will relax. The retardation time d_1/c_1 for all models independent of the initial displacement is less than 10 seconds (Figure 5-

41), and is significantly higher for the constant parameter with one exponential function than for the remaining two models. For all of the models, the first retardation time increases with allowed relaxation time, although the increase is much greater for the model with only one exponential function than for the other 2.

The second retardation time d_2/c_2 (for the two exponential functions and the constant parameter with two exponential functions only) also increases with allowed relaxation time (Figure 5-42), indicating that there is probably a third (or more) retardation time in the system. It should be noted that the two retardation times for both models are very different in magnitude and that the changes are much greater with relaxation time (logarithmic scale in Figure 5-42).

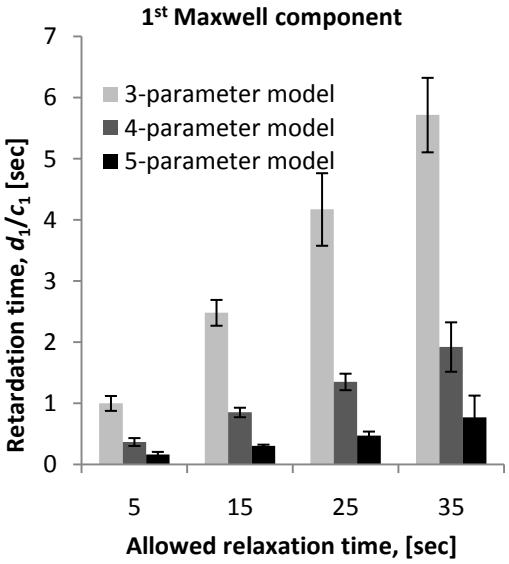

Figure 5-41: Retardation time d_1/c_1 [sec]of the 1st Maxwell component for PDL applied to different relaxation times [sec] for the three different models

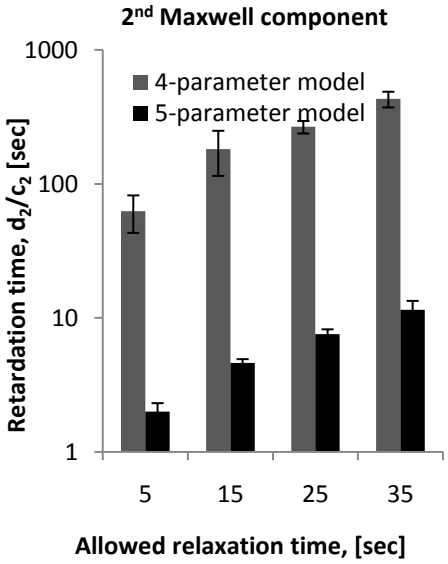

Figure 5-42: Retardation time d_2/c_2 [sec]of the 2nd Maxwell component for PDL applied to different relaxation times [sec] for 4-and 5-parameter model

It should be noted that the experiments were done randomly in a sequence listed in Table 4-1. After separating the complete data set of all initial displacements with all relaxation times allowed it can be seen that not each initial displacements was done with each relaxation times allowed (Table 5-4). However to see the influence of initial displacement on the retardation time it is possible to use the 107µm initial displacement with relaxation times allowed of 5s, 15s and 25s, and to see the influence of allowed

relaxation time on the initial stiffness, the 5 seconds allowed relaxation time can be used with varying initial displacement of 107µm, 175µm and 245µm.

The average initial stiffness with the standard deviation for all repeated experiments for the 105µm initial displacement for varying the allowed relaxation time is to see in Figure 5-43 and seems to be consistent for different relaxation times. The 3-parameter model again is lowest compared with the other 2 models. Figure 5-44 and Figure 5-45 show the average retardation times with the standard deviation of all repeated experiments. Figure 5-44 includes the retardation time d_1/c_1 for all models for a 5 seconds allowed relaxation time in relation to the initial displacement and Figure 5-45 includes the retardation time d_2/c_2 for the 4-and 5-parameter model for a 5 seconds allowed relaxation time in relation to the initial displacement. Between the models, the same behaviour appears as to see in Figure 5-41 and Figure 5-42 respectively. However increasing the initial displacement slightly increases the retardation time d_1/c_1 of all models (Figure 5-44) which is again more dominant for the 3-parameter model. This could not been proven with the second retardation time d_2/c_2 for the 4-and 5-parameter model (Figure 5-45).

Allowed relaxation time / Initial displacement	5s	15s	25s	35s
70µm	-	✓	-	-
107µm	✓	✓	✓	-
175µm	✓	-	✓	-
245µm	✓	-	-	✓

Table 5-4: All PDL experiments categorised for initial displacement and allowed relaxation time

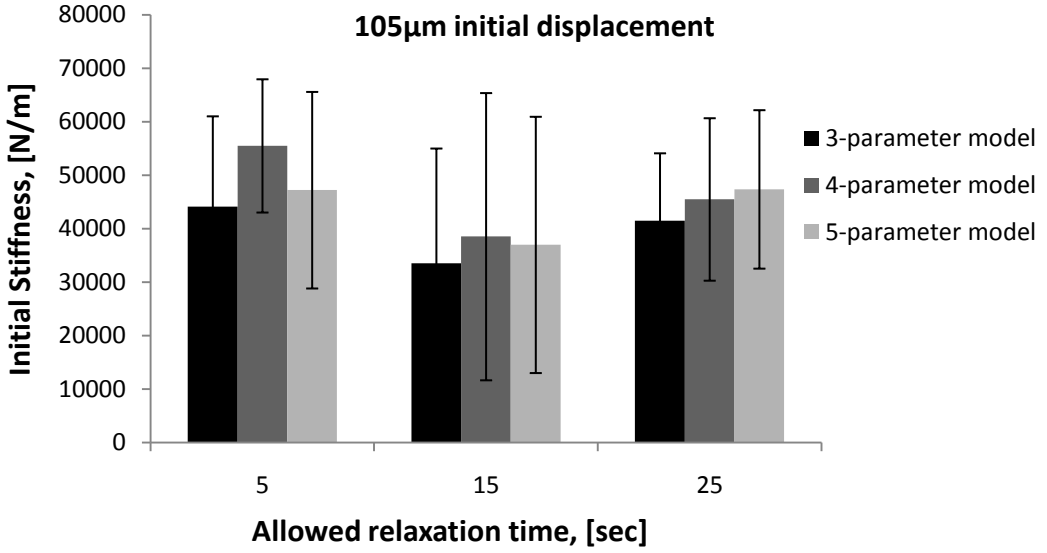

Figure 5-43: Initial stiffness [N/m] for 105µm initial displacement in related to the allowed relaxation time [sec] for all three model

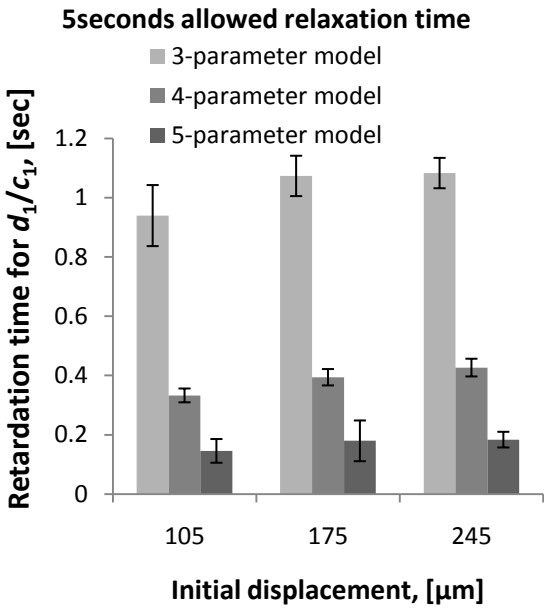

Figure 5-44: Retardation time d_1/c_1 [sec] for 5seconds allowed relaxation time in relation to varying initial displacement [µm]

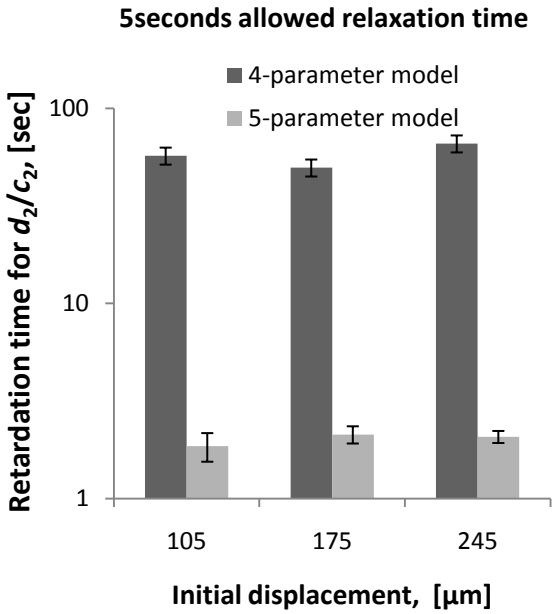

Figure 5-45: Retardation time d_2/c_2 [sec] for 5seconds allowed relaxation time in relation to varying initial displacement [µm]

Reflecting the observations on initial stiffness and retardation time, two effects appeared to be consistent for the individual parameters for all of the models. The first is the pre-displacement affected the stiffness parameters much more significantly than the viscous parameters. The second is that the allowed relaxation time affected the viscous parameters much more than the stiffness parameters. Therefore, in the following, the *c*

parameters are only segmented per initial displacement and the *d* parameters are only segmented per allowed relaxation time. A summary of the parameters for each model is presented thus in Figures 5-46 to 5-48.

The models which have a single spring in parallel to the Maxwell model(s) (3-and 5-parameter model) show a clear increase in c_s with increasing initial displacement. This trend is more distinctive for the 5-parameter model as the error bars are much smaller. In the 4-parameter model, one of the Maxwell stiffness parameters (c_1) has to serve to increase with initial displacement although this is accompanied by a degradation of the quality of fit, reflected in a high variance of the parameter. The fact that these parameters (c_s for 3-and 5-parameter model c_1 for 4-parameter model) are performing the same function in fitting the data can be seen by the fact that their values are essentially the same (around 40kN/m), albeit with different variances. The remaining stiffness parameters for all of the models do not change with initial displacement and have values less than 10kN/m.

All of the dashpot parameters increase with increasing allowed relaxation time. However the parameter values are very sensitive to the model used, with the 3-parameter model showing generally the lowest values with the lowest variations. The addition of the extra fully functional viscous parameter in the 5-parameter model allows them to be identifiably different and to be relatively stable with allowed relaxation time. The values of the viscous parameters are rendered somewhat unstable in the 4-parameter model (logarithmic scale), probably because one of the damped springs has to perform an additional function.

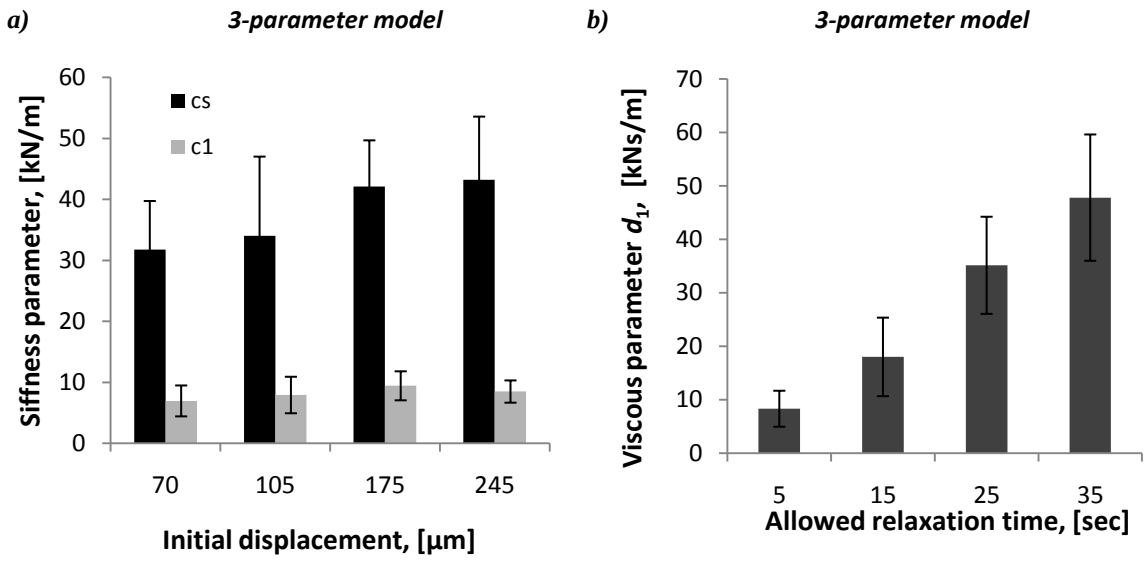

Figure 5-46: 3-parameter model parameters for PDL a) stiffness parameter(c_s and c_1) [kN/m] separated per displacement [µm] and b) viscous parameter d_1 [kNs/m] separated per allowed relaxation time [sec]

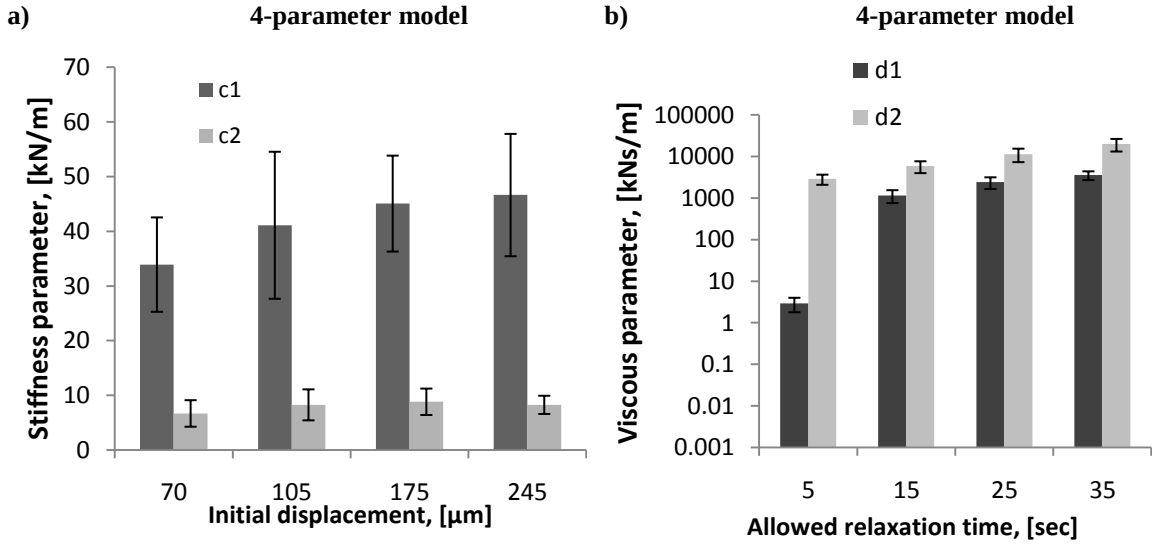

Figure 5-47: 4-parametrer model parameters for PDL a) stiffness parameter (c_1 and c_2) [kN/m] separated per displacement [µm] and b) viscous parameters (d_1 and d_2) [Ns/m] separated per allowed relaxation time [sec]

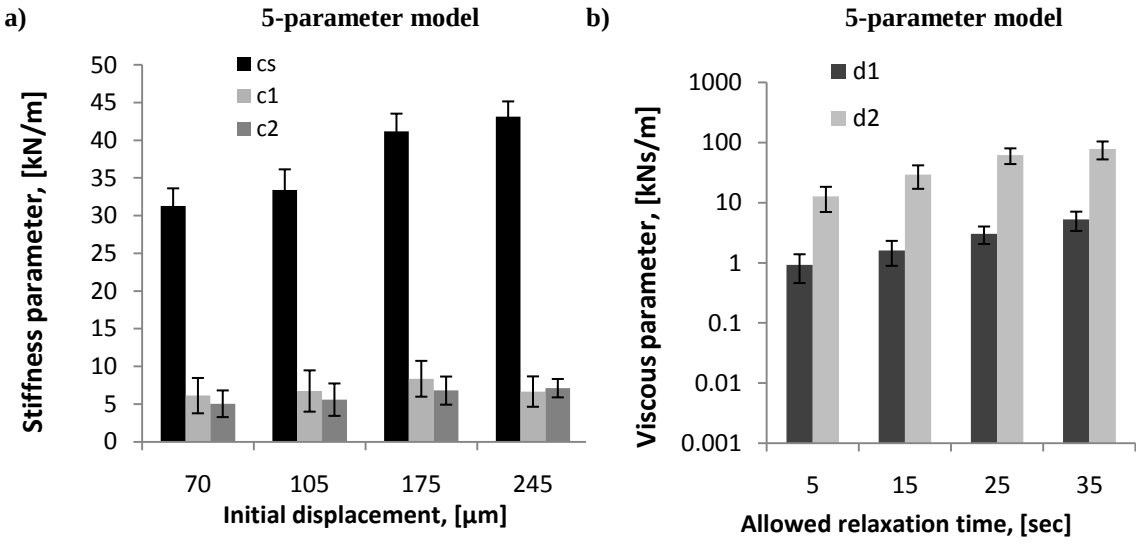

Figure 5-48: 5-parameter model parameters for PDL a) stiffness parameters (c_s, c_1 and c_2) [kN/m] separated per displacement [µm] and b) viscous parameter (d_1 and d_2) [Ns/m] separated per allowed relaxation time [sec]

Chapter 6: Discussion

This chapter discusses the significance of the experimental measurements and is presented in four areas.

Firstly, the mechanical eyeball is discussed in terms of its usefulness to identify the contributions of IOP, cornea and drainage effects in a real eyeball *in vivo* by using dynamic palpation and more generally, on how dynamic palpation can be used to separate the contributions from components which are more fluid-dominated from those which are more solid-dominated in multi-component biological architectures. Therefore the results in the result section were investigated, curve fits of certain QLV models were applied and the parameters were used to separate IOP from CCT.

The second section deals with how the results from the mechanical eyeball and those from the porcine eyeball can be combined using the damper parameter to address the potential for enhanced IOP measurement.

Next, the clinical application of *in situ* measurements on human teeth is assessed.

Finally, the general contribution in the area of soft tissue mechanical properties is discussed, focussing on the mechanical properties measured and how these compare with the work of other authors.

6.1 Mechanical eyeball

As long ago as 1965, Sticksel [85] reported that the indentation method introduced by Schoitz to measure true IOP is affected more by CCT and cornea rigidity than is the applanation method. Further, all of the new approaches that have been advocated so far have aimed at reducing the effect of CCT and cornea stiffness, albeit with limited success [63, 88-90, 96]. It was hoped at the outset of the current research that the added dimension of frequency in dynamic palpation would allow a separation of the effects of the cornea and of IOP on the palpation resistance. It has been observed elsewhere that the cornea behaves in a visco elastic fashion at lower frequencies and the aqueous humour in the eye resonates at about 35Hz [39, 97]. It was envisaged that a dynamic indentation method could probe the eyeball while sweeping through a range of frequencies and so separate out cornea properties and fluid structure interaction effects. Whilst the mechanical eyeball is not a perfect simulation of a real eyeball, it was expected that controlling the individual components would offer the ability to make systematic changes to the dynamic response. Hence, with the help of a visco elastic model to characterise the results, it would, in principle, be possible to attribute the model parameters to the systematic changes.

The results for force amplitude ratio and phase difference were indeed found to change with frequency, thus indicating visco elastic behaviour. The simplest SLS model from Chapter 3 was fitted to the data on the principle that the fewer parameters that were used, the more likely each would be to characterise the system. The phase difference varied much more weakly with frequency and so the parameters found from the amplitude ratio were applied to the phase difference curves for error estimation and compatibility assessment rather than using them directly to determine the model parameters. Tables 6-1 and 6-2 show the parameters c_s, c_M and d_M with the 95% confidence limits for the amplitude ratio along with the R^2 value for both phase and amplitude ratio for the open-ambient and closed-pressurised configurations, respectively. The amplitude ratio was plotted in Matlab where a least squares algorithm was applied to the curves using the dynamic equations for amplitude ratio from Table 3-1. As can be seen, all of the c_s values in Table 6-1 and Table 6-2 increase both with increasing membrane thickness and with increasing pre-pressure. The c_M parameter does not vary significantly (considering the confidence interval) with membrane

thickness for the open-ambient configuration, but increases with membrane thickness in the closed-pressurised configuration. The only parameter that seems to be affected by the membrane thickness alone for both open-ambient and closed-pressurised configurations, even without knowing the reason for it, is the damping parameter d_M, see Figure 6-1 which can be encapsulated in the following:

$$t = 0.4 \cdot \ln(6.79 * d_M) \quad (6\text{-}1)$$

where t is the membrane thickeness.

membrane thickness	**0.4mm**	**0.6mm**	**1.0mm**
c_s,[kN/m] 95% c-bound	**0.25** **0.25 – 0.26**	**0.54** **0.53-0.54**	**2.1** **2.1 – 2.1**
c_M,[N/m] 95% c-bound	**511** **0 – 1500**	**320** **150 – 489**	**477** **322 - 631**
$d_{M.}$,[Ns/m] 95% c-bound	**0.44** **0.29 – 0.50**	**0.55** **0.49 – 0.6**	**1.5** **1.18 – 1.8**
R^2 (amplitude ratio)	**0.96**	**0.97**	**0.95**
R^2 from phase	**0.56**	**0.67**	**0.54**

Table 6-1: Parameters from the SLS model applied to the open-ambient configuration

membrane thickness	**0.4mm**		**0.6mm**		**1.0mm**	
pre-applied pressure	**1.8kPa**	**3.3kPa**	**1.8kPa**	**3.3kPa**	**1.8kPa**	**3.3kPa**
c_s,[kN/m] **95% c-bound**	**0.50** **0.48-0.50**	**0.53** **0.52–0.54**	**0.94** **0.93 – 0.94**	**1.06** **1.05 – 1.07**	**3.99** **3.96 – 4.02**	**4.03** **4.00 – 4.06**
c_M,[N/m] **95% c-bound**	**87** **69 – 104**	**78** **58 - 98**	**492** **0 – 1169**	**638** **0 – 2151**	**807** **533 – 1082**	**814.4** **541 – 1088**
$d_{M.}$,[Ns/m] **95% c-bound**	**0.43** **0.31 – 0.56**	**0.37** **0.25 0.47**	**0.64** **0.4 – 0.88**	**0.748** **0.34 – 1.25**	**2.19** **1.99 – 2.39**	**2.22** **2.02 – 2.42**
R^2 (amplitude ratio)	**0.87**	**0.85**	**0.93**	**0.88**	**0.94**	**0.95**
R^2 from phase	**0.66**	**0.74**	**0.56**	**0.64**	**0.49**	**0.43**

Table 6-2: Parameters from the SLS model applied to the closed-pressurised configuration

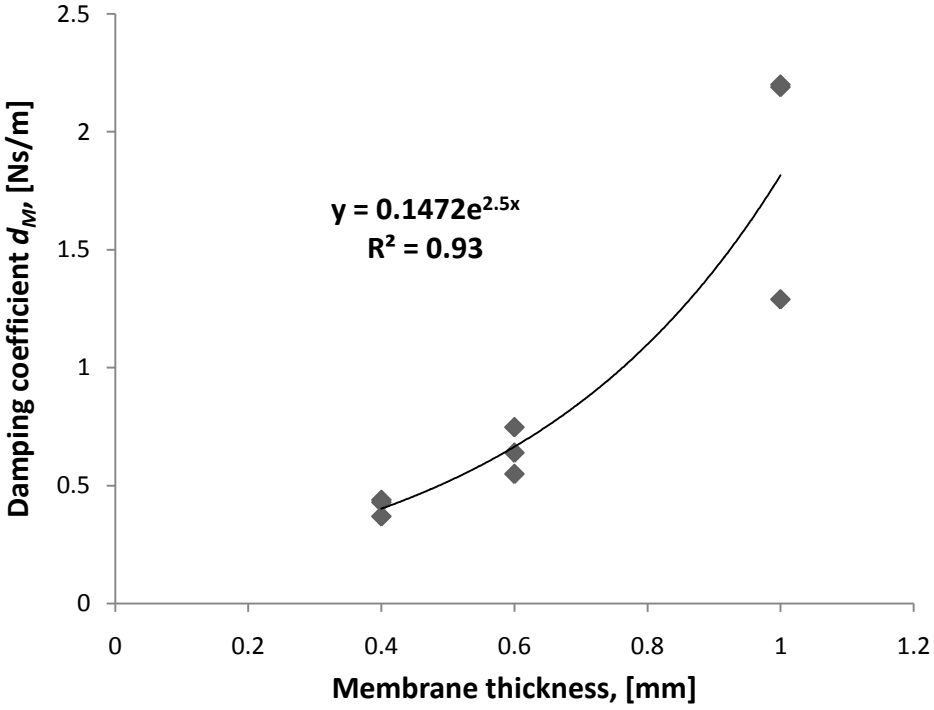

Figure 6-1: Relationship between damping coefficient d_M and membrane thickness for closed-pressurised and open-ambient configurations.

The open-ambient configuration, where the membrane was suspended over the mechanical eyeball cavity, allowed an independent measurement of the large-deflection bending of the membrane. Equation (6-2) [184] describes the large-deflection behaviour of an elastic spherical shell of radius *R* attached to a circular annular plate, which is clamped at the edges at radius *a* with a concentrated load *F* applied at the centre [185]:

$$d = \frac{F^2 R^2}{0.32\pi^2 E^2 t^5} + \frac{kFa^2}{Et^3} \tag{6-2}$$

where *d* is the indentation depth and *k* is a constant which depends on *a*/*R* (here equal to the radius of the dome). The constant *k* was taken to be 0.0242, derived from the values established by Wahl and Lobo [186] and later rearranged in [185]. The first term represents the deformation of the elastic shell [184] and the second represents the deformation of the annular plate [185].

Solving equation (6-2) for the force, *F*, under a given displacement, yields two solutions, only one of which is real and positive and hence suitable.

$$F_{1/2} = \frac{-\left[3.2ka^2 \pm \sqrt{9.61k^2a^4 + 12.8R^2d \cdot t}\right]t^2E}{2R^2} \quad (6\text{-}3)$$

Figure 6-2 compares the mean force values calculated using equation (6-3) with E = 6MPa (value supplied by Honigum from DMG Chemisch-Pharmazeutische Fabrik GmbH) for a deflection of 0.5mm for the three thicknesses, with the experimental values for the open-ambient and closed-pressurised configurations. The measured force includes the pressure in the cavity (pressure × probe area) but this contribution is negligible, being about 10 times smaller than the measurement for the 0.4mm thick membrane thickness and around 120 times smaller for the 1.0mm thick membrane.

As can be seen in Figure 6-2, the results for the mean force in the open-ambient configuration (where no pressure was used) are in good agreement with equation (6-3). Pressurising the membrane and increasing the pressure, the membrane strain increases, which increases the effective stiffness [62], although, from equation (6-3), the force would still be expected to increase with $t^{2.5}$. All of the data can therefore be conveniently summarised using a constant p_k, where:

$$F = p_k \cdot t^{2.5} \quad (6\text{-}4)$$

giving values of p_k of 0.93, 1.32 and 1.54 for open-ambient, and closed-pressurised at 1.8kPa and 3.3kPa, respectively. The rate of increase of p_k with pressure decreases at higher pressures. Plotting the p_k values and fitting an exponential function gives an expression for the true IOP (pre-pressure) in the cavity.

$$p_k = f - l \cdot exp[-c \cdot IOP] \quad (6\text{-}5)$$

Solving this equation for IOP gives:

$$IOP = -\frac{\ln\left[\frac{-p_k + f}{l}\right]}{c} \quad (6\text{-}6)$$

where f, l and c are constants with values 2.06, 1.13 and 0.24 respectively as shown in Figure 6-3. Using this equation and the damper parameter, d_M, the true IOP can be measured in relation to the membrane thickness with a predictive capability of ±0.8kPa.

However these values are based on the mechanical eyeball configurations and new constants (*f*, *l* and *c*) have to be found for the pig eyes.

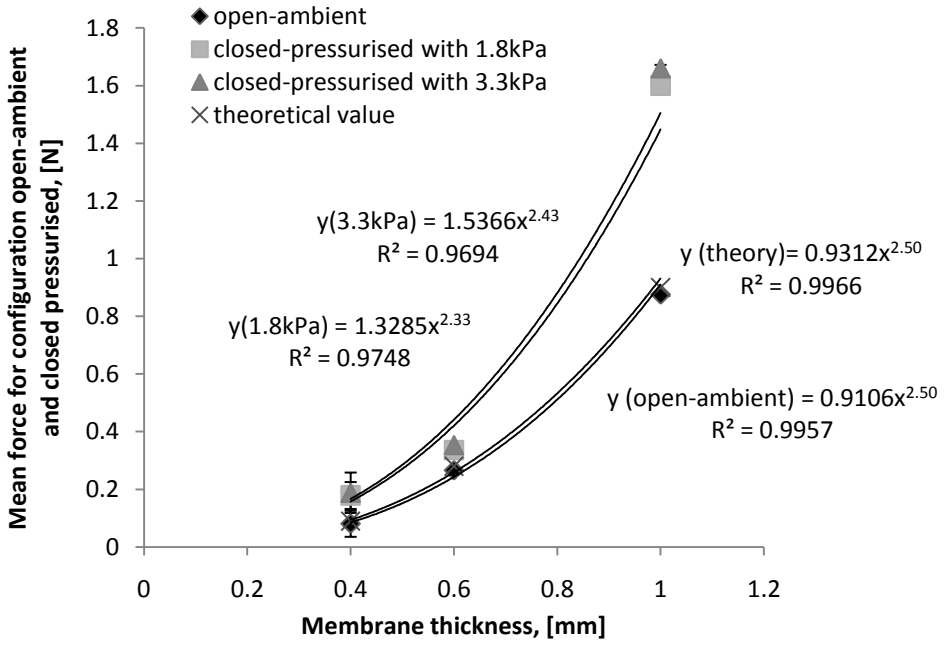

Figure 6-2: Measured and calcuated mean force at a displacement of 0.5mm versus membrane thickness

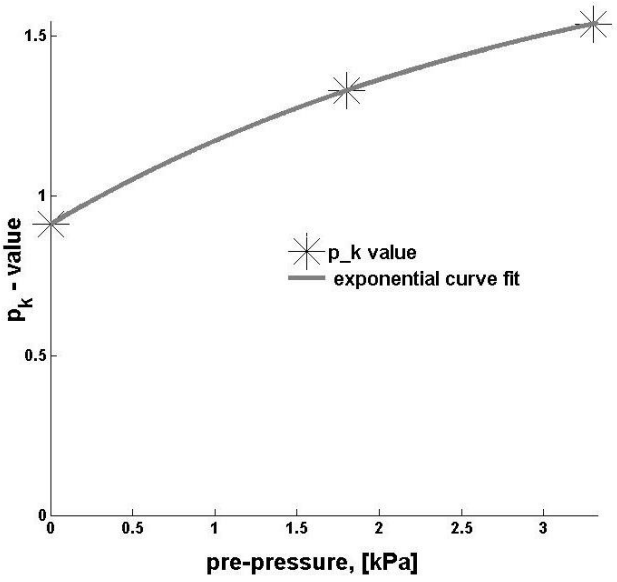

Figure 6-3:Variation of the parameter p_k with the pre-applied pressure and associated exponential curve fit.

The choked-pressurised system represents a complex coupled fluid-structure interaction, and this can be investigated through the pressure measurements as well as the force measurements, although in practice only the latter would be available. The mean

pressure for all choked-pressurised experiments was precisely the applied pre-pressure throughout the whole frequency bandwidth and shows that the dynamic pressure oscillates around the pre-set pressure. The different orifice sizes did not affect the force mean ratio (Figure 5-3a), but the membrane thicknesses and pre-pressure both did. This was expected in so far as the orifice size was big and the water column height forces the liquid to move back to the anterior chamber, which will not be the case in the drainage channels in real eyes. This shows again that the static force is dependent on the rigidity of the membrane and also the pressure in the cavity, something that was observed by Goldman [5] for palpating real cornea tissue.

The dynamic response of both pressure and force in the choked-pressurised experiments is summarised in Figures 5-9 and 5-10, a feature of which is what appear to be resonance peaks in the 40 to 60Hz range, one for each experiment. A single degree-of-freedom mass spring damper model (series model with displacement excitation of parallel elements, Figure 3-19) gives a maximum amplitude which depends heavily on the damping coefficient. The damping coefficient can be identified in this system with friction of the liquid passing through the orifice since the smaller orifice sizes gave rise to smaller resonance amplitudes for a given membrane thickness and pre-pressure. Thicker (stiffer) membranes can displace more liquid and so the pressure waves have more energy resulting in higher amplitudes at resonance for a given orifice size and pre-pressure. After resonance, the choked-pressurised and the closed-pressurised configurations show similar force amplitudes where the choke is no longer able to accommodate the flow rates and so the system behaves as if closed. Furthermore decreasing the orifice size decreases the resonance frequency (Figure 6-4) and, given that the system behaves like the closed-pressurised configuration beyond the resonance, this strongly suggests that pig eyeballs (and, indeed, human eyeballs) will behave more like the closed-pressurised configuration at the frequencies used here, because the drainage pathway through iris and lens is only around 5μm in size [43, 45].

Given the above observations, it might be expected that the phase lag between force or pressure and displacement might be due to pulses reflecting on the water surface, on the tube walls or on the orifice ("water hammer"). The speed, c, of waves would then change with orifice size and water column height, since pressure changes and friction in the orifice affect the wave propagation. In plastic pipes, visco elastic behaviour of the

wall material is also known to influence the wave dynamics [187, 188] an effect that will be emphasised here with the soft visco elastic membrane. One resonance might be expected where the period of the oscillation synchronises with some multiple of the fundamental *4L/c*, where *L* is the length of the water tube and *c* the speed of waves in the tube [189]. This would give a resonant frequency ω_0 of:

$$\omega_0 = 0.785 \cdot \frac{c}{L} \tag{6-7}$$

However, for this coupled fluid–structure problem, the situation will be a deal more complex and, given that the configuration is somewhat artificial, a precise quantitative mathematical definition is not worthwhile.

Fitting a one DOF mass spring damper model to the amplitude ratio results yielded the values shown in Figure 6-5 where the best fit R^2 of all curves was between 0.99 and 0.92.

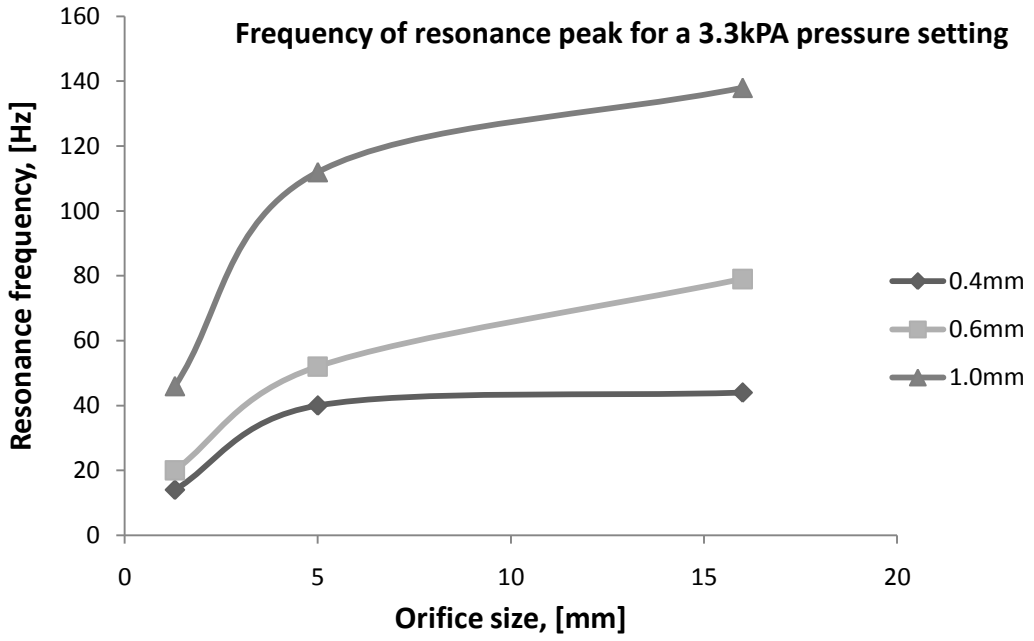

Figure 6-4: Frequency of the resonance peak for different membrane thicknesses versus orifice size for a pressure setting of 3.3kPa

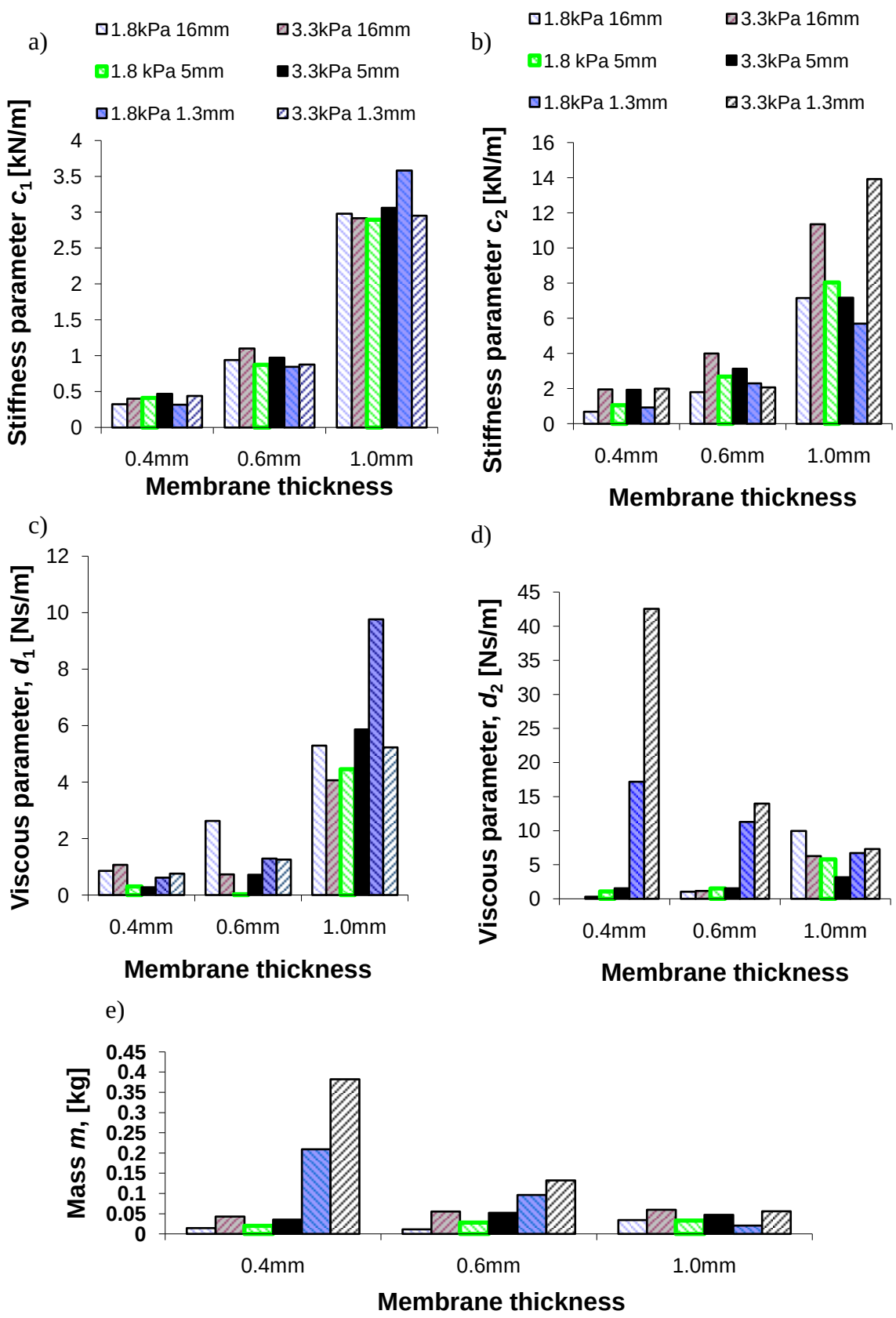

Figure 6-5: All parameters ($c_{1/2}$, $d_{1/2}$ and m) of the one degree of freedom MSD model (combination spring – dashpot in parallel – displacement excitation) applied to the mechanical eyeball results

Fitting the expression for the phase difference is rather difficult as the moving mass produces a phase shift through several quadrants, and the tangent passes through $\pm\infty$ every 90°. For this reason, the parameters obtained from the amplitude ratio fits were calculated using equation (3-90), and Figure 6-6 shows an example of the calculated and measured force-displacement phase differences for the 0.4 mm thick membrane with a 5mm orifice at 1.8kPa pressure. The best fit R^2 of all phase difference curves smaller than -90˚ were between 0.7 and 0.9.

The good fits to the phase plots confirm that the parameters shown in Figure 6-5 represent the results acceptably and that the model is suitable. The model describes a fluid mass whose freedom of movement under certain conditions can lead to resonance. Higher pressures were generated by a higher water column and therefore more liquid mass, clearly seen in Figure 6-5e) where all the 1.8kPa tests have a lower mass than the 3.3kPa ones. Damper d_2 represents the friction in the orifice, and, accordingly, decreases as the orifice size increases for a given pressure and membrane thickness, although the effect becomes less pronounced as the membrane thickness increases, Figure 6-5d). The parameters c_1, c_2 and d_1 (Figure 6-5 a, b, c), all increase substantially with membrane thickness and therefore appear to be good indicators of the visco elastic behaviour of the membrane itself. The parameters c_1 and c_2 are particularly insensitive to orifice size and pressure and potentially can be used to identify the membrane stiffness without being affected by IOP.

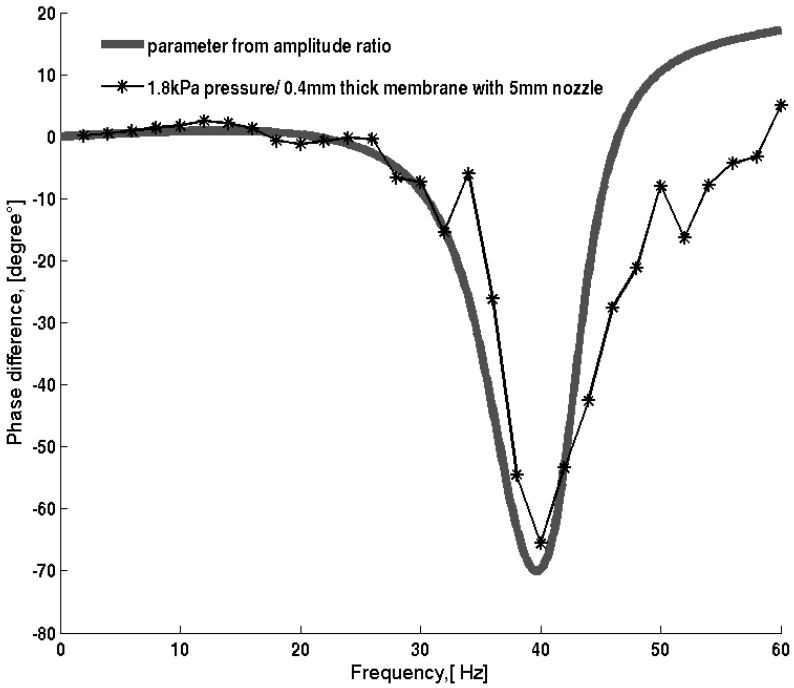

Figure 6-6: Comparison of example measured force-displacement phase difference (*) with values calculated using the paramenets obtained from from the coresponding amplitude ratioresults.

6.2 Pig eyeballs

The pig eyeballs were tested statically and dynamically and QLV models were fitted to the results of both experiments. The static test was used to make comparisons of initial stiffness and retardation time with other literature and to explain differences in retardation time. The dynamic results allowed some conclusions to be drawn about the applicability of the dynamic test.

6.2.1 Static tests

As described in Chapter 5 the static test results for 3sec and 10sec relaxation time were fitted to the SLS model and those for 10sec relaxation time were fitted to the five parameter model in order to assess if a better fit could be obtained with multiple relaxation times. The substantial improvement in fit with the five parameter model suggests that single relaxation time models (i.e. three-parameter models) are unlikely to be suitable for describing such systems, unless over a limited range of test times. This has implications for the selection of test frequencies for such systems as discussed later.

Aherne *et al.* [153] measured the force relaxation under a predetermined displacement of clamped human and porcine corneas (Figure 6-7) and fitted the relaxation curve to Fung's [9] quasi visco elastic model:

$$g(t) = A_0 + A_1 e^{\frac{-t}{\tau_1}} + A_2 e^{\frac{-t}{\tau_2}} \tag{6-8}$$

which is essentially a 5 parameter two-component Maxwell model. The instantaneous displacement was 0.5mm and the corresponding force at time *t*=0 was 10.3mN, giving an initial stiffness of 20.6N/m. The values of the retardation times τ_1 and τ_2 were in the range of 100sec and 1000sec, respectively, whereas the relaxation times d_1/c_1 and d_2/c_2 from the 5-parameter model in this work were in the range of 0.4 sec and 5 sec, respectively. The reason for this big difference is clearly to do with the allowed relaxation times, about 7000 sec for Aherne *et al.* compared with about 10 sec in this work. On closer examination of the force relaxation plot from the study of Aherne *et al.* (Figure 6-8), it can be seen that, whereas the fit is generally good, the curve does not fit well to the first 10 sec. Combining their model (which is nothing else as a 5-parameter

model) with the five parameter model of this work would result in a 10 parameter model which would be able to describe the first 10sec as well as the following 6990 sec. This reinforces the observation made earlier about the range of applicability of multi-component visco elastic models.

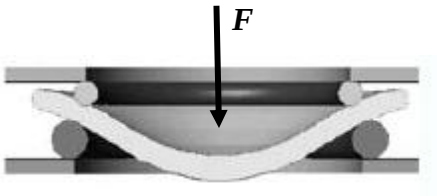

Figure 6-7: Clamped cornea and the direction of testing from Aherne *et al.* [153]

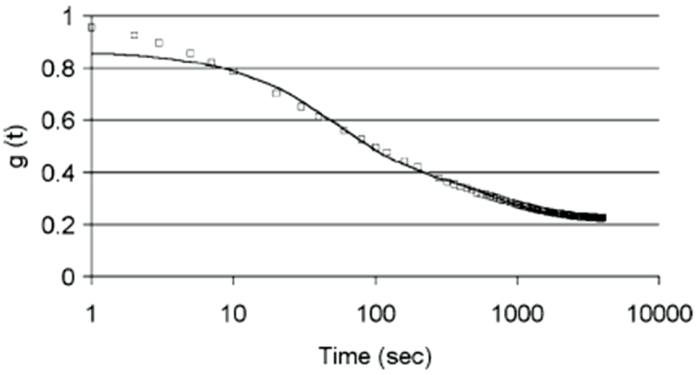

Figure 6-8: Normalised force relaxation curve from Aherne *et al.* where the white squares show the experimental results and the black line shows the fitted curve [153]

Within the current work, comparing the open system, with the closed system, shows force relaxation characteristics (Figure 6-9) for all SLS (3-parameter) models. But it also shows that the SLS model is not sufficient to explain multiple relaxation times which seem to act on the cornea (long relaxation time for d_2/c_2). This means that the relaxation in the closed system can be attributed to relaxation of the cornea rather than liquid leakage. Fitting the SLS model to the 10sec allowed relaxation time always gives a higher relaxation time compared to the fits where only 3sec relaxation time was allowed. Here, again, the 10sec allowed relaxation time the curve fit aligns more to the longer times, and, in all cases, both of the relaxation times (3sec and 10sec allowed time) from the SLS model lie between the first and second relaxation times of the 5-parameter model, confirming the need for higher order models. Also, whereas the SLS model parameters cannot differentiate between the open system and the closed system or between the different velocities, the five parameter model does so through its d_1 parameter (Figure 5-18). This illustrates the advantage of the dynamic test which

allows an examination of separate relaxation components by appropriate choice of the frequency bandwidth for testing.

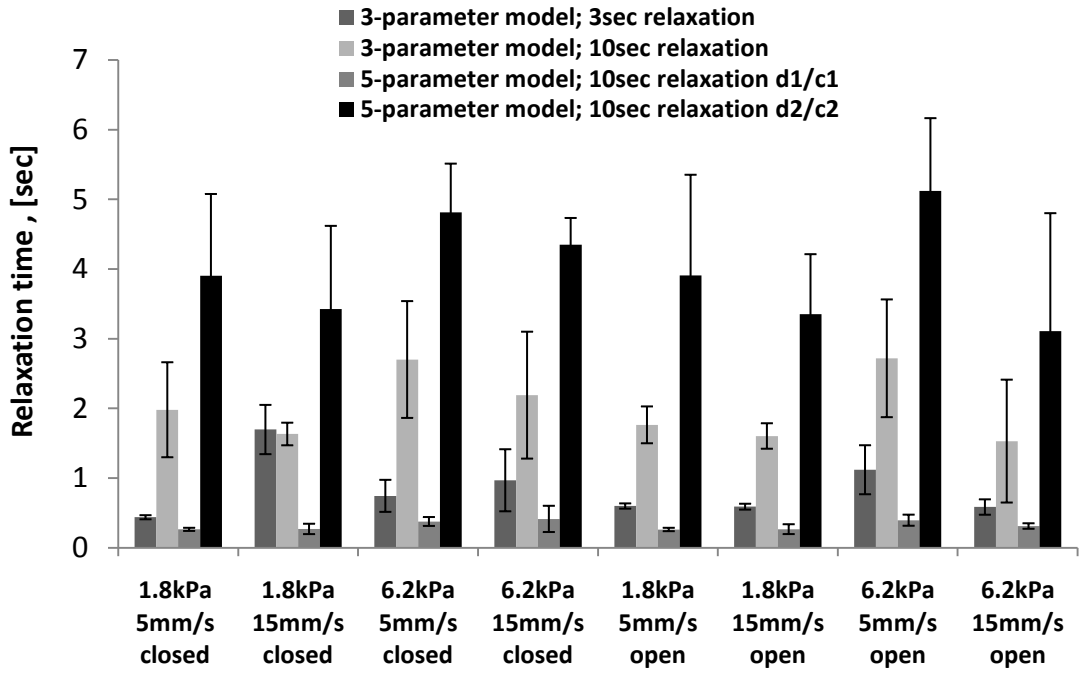

Figure 6-9: Relaxation times measured from the force relaxation curve using 3- and 5- parameter models

The results from this work can be compared directly with those of Kurita *et al.*, who investigated the cornea stiffness *in vivo* of 37 human subjects using an applanation device, measuring both force and displacement [190]. Their study clearly indicates increasing stiffness with increasing IOP (black circles, Figure 6-10) and the stiffness values are comparable with the initial stiffness values in this work which were 100-150N/m and 170-250N/m for 1.8kPa (13mmHg) IOP and 6.2kPa (46mmHg) respectively (red dots, Figure 6-10).

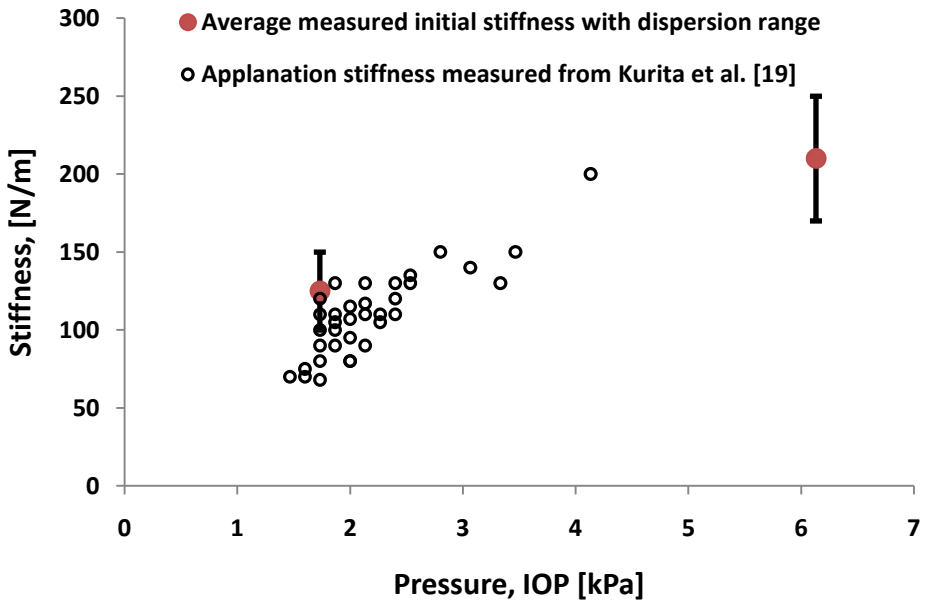

Figure 6-10: IOP versus Stiffness for applanation tonometers from Kurita *et al.* [190] and average initial stiffness measured in this work

6.2.2 Dynamic tests

The mean ratio was found to be constant around the pre-applied displacement for the whole frequency range tested (Figure 4-24a) which demonstrates that preconditioning did not affect the results. The results for the two different pre-displacements (0.5 and 1.5mm, Figure 5-26) show that the cornea tissue is not linear, a much higher stiffness being recorded for eyeballs with a 1.5mm pre-displacement which is due to geometric (Figure 6-11) and constitutive non linearity (inflation tests by Elsheikh [62]).

To compare the measurements with the literature, the equation by Uvarov [184] for the large deflection behaviour of a thin elastic spherical shell of radius R and wall thickness t was used:

$$d = \frac{F^2 R^2}{0.32\pi^2 E^2 t^5} \tag{6-9}$$

to calculate the apparent Young's modulus:

$$E_{app} = \frac{R}{0.57\pi t^{\frac{5}{2}}} \frac{F}{\sqrt{d}} = k \times F \tag{6-10}$$

The average pig cornea thickness is around 1mm (Elsheikh *et al.* [179]) and the radius of curvature of porcine eyes R varies from 7.8mm to 9mm depending on the pressure [191]. For this calculation the smallest radius R was used which also happens to be close to the value for humans. The thickness t , again was chosen to be 1.0mm. After adjusting the force to account for the action of the pressure on the probe surface, values of k were calculated to be $3.5\times10^{6}\text{m}^{-2}$ and $6.2\times10^{6}\text{m}^{-2}$ for pre-displacements d of 1.5mm and 0.5mm respectively.

Figure 6-12 shows the apparent Young's modulus for each of the pressures and each of the pre-displacements, compared with those measured by Elsheikh *et al.* [62], who directly determined the secant modulus for inflated corneas separated into three different age groups (50-64, 65-79 and 80-95). As can be seen, the apparent modulus for this work increases with pressure as do those of Elsheikh *et al.* Also, the slope of the line for modulus *vs* pressure is about 1.3 times higher for the 1.5 mm pre-displacement than for the 0.5mm pre-displacement. The higher gradient for apparent moduli in this work compared to Elsheikh *et al.* has to do with higher strain (higher displacement) when indenting the cornea tissue, since the inflation test was only taken to a maximum strain of 0.07% (Figure 6-13). At higher displacements and higher pressures, three factors will lead to a change in apparent modulus. Firstly, the strain in the cornea will generally be higher and, because the stress-strain curve is not linear (Figure 6-13), then a change in the actual modulus will result. Secondly, the radius of curvature will change (depending on the clamping conditions) as the pressure increases, thus changing the apparent modulus (which is calculated assuming a constant radius of curvature). Finally, at lower pressures the cornea will be more applanated (Figure 6-11a), whereas higher pressures will result in bending (Figure 6-11b) which changes the support conditions from those assumed in Equation 6-9.

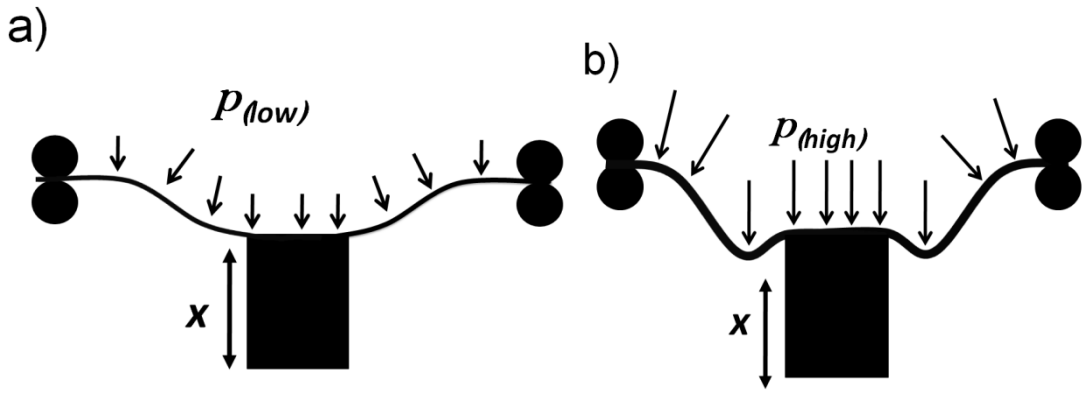

Figure 6-11: Schematic diagram (with shape exaggerated) of indentation of cornea a) under low pressure and b) under high pressure

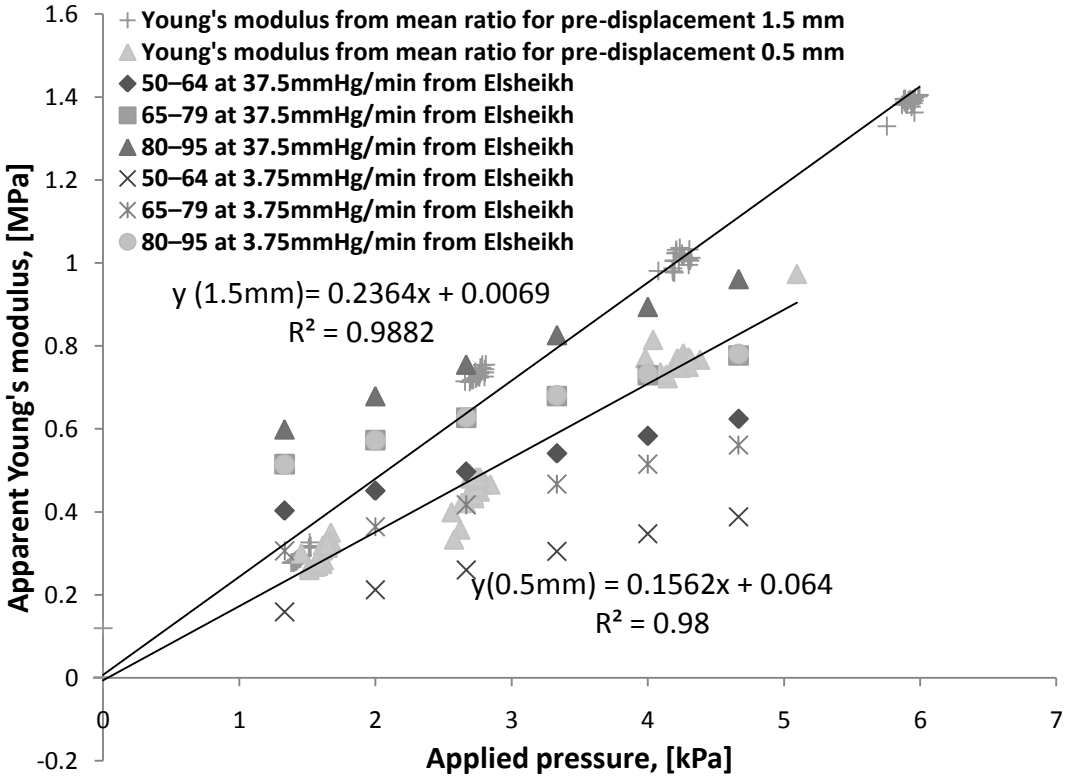

Figure 6-12 Apparent Young's moduli for varying IOP derived from mean ratio in this work, compared with equivalent data from Elsheikh *et al.* [62]

The mean force obtained for the excised cornea tested in open-ambient configuration (i.e. with no IOP) yielded a Young's modulus of only 0.036MPa (also shown in Figure 6-12). Lui *et al.* [59] have stated that a Young's modulus below 0.01 is not realistic although their study did not account for nonlinear stress strain behaviour. A Young's modulus of around this value for very low strains can be read from several published

stress strain curves either for inflation tests or tensile tests, for example those of Elsheikh *et al.* [63, 179] reproduced in Figure 6-13.

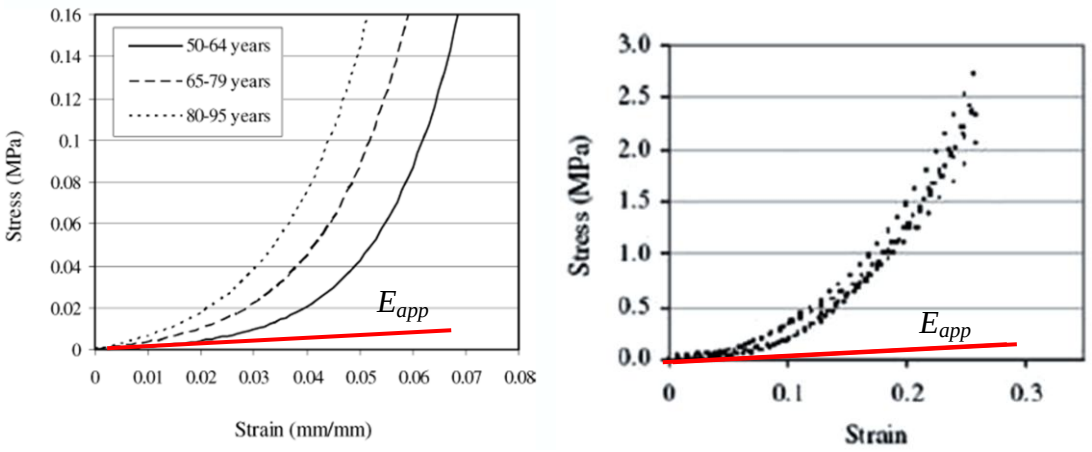

Figure 6-13: Stress-strain behaviour of human cornea from Elsheikh *et al.* [63, 179] for (left) inflation tests and (right) tensile tests

The dynamic results for the cornea section tested in the open-ambient configuration were fitted to the three-parameter spring-damper models described in Chapter 3. The SLS model and the model with the spring in series to the Kelvin model (Kelvin + spring model) seemed, by inspection (Figures 9-1 to 9-3 and 9-20 to 3-23), to be the most appropriate of the models described in chapter 3. The best fit parameters are shown in Table 6-3 along with the goodness-of-fit (R^2) and the 95% confidence bound on the parameter, those for the SLS model being designated c_s, c_M and $d_{M.}$ and those for the Kelvin + spring model being designated c_s, c_K and d_K (see Table 3.1).

For both models used (SLS model and Kelvin + spring model), the phase difference gave a better fit, and the Kelvin + spring model gave a better overall fit than the SLS model. In all cases (both models, phase and amplitude) the 95% confidence band was large, being lowest for the parameter c_s and highest for the damping parameters, d_m and d_k.

Parameter	SLS Model		Kelvin + spring model	
	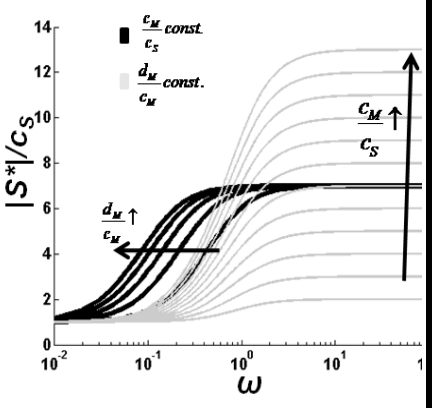		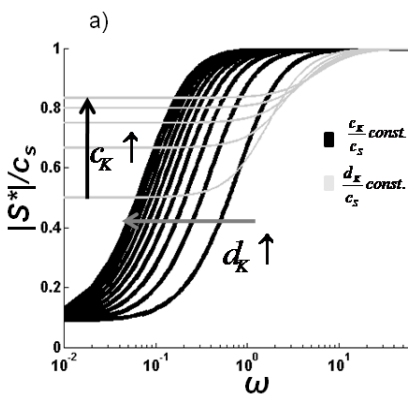	
	amplitude ratio	phase difference	amplitude ratio	phase difference
c_s, [N/m]	4.2 1.7- 6.6	16.96 13- 20	20 13-33	20 5-45
c_M / c_K, [N/m]	7 4-12	4 1-9	4 0-45	84.8 0- 4×10^{8}
d_M / d_K, [Ns/m]	0.27 0.0032-0.50	0.01189 0.0069-0.0169	0.045 0.038-0.052	0.31 0- 1.6×10^{6}
R^2	0.55	0.87	0.76	0.87

Table 6-3: Best-fit parameters for the SLS model and Kelvin + spring model for the dynamic test on excised cornea in open-ambient configuration.

Again, the force phase difference and force amplitude ratio (closed-pressurised) seemed to exhibit a similar pattern to those of the SLS and the Kelvin + spring model and the results were again fitted to these two models, the parameters being shown, along with the associated standard deviation of the repeated experiments in Tables 6-4 and 6-5 for the SLS parameter for the 0.5mm and 1.5mm pre-displacements, respectively and in Tables 6-6 and 6-7 for the Kelvin + spring model parameter for the 0.5mm and 1.5mm pre-displacements, respectively. It is immediately apparent that, although the fits are rather poorer than for the open-ambient configuration, the consistency between repeats and between parameters derived from phase plots and amplitude plots are relatively good. Comparing Tables 6-4 and 6-5 it can be seen that c_M and c_s values for the 1.5mm pre-displacement are around twice those for the 0.5mm pre-displacement and d_M is around six times higher for the 1.5mm pre-displacement. This translates to around a three times higher retardation time (d_M/c_M) for the 1.5mm pre-displacement. As the pressure is increased, all of the parameters increase, although the values of d_M are weakly dependent on pressure, most notably for the 0.5mm pre-displacement. This parameter also shows the largest variance (as a percentage of the value) which could be

due to variations in cornea thickness (0.975mm±0.105mm, as measured from [179]), although this cannot be tested as it was not possible to measure the cornea thickness for the pig eyeballs.

The open-ambient, and closed pressurised experiments on the mechanical eyeball showed that the damper parameter could be attributed to the effect of cornea thickness alone using the d_m parameter (Figure 6-1). The force, $F_{(\text{total})}$, to deform the eyeball is a function of the *IOP*, the Young's modulus *E*, the cornea thickness *t*, the indentation depth *d* , the probe area *a* and the radius of curvature of the cornea, *R*:

$$F_{(total)} = f(IOP, E, t, R, d, a) \tag{6-11}$$

where *IOP* and *d* are the experimental variables. In the case of the mechanical eyeball it was possible to control *t* and *E* but, for the pig eyeballs, these are not known precisely. The pig eyeball experiment can be compared with the mechanical eyeball in the closed-pressurised configuration if we assume a range in thickness *t* =0.975mm±0.105mm [179]). Using the apparent modulus correlation shown in Figure 6-12 for the 1.5mm pre-displacement, equation (6-9) can be used with the range of cornea thicknesses suggested above (0.870mm, 0.975mm and 1.080mm) to calculate the variation in required force (Figure 6-14). Plotting this range alongside the experimental data (Figure 6-15) it can be seen that the scatter around the mean force line can easily be attributed to a variation in cornea thickness as observed by Elsheikh *et al.* [179] but also to IOP change. This behaviour makes it hard to filter the different configurations (CCT and IOP) as they are interconnected in the force reading.

More importantly, Figure 6-15 shows that the effect of thickness on the measured force increases with increasing pressure, and this perhaps explains the reported differences in the error associated with thickness change for equivalent devices. The range of reported error for the GAT, for example, is between 0.24-1.2kPa pressure increase for a 0.1mm cornea thickness increase (associated with the average eye of CCT 0.547mm-0.552mm) [79, 89, 99]. Razeghinejad *et al.* [79] reported the biggest error with 1.2kPa/0.1mm cornea thickness change although they worked exclusively on glaucoma patients who had a higher IOP reading whereas Shimmyo *et al.* [89], who found the lowest error of 0.24kPa/0.1mm thickness change, tested 2,479 eyes without ocular pathology. For the current work, the IOP error would be 0.45kPa/0.1mm cornea thickness change for

1.8kPa pre-pressure setting and 0.76kPa/0.1mm cornea thickness change for 3.3kPa pre-pressure, although these changes are on a cornea which is almost twice as thick as the human one in the first place. Thus, it seems that the current work fits with the effect of CCT reported in the literature [79, 89, 98, 99, 192]. It might also be noted that the Schoitz tonometer does not measure the pressure as directly as the current work because the forces which act when deforming the cornea are 12 times higher than the force resulting from the pressure × the probe area (Figure 6-15).

	1.8kPa		2.7 kPa		4.4kPa		6.2kPa	
	AR	Phase	AR	Phase	AR	Phase	AR	Phase
c_M(N/m)	13±8	16±13	27±14	36±7	11±9	45±23	21±17	46±32
c_s (N/m)	59±18	38±12	71±32	96±45	136±23	141±17	174±31	156±33
d_M(Ns/m)	0.25±0.1	0.24±0.2	0.22±0.2	0.48±0.3	0.28±0.2	0.62±0.3	0.43±0.4	0.75±0.4
R^2	0.61	0.24	0.38	0.30	0.77	0.45	0.82	0.43

Table 6-4: Parameters of the SLS model derived from dynamic testing of pig eyeballs with 0.5mm pre-displacement

	1.8kPa		2.7 kPa		4.4kPa		6.2kPa	
	AR	Phase	AR	Phase	AR	Phase	AR	Phase
c_M(N/m)	24±7.5	43±26	53±24	59±26	92±23	120±63	117±68	162±23
c_s (N/m)	90±13	84±35	154±44	134±38	248±35	230±34	304±19	293±29
d_M(Ns/m)	1.43±0.6	0.69±0.6	1.70±0.9	1.02±0.5	2.51±0.5	1.95±0.7	2.57±1.2	2.70±1.4
R^2	0.61	0.31	0.85	0.53	0.93	0.61	0.96	0.72

Table 6-5: Parameters of the SLS model derived from dynamic testing of pig eyeballs with 1.5mm pre-displacement

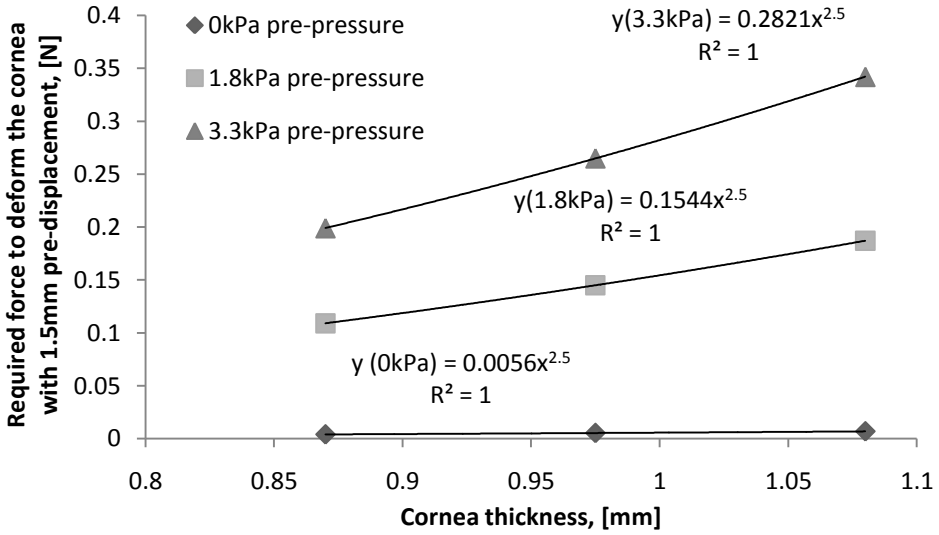

Figure 6-14: Calculated force to deform the cornea with 1.5mm pre-displacement versus central cornea thickness at three values of IOP

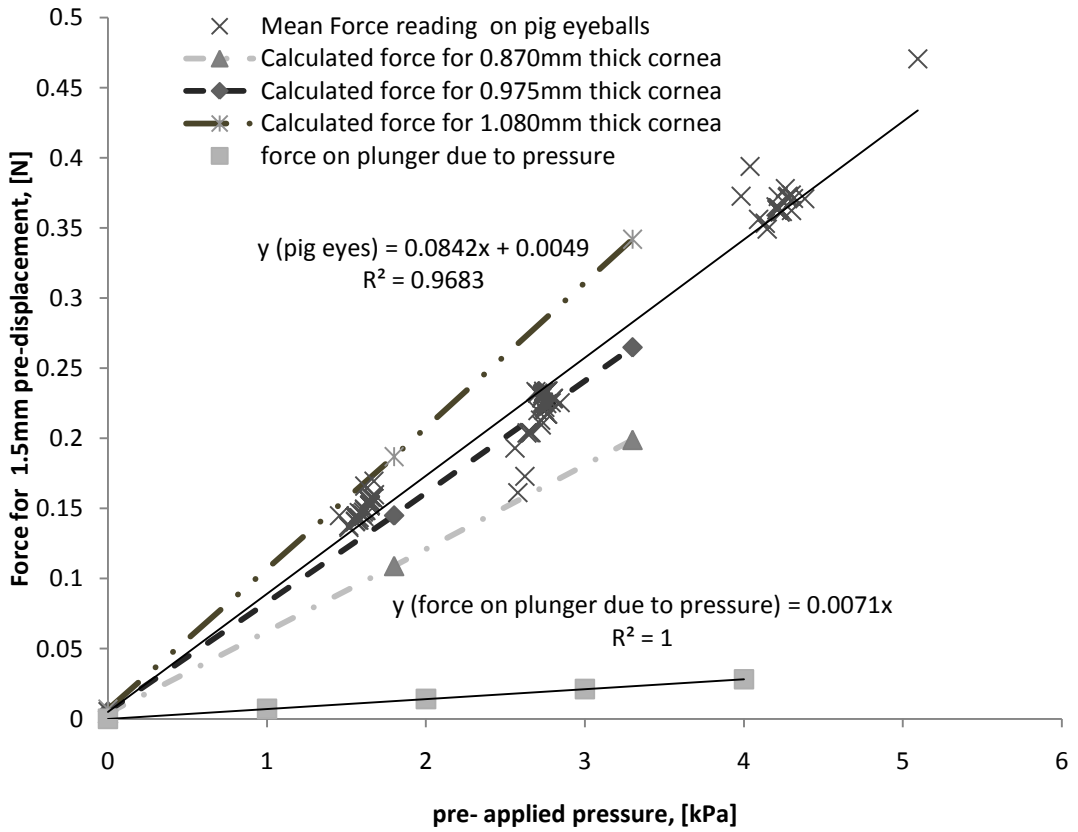

Figure 6-15: Comparision of calculated forces with measured forces for a range of cornea thickness and forces on the plunger due to pre-applied pressure × plunger area.

As before, the constants p_k were extracted from Figure 6-14 and are plotted against the pre-pressure in Figure 6-16. As for the mechanical eyeball, the p_k values were fitted with equation (6-5) and the parameters *f*, *l* and *c* found to be 2.285, 2.281 and 0.039 respectively Substituting equation (6-4) into equation (6-5) gives the true *IOP* in relation to the measured force *F* for deforming the cornea by 0.5mm for a cornea thickness *t* :

$$\mathrm{IOP} = -\frac{\ln\left[\frac{-\frac{\mathrm{F}}{\mathrm{t}^{2.5}}+\mathrm{f}}{\mathrm{l}}\right]}{\mathrm{c}} \qquad (6\text{-}12)$$

At 2.285, the parameter *f* for the pig eyeballs is very similar to that for the mechanical eyeball (2.06). The value of *c* is about 5.9 times bigger and the value of *l* about two times bigger for the mechanical eyeball than for the pig eyeballs. Therefore *f* can be associated with the factors that were kept constant between the pig eyes and the mechanical eyeball; indentation depth *d*, indenter area *a*, and curvature radius *R* ($f = f(d, a, R)$. The 600-fold higher Young's modulus for the mechanical eyeball compared

with the cornea in the open-ambient configuration and the fact that the mechanical reservoir is rigid whereas the eyeball is compliant can be attributed to the *c* and *l* parameters. The extrapolated Young's modulus of the cornea is much smaller than the modulus of the mechanical cornea rubber. However according to the literature any Young's modulus between 0.01MPa to 1GPa [54, 58, 59, 61, 64-67] could have been the right one. Therefore it should have been recognised that the choice of the mechanical eyeball material was done before measuring cornea tissue *in vitro.*

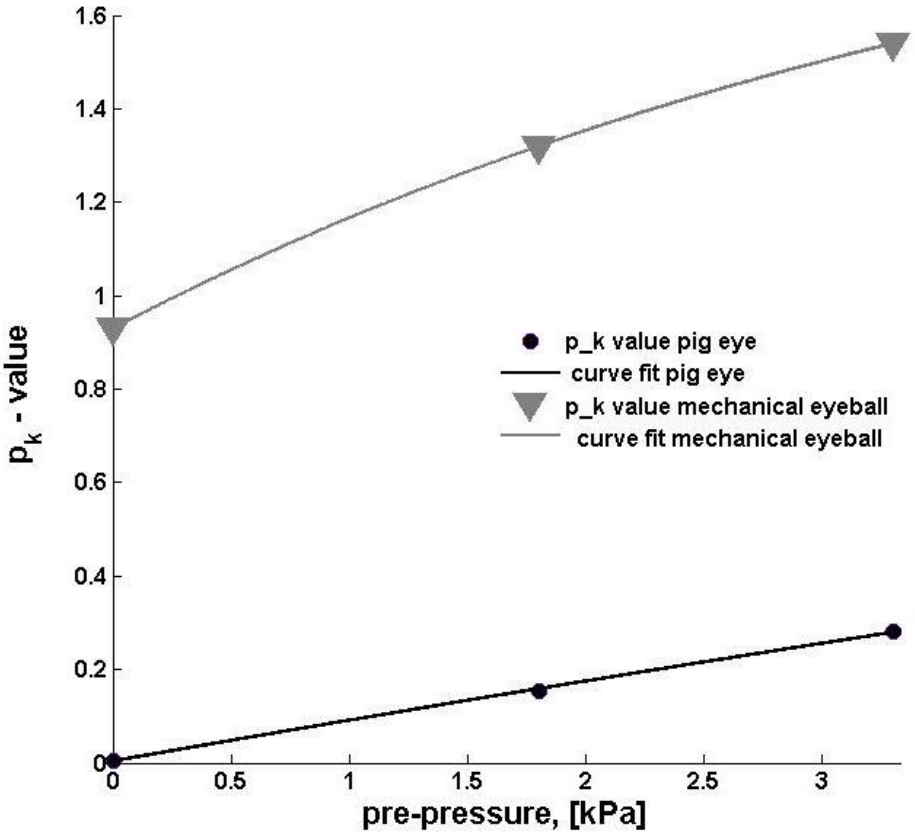

Figure 6-16: Values of p_k vs pre-pressure for pig eyeballs (dots) and for mechanical eyeball (triangles)

The best-fit parameters of a Kelvin + spring model were obtained for phase difference and amplitude ratio in the same way as was done for fitting the SLS model. Comparing first the different pre-displacements (Table 6-6 compared with Table 6-7) only the c_s parameter is always higher for the 1.5mm pre-displacement and parameters c_K and d_K are only higher for pressure 1.8kPa and 2.7kPa for the 1.5mm pre-displacement. However, all parameters within the same pre-displacement group increase monotonically with increasing pressure. In Chapter 3 it was shown, that the Kelvin + spring model is equivalent to the SLS model as seen by the fact that the values of $\frac{c_K c_S}{c_K + c_S}$

are almost identical to c_s from the SLS model. It can be concluded from this that, whereas the models give essentially the same shape of curves, the SLS provides a set of parameters which can more usefully differentiate between the experimental variables.

	1.8kPa		2.7kPa		4.4kPa		6.2kPa	
	AR	Phase	AR	Phase	AR	Phase	AR	Phase
c_K (N/m)	339 ±195	180 ±87	633 ±480	591 ±100	1816 ±940	1800 ±987	1581 ±538	1681 ±32
c_s (N/m)	72±7	79±42	106±7	218±45	146±4	575±412	196±11	490±33
d_K(Ns/m)	7±3	4±3	11±11	11±4	58 ±35	38±23	36±17	35±0.2
$\frac{c_K c_s}{c_K+c_s}$(N/m)	59	54	72	111	240	844	155	545
R^2	0.81	0.23	0.38	0.30	0.77	0.45	0.82	0.43

Table 6-6: Parameters of the Kelvin + spring model model derived from dynamic testing of pig eyeballs with 0.5mm pre-displacement

	1.8kPa		2.7kPa		4.4kPa		6.2kPa	
	AR	Phase	AR	Phase	AR	Phase	AR	Phase
c_K(N/m)	521±174	231±26	699±253	801±306	764±251	806±312	1595±700	971±400
c_s (N/m)	119±10	118±35	225±67	351±38	339±62	420±23	403±72	539±134
d_K(Ns/m)	19±8	5.6±3	19±7	21±12	32±6	20±9	39±4.2	25±14
$\frac{c_K c_s}{c_K+c_s}$(N/m)	96	78	170	251	234	264	321	346
R^2	0.44	0.31	0.79	0.53	0.83	0.61	0.81	0.72

Table 6-7: Parameters of the Kelvin + spring model derived from dynamic testing of pig eyeballs with 1.5mm pre-displacement

The amplitude ratio for all dynamic tests shows an increase in the magnitude of the complex stiffness with increasing frequency, consistent with Elsheikh *et al.*, who observed a stiffening of the cornea when increasing the inflation speed [62]. The c_s parameter of the SLS model can be used as the low frequency limit of the apparent complex modulus $|E^*|$(since $E^*_{Maxwell} \to 0$ when $f \to 0$). For the high frequency limit, the Maxwell damper will not deform and the spring in series will act alone and the SLS maximum modulus is thus the c_s parameter of the spring in parallel with the Maxwell spring c_M, i.e. $c_{max} = c_s + c_M$. To obtain the values for apparent complex modulus$\left|E_{app}{}^*\right|$ [N/m^2], the stiffness $|S^*|$ [N/m] was converted using equation (6-10) with a *k*-factor of 12.9 × 10^{6}m^{-2}, calculated by replacing the deformation *d* with the amplitude of 0.115mm. As can be seen from Table 6-8, all apparent complex moduli are slightly smaller than the apparent Young's modulus obtained from the mean ratio (Figure 6-12) and increase across the frequency bandwidth (2Hz-40Hz) from a minimum (min) for low frequency to a maximum (max) for high frequency. This

observation reinforces the suitability of a three-parameter model to describe the frequency range used, where the modulus varies monotonically between a low-frequency limit and a high frequency limit.

The viscosity ϑ [MPas] is related to the damping parameter *d* [Ns/m] using the same *k*-factor as for stiffness. Here, the two models produced different viscosities, the SLS model yielding 0.29-1.45kPas and 2.7-5.2kPas for 0.5mm pre-displacement and 1.5mm pre-displacement, respectively, and the Kelvin + spring model 27-112kPas and 10-75kPas for 0.5mm pre-displacement and 1.5mm pre-displacement, respectively. Thus, the two models are inconsistent in terms of the effect of pre-deformation on viscosity, although, given that its parameters offer better separation of component effects, more weight might be put on the observation of the SLS damping coefficient. It therefore appears that increased pre-displacement yields higher viscosity values. The only reported values of viscosity of collagen are those of Stromberg and Wiederhielm [36] who measured around 170kPas using a Kelvin + spring model applied to the creep behaviour. Although the strain level was under 5%, which is very small compared to other workers who have used strains of up to 70% [9, 11, 19, 20, 25], the values are not inconsistent with those measured here (using the Kelvin + spring model) for a strain less than 5%.

	1.8kPa		2.7 kPa		4.4kPa		6.2kPa	
	AR min-max	Phase min-max	AR min-max	Phase min-max	AR min-max	Phase min-max	AR min-max	Phase min-max
$\left\|E_{app}{}^{*}\right\|$[MPa] · 10^{-1} at 0.5mm	0.9-1.4	0.6-1.5	1.1-2.1	1.4-4.2	2.8-12	2.1-3.8	2.6-3.8	2.3-9.5
$\left\|E_{app}{}^{*}\right\|$[MPa] · 10^{-1} at 1.5mm	1.3-2.3	1.6-2.3	3.0-4.3	2.6-6.8	4.8-6.5	4.4-8.2	5.9-7.8	5.7-10

Table 6-8: Magnitude of the apparent complex modulus *E for the two pre-displacements (0.5mm and 1.5mm) achieved from SLS model**

Goldman [5, 193] recommended that measurements should be done in less than 1minute to keep the variation in liquid drainage and the creep of the cornea small. The force amplitude with a pre-displacement of 0.5mm at 24Hz offered an accurate method of determining IOP, with the best correlation coefficient of R^2=0.91 (Figure 5-30). The accuracy was within ±0.9kPa (7mmHg) which was only slightly above the allowed standard for tonometers (0.7kPa or 5mmHg). However, since CCT was not controlled

in the current work, this recommendation is confined to speed and could be further improved taking into account cornea thickness.

A 5-parameter MSD-model with inertia forces was used to explain the behaviour of the mechanical eyeball with drainage effects. This behaviour was not expected in the eyeballs as, due to the size of channels, a drainage effect would only be expected at frequencies lower than 0.01Hz, well below the minimum of 2Hz used here. The pressure phase difference for the choked-pressurised system for the mechanical eyeball (Figure 5-8b) started to resonate, when the pressure was about 270° out of phase with the displacement and the pressure phase difference measured in the pig eyeballs (Figure 5-31) has a phase shift of 150° to 250° at 40Hz, which suggests that there may be a resonance peak at higher frequency, although this would not be associated with drainage. Halberg [7] and Drescher [39] have both simulated the human eyeball and showed that there would be a resonance of the liquid itself at about 35Hz [39, 97]. Measurements of resonance in human and pig eyeballs indicate a range of 170-300 Hz [194], and Drescher [39], who also measured the resonance on enucleated pig eyes and found a first resonance frequency of the whole pig eye starting from 130 Hz for 1.3kPa (10mmHg) up to 165 Hz for 6.6kPa (50mmHg), Figure 6-17.

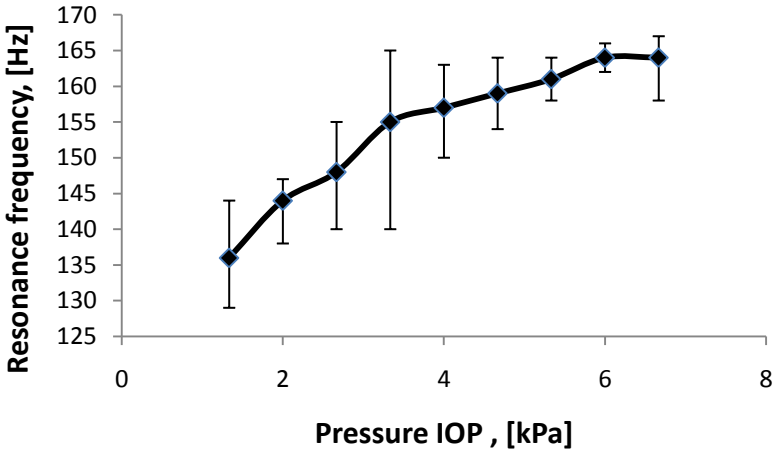

Figure 6-17: Resonance frequency for enucleated pig eyeballs from Drescher [39]

For the pig eyeballs either the range of frequency was not wide enough or the device was not sensitive enough to be affected by liquid vibrations, most likely the former. If the liquid mass is small, the mass m can be taken as zero and the damping coefficient damper d_2 is also zero if no liquid moves through the orifice. Reducing the mass m and the damper d_2 to zero reduces the 5-parameter MSD-model to a three parameter Kelvin

+ spring model (Figure 6-18), so the observations in this work are not inconsistent with the findings of Drescher, and complement them.

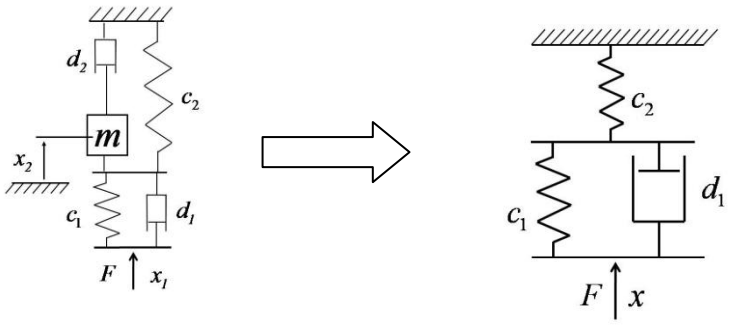

Figure 6-18: Reduction of MSD – model to Kelvin + spring model

Using the SLS model, the stiffness parameter c_s can be directly related to the pressure increase and the parameter c_m can be used to describe the cornea stiffness. As observed earlier, the pressure in the eyeball has an effect on the stiffness of the cornea and this leads to a slight increase in overall stiffness, c_s, which can be seen as well in the parameter c_m. The experiments with higher pre-displacement have a higher c_s parameter as the pressure increases due to higher deformation. Figure 6-19 shows that the retardation time d_M/c_M decreases with increasing pressure for a given pre-displacement. A fast retardation time at high pressure is important. For example when humans (or other animals) rub their eye, the IOP can rise to up to 10 times the normal and should not be done too long and too often otherwise lasting damage can result [195]. The faster retardation time for increasing pressure is the cornea's reaction to decrease the temporarily heightened IOP. The higher the temporary IOP becomes, the more important it is to reduce it quickly, which is exactly what cornea does according to the results of this research. However this recovery will not help with glaucoma where the source of the heightened IOP is not an external mechanical stimulus to which the cornea can react, but is a disruption to the biochemical equilibrium which leads to the IOP and the biomechanical drainage mechanisms.

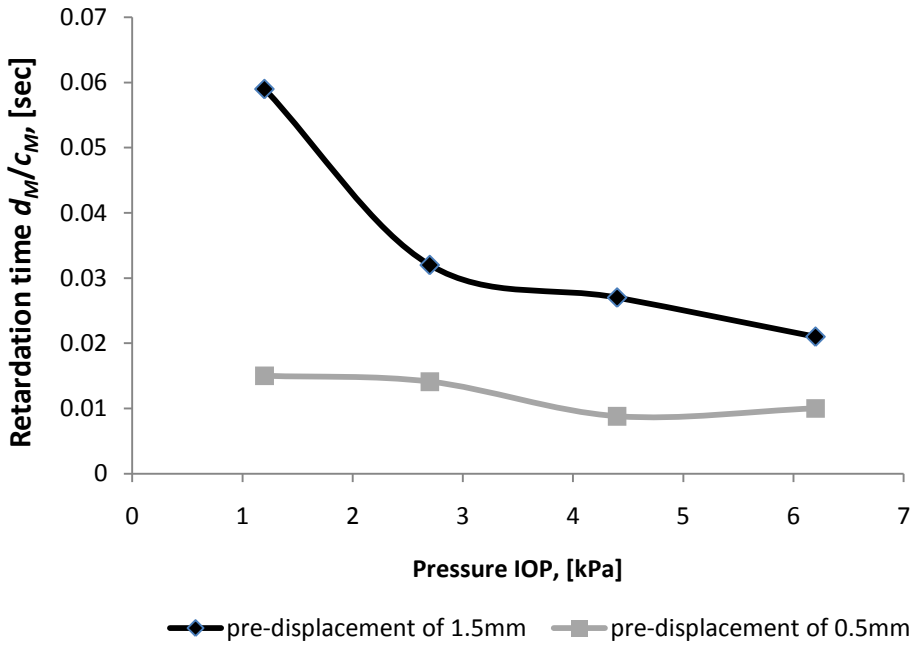

Figure 6-19: Effect of pressure on retardation time for the two pre-displacements

Table 6-9 shows the SLS model parameters derived from the amplitude ratios and the phase differences compared with the five parameters from the static tests, both for the 1.5mm pre-displacement for pressure groups 1 (1.8kPa) and 4 (6.2kPa). The comparison shows that both tests give entirely consistent results, given the constraints of the frequency range used in the dynamic tests, and illustrates an important point about the selection of the frequency range for testing. When the retardation time for a given Maxwell element d_i/c_i is much greater than the period of oscillation, the damper will not be able to respond and the Maxwell element behaves as a spring of stiffness c_i, which acts in parallel with the existing parallel spring c_s and hence can be added to it. Thus, the spring c_2, which is in series with the damper d_2 can be summed up with the spring c_s in the frequency range 2-40Hz and further supports the SLS model as the most suitable one to fit to the dynamic results.

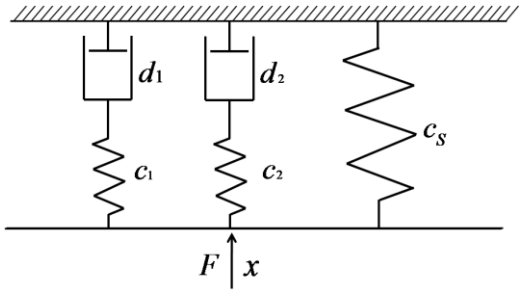

for static test

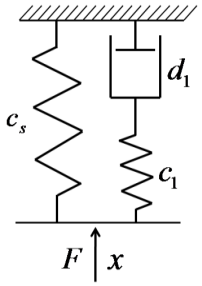

for dynamic test

	Parameter force relaxation		Parameter phase lag		Parameter amplitude ratio	
Pressure group	1 (1.8kPa)	4 (6.2kPa)	1 (1.8kPa)	4 (6.2kPa)	1 (1.8kPa)	4 (6.2kPa)
R^2	0.98	0.99	0.57	0.73	0.61	0.96
c_1 [N/m]	35	114	24	140	45	114
d_1 [Ns/m]	1.50	2.70	1.4	2.74	1.53	2.68
c_s ($+c_2$) [N/m]	22+88=110	57+177=234	84	260	82	296
d_2 [Ns/m]	67	206,2	$d_2 >> T^* c_2$ $0.016 < T < 0.5$			

Table 6-9: Comparison of static test with a 5 parameter model and the dynamic test with 3 parameter model (SLS)

It appears, therefore, that the eyeball system has at least two retardation times which are not observed in the test frequency range; one which would appear at higher frequencies, and may be associated with liquid oscillations, and one at lower frequencies, which may be associated with longer relaxation behaviour of the cornea or perhaps drainage or leakage. This would suggest that a multi-parameter model with a Maxwell element to describe each retardation time might be a useful way of testing and describing such systems. Unfortunately, it is not possible to devise sufficient boundary conditions to

solve the differential equation of even a 4 parameter model, although, by describing the system as a feedback control system, a transfer function can be set up.

$$tf = \frac{F}{x} = \frac{c_1}{1 + \frac{c_1}{s \cdot d_1}} + \frac{c_2}{1 + \frac{c_2}{s \cdot d_2}} + c_s \tag{6-13}$$

For a simple spring, the result would be linear and no feedback is needed, but a damper in series with a spring needs a reaction coupling as illustrated in Figure 6-20 for the five-parameter model. The control system starts with a deformation x_{spring} (1) which results in a force output (2). The force affects the damper (3) and moves the damper with a certain velocity v_{damper} (4). The deformation of the damper is the integral of the velocity (5) and is fed back where it has to be subtracted from the input deformation (6) to correct the spring deformation. This circuit has to be repeated in parallel with two different sets of parameters (Figure 2-21).

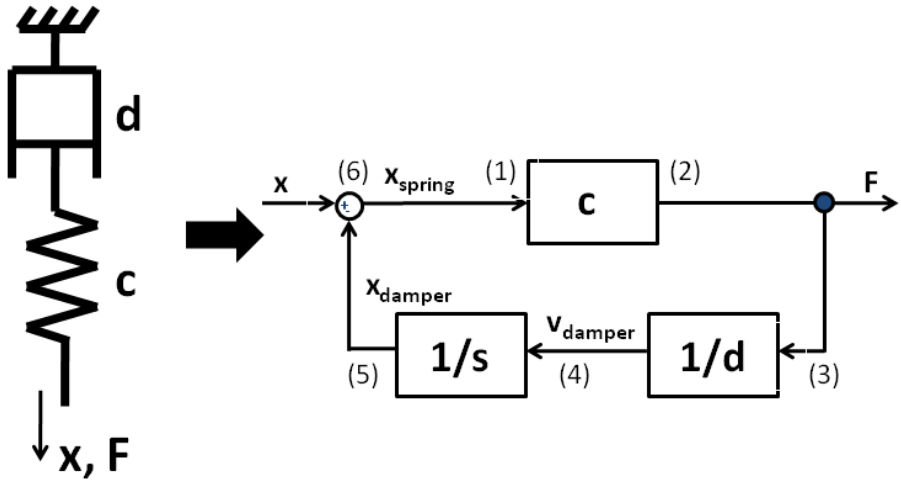

Figure 6-20 Feedback control system of a simple damper in series with a spring (Maxwell model)

The transfer function was designed and solved[1] in Simulink (MATLAB) [196] to give the amplitude ratio and phase lag for a 5 parameter model using the parameters obtained from the static tests (Table 6-9), and the result is shown in Figure 6-22. This simulation illustrates very well that that the frequency bandwidth from 2Hz to 40Hz will only merit the use of an SLS model because the second, more viscous damping element behaves as a solid material.

[1] The author is grateful to Benjamin Meindl, Bachelor student working between FH Regensburg and Heriot-watt University for the simulation work.

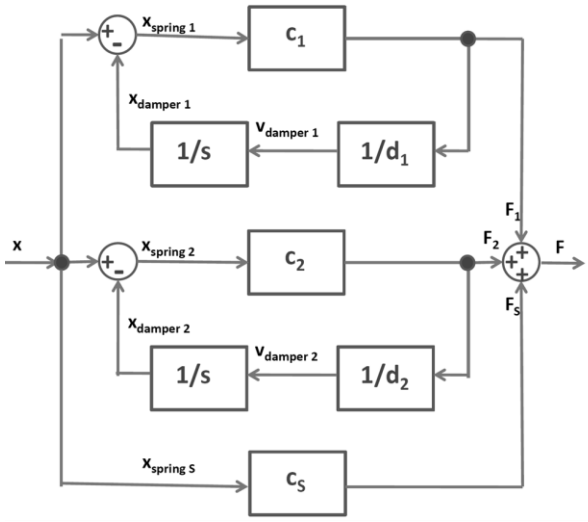

Figure 6-21 Feedback control system of the five parameter model

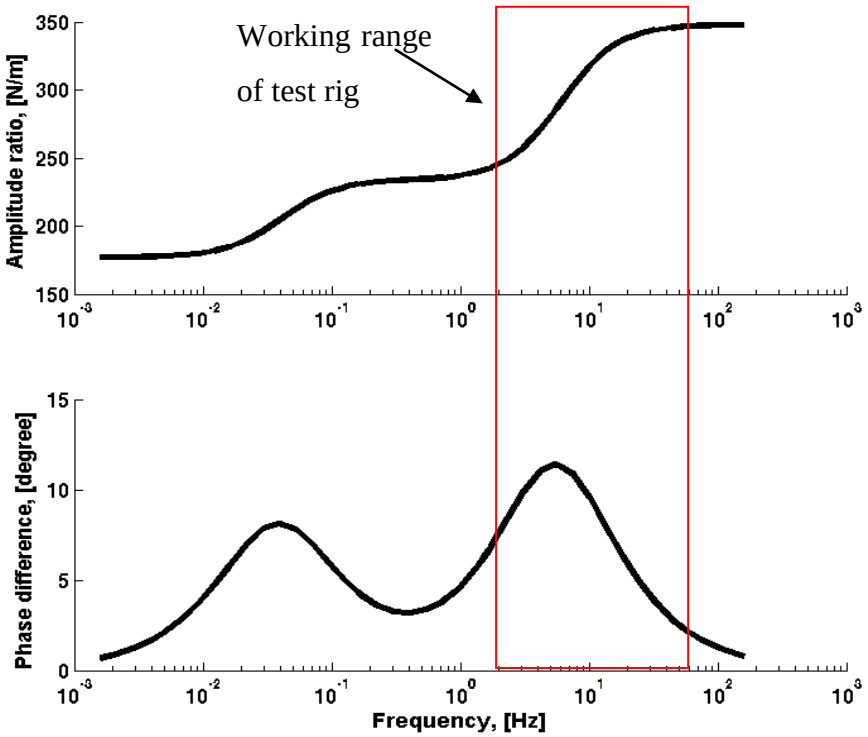

Figure 6-22: Bode diagram of the transfer function of a 5 parameter model with values from the static test

6.3 Periodontal ligament

The format of the data (stress relaxation) allowed a wider range of visco elastic models to be tested for the tooth displacement tests than for the eyeball tests. As shown in Chapter 5, longer observation times revealed the inadequacy of a three-parameter model, and the four parameter model, even though it allowed for two relaxation times, is not sufficiently flexible to fit the data well (essentially because the two relaxation times need to be related to each other). Thus, the best model for describing the results was a 5-parameter model with two Maxwell elements giving two relaxation times; one a little below 1sec and the other around 10sec. Repeat testing of the jaws also revealed a longer-term drift in stress relaxation with a characteristic time in the region of 100sec, suggesting that the PDL might have multiple relaxation times. These observations all show remarkable similarity to the findings on the eyeballs despite the fact that the method of testing is entirely different.

It was decided to study the PDL using force relaxation instead of stress relaxation because this offered the best opportunity for application *in vivo* on human teeth, not only to improve understanding of PDL behaviour but also as one of the easiest-to-access biomechanical systems. Despite the fact that force rather than stress and displacement rather than strain were measured, the shapes of the relaxation curves should be similar so that retardation times can easily be compared between investigators measuring force or stress. One of the best sets of data are those by Komatsu *et al.* [127] who tested PDL sections for stress relaxation with a tensile test machine. These authors used observation times up to 300 sec and found that two exponential curves were not enough to describe the observed force relaxation. Accordingly, they used a three-exponential curve with one constant, rewritten here as a 7-parameter model with three Maxwell elements as equation (6-14).

$$F(t) = x\left[c_s + c_1 \cdot e^{-\frac{c_1 t}{d_1}} + c_2 \cdot e^{-\frac{c_2 t}{d_2}} + c_3 \cdot e^{-\frac{c_3 t}{d_3}}\right] \tag{6-14}$$

Their first retardation time d_1/c_1, at about 0.2-0.4sec sec matches very well with the 4- and 5-parameter models of the current work (Figure 5-44) and with the three-parameter models, provided that only the short relaxation times are considered. Also, the

retardation time d_2/c_2 of the 5-parameter model in this work (Figure 5-45) matches the 4.12 sec of Komatsu's second characteristic time [127], again provided that the longer observation times (above 25 sec) are not used. The 4-parameter model does not provide a second retardation time (Figure 5-45) which can be compared with Komatsu's results because the second Maxwell component has to provide spring characteristics in order to perform the purely elastic functions, which could only be achieved by the curve fitting tool increasing the damping parameter to very high values (Figure 5-45). Komatsu's third relaxation time was 100sec to 400sec which reflected the third relaxation time observed in the drift between repeat tests.

Komatsu *et al.*[127] and van Driel *et al.*[109] used several hours of observation to measure the visco elastic behaviour of PDL and found that complete relaxation takes minutes or even hours. The force recorded in this work after 35 sec was, on average, 70% of the initial force (30% force reduction), whereas Natali *et al.* [197] found a stress reduction of 30% (70% of initial stress) after 400 sec and Dorow et al.[126] found a 33% (67% of initial stress) stress reduction after 14 minutes, both measured on bone-PDL-tooth sections. This would suggest that compressing PDL tissue leads to faster relaxation than stretching a section of PDL. Overall, it would appear that, by allowing the PDL to relax for a longer period, other characteristic times reveal themselves, probably corresponding to different sets of processes. As more fibres align in the tension direction and more liquid drains out of the compressed tissue [198], it would seem that a multi component Maxwell model will be needed, although it is not yet clear what aspects of the tissue structure will govern the relevant characteristic times.

To add to the difficulty, the experiments on the pig PDL were carried out *in vitro* and it is very likely that different results will be obtained *in vivo*, where an intact vasculature and its blood circulation may well have a big influence on how the PDL responds to compression or tension [199]. One further issue is the condition of the *in vitro* sample. Different behaviour would be expected between dried out and hydrated tissue. For example dried out collagen samples have been observed to have a much higher Young's modulus than hydrated samples [22] and losing liquid in the tissue also reduces the viscous behaviour [200], affected material behaving in a more elastic fashion. Although every effort was made to keep the jaws in good condition and to retain as much tissue

around the PDL as is reasonable, there are bound to be differences between *in vitro* behaviour and the *in vivo* behaviour which it is important to understand.

Porcine premolar teeth are single rooted and have similar dimensions to the second incisor from the human dentition. Therefore, the published dimensions from Provatidis [114] were used where the root length (apex to alveolar crest) is 13.0mm and the PDL area is 101.4mm^2. The force was applied 5.8mm apical to the alveolar crest and the bearing area, *A* was taken as half the PDL area. The stress distribution will not be uniform in the PDL and, following Choy *et al.* [121], and in the interest of obtaining values of modulus and viscosity, it will be assumed that the loading produces a direct compression on the bearing area and a stress that varies between compression and tension due to moment of the applied force about the centre of resistance (Equation (6-15)):

$$\sigma_{total} = \frac{My}{J_x} + \frac{F}{A} \tag{6-15}$$

where *M* is the moment ($F \times a$), where *a* is the axial distance between the point of application of force *F* and the centre of resistance, *y* is a variable axial distance from the centre of resistance, $J_x = \frac{gl^3}{36}$ is the second moment of the axial cross-sectional area of the tooth and *A* is the bearing area of the PDL.

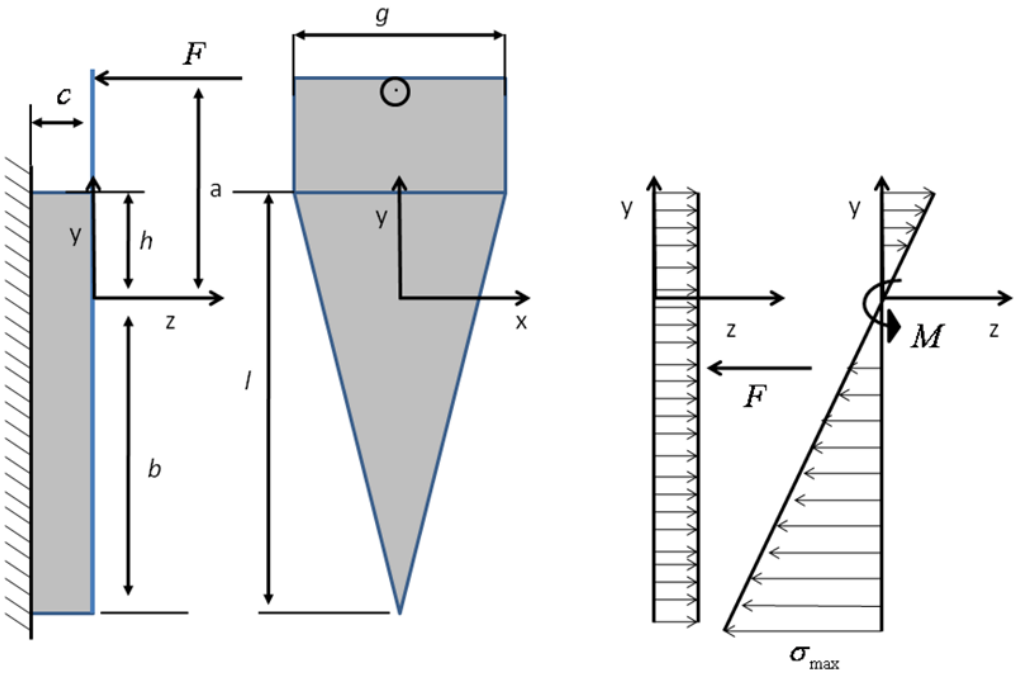

Figure 6-23: Simplified stress distribution in PDL due to a force in the buccal or lingual direction.

The maximum total stress is strongly dependent on the distance *a*, which, for the model to hold, has to be larger than $\frac{2J_x}{A(c+b)}$, to have the maximum total stress σ_{total} at the apex of the root. This means that, for the pig jaws, *a* has to be bigger than 0.7mm which was always the case as the PDL and the gum covers the lower limiting point and no access to the tooth is possible.

Using this simplified analysis, it is possible to transfer the force relaxation curves into stress relaxation curves and compare them with literature. In the experiments, the teeth were moved by amounts of 70µm, 107µm, 175µm and 245µm which correspond to strains of 16%, 25%, 42% and 59%, respectively, at the centre of resistance with a = 10.33mm (5.8mm+1/3×13mm) and b = 8.66mm (2/3×13mm) and the PDL thickness c = 0.229mm (values obtained from Provatidis [114]). The stiffness parameters c_s and c_1 for the three parameter SLS model (Figure 5-46) and the retardation times (Figure 5-41) can be used in equations 6-16 to 6-17):

$$E_s = \frac{c_s x \frac{a+b}{b}}{A\varepsilon};\ E_1 = \frac{c_1 x \frac{a+b}{b}}{A\varepsilon} \qquad \text{(6-16 and 6-17)}$$

$$\mu = t * E_1 \qquad \text{(6-18)}$$

to calculate the apparent Young's moduli *Es* and E_1 and the viscosity μ.

The apparent Young's modulus E_s increases with increasing strain as did the apparent Young's modulus E_1 (Figure 6-24). The viscosity μ is more dependent on the allowed relaxation time and was found for the SLS model to be between 0.27MPas and 2.17MPas and increased with increasing allowed relaxation time from 5 sec to 35 sec. Using Provatidis' [114] parameters from the creep curve yields values for E_1, E_s and μ of 0.47MPa, 0.034MPa and 0.43MPas respectively. For the stress relaxation in this experiment, the E_1 modulus is about 10 times smaller than the E_s modulus, but for the creep behaviour of Provatidis it is exactly the other way round. Only the viscosity parameter is in the same range with 0.43Pas. However, using the relaxation function and the creep function at t=0 the initial complex modulus from the creep curve fit perfectly to the initial apparent Young's modulus from this experiment. The initial

strain of the creep function of Provatidis was calculated to be only 3.3% which is more than ten times lower as the strain that was used in this experiment. This again shows that tissue is very dependent on strain and PDL stress-strain-time behaviour is more complex than a simple SLS model and creep behaviour might be different to relaxation behaviour.

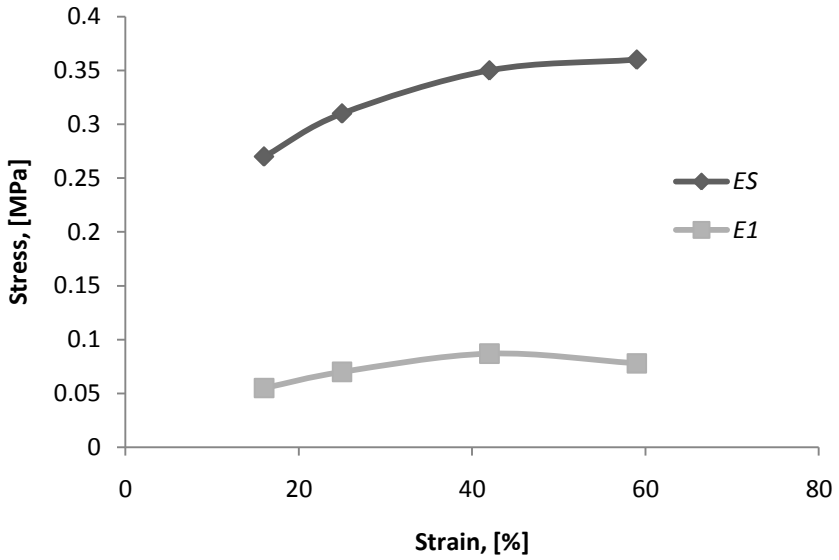

Figure 6-24: Apparent Young's modulus [MPa] with varying strain

The initial apparent Young's modulus values (stress relaxation at t=0) in the centre of resistance for the 3-,4- and 5- parameter model are shown in Figure 6-25. The initial apparent Young's modulus is the maximum modulus and, for extrapolations, it needs to be acknowledged that a different mechanism applies after the first 20 or so days of force application, when remodelling of the PDL and the alveolar bone changes the force-PDL interaction and therefore the stress-strain behaviour.

The total maximum compressive stress σ_{total} before any relaxation was also calculated from equation 6-15 giving values between -0.38MPa for the smallest displacement of 70µm down to -2.5MPa for a deformation of 245µm. Even at the smallest displacement, these stresses are well in excess of the maximum suggested by Choy *et al.* [121] which is the systolic pressure in the PDL (16kPa) . Extrapolating the stress - strain data of this work would only permit a 4.4µm displacement 5.8mm form the apex of the alveolar crest not to exceed the 16kPa for optimal OTM.

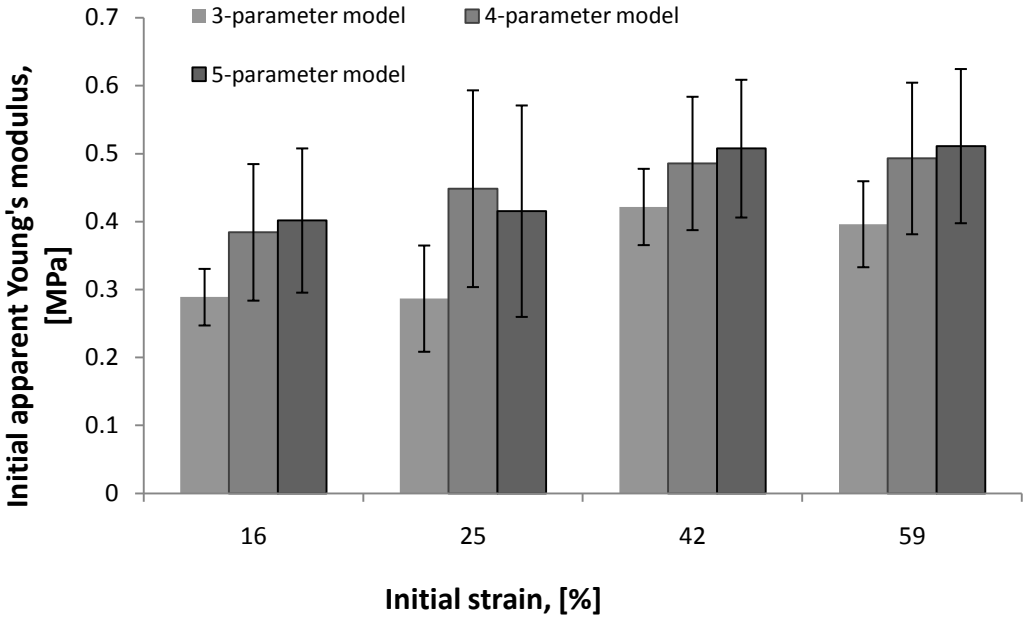

Figure 6-25: Initial apparent Young's modulus [MPa] at the centre of resistance for several strains [%] using the 3-, 4- and 5-parameter models

Waever *et al.* [201] and Ziegler *et al.* [141] have confirmed that pigs have a comparable tooth structure and tooth development to humans. Pigs are also omnivores with a grinding chewing movement similar to humans, although the teeth are different in shape and size. This last point could mean that the stresses calculated above are overestimated and that responses may also be different even if *in vivo* studies were done. It therefore makes more sense for *in vivo* measurements to be carried out on humans. To this end, a preliminary design study, based on the observations above, has been carried out by Meindl [196] to assess mechanical properties directly *in vivo* on human teeth (Figure 6-26). The design (Orthometer) is configured to move the front teeth dynamically using a piezo actuator (CEDRAT APA 150XXS) while the patient provides the reaction force by biting onto a plate with the premolars. The micrometer screw provides a coarse adjustment for the end-effector of the piezo-actuator which is in series with a load cell (S beam load cell FUTEK lsb200). The ball joint allows adjustment of pan and tilt to allow the probe to address any one of the front teeth at right angles and at a chosen height from the gum line. A proximity probe (MX-E series from OMRON) allows the measurement of the actual tooth movement during the assessment and provides important confirmation whether or not the patient is allowing the device to slip. Figure 6-27 shows a detailed overview of main working part of the device, a module built onto one part of the ball joint which includes all the sensors and actuators. The probe at the

end of the piezo actuator has a spherical shape to transfer a point load to the right position on the tooth. The actuator is able to oscillate at various speeds with a maximum force of 3N and a travel of accuracy and repeatability of less than 1 µm and a maximal range of 120µm. All parts touching the patient can be removed and cleaned easily. Parts which are close to the patient such as the plastic housing can be disinfected to meet the standards of the Medical Devices Directive 93/42/EEC.

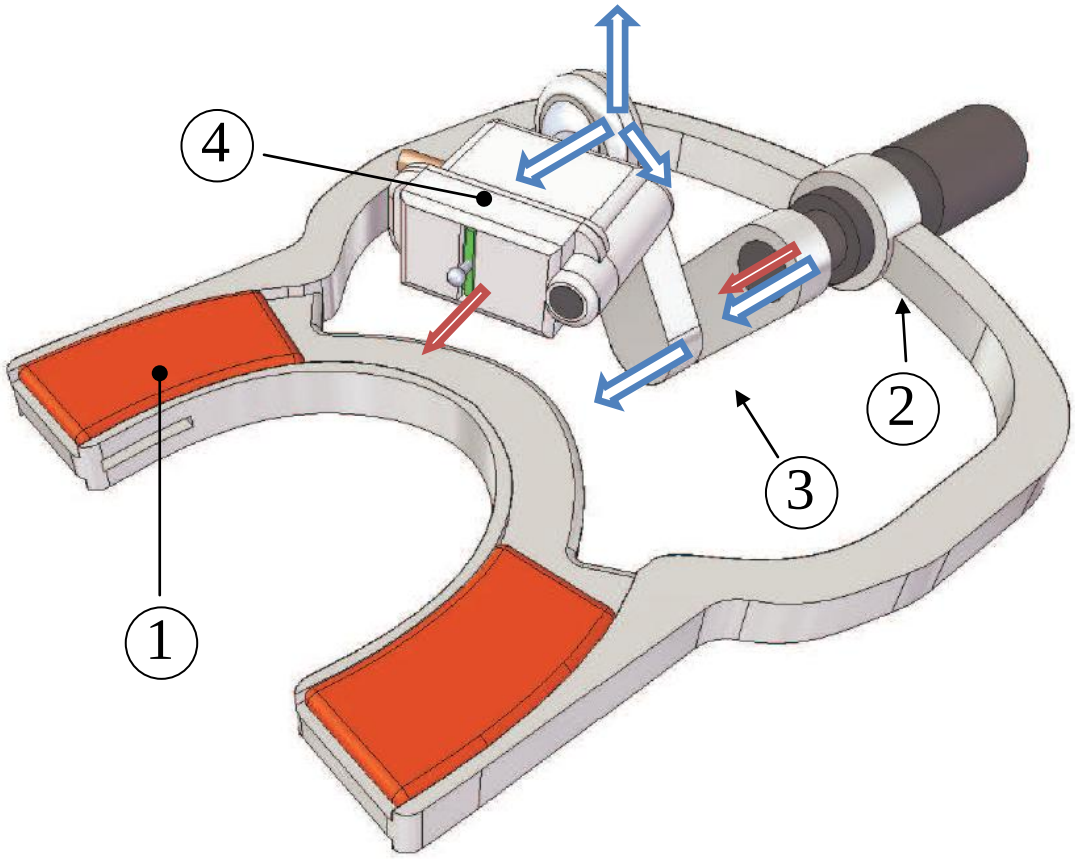

Figure 6-26: Design of the prototype Orthometer for *in vivo* measurements on human teeth: (1) the bite plate, (2) and (3) micrometer screw and lever arm for adjustment and (4) is the core module with containing actuators and sensors. From [196].

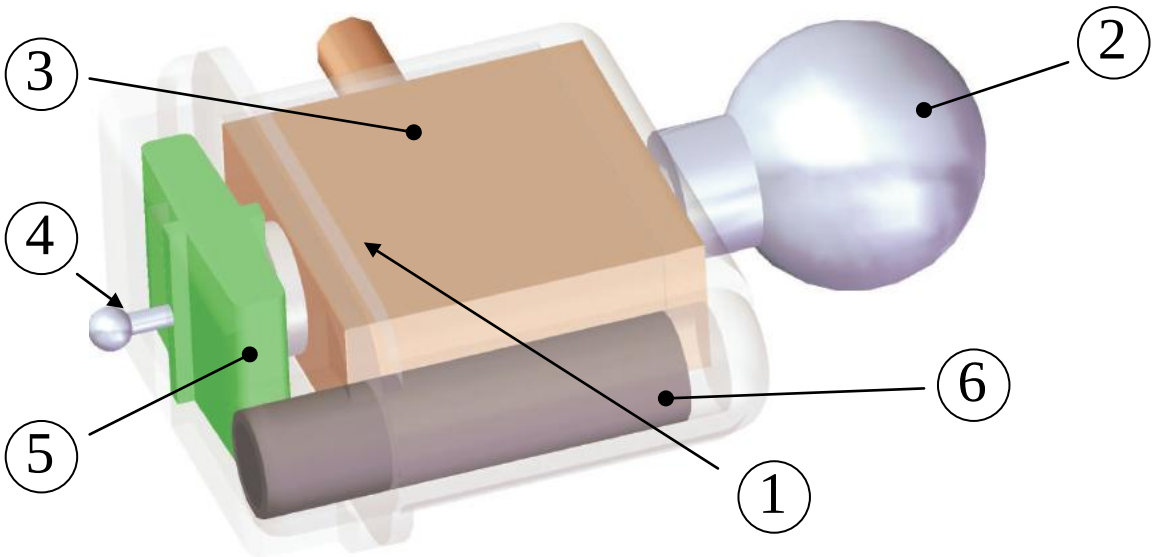

Figure 6-27: Core module for Figure 6:25, with the plastic housing (1), ball joint for adjustment (2), the load cell (3) in series to the piezo actuator (5) with probe (4) and proximity probe (6). From [196]

The device is intended to be used for dynamic measurements on teeth as opposed to the statsic stress-relaxation tests carried out in this work. It is therefore necessary to assess suitable frequencies, based on the static tests. The parameters for the 5-parameter model from Figure 5-48 (c_s=30kN/m, c_1=6kN/m, c_2= 4kN/m d_1=8kNs/m, d_2=200kNs/m) were used in the transfer function (Equation (6-13)), as before and solved through Simulink to obtain the phase and amplitude responses as a function of frequency, as shown in Figure 6-28. As can be seen, the characteristic times translate into clear peaks in the phase difference at 0.003 Hz and 0.11Hz suggesting a similar strategy to that for pig eyeballs, where a coarse sweep of frequencies (or, indeed, mixed frequencies) might be used to reveal characteristic times in an efficient way.

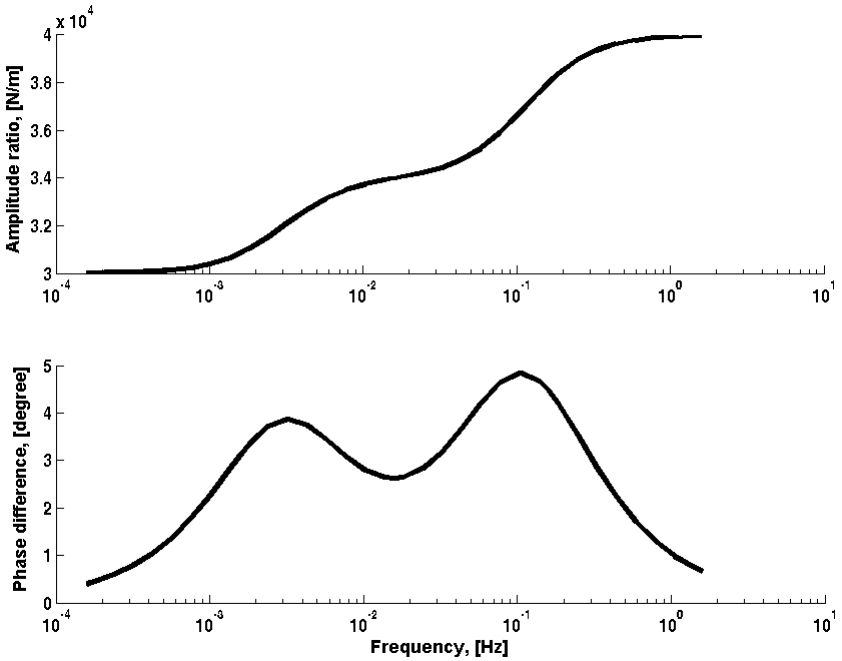

Figure 6-28: Bode diagram for parameters of the PDL

6.4 General discussion on soft tissue properties

Humphrey [10, 148] observed that each soft tissue behaves differently but that there are common characteristics. The force response of a soft tissue to an applied deformation, essentially how it feels, depends on its internal constitution which is defined by the orientations, distributions and interconnections of its micro- and macro- structural components [10, 202] a fact that has been used throughout the ages by clinicians in making diagnoses using palpation.

Although the two material systems investigated (indentation of eyeballs through the cornea and loading the PDL via a tooth) lie in different force and displacement orders (up to 2N and 1.5mm for pig eyeballs and up to 20N and 0.245mm for the pig PDL), and the macroscopic and microscopic orientations, distributions and interconnections are entirely different, some characteristics of both systems were remarkably similar.

Both systems were tested statically, where the decay of force with time was measured at constant deformation. Force relaxation studies for soft tissue are not new and have been presented by Fung [9] for ligaments, by Duenwald *et al.* [203] and by Ciarletta *et al.* [204] for tendons, along with many others. However, the way in which nonlinearity,

hyper elasticity and visco elasticity are reported differ widely with some using a simple power law, others a complex recruitment model and others again using QLV models, as for this work. The deformation history of a tissue is very important to some investigators, the so called "preconditioning" effect. For non-living material, this effect is either due to the tissue not having had enough time to recover after taking the probe away, or to plastic deformation of the tissue which will never recover [203]. Plastic deformation can result from permanent liquid drainage away from the deformed tissue area [205] or plastic sliding or movement of entire collagen fibrils [29, 106, 204].

The time of testing has a critical effect on measured properties, and is the source of most variation in reported properties. For example, in this work, Figure 3-25 clearly shows that the tissue behaviour is not only described by the five force relaxation curves although these give a very consistent measurement. There is a second, much slower retardation time, which can be represented by simply connecting the initial forces of each of the short relaxation curves. Also, fitting the relaxation curves for pig eyeballs (Figure 5-11) or for PDL tissue (Figure 5-34) yields different properties depending on the time allowed for relaxation and the order of model used. This effect was not visible in the dynamic tests where the test times were relatively short with the slowest experiment at 2Hz taking only 5sec for 10 oscillations and only 0.25sec at 40Hz.

However, this is not the only difficulty in applying QLV functions to describe biological tissue mechanical behaviour. The nonlinearity of many soft tissues means that different stiffness parameters will be measured at different strains, as illustrated, for example, in Figure 5-38 for the initial stiffness parameter of PDL at different displacements. Collagen fibres have a non-linear stress-strain behaviour for compression as well as for tension which results in much higher force reading for only a slight increase in displacement [29, 33, 34]. Romero *et al.* [206] devised a "recruitment" model to describe the deformation behaviour of lung tissue, where springs and dampers are latched (recruited) into a multi-component SLS model as the deformation increases, Figure 6-29. Equally, the sequential de-recruitment of SLS elements was used in their study to explain the force relaxation of lung tissue over 10 sec. Romero *et al.* obtained very good results although it must be said that applying 9 parameters will almost inevitably produce a good fit. They used one stiffness for all springs and one viscous parameter for all dashpots, simply varying the number of

elements and the strains at which they are recruited. The approach taken in the current work attempts to devise a single set of parameters for all strains, and at least has the advantage of allowing a comparison with other workers, notwithstanding the difficulties with non-linear stress-strain curves.

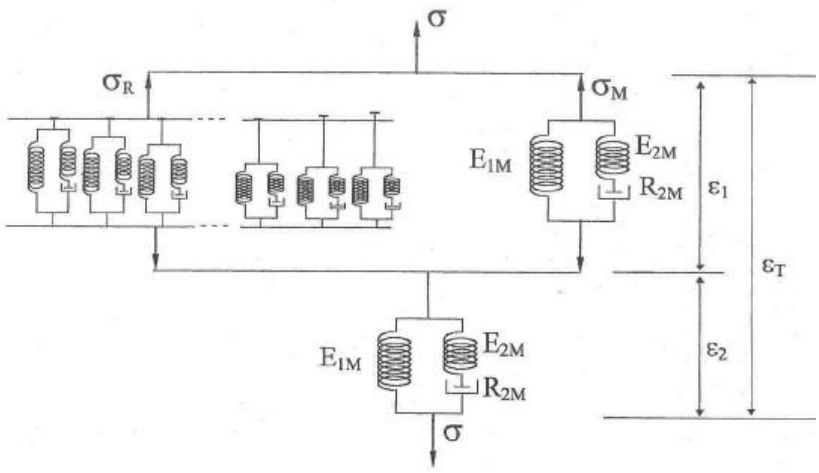

Figure 6-29: Recruitment model by Romero *et al.* [206]. Where all recruted SLS models (left with tensile stress σ_R) have the parameter E_{1M}, E_{2M} and R_{2M}.

The fitting of competing models to any set of stress-strain data requires a judgement as to how many parameters to include and the guiding principle in this work has been to find the simplest model (least parameters) which acceptably describes the data. The R^2 value has been used extensively as it measures how far away, on average, the points are from the fitted curve. This has drawbacks, especially in the fitting of exponential curves where longer times with, say, a single relaxation exponential will inevitably produce a poor fit at the initial stages and distort results. This behaviour explains why, for example, in Figure 5-38 the 5- and 4- parameter models suggested the highest initial stiffness parameters and why, in Figure 5-43, the highest stiffness parameters are suggested for a very short observation time.

Some authors, such as Bates *et al.* [207], Hildebrandt [208] and Suki *et al.* [209] have used a power law $t^{-\beta}$ (where t is the time and β is a constant) or a combination of power law and recruitment model, to describe nonlinear force relaxation. The power law is very effective in fitting force relaxation curves with very few parameters, although it does not translate easily into familiar terms such as stiffness and relaxation time. The power law used by Suki *et al.* [209] can be stated:

$$F(t) = cx(t) + QD^{\beta} \cdot x(t) \tag{6-19}$$

where the first term is the elastic term and the second term is called the fractional calculus element, with Q as the viscous parameter and with D^{β} as the fractional derivative operator. It can be seen that $\beta = 1$ (corresponding to a first derivative) has the same properties as a regular dashpot so that the power law equation reduces to the differential equation which arises from a simple Kelvin model (spring and a dashpot in parallel). If $\beta = 0$ the second term becomes an elastic spring parameter as is the first term, so the model becomes linear elastic. For the model to work properly, the value of β has to be between zero and 1. The power law can also be used to describe dynamic behaviour. The so called constant–phase model has been used to describe lung tissue very successfully. This model gives an increase in resistance of the tissue to deformation with increasing frequency while the phase remains constant [209, 210]. For this reason, the power law is not applicable to much of the data recorded here, including cornea tissue, where the phase changes with frequency.

Similar behaviour to the power law can be produced by simply adding more and more Maxwell components to a multi component generalized Maxwell model (Figure 3-9) with only slightly different retardation times. This would allow the complex modulus to constantly increase with increasing frequency, but the phase difference would be constant but non-zero (Figure 6-30).

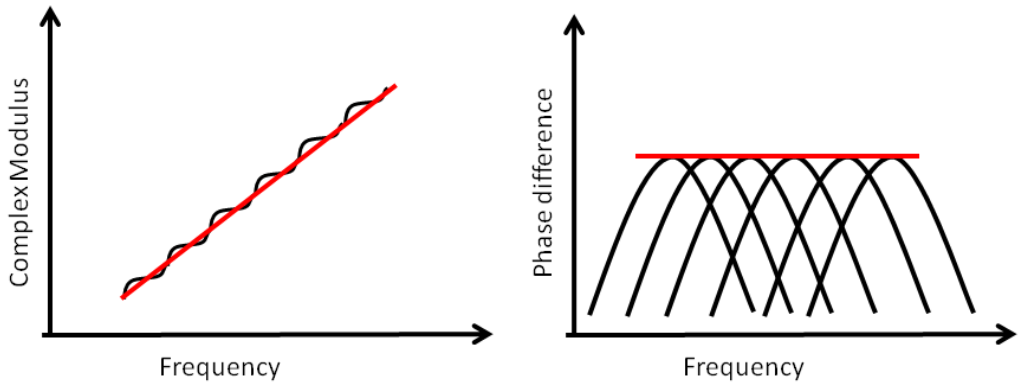

Figure 6-30: Constant phase model using a multi component generalized Maxwell model

Chapter 7: Conclusions

Generally, it has been found that the technique of instrumented palpation can deliver the broad aim of the work, which was to yield a relationship between tissue structure and the mechanical properties of soft biological tissue. This has been shown in particular for the two systems under investigation, the eyeball and the tooth-PDL-mandible system.

For the eyeball, with the use of dynamic palpation:

- The mechanical eyeball results show that it is possible to separate IOP from membrane thickness by using the damper parameter of an SLS model.
- The separation of membrane thickness and IOP was even better using MSD models, provided that the applied frequency was in the resonance area of the mechanical eyeball (configuration open – pressurised).
- The finding that it is possible to separate IOP from membrane thickness by using the damper parameter can be applied to the *in vitro* tests for pig eyes.
- It is possible to focus on certain frequency windows, which allow separation of multiple retardation times that are represented by the sum of several Maxwell components.
- The clinical applanation frequency was found to be most effective between 18-24Hz. At these frequencies, the IOP versus amplitude ratio correlation shows the highest R^2 and measurements with an accuracy of ±7mmHg were possible (slightly above the ISO standard for clinical tonometers (±5mmHg)).
- At 12 Hz, the pig eyeball behaves as if 21% viscous and 79% elastic (12° phase difference) which changes to 100% elastic behaviour (0° phase difference) above 20Hz.

Further contributions relevant to clinical tonometers:

- Using the results from this work, it has been found that the error in IOP reading of current tonometers can be attributed to a combination of IOP increase itself, and the effect of IOP in increasing the stiffness of the cornea. Therefore thicker corneas with higher IOP will have a much higher IOP error than thicker corneas at low IOP. The force required to deform the cornea was found to be:

$$F = k * E * t^{2.5}$$

where *E* is the effective Young's modulus (itself related to the IOP) *k* is a constant factor related to cornea curvature, indentation depth and indentation area and *t* is the thickness of the cornea. This behaviour further complicates the separation of IOP from cornea stiffness.

- The apparent complex modulus *E** increases with increasing pressure and with increasing frequency. The increase of *E** from low frequency (2Hz) to high frequency (40Hz) was 1.5 times higher for low pressure and up to 3 times higher for high pressure.

Contribution made to measuring the PDL in vivo:

- The applied displacement should not exceed a value of about 5µm at 5.8mm apically from the crest, otherwise the stress in the apex area of the root becomes higher than the blood pressure in the PDL (16kPa) and destroys the tissue.
- The allowed relaxation time of the force relaxation curve has a major influence on the choice of the QLV model.
- It was found that PDL has several retardation times, and, by simulation of the 5-parameter model appropriate frequencies of around 0.01Hz to 0.1Hz were found. In this frequency range, amplitude ratio transitions and phase lags should appear.
- For improving OTM, a short test within an acceptable time is the only way to test patients *in vivo*. The dynamic indentation method reduces the application time and helps to find the right visco elastic force displacement parameters which can be applied to generate a painless, riskless OTM without root resorption. If sufficiently non-invasive, the test could be performed on each individual front tooth.

Chapter 8: Future work

This chapter describes some areas for immediate development suggested by the work in the thesis. These areas are essentially about practical applications, firstly in eyeball palpation and secondly in measurement of the PDL. Finally some initial evaluation of a micro-fabricated palpation device is described. This device was originally designed for trans-urethral palpation of the prostate, but its principles could be adapted to other applications.

8.1 Future work for measuring the mechanical properties of eyeballs

Improvement of the dynamic palpation device to monitor mechanical properties

The test rig designed for this work uses a piezo driven actuator to provide the oscillating and the load cell for measuring the force is carried with the actuator. The load cell has to be in series with the actuator and could not be installed on the sample mount because of the variety of sizes and clamping arrangements for the samples (eyeballs in cylindrical aluminium cavity). This would be equally the case in a clinical application, where the reaction in the eye socket cannot be measured any more easily than could be the IOP itself. The inertia forces resulting from the acceleration of the load cell distort the force reading and this needed to be filtered out by using the superposition principle as described in chapter 3. This is time consuming and limits the upper frequency that can be used, as well as inhibiting search for frequencies where the force amplitude decreases or increases or phase differences between displacement and force arise.

However, installing an accelerometer in parallel with the load cell will allow a direct measurement of the inertia force allowing it to be subtracted from the load measurement while palpating on the tissue [211] in real time. One critical issue is the test time required to obtain a diagnosis. In the experiments, a frequency bandwidth from 2 – 60 Hz in 2Hz steps was applied by switching a signal generator manually between the frequencies. For *in vivo* measurement, tissue should be tested with a minimum number of cycles and therefore the signal generator could be controlled by LabView to increase

or decrease the frequency automatically, and record only ten cycles at each frequency. Alternatively, mixed frequencies could be used and the data deconvoluted after testing.

Further investigation on the indenter size for dynamic probing on porcine eyeballs

Goldmann [5, 193] chose the indenter size to achieve a balance between the surface tension of the tear film and the stiffness of an average cornea, thus making the IOP error dependent on CCT. For dynamic palpation, the influence of the visco- elastic cornea can be altered by increasing or decreasing the indenter size. This behaviour could be very useful for investigating the effect of cornea stiffness as well as IOP. If a smaller indenter area has less influence on the IOP reading, than there might be a good chance to increase the influence of the stiffness reading of the cornea itself. This would help to find more information about cornea properties. Reduction of the indenter area has to be done carefully to avoid the danger of pain or damage to patients during an *in vivo* test. Also, enlarging the indenter from the original 3.06mm diameter could help to improve the accuracy of measurement of IOP. Using a bigger applanation area would result in higher forces and so the inertia forces would be less significant.

8.2 Future work for measuring the mechanical properties on periodontal ligament using the dynamic method

Static testing of PDL can be used to find significant frequencies for more detailed dynamic testing as was done in this work. A 5 parameter model was used to obtain a response with two characteristic times and the dynamic response was simulated using a transfer function and feedback control system. The simulated response shows that a dynamic test should be able to detect characteristic times (and hence visco elastic parameters) in the phase-frequency and amplitude-frequency plots (Figure 8-1). Again, instead of frequency-scanning, mixed frequencies could be used to improve the efficiency of measurement in an *in vivo* application.

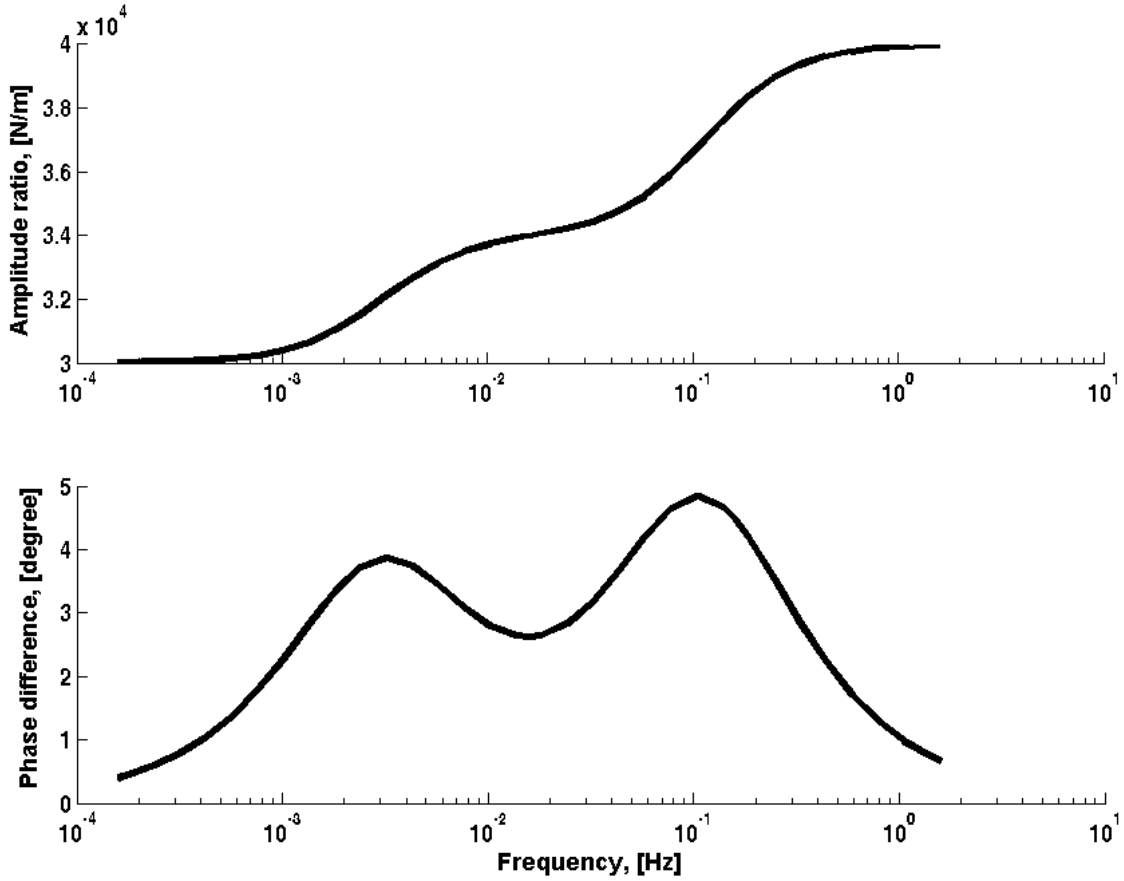

Figure 8-1: Bode diagram for parameters of the PDL

References

1 Fatemi, M., Manduca, A. and Greenleaf, J. F. (2003). "Imaging elastic properties of biological tissues by low-frequency harmonic vibration." *Proceedings of the IEEE*, 91(10), 1503-18.

2 The National Collaborating Centre for Acute Care. (2009). "Glaucoma: diagnosis and management of chronic open angle glaucoma and ocular hypertension - methods, evidence and guidance." Commissioned by the National Institute for Health and Clinical Excellence, ed., The National Collaborating Centre for Acute Care at The Royal College of Surgeons of England, London.

3 Collaborative Normal-Tension Glaucoma Study Group. (1998). "The effectiveness of intraocular pressure reduction in the treatment of normal-tension glaucoma. ." *Am J Ophthalmol*, 126(4), 498-505.

4 Heijl, A., Leske, M. C., Bengtsson, B., *et al.* (2002). "Reduction of intraocular pressure and glaucoma progression: results from the Early Manifest Glaucoma Trial." *Arch Ophthalmol*, 120(10), 1268-79.

5 Goldmann, H., and Schmidt, T. (1957). "Applanation tonometry." *Ophthalmologica*, 134(4), 221-42.

6 Goldmann, H., and Schmidt, T. (1957). "Friedenwald's rigidity coefficient." *Ophthalmologica*, 133(4-5), 330-5; discussion, 335-6.

7 Pilon, J. J., Kuijpers-Jagtman, A. M., and Maltha, J. C. (1996). "Magnitude of orthodontic forces and rate of bodily tooth movement. An experimental study." *Am J Orthod Dentofacial Orthop*, 110(1), 16-23.

8 Noda, K., Nakamura, Y., Oikawa, T., *et al.* (2006). "Tooth movement limited to periodontal ligament width using interrupted orthodontic force." *Orthodontic waves*, 65, 73-80.

9 Fung, Y. C. (1993). *Biomechanics, mechanical properties of living tissues.*,Springer-Verlag, New York.

10 Humphrey, J. D. (2003). "Review paper: Continuum biomechanics of soft biological tissue." *Proc R Soc Lond A*, 459, 3-46.

11 Humphrey, J. D. (2002). *Cardiovascular solid mechanics: cells, tissues and organs*,Springer-Verlag, New York.

12 Seeley, R. R., Stephens, T. D., and Tate, P. (2003). *Anatomy & physiology*,6th ed.; McGraw-Hill, New York.

13 Williams, P., and Warwick, R. (1980). *Gray's anatomy*,36th ed.; Churchill, Livingstone.

14 Wheater, P. R., Heath, J. W., and Young, B. (2000). *Wheater's functional histology: a text and colour atlas*,4th edition; Churchill Livingstone.

15 Fung, Y. C., and Sobin, S. S. (1981). "The retained elasticity of elastin under fixation agents." *J Biomech Eng*, 103(121).

16 Carlton, R. W., Dainauskas, J., and Clark, J. W. (1962). "Elastic properties of single elastic fibers." *Journal of Applied Physiology*, 17, 547-551.

17 McCrum, N. G., Buckley, C. P., and Bucknall, C. B. (1997). *Principles of polymer engineering*,2nd ed.; OUP, Oxford.

18 Hoeve, C. A. J., and Flory, P. J. (1958). "The elastic properties of elastin." *J Appl Physiol*, 80, 6523-6526.

19 Lillie, M. A., and Gosline, J. M. (2007). "Mechanical properties of elastin along the thoracic aorta in the pig." *J Biomech*, 40(10), 2214-21.

20 Lillie, M. A., and Gosline, J. M. (2002). "The viscoelastic basis for the tensile strength of elastin." *Int J Biol Macromol*, 30(2), 119-27.
21 Yang, J. (2007). "Structure-properties in biological tissues ", Heriot Watt University,Edinburgh.
22 Yang, L. (2008). "Mechanical properties of collagen fibrils and elastic fibers explored by AFM," University of Twente,Enschede.
23 Silver, F. H., Freeman, J. W., and Seehra, G. P. (2003). "Collagen self-assembly and the development of tendon mechanical properties." *J Biomech*, 36(10), 1529-53.
24 Soderhall, C., Marenholz, I., Kerscher, T., *et al.* (2007). "Variants in a novel epidermal collagen gene (COL29A1) are associated with atopic dermatitis." *PLoS Biol*, 5(9), e242.
25 Berkovitz, B. K. (1990). "The structure of the periodontal ligament: an update." *Eur J Orthod*, 12(1), 51-76.
26 Sun, Y., Luo, Z., and An, K. "Mechanical properties of single type II collagen molecule." *48th Annual Meeting of the Orthopaedic Research Society*, Dallas.
27 Sun, Y. L., Luo, Z. P., Fertala, A., *et al.* (2004). "Stretching type II collagen with optical tweezers." *J Biomech*, 37(11), 1665-9.
28 Lodish, H., Berk, A., Zipursky, L., *et al. Molecular Cell Biology*,5th ed.; W.H. Freeman and Company, New York.
29 Puxkandl, R., Zizak, I., Paris, O., *et al.* (2002). "Viscoelastic properties of collagen: synchrotron radiation investigations and structural model." *Philos Trans R Soc Lond B Biol Sci*, 357(1418), 191-7.
30 Wang, J. H. (2006). "Mechanobiology of tendon." *J Biomech*, 39(9), 1563-82.
31 Dowling, B. A., and Dart, A. J. (2005). "Mechanical and functional properties of the equine superficial digital flexor tendon." *Vet J*, 170(2), 184-92.
32 Yang, L., van der Werf, K. O., Fitie, C. F., *et al.* (2008). "Mechanical properties of native and cross-linked type I collagen fibrils." *Biophys J*, 94(6), 2204-11.
33 Wu, J. J. (2006). "Quantitative constitutive behaviour and viscoelastic properties of fresh flexor tendons." *Int J Artif Organs*, 29(9), 852-7.
34 Lynch, H. A., Johannessen, W., Wu, J. P., *et al.* (2003). "Effect of fiber orientation and strain rate on the nonlinear uniaxial tensile material properties of tendon." *J Biomech Eng*, 125(5), 726-31.
35 Wenger, M. P., Bozec, L., Horton, M. A., *et al.* (2007). "Mechanical properties of collagen fibrils." *Biophys J*, 93(4), 1255-63.
36 Stromberg, D. D., and Wiederhielm, C. A. (1969). "Viscoelastic description of a collagenous tissue in simple elongation." *J Appl Physiol*, 26(6), 857-62.
37 Hubbard, R. P., and Chun, K. J. (1988). "Mechanical responses of tendons to repeated extensions and wait periods." *J Biomech Eng*, 110(1), 11-9.
38 Martini, F., Garrison, C., Welch, K., *et al.* (2001). *Fundamentals of anatomy and physiology*,5th ed.; Prentice Hall.
39 Drescher, J. (2000). "Bestimmung des Intraoculardrucks aus dem Schwingungsverhalten des Humanauges," University Fridericiana Karlsruhe.
40 Human eye (Anatomy). (1994). "Encyclopædia Britannica." available from: http://www.britannica.com/EBchecked/topic/199272/eye.
41 To, C. H., Kong, C. W., Chan, C. Y., *et al.* (2002). "The mechanism of aqueous humour formation." *Clin Exp Optom*, 85(6), 335-49.
42 Grant, M. (1955). "Physiological and pharmacological influences upon intraocular pressure " *Pharmacological Reviews*, Vol 7, 143-182.

43 Heys, J. J., Barocas, V. H., and Taravella, M. J. (2001). "Modeling passive mechanical interaction between aqueous humor and iris." *J Biomech Eng*, 123(6), 540-7.

44 Fontana, S. T., and Brubaker, R. F. (1980). "Volume and depth of the anterior chamber in the normal aging human eye." *Arch Ophthalmol*, 98(10), 1803-8.

45 Huang, E. C., and Barocas, V. H. (2006). "Accommodative microfluctuations and iris contour." *J Vis*, 6(5), 653-60.

46 Heys, J., and Barocas, V. (2002). "Computational evaluation of the role of accommodation in pigmentary glaucoma." *Invest Ophthalmol Vis Sci*, 43, 700-708.

47 Farmati, O., Freeman, A., and Moya, F. (1967). "Changes in retinal arterial blood pressure during cyclopropane and halothane anaesthesia in children." *Can Anaesth Soc J*, 14(1), 26-32.

48 Silver, D. M., and Quigley, H. A. (2004). "Aqueous flow through the iris-lens channel: estimates of differential pressure between the anterior and posterior chambers." *J Glaucoma*, 13(2), 100-7.

49 National Eye Institute, N. I. o. H. (2008). "NEA11." available from: http://www.nei.nih.gov/photo/.

50 Johnstone, M. A. (2004). "The aqueous outflow system as a mechanical pump: evidence from examination of tissue and aqueous movement in human and nonhuman primates." *J Glaucoma*, 13, 421–438.

51 Johnstone, M. A. (2006). "A new model describes an aqueous outflow pump and explores causes of pump failure in glaucoma." Glaucoma, F. Grehn and R. Stamper, eds., Springer-Verlag Berlin.

52 Johnson, M. C., and Kamm, R. D. (1983). "The role of Schlemm's canal in aqueous outflow from the human eye." *Invest Ophthalmol Vis Sci*, 24(3), 320-5.

53 Johnstone, M. A. (1979). "Pressure-dependent changes in nuclei and the process origins of the endothelial cells lining Schlemm's canal." *Invest Ophthalmol Vis Sci*, 18(1), 44-51.

54 Andreassen, T. T., Simonsen, A. H., and Oxlund, H. (1980). "Biomechanical properties of keratoconus and normal corneas." *Exp Eye Res*, 31(4), 435-41.

55 Al-Sereiti, M. R., Quik, R. F., and Turner, P. (1989). "The effect of a single oral dose of pergolide on intraocular pressure and pupil diameter." *Br J Clin Pharmacol*, 28(3), 263-8.

56 Doughty, M. J., and Zaman, M. L. (2000). "Human corneal thickness and its impact on intraocular pressure measures: a review and meta-analysis approach." *Surv Ophthalmol*, 44(5), 367-408.

57 Feltgen, N., Leifert, D., and Funk, J. (2001). "Correlation between central corneal thickness, applanation tonometry, and direct intracameral IOP readings." *Br J Ophthalmol*, 85(1), 85-7.

58 Elsheikh, A., Wang, D., Kotecha, A., *et al.* (2006). "Evaluation of Goldmann applanation tonometry using a nonlinear finite element ocular model." *Ann Biomed Eng*, 34(10), 1628-40.

59 Liu, J., and Roberts, C. J. (2005). "Influence of corneal biomechanical properties on intraocular pressure measurement: quantitative analysis." *J Cataract Refract Surg*, 31(1), 146-55.

60 Moreale, B. (2007). "Living with glaucoma." A Program of the American Health Assistance Foundation, Nationa lGlaucoma Research, ed., http://www.ahaf.org/, 35.

61 Smolek, M. K. (1994). "Holographic interferometry of intact and radially incised human eye-bank corneas." *J Cataract Refract Surg*, 20(3), 277-86.

62 Elsheikh, A., Wang, D., and Pye, D. (2007). "Determination of the modulus of elasticity of the human cornea." *J Refract Surg*, 23(8), 808-18.
63 Elsheikh, A., Wang, D., Brown, M., *et al.* (2007). "Assessment of corneal biomechanical properties and their variation with age." *Curr Eye Res*, 32(1), 11-9.
64 Jue, B., and Maurice, D. M. (1986). "The mechanical properties of the rabbit and human cornea." *J Biomech*, 19(10), 847-53.
65 Hoeltzel, D. A., Altman, P., Buzard, K., *et al.* (1992). "Strip extensiometry for comparison of the mechanical response of bovine, rabbit, and human corneas." *J Biomech Eng*, 114(2), 202-15.
66 Foster, C. S., and Yamamoto, G. K. (1978). "Ocular rigidity in keratoconus." *Am J Ophthalmol*, 86(6), 802-6.
67 Nash, I. S., Greene, P. R., and Foster, C. S. (1982). "Comparison of mechanical properties of keratoconus and normal corneas." *Exp Eye Res*, 35(5), 413-24.
68 Kaufman, P. L., and Gabelt, B. A. T. (2006). "Future of IOP-lowering medication for glaucoma therapy." Glaucoma, F. Grehn and R. Stamper, eds., Springer-Verlag, Berlin.
69 Foster, P. J., and Thomas, R. (2004). "Glaucoma care in developing countries of Asia." *Invest Ophthalmol Vis Sci*, 45(9), 3118-21.
70 Foster, P., Oen, F., Machin, D., *et al.* (2000). "The prevalence of glaucoma in Chinese residents of Singapore. A cross-sectional population survey in Tanjong Pagar district." *Arch Ophthalmol*, 118, 1105–1111.
71 Coleman, A. L. (1999). "Glaucoma." *Lancet* 354, 1803–10.
72 Mayo Foundation for Medical Education and Research (MFMER). (© 1998-2009). "Glaucoma." available from : http://www.mayoclinic.com/.
73 Draeger, J. (1993). *Tonometrie*, Georg Thieme Verlag, New York.
74 Anderson, K., El-Sheikh, A., and Newson, T. (2004). "Application of structural analysis to the mechanical behaviour of the cornea." *J R Soc Interface*, 1(1), 3-15.
75 Tonnu, P. A., Ho, T., Newson, T., *et al.* (2005). "The influence of central corneal thickness and age on intraocular pressure measured by pneumotonometry, non-contact tonometry, the Tono-Pen XL, and Goldmann applanation tonometry." *Br J Ophthalmol*, 89(7), 851-4.
76 Friedenwald, J. (1937). "Contribution to the theory and practice of tonometry." *American Journal of Ophthalmology*, 20, 985-1025.
77 Saeteren, T. (1960). "Scleral rigidity in normal human eyes." *Acta Ophthalmol*, 38, 303-11.
78 Elsheikh, A., Alhasso, D., and Rama, P. (2008). "Biomechanical properties of human and porcine corneas." *Exp Eye Res*, 86(5), 783-90.
79 Razeghinejad, M.-R., Amini, H., Torkaman, F., *et al.* (2007). "Correlation of central corneal thickness with Schiotz and Goldmann tonometry." *Iranian Journal of Ophthalmic Research*, 2(2), 101-106.
80 Moses, R. A. (1971). "Theory and calibration of the Schiotz tonometer. IV. A mathematical model of Schiotz tonometry: scale reading and tonometric pressure." *Invest Ophthalmol*, 10(8), 592-600.
81 Moses, R. A., and Grodzki, W. J. (1971). "Theory and calibration of the Schiotz tonometer. VI. Experimental results of tonometric measurements: scale reading versus tonometric pressure." *Invest Ophthalmol*, 10(9), 710-5.
82 Moses, R. A., and Grodzki, W. J. (1971). "Theory and calibration of the Schiotz tonometer. 3. Friction between tonometer footplate and cornea." *Invest Ophthalmol*, 10(8), 589-91.

83 Danielsen, C. C. (2004). "Tensile mechanical and creep properties of Descemet's membrane and lens capsule." *Exp Eye Res*, 79(3), 343-50.
84 Pallikaris, I. G., Kymionis, G. D., Ginis, H. S., *et al.* (2005). "Ocular rigidity in living human eyes." *Invest Ophthalmol Vis Sci*, 46(2), 409-14.
85 Sticksel, H. A. (1965). "Calibration and validation of tonometers." *The Australian Journal of Optometry*, 48(5), 131-135.
86 Fick, A. (1888). "Ueber Messung des Druckes im Auge " *Pflügers Archiv European Journal of Physiology*, 42(1), 86-90.
87 Haag-Streit International AG. (2008). *Goldmann AT 900/870 Applanation Tonometer to slit lamp*, Koeniz.
88 Boehm, A. G., Weber, A., Pillunat, L. E., *et al.* (2008). "Dynamic contour tonometry in comparison to intracameral IOP measurements." *Invest Ophthalmol Vis Sci*, 49(6), 2472-7.
89 Shimmyo, M., Ross, A. J., Moy, A., *et al.* (2003). "Intraocular pressure, Goldmann applanation tension, corneal thickness, and corneal curvature in Caucasians, Asians, Hispanics, and African Americans." *Am J Ophthalmol*, 136(4), 603-13.
90 Kniestedt, C., Lin, S., Choe, J., *et al.* (2005). "Clinical comparison of contour and applanation tonometry and their relationship to pachymetry." *Arch Ophthalmol*, 123(11), 1532-7.
91 Mackay, R. S., and Marg, E. (1959). "Fast, automatic, electronic tonometers based on an exact theroy." *Acta Ophthalmol* 37, 495-507.
92 Kanngiesser, H., and Kniestedt, C. (2005). "Tonometry in change. From indentation and applanation to contour adaptation." *Ophthalmologe*, 102(9), 849-55.
93 Kanngieser, H. (2005). "Device for measuring intraocular pressure, in particular pressure, in particular a tonometer." United States Patent, ODC Ophthalmic Development Company AG, Zurich (CH), Switzerland.
94 Schneider, E., Kanngiesser, H. E., and Kniestedt, C. (2006). "Dynamic contour tonometry." Essentials in Ophthalmology, Springer-Verlag, Berlin.
95 ElMallah, M. K., and Asrani, S. G. (2008). "New ways to measure intraocular pressure." *Curr Opin Ophthalmol*, 19(2), 122-6.
96 Francis, B. A., Hsieh, A., Lai, M. Y., *et al.* (2007). "Effects of corneal thickness, corneal curvature, and intraocular pressure level on Goldmann applanation tonometry and dynamic contour tonometry." *Ophthalmology*, 114(1), 20-6.
97 Hallberg, P. (2006). "Applanation resonance tonometry for intraocular pressure measurement," University Umea,Sweden.
98 Doughty, M. J., Laiquzzaman, M., Muller, A., *et al.* (2002). "Central corneal thickness in European (white) individuals, especially children and the elderly, and assessment of its possible importance in clinical measures of intra-ocular pressure." *Ophthalmic Physiol Opt*, 22(6), 491-504.
99 Kohlhaas, M., Boehm, A. G., Spoerl, E., *et al.* (2006). "Effect of central corneal thickness, corneal curvature, and axial length on applanation tonometry." *Arch Ophthalmol*, 124(4), 471-6.
100 Martinez-de-la-Casa, J. M., Garcia-Feijoo, J., Fernandez-Vidal, A., *et al.* (2006). "Ocular response analyzer versus Goldmann applanation tonometry for intraocular pressure measurements." *Invest Ophthalmol Vis Sci*, 47(10), 4410-4.
101 Davidovitch, Z., and Krishnan, V. (2009). "Role of basic biological sciences in clinical orthodontics: a case series." *Am J Orthod Dentofacial Orthop*, 135(2), 222-31.

102 Ren, Y., Maltha, J. C., and Kuijpers-Jagtman, A. M. (2003). "Optimum force magnitude for orthodontic tooth movement: a systematic literature review." *Angle Orthod*, 73(1), 86-92.

103 Proffit, W. R., Fields, H. W., and Sarver, D. M. (2007). *Contemporary orthodontics*,4th ed., Mosby.

104 Dorow, C., Krstin, N., and Sander, F.-G. (2003). "Determination of the mechanical properties of the periodontal ligament in an uniaxial tensional experiment." *Journal of Orofacial Orthopedics*, 64, 100-7.

105 Toms, S. R., Dakin, G. J., Lemons, J. E., *et al.* (2002). "Quasi-linear viscoelastic behavior of the human periodontal ligament." *J Biomech*, 35(10), 1411-5.

106 Pini, M., Zysset, P., Botsis, J., *et al.* (2004). "Tensile and compressive behaviour of the bovine periodontal ligament." *J Biomech*, 37(1), 111-9.

107 Pini, M., Wiskott, H. W., Scherrer, S. S., *et al.* (2002). "Mechanical characterization of bovine periodontal ligament." *J Periodontal Res*, 37(4), 237-44.

108 Middleton, J., Jones, M., and Wilson, A. (1996). "The role of the periodontal ligament in bone modeling: the initial development of a time-dependent finite element model." *Am J Orthod Dentofacial Orthop*, 109(2), 155-62.

109 van Driel, W. D., van Leeuwen, E. J., Von den Hoff, J. W., *et al.* (2000). "Time-dependent mechanical behaviour of the periodontal ligament." *Proc Inst Mech Eng H*, 214(5), 497-504.

110 Cattaneo, P. M., Dalstra, M., and Melsen, B. (2009). "Strains in periodontal ligament and alveolar bone associated with orthodontic tooth movement analyzed by finite element." *Orthod Craniofac Res*, 12(2), 120-8.

111 Tohill, R. (2008). "Development of a device to study the mechanical properties of the periodontal ligament," MSc thesis, Postgraduate Dental Institute, University of Edinburgh, Edinburgh.

112 Grimm, F. M. (1972). "Bone bending, a feature of orthodontic tooth movement." *Am J Orthod*, 62(4), 384-93.

113 McGuinness, N. J., Wilson, A. N., Jones, M. L., *et al.* (1991). "A stress analysis of the periodontal ligament under various orthodontic loadings." *Eur J Orthod*, 13(3), 231-42.

114 Provatidis, C. G. (2000). "A comparative FEM-study of tooth mobility using isotropic and anisotropic models of the periodontal ligament. Finite Element Method." *Med Eng Phys*, 22(5), 359-70.

115 Norton, L. A. (1988). "The effect of aging cellular mechanisms on tooth movement." *Dent Clin North Am*, 32(3), 437-46.

116 Sandy, J. R., Farndale, R. W., and Meikle, M. C. (1993). "Recent advances in understanding mechanically induced bone remodeling and their relevance to orthodontic theory and practice." *Am J Orthod Dentofacial Orthop*, 103(3), 212-22.

117 Davidovitch, Z. (1991). "Tooth movement." *Crit Rev Oral Biol Med*, 2(4), 411-50.

118 Rygh, P. (1973). "Ultrastructural changes of the periodontal fibers and their attachment in rat molar periodontium incident to orthodontic tooth movement." *Scand J Dent Res*, 81(6), 467-80.

119 Pryputniewicz, R. J., and Burstone, C. J. (1979). "The effect of time and force magnitude on orthodontic tooth movement." *J Dent Res*, 58(8), 1754-64.

120 Burstone, C. J., Pryputniewicz, R. J., and Bowley, W. W. (1978). "Holographic measurement of tooth mobility in three dimensions." *J Periodontal Res*, 13(4), 283-94.

121 Choy, K., Pae, E. K., Park, Y., *et al.* (2000). "Effect of root and bone morphology on the stress distribution in the periodontal ligament." *Am J Orthod Dentofacial Orthop*, 117(1), 98-105.

122 Tomizuka, R., Kanetaka, H., Shimizu, Y., *et al.* (2006). "Effects of gradually increasing force generated by permanent rare earth magnets for orthodontic tooth movement." *Angle Orthod*, 76(6), 1004-9.

123 Kohno, T., Matsumoto, Y., Kanno, Z., *et al.* (2002). "Experimental tooth movement under light orthodontic forces: rates of tooth movement and changes of the periodontium." *J Orthod*, 29(2), 129-35.

124 Tanne, K., Yoshida, S., Kawata, T., *et al.* (1998). "An evaluation of the biomechanical response of the tooth and periodontium to orthodontic forces in adolescent and adult subjects." *Br J Orthod*, 25(2), 109-15.

125 Rees, J. S., and Jacobsen, P. H. (1997). "Elastic modulus of the periodontal ligament." *Biomaterials*, 18(14), 995-9.

126 Dorow, C., Krstin, N., and Sander, F. G. (2002). "Experiments to determine the material properties of the periodontal ligament." *J Orofac Orthop*, 63(2), 94-104.

127 Komatsu, K., Sanctuary, C., Shibata, T., *et al.* (2007). "Stress-relaxation and microscopic dynamics of rabbit periodontal ligament." *J Biomech*, 40(3), 634-44.

128 Komatsu, K., and Viidik, A. (1996). "Changes in the fibre arrangement of the rat incisor periodontal ligament in relation to various loading levels *in vitro*." *Arch Oral Biol*, 41(2), 147-59.

129 Jonsdottir, S. H., Giesen, E. B., and Maltha, J. C. (2006). "Biomechanical behaviour of the periodontal ligament of the beagle dog during the first 5 hours of orthodontic force application." *Eur J Orthod*, 28(6), 547-52.

130 Andersen, K. L., Pedersen, E. H., and Melsen, B. (1991). "Material parameters and stress profiles within the periodontal ligament." *Am J Orthod Dentofacial Orthop*, 99(5), 427-40.

131 Andersen, K. L., Mortensen, H. T., Pedersen, E. H., *et al.* (1991). "Determination of stress levels and profiles in the periodontal ligament by means of an improved three-dimensional finite element model for various types of orthodontic and natural force systems." *J Biomed Eng*, 13(4), 293-303.

132 Tanne, K., and Sakuda, M. (1983). "Initial stress induced in the periodontal tissue at the time of the application of various types of orthodontic force: three-dimensional analysis by means of the finite element method." *J Osaka Univ Dent Sch*, 23, 143-71.

133 Tanne, K., Sakuda, M., and Burstone, C. J. (1987). "Three-dimensional finite element analysis for stress in the periodontal tissue by orthodontic forces." *Am J Orthod Dentofacial Orthop*, 92(6), 499-505.

134 Williams, K. R., and Edmundson, J. T. (1984). "Orthodontic tooth movement analysed by the Finite Element Method." *Biomaterials*, 5(6), 347-51.

135 Korioth, T. W., and Hannam, A. G. (1994). "Deformation of the human mandible during simulated tooth clenching." *J Dent Res*, 73(1), 56-66.

136 Takahashi, N., Kitagami, T., and Komori, T. (1980). "Behaviour of teeth under various loading conditions with finite element method." *J Oral Rehabil*, 7(6), 453-61.

137 Atmaram, G. H., and Mohammed, H. (1981). "Estimation of physiologic stresses with a natural tooth considering fibrous PDL structure." *J Dent Res*, 60(5), 873-7.

138 Thresher, R. W., and Saito, G. E. (1973). "The stress analysis of human teeth." *J Biomech*, 6(5), 443-9.

139 Jones, M. L., Hickman, J., Middleton, J., *et al.* (2001). "A validated finite element method study of orthodontic tooth movement in the human subject." *J Orthod*, 28(1), 29-38.

140 Poppe, M., Bourauel, C., and Jager, A. (2002). "Determination of the elasticity parameters of the human periodontal ligament and the location of the center of resistance of single-rooted teeth a study of autopsy specimens and their conversion into finite element models." *J Orofac Orthop*, 63(5), 358-70.

141 Ziegler, A., Keilig, L., Kawarizadeh, A., *et al.* (2005). "Numerical simulation of the biomechanical behaviour of multi-rooted teeth." *Eur J Orthod*, 27(4), 333-9.

142 McPhee, S. J., Lingappa, V. R., Ganong, W. F., *et al.* (1995). *Pathophysiology of disease, an introduction to clinical medicine*, 1st ed.; Appleton & Lange Stamford, Connecticut.

143 Roehrborn, C. G., Bartsch, G., Kirby, R., *et al.* (2001). "Guidelines for the diagnosis and treatment of benign prostatic hyperplasia: a comparative, international overview." *Urology*, 58(5), 642-50.

144 Krouskop, T. A., Wheeler, T. M., Kallel, F., *et al.* (1998). "Elastic moduli of breast and prostate tissues under compression." *Ultrason Imaging*, 20(4), 260-74.

145 Phipps, S., Yang, T. H., Habib, F. K., *et al.* (2005). "Measurement of the mechanical characteristics of benign prostatic tissue: a novel method for assessing benign prostatic disease." *Urology*, 65(5), 1024-8.

146 Phipps, S., Yang, T. H., Habib, F. K., *et al.* (2005). "Measurement of tissue mechanical characteristics to distinguish between benign and malignant prostatic disease." *Urology*, 66(2), 447-50.

147 Parker, K. J., Fu, D., Graceswki, S. M., *et al.* (1998). "Vibration sonoelastography and the detectability of lesions." *Ultrasound Med Biol*, 24(9), 1437-47.

148 Humphrey, J. D., and Delange, S. L. (2004). *An introduction to biomechanics: solids and fluids, analysis and design*, Springer-Verlag, New York.

149 Bischoff, J. E., Arruda, E. M., and Grosh, K. (2004). "A rheological network model for the continuum anisotropic and viscoelastic behavior of soft tissue." *Biomech Model Mechanobiol*, 3(1), 56-65.

150 Boyce, B. L., Jones, R. E., Nguyen, T. D., *et al.* (2007). "Stress-controlled viscoelastic tensile response of bovine cornea." *J Biomech*, 40(11), 2367-76.

151 McCreery, G. L., Trejos, A. L., Patel, R. V., *et al.* "Evaluation of Force Feedback Requirements for Minimally Invasive Lung Tumour Localization." *IEEE/RSJ International Conference on Intelligent Robots and Systems*, San Diego.

152 Finlay, J. B., and Brown, I. A. (1971). "Dynamic mechanical testing of living skin " *Rheologica Acta*, 10(1), 71-76.

153 Ahearne, M., Yang, Y., Then, K. Y., *et al.* (2007). "An indentation technique to characterize the mechanical and viscoelastic properties of human and porcine corneas." *Ann Biomed Eng*, 35(9), 1608-16.

154 Elsheikh, A. (2008). "Material Characterisation of Corneal Tissue." available from :http://www.personal.dundee.ac.uk/~aielshei/material%20charaterisation.html.

155 Viidik, A. (1972). "Simultaneous mechanical and light microscopic studies of collagen fibers." *Z Anat Entwicklungsgesch*, 136(2), 204-12.

156 Menard, K. (1999). *Dynamic mechanical analysis: a practical introduction* CRC Press LLC, New York.

157 Kiss, M. Z., Hobson, M. A., Varghese, T., *et al.* (2006). "Frequency-dependent complex modulus of the uterus: preliminary results." *Phys Med Biol*, 51(15), 3683-95.

158 Worthington, A. E., and Sherar, M. D. (2001). "Changes in ultrasound properties of porcine kidney tissue during heating." *Ultrasound Med Biol*, 27(5), 673-82.

159 Worthington, A. E., Trachtenberg, J., and Sherar, M. D. (2002). "Ultrasound properties of human prostate tissue during heating." *Ultrasound Med Biol*, 28(10), 1311-8.

160 Barnett, S. B., Rott, H. D., ter Haar, G. R., *et al.* (1997). "The sensitivity of biological tissue to ultrasound." *Ultrasound Med Biol*, 23(6), 805-12.

161 Zheng, Y. P., and Mak, A. F. (1996). "An ultrasound indentation system for biomechanical properties assessment of soft tissues in-vivo." *IEEE Trans Biomed Eng*, 43(9), 912-8.

162 Zheng, Y. P., and Mak, A. F. T. "Extraction of effective Young's Modulus of skin and subcutaneous tissues from manual indentation data." *19th International Conference - IEEE/EMBS* Chicago.

163 Hayes, W. C., Keer, L. M., Herrmann, G., *et al.* (1972). "A mathematical analysis for indentation tests of articular cartilage." *J Biomech*, 5(5), 541-51.

164 Krouskop, T. A., Dougherty, D. R., and Vinson, F. S. (1987). "A pulsed doppler ultrasonic system for making noninvasive measurements of the mechanical properties of soft tissue." *J Rehabil Res Dev*, 24(2), 1-8.

165 Heers, G., Jenkyn, T., Dresner, M. A., *et al.* (2003). "Measurement of muscle activity with magnetic resonance elastography." *Clin Biomech*, 18(6), 537-42.

166 Manduca, A., Oliphant, T. E., Dresner, M. A., *et al.* (2001). "Magnetic resonance elastography: non-invasive mapping of tissue elasticity." *Med Image Anal*, 5(4), 237-54.

167 Kruse, S. A., Rose, G. H., Glaser, K. J., *et al.* (2008). "Magnetic resonance elastography of the brain." *Neuroimage*, 39(1), 231-7.

168 Huwart, L., Sempoux, C., Vicaut, E., *et al.* (2008). "Magnetic resonance elastography for the noninvasive staging of liver fibrosis." *Gastroenterology*, 135(1), 32-40.

169 Huwart, L., and van Beers, B. E. (2008). "MR elastography." *Gastroenterol Clin Biol*, 32(6 Suppl 1), 68-72.

170 Huwart, L., Peeters, F., Sinkus, R., *et al.* (2006). "Liver fibrosis: non-invasive assessment with MR elastography." *NMR Biomed*, 19(2), 173-9.

171 Davis, J. L. (1987). *Introduction to dynamics of continuous media*, Macmillian, New York.

172 Mondaini, R. P., and Pardalos, P. M. (2008). *Mathematical modelling of biosystems*, Springer-Verlag, Berlin.

173 Ward, I. M., and Sweeney, J. (2004). *An introduction to the mechanical properties of solid polymers*, 2nd ed.; John Wiley & Sons Ltd, West Sussex.

174 Meyers, M. A., and Chawla, K. K. (2008). *Mechanical behaviour of materials*,2nd ed.; Cambridge University Press, Cambridge.

175 Markert, R. (2006). "Strukturdynamik," Technische Universität Darmstadt, Darmstadt.

176 Gasch, R., and Knothe, K. (1987). *Strukturdynamik Band 1: Diskrete Systeme*, Springer-Verlag Heidelberg.

177 Stroud, K. A. (1992). *Further engineering mathematics* 2nd ed.; MacMillian, London.

178 Dietrich, E., and Schulze, A. (1998). *Richtlinien zur Beurteilung von Messsystemen und Prozessen, Abnahme von Fertigungseinrichtungen (mit Originalrichtlinien von Ford, General Motors und Daimler-Benz)*, Carl Hanser Verlag München

179 Elsheikh, A., Brown, M., Alhasso, D., *et al.* (2008). "Experimental assessment of corneal anisotropy." *J Refract Surg*, 24(2), 178-87.

180 Doughty, M. J., and Bergmanson, J. P. (2004). "Collagen fibril characteristics at the corneo-scleral boundary and rabbit corneal stromal swelling." *Clin Exp Optom*, 87(2), 81-92.

181 Huang, Y., and Meek, K. M. (1999). "Swelling studies on the cornea and sclera: the effects of pH and ionic strength." *Biophys J*, 77(3), 1655-65.

182 Tohill, R., Hien, M. R., McGuinness, N., *et al.* (2009). "Short-term stress relaxation of porcine periodontal ligament – finding an appropriate visco-elastic model." *IFMBE proceedings series*, 25/11, 335-338.

183 Tohill, R., Hien, M., McGuinness, N., *et al.* (2008). "Measurement of the short-term viscoelastic properties of the periodontal ligament using stress relaxation." 4th European Conference of the IFMBE, 1467-1470.

184 Uvarov, A. I. (1987). "Large axisymmetric flexure and stability of locally loaded shell of revolution." *International Applied Mechanics*, 23(3), 234-238.

185 Ugural, A. C. (1999). *Stresses in plates and shells*, 2nd; McGraw-Hill Iinternational Editions, Singapore.

186 Wahl, A. M., and Lobo, G. (1930). "Stresses and deflections in flat circular plates with circular holes." *Trans. ASME, J. Appl. Mech.*, 52(3), 29-43.

187 Tijsseling, A. S., Lambert, M. F., Simpson, A. R., *et al.* (2008). "Skalak's extended theory of water hammer." *Journal of Sound and Vibration*, 310, 718-728.

188 Massey, B., and Ward-Smith, J. (2006). *Mechanics of Fluids* Taylor & Francis, London

189 Sharp, B. B. (1996). *Water hammer: practical solutions*,2nd ed.; Butterworth-Heinemann, Oxford

190 Kurita, Y., Kempf, R., Iida, Y., *et al.* (2008). "Contact-based stiffness sensing of human eye." *IEEE Trans Biomed Eng*, 55(2,1), 739-45.

191 Pierscionek, B. K., Asejczyk-Widlicka, M., and Schachar, R. A. (2007). "The effect of changing intraocular pressure on the corneal and scleral curvatures in the fresh porcine eye." *Br J Ophthalmol*, 91(6), 801-3.

192 Dohadwala, A. A., Munger, R., and Damji, K. F. (1998). "Positive correlation between Tono-Pen intraocular pressure and central corneal thickness." *Ophthalmology*, 105(10), 1849-54.

193 Goldmann, H., and Schmidt, T. (1961). "Further contribution to applanation tonometry." *Ophthalmologica*, 141, 441-56.

194 Coquart, L., Depeursinge, C., Curnier, A., *et al.* (1992). "A fluid-structure interaction problem in biomechanics: prestressed vibrations of the eye by the finite element method." *J Biomech*, 25(10), 1105-18.

195 McMonnies, C. W. (2008). "Management of chronic habits of abnormal eye rubbing." *Cont Lens Anterior Eye*, 31(2), 95-102.

196 Meindl, B. (2010). "Research on the PDL: analysis of the vibration properties and design of a testing device," University of Applied Sciences,Regensburg.

197 Natali, A., Pavan, P., Carniel, E., *et al.* (2004). "Viscoelastic response of the periodontal ligament: an experimental-numerical analysis." *Connect Tissue Res*, 45(4-5), 222-30.

198 Komatsu, K., Shibata, T., Shimada, A., *et al.* (2004). "Age-related and regional differences in the stress-strain and stress-relaxation behaviours of the rat incisor periodontal ligament." *J Biomech*, 37(7), 1097-106.

199 Mazza, E., Nava, A., Bauer, M., *et al.* (2006). "Mechanical properties of the human uterine cervix: an *in vivo* study." *Med Image Anal*, 10(2), 125-36.

200 Brosh, T., Machol, I. H., and Vardimon, A. D. (2002). "Deformation/recovery cycle of the periodontal ligament in human teeth with single or dual contact points." *Arch Oral Biol*, 47(1), 85-92.

201 Weaver, M. E., Sorenson, F. M., and Jump, E. B. (1962). "The miniature pig as an experimental animal in dental research." *Arch Oral Biol*, 7, 17-23.

202 Gasser, T. C., Ogden, R. W., and Holzapfel, G. A. (2006). "Hyperelastic modelling of arterial layers with distributed collagen fibre orientations." *J R Soc Interface*, 3(6), 15-35.

203 Duenwald, S. E., Vanderby, R., Jr., and Lakes, R. S. (2009). "Viscoelastic relaxation and recovery of tendon." *Ann Biomed Eng*, 37(6), 1131-40.

204 Ciarletta, P., Micera, S., Accoto, D., *et al.* (2006). "A novel microstructural approach in tendon viscoelastic modelling at the fibrillar level." *J Biomech*, 39(11), 2034-42.

205 Carter, D. R., and Wong, M. (2003). "Modelling cartilage mechanobiology." *Philos Trans Roy Soc Lond B Biol Sci*, 358(1437), 1461-71.

206 Romero, F. J., Pastor, A., Lopez, J., *et al.* (1998). "A recruitment-based rheological model for mechanical behavior of soft tissues." *Biorheology*, 35(1), 17-35.

207 Bates, J. H. (2007). "A recruitment model of quasi-linear power-law stress adaptation in lung tissue." *Ann Biomed Eng*, 35(7), 1165-74.

208 Hildebrandt, J. (1970). "Pressure-volume data of cat lung interpreted by a plastoelastic, linear viscoelastic model." *J Appl Physiol*, 28(3), 365-72.

209 Suki, B., Barabasi, A. L., and Lutchen, K. R. (1994). "Lung tissue viscoelasticity: a mathematical framework and its molecular basis." *J Appl Physiol*, 76(6), 2749-59.

210 Thamrin, C., Janosi, T. Z., Collins, R. A., *et al.* (2004). "Sensitivity analysis of respiratory parameter estimates in the constant-phase model." *Ann Biomed Eng*, 32(6), 815-22.

211 Egiazaryan, É. L. (2001). "Microelectronic Accelerometer with Lateral Compensation." *Measurement Techniques*, 44(5), 488-493.

Appendix

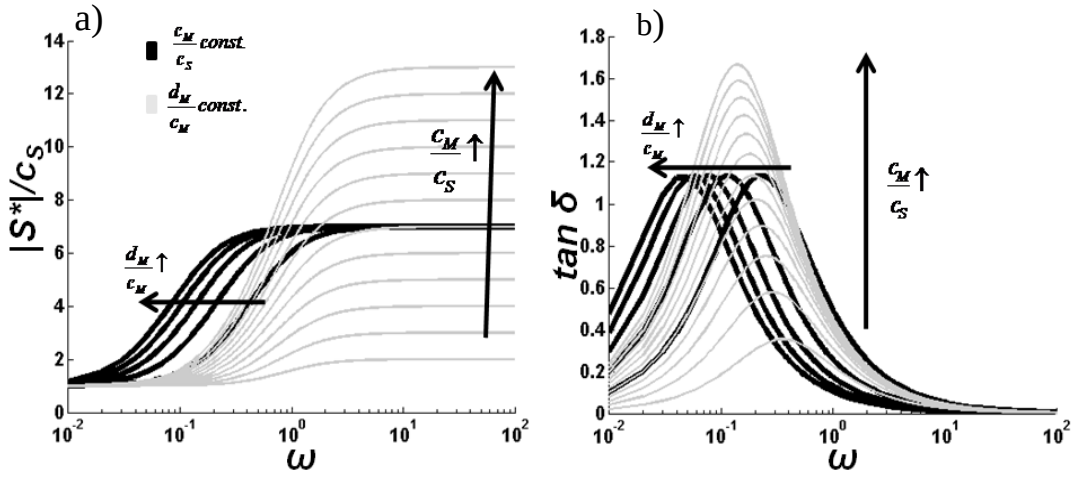

Figure 9-1: Mechanical behaviour of SLS model with frequency for various values of the parameters a) amplitude ratio b) phase difference

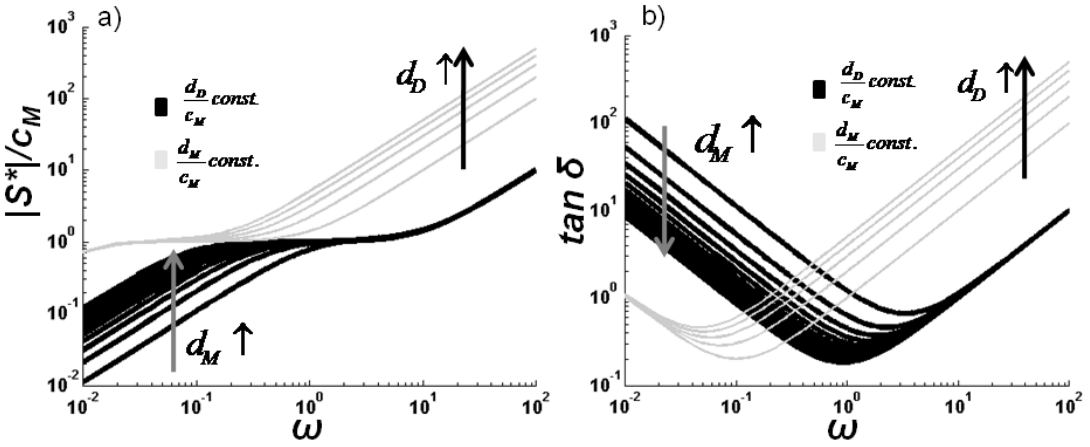

Figure 9-2: Mechanical behaviour with frequency of a damper in parallel with a Maxwell model for various values of the parameters a) amplitude ratio b) phase difference

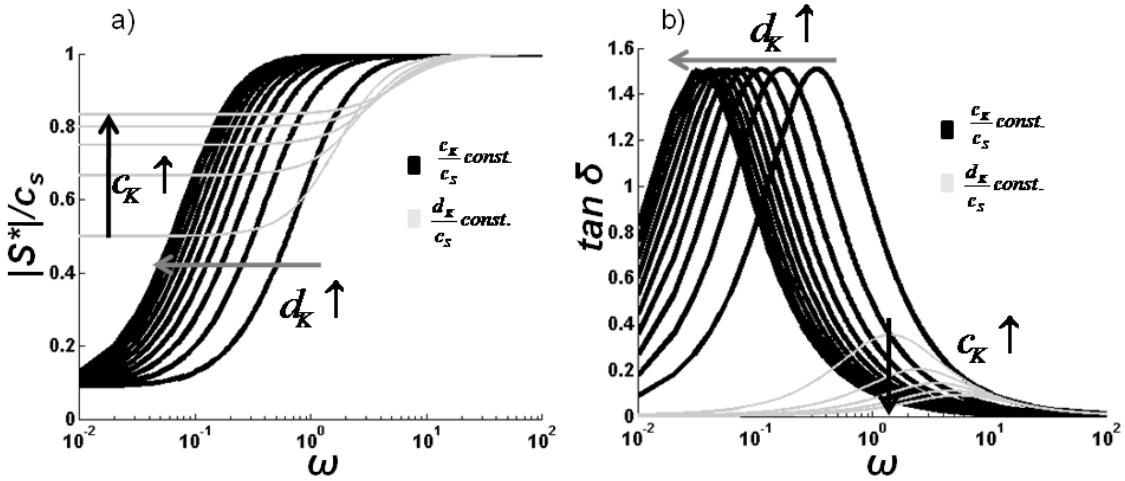

Figure 9-3: Mechanical behaviour with frequency of a Spring in series with a Kelvin model for various values of the parameters a) amplitude ratio b) phase difference

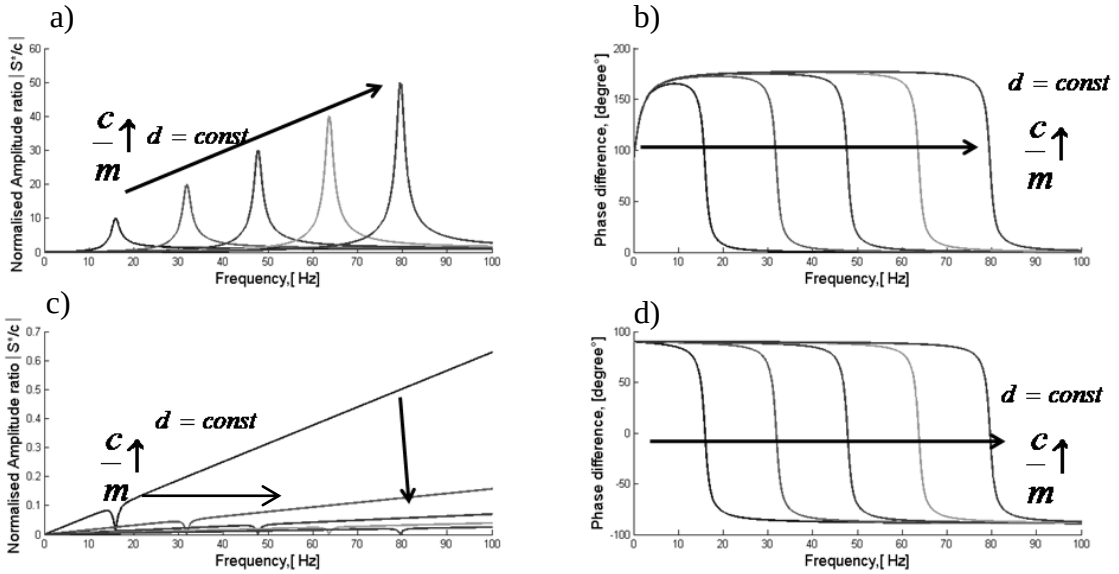

Figure9-4: Series model, displacement excitation of spring: a),b) normalised amplitude ratio and phase difference for varying *c*/*m* with constant damper parameter. Series model, displacement excitation of dashpot: c), d) normalised amplitude ratio and phase difference for varying *c*/*m* with constant damper parameter.

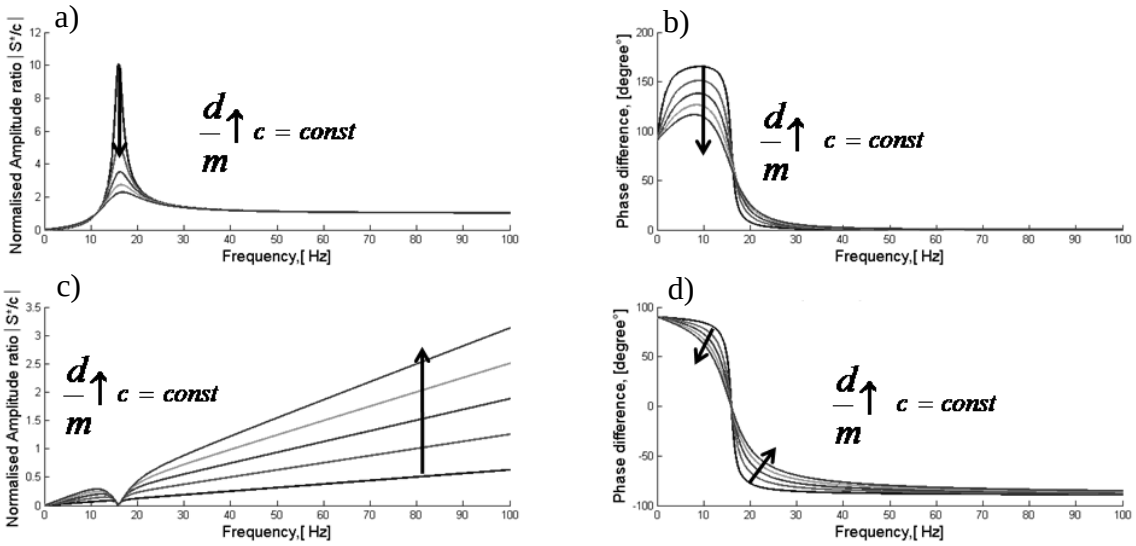

Figure 9-5: Series model, displacement excitation of spring: a), b) normalised amplitude ratio and phase difference for varying *d*/*m* with constant spring parameter. Series model, displacement excitation of spring: c), d) normalised amplitude ratio and phase difference for varying *d*/*m* with constant spring parameter.

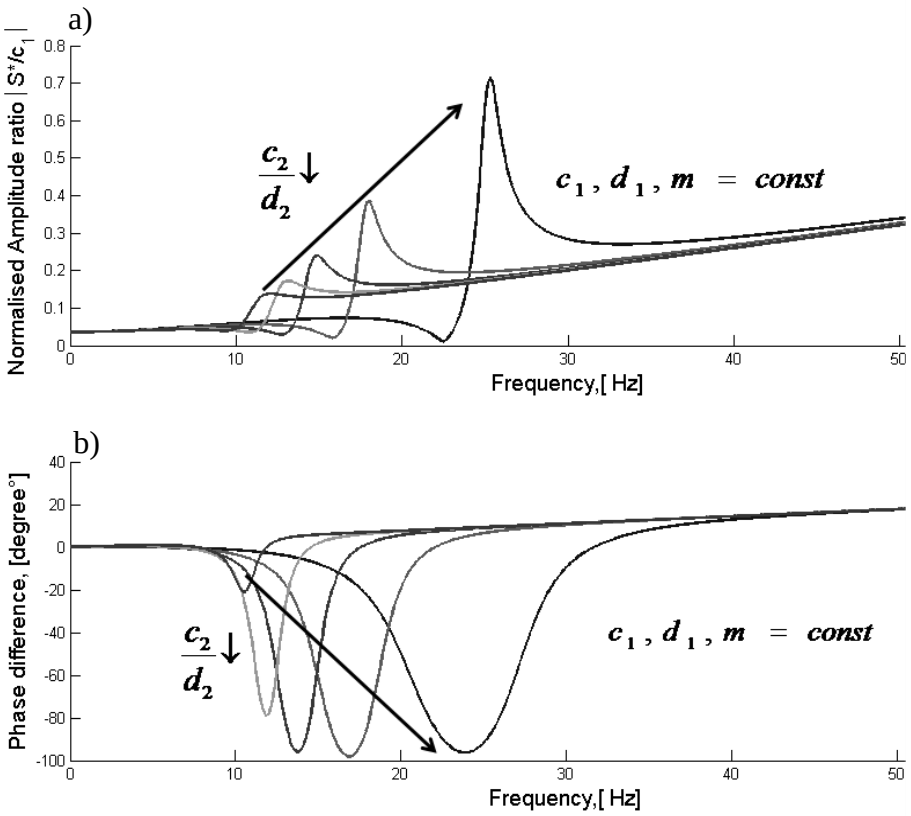

Figure 9-6: Parallel-series model with displacement excitation of parallel elements for varying c_2/d_2 with constant c_1, d_1 and m.

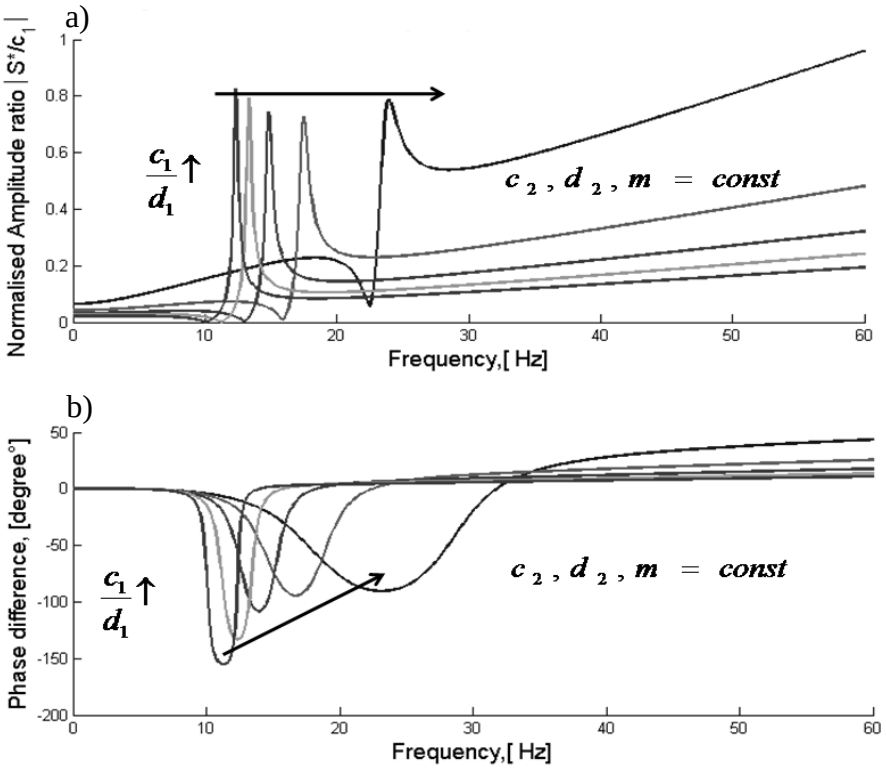

Figure 9-7: Parallel-series model with displacement excitation of parallel elements for varying c_1/d_1 with constant c_2, d_2 and m parameter